The Dynamics of Geometrically Compliant Mooring Systems

by

Jason I. Gobat

S.M., MIT/WHOI Joint Program (1997)
B.S., University of California, San Diego (1993)
B.A., University of California, San Diego (1993)

Submitted to the
Department of Applied Ocean Physics and Engineering, WHOI
and the
Department of Ocean Engineering, MIT
in partial fulfillment of the requirements for the Degree of

Doctor of Philosophy in Oceanographic Engineering

at the

MASSACHUSETTS INSTITUTE OF TECHNOLOGY
and the
WOODS HOLE OCEANOGRAPHIC INSTITUTION

June 2000

© Jason I. Gobat, 2000

Author........ ....
Department of Applied Ocean Physics and Engineering, WHOI
Department of Ocean Engineering, MIT
April 25, 2000

Certified by ....
/
Dr. Mark A. Grosenbaugh
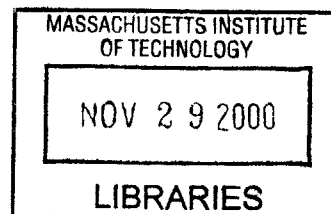Associate Scientist
Thesis Supervisor

Accepted by... ....
Prof. Michael S. Triantafyllou
Professor of Ocean Engineering
Chairman, Joint Committee on Oceanographic Engineering

The Dynamics of Geometrically Compliant Mooring Systems

by

Jason I. Gobat

Abstract

Geometrically compliant mooring systems that change their shape to accommodate deformations are common in oceanographic and offshore energy production applications. Because of the inherent geometric nonlinearities, analyses of such systems typically require the use of a sophisticated numerical model. This thesis describes one such model and uses that model along with experimental results to develop simpler forms for understanding the dynamic response of geometrically compliant moorings.

The numerical program combines the box method spatial discretization with the generalized-α method for temporal integration. Compared to other schemes commonly employed for the temporal integration of the cable dynamics equations, including box method, trapezoidal rule, backward differences, and Newmark's method, the generalized-α algorithm has the advantages of second-order accuracy, controllable numerical dissipation, and improved stability when applied to the nonlinear problem. The numerical program is validated using results from laboratory and field experiments.

Field experiment and numerical results are used to develop a simple model for dynamic tension response to vertical motion in geometrically compliant moorings. As part of that development, the role of inertia, drag, and stiffness in the tension response are explored. For most moorings, the response is dominated by inertial and drag effects. The simple model uses just two terms to accurately capture these effects, including the coupling between inertia and drag. The separability of the responses to vertical and horizontal motions is demonstrated and a preliminary model for the response to horizontal motions is presented.

The interaction of the mooring line with the sea floor in catenary moorings is considered. Using video and tension data from laboratory experiments, the tension shock condition at the touchdown point and its implications are observed for the first time. The lateral motion of line along the bottom associated with a shock during unloading may be a significant cause of chain wear in the touchdown region. Results from the laboratory experiments are also used to demonstrate the suitability of the elastic foundation approach to modeling sea floor interaction in numerical programs.

Thesis Supervisor: Dr. Mark A. Grosenbaugh

Acknowledgments

Like anyone else, I have relied on other graduate students, past and present, to help me through the past several years. Though they maybe would not recognize it in its current instantiation, the foundation for the numerical program described in this thesis was ably

laid down by Chris Howell and Thanassis Tjavaras in their Ph.D. theses. On the software front I must also thank Darren Atkinson, who taught me just about everything useful that I know about programming. My neighbor in the trailer for many years, Tad Snow, was a good friend and a willing and capable sounding board as I developed many of the ideas that form the basis of the thesis. Sean McKenna and I are just about on the same academic schedule and I have greatly appreciated having him as a friend throughout the many phases of graduate school.

My mom and dad have always been supportive of my goals, even when they seemed to change overnight. Their love and support is a great gift. I would also like to thank Squombat for making sure that I will have something to keep me busy long past graduate school.

Finally, and in words that must be inadequate, I thank my wife Allison. If not for her I would almost certainly be someplace else right now and I know I wouldn't be having this much fun. A degree is nice, but her love is unquestionably the greatest thing in my life.

Contents

List of Figures

14

15

17

List of Tables

Chapter 1

Introduction

A mooring system is typically understood as any type of cable, chain, rope, or tether assembly that connects a floating or subsurface buoyant object (ship, buoy, platform) to an anchoring system fixed on the sea floor. The floating object will move with environmental forcing, but the mooring system will contain the movements to some area (the watch circle) centered about the anchoring system. Any mooring system must provide compliance or flexibility to accommodate deformations induced by currents and by forcing with periods ranging from hours (tides) to seconds (wind waves) without over-tensioning the system components.

This flexibility is typically achieved either through the use of elastically compliant members such as rubber tethers or long lengths of synthetic rope, or through geometrically compliant configurations in which the system accommodates deformations by changing shape without stretching. The geometrically compliant approach is more common in situations where adequate compliance or a combination of strength and compliance cannot be provided by taught elastic members. This is the case in extremely shallow water, where the lengths of the rope or tethers are so short as to limit their compliance. Geometric compliance is also often found in offshore deep water applications where the pipe sections can be made relatively flexible in bending (through the use of short lengths of pipe and flexible joints), but not in axial stretching. Examples of geometrically compliant mooring shapes are shown in figure 1-1.

The shallow water mooring shown in figure 1-1(a) illustrates the type of mooring typically used to moor oceanographic, meteorological, and aids-to-navigation buoys in shallow
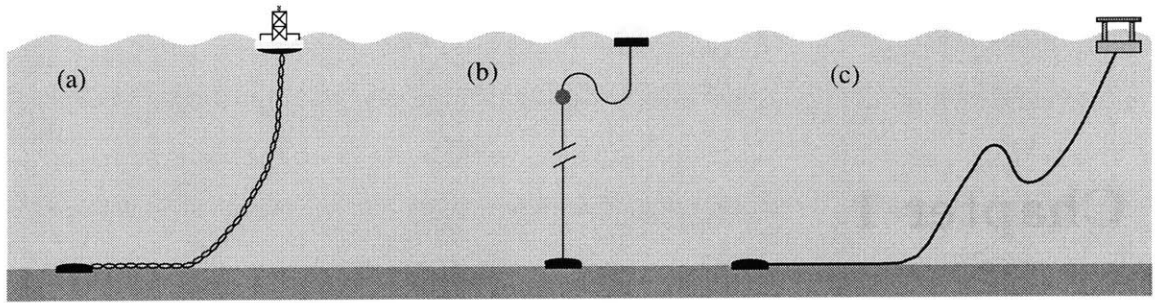
Figure 1-1: Examples of geometric compliance in mooring and riser systems: (a) shallow water buoy mooring, (b) deep water oceanographic mooring, and (c) lazy wave riser configuration.

water (on the order of 100 m) [5, 13]. The typical mooring for this sort of application consists entirely of lengths of chain, with instruments possibly attached between chain segments. We say that this type of system is geometrically compliant because its primary mechanism to accommodate the motion of the buoy is to lift and lower chain to and from the bottom, thus changing its shape. As long as chain remains on the bottom in the steady state configuration, the system is typically more flexible geometrically than it is elastically.

The advantages to this arrangement include very high strength due to the use of chain as the primary strength member, and the ability to deploy this configuration in a variety of water depths. The primary disadvantage to this type of mooring is the need for regular replacement of the chain near the bottom of the mooring due to the abrasion of the chain on the sea bed [5, 23]. A recent alternative to this type of mooring uses elastic tethers as the primary compliance mechanism [57, 77]. These systems feature significantly reduced tensions in most sea conditions because of the much lower mass of the tethers compared to chain moorings. Drawbacks to elastic tether moorings include the inability to place instruments along the tether and their susceptibility to cutting, either in an accident or through vandalism.

The second type of system in figure 1-1 is an increasingly popular configuration for deep water surface moorings for oceanographic applications [31]. Variations on this shape are also used to moor meteorological buoys [13]. The s-curve in the mooring shape is achieved through careful placement of flotation and ballast along the line. The location of this curve at mid-depth allows for geometric compliance without a rigid bottom. Previous deep water

surface moorings achieved compliance through the incorporation of long lengths of highly stretchable synthetic rope [5]. The advantage to the geometrically compliant system in figure 1-1(b) is the ability to run conductive electromechanical cable along the full length of the mooring to bring signals from subsurface instruments to the surface for telemetry. Elastically compliant electromechanical members have only recently been introduced [75, 76] in the oceanographic community and are difficult to handle and relatively expensive, particularly for very long lengths.

Both of the above described mechanisms, an s-shape at mid-depth, and a catenary shape along the bottom are often employed together in offshore energy production systems, as pictured in figure 1-1(c). In this case the mooring line of interest is typically a pipe running from the platform to the wellhead. The platform may also be anchored (anchoring lines not shown in figure 1-1(c)) at multiple points by taut synthetic lines or heavy chain and wire lines forming a catenary similar to that described for the shallow water buoy mooring. The need for geometric compliance in the riser pipe arises from the inflexibility of these pipes to axial (elastic) deformation.

As a final consideration in this brief overview of compliant moorings, it should be noted that in addition to achieving compliance through the mooring line, either geometrically or elastically, it is possible in some cases to introduce compliance at the surface by using buoys or platforms which have a very low natural frequency (very far below typical wave frequencies) such as a spar buoy. This effectively puts a very soft compliant element between the wave forcing and the mooring line. Because spar buoys are very long and slender, they typically have low reserve buoyancy and are difficult to handle.

All of the systems pictured in figure 1-1 provide significant compliance to surface wave motions under most conditions. One well known mode under which these configurations do not provide good compliance is in the case of large currents that pull the geometric shaping out of the mooring. The impact of this failure mode can be lessened with the addition of elastic compliance into the design. The geometric compliance in these systems can also break down during a large storm in which the ability of the mooring to change shape may be limited by fluid drag on the cable. This second failure mode is more difficult to design for as it can occur even in conditions under which the static shape is preserved and may not be alleviated by secondary elastic compliance. Finally, for cases with cable resting on the sea floor, friction, adhesion and the elasticity of the bottom can affect the

ability of the system to deform geometrically. A loss of geometric compliance as a result of any of these mechanisms can lead to dangerously high tensions. A detailed analysis of geometrically compliant systems, which will lead to better prediction of these types of failures, is the primary goal of this thesis.

1.1 Analysis of compliant systems

Much of the recent analytical work relating to geometrically compliant systems has been conducted in the context of calculating the contribution of the mooring line damping to the overall system dynamics. Brown *et al.* [7] provide a review of much of the literature to date in this area. Most of the work has focused on frequency domain quasi-linearized numerical solutions for the slow drift case. Extensive model scale tests have also been carried out [55, 59, 67].

Large floating structures (ships, offshore platforms) typically have little damping and low natural frequencies for motions in the horizontal plane. For these large structures, mooring tensions at wave frequencies are much smaller than the excitation forces. At lower frequencies, the mooring forces and wave forces are more comparable. Thus, the damping provided by the motion of the mooring system plays a critical role in the response of these structures to slow drift motions [59, 96].

Motions and dynamic tension at wave frequencies are often ignored in these studies. This allows for a simplified treatment of the dynamics. For example, Nakamura *et al.* [67] used catenary formulae to calculate the integrated quasi-static velocity and acceleration along the mooring. These integrated motions allowed them to write the dynamic tension due to slow drift motions in a very simple form.

In the analyses of compliant systems developed in this thesis, the quantity of interest is typically dynamic tension rather than platform motion. Such an approach is particularly relevant in oceanographic applications where the motion of the surface platform may not be critical, but dynamic tension is dominated by wave induced motions. Knowledge of the tension is critical in these applications because components are typically not specified with large safety factors for fatigue and ultimate failure (both for cost and ease of handling reasons).

Several authors have considered the impact of wave frequency dynamics on the slow

drift damping problem. Huse and Matsumoto [52–55] used a linearized finite element model to compute the mooring line damping in the presence of a slow drift regular motion superposed with a spectrum of high frequency first-order wave motions. Their calculations showed that the damping was two to four times higher when the high frequency motions were taken into account. Similar results were obtained by Dercksen *et al.* [22] and Fylling *et al.* [32] with more sophisticated numerical models.

In other work that looked at both slow drift and wave frequency excitation, Webster [99] characterized the mooring line damping of a non-dimensionalized catenary riser system (a system shaped like that shown in figure 1-1(a)) as a function of static tension, excitation frequency and amplitude, scope, stiffness, drag, and current. The excitation was sinusoidal and either purely vertical or purely horizontal. The numerical model that he used was a time-domain nonlinear finite element code.

Webster [99] also briefly touches on the "impedance" of mooring systems which he describes in terms of the trade-offs between geometric and elastic compliance. This is a concept first introduced by Triantafyllou *et al.* [94] to characterize the ratio of elastic to catenary stiffness. They noted that fluid drag limits the ability of the mooring to deform geometrically and as a result, dynamic tensions increase.

1.2 Bottom interaction

An important part of the response in many geometrically compliant systems is the interaction of grounded line with the sea floor. Several recent papers have described numerical methods for modeling this interaction [16,56,63,89,90]. To date, however, these models have not been used to extensively analyze the implications of the bottom interaction on the total mooring response.

Thomas and Hearn [91] and Liu and Bergdahl [63] examined the bottom interaction problem in the context of mooring line damping. The results from both papers suggest that bottom interaction effects do contribute to mooring line damping, with the in-plane friction being more important than the out-of-plane effects [91].

Aranha *et al.* [2], Pesce, Aranha, and Martins [79], and Pesce *et al.* [80] have examined the curvature of riser pipes in the touchdown region using an analytical boundary layer approximation. Their goal is to provide better predictions of the bending moment to re-

duce fatigue failures. Some of the background for their analytical approach comes from work by Burridge *et al.* [12] and Burridge and Keller [11] for the motion of a string on a unilateral constraint. That work demonstrated that a shock wave will form when the velocity of the touchdown point exceeds the transverse wave speed of the cable. The analytical development in Aranha *et al.* [2] assumes that the touchdown point speed is always below this critical limit. No work has been performed that examines the implications for mooring dynamics when this assumption does not hold and shock waves do form.

1.3 Modeling tools

The problem of predicting the steady state configurations and transient motions of pipe, hose, cable, chain, and rope systems in a marine environment is encountered in numerous applications. Oftentimes, the methods of solving the problem seem equally numerous. Buoy and ship moorings, offshore platforms, and towed systems are often analyzed in very different ways, yet are at heart very similar types of structural systems.

In a 1970 survey paper, Casarella and Parsons [14] compiled an extensive list of work related to the hydrodynamic response of cable systems. Their history starts with analytical work dating from 1917 to calculate the steady state configuration of cables in air. Through 1950, treatments of the steady state problem dominated the literature in this area, with the first dynamic models for cables in water appearing in 1957. Thomas [90] provides a detailed summary of the development of the modern dynamic models, beginning with Walton and Polachek's paper in 1960 [98], and emphasizing developments in the literature from the offshore energy field.

The model developed as part of this thesis provides a nonlinear time-domain solution to the mooring dynamics problem. The other modern models described below can be similarly classified. Other types of models include frequency domain and linearized or quasi-static time domain models. While attractive for their computational efficiency, these latter types of models are typically not used for the types of highly nonlinear motions that are inherent in the phenomena that are analyzed in the thesis.

1.4 State-of-the-art time-domain models for mooring systems

Numerical models for mooring systems can be categorized in several different ways. The most often cited distinguishing characteristic of a model is the method used to discretize the physical system in space. Among the most common methods are finite elements, finite differences, and lumped parameter. While there is more universal agreement on the temporal discretization method (most use finite differences), there is some variation in the way that the temporally discretized equations are integrated in time. Beyond these distinctions are the mathematical and physical features incorporated by the various models such as bending stiffness, sea bed interaction effects, and treatment of vortex-induced vibrations.

1.4.1 Spatial discretization

Walton and Polachek [98] published the first treatment of the dynamic solution that resembles very closely the solution methods in use today. They formulate the equations of motion for discrete elements and use centered finite differences to discretize the time derivative terms and step the solution forward in time. With the addition of cable extensibility by Polachek *et al.* [81], a remarkably complete treatment of the nonlinear time domain problem existed as early as 1963. This first solution, using a force balance on discrete elements to write the equations of motion is what we now categorize as a lumped parameter method. The terminology arises from the lumping of the mass and externally applied forces at adjacent nodes which are joined by massless springs. This discretization approach has an intuitive simplicity to it and as such is relatively easy to implement. Recent models that make use of this approach are described by Huang [47] and Thomas [90, 91].

In contrast to the summation of forces approach used by lumped parameter methods, finite element methods derive their governing equations through principles of virtual work. One advantage of this approach is the possibility of a more sophisticated treatment of mass. Lumped parameter derivations must necessarily place all mass at discrete nodes and then write the governing equations. Finite element methods can derive the governing equations using an integration of the mass over the entire element, thus leading to the "consistent" mass formulation [62]. The starting point for finite element methods as

applied to the marine cable problem is typically a discrete element, much like the lumped parameter methods. Examples of such derivations include Engseth [28] and McNamara *et al.* [64]. Paulling and Webster [78], following Garrett [33], take the alternative approach of formulating differential equations of motion which are solved by the substitution of a discrete collection of shape functions which minimize the element energy. The majority of state-of-the-art programs currently being used for riser modeling are based on finite elements [61].

A third approach is to write the continuous partial differential equations and then apply a spatial discretization scheme based on finite differences. This is the approach taken by Ablow and Schechter [1] among others. We distinguish between this and lumped parameter methods based on the starting point, which in this case is an infinitesimally small differential element and in the lumped parameter case is a finite discrete element. Given similar physical assumptions the two methods are entirely equivalent, as demonstrated by Huang [47]. The distinction between this and the lumped parameter approach is based largely on the applications of the method. Many of the numerical solutions for tow cable dynamics have used finite differences of the continuous partial differential governing equations. Another reason for the distinction in this case is simply that, to date, most pure lumped parameter methods do not include the effects of bending stiffness in the equations of motion [91][1]. Authors deriving continuous forms of the governing equations have easily incorporated this effect [10,46,93]. The model development detailed in chapter 2 is based on this approach.

Finally, a few alternatives to the spatial discretizations outlined above have appeared in the literature. Chiou and Leonard [17] and Sun *et al.* [86] describe the Direct Integration Method, whereby a boundary value problem is recast as a set of initial value problems. Each initial value problem is integrated spatially from a boundary with known boundary conditions, and the solutions from these integrations are combined to form a total solution that satisfies all boundary conditions. Because the initial value approach allows for explicit numerical integration in space, the method has the advantage that the solution of large linear systems of equations typical in implicit finite difference and finite element schemes can be avoided. There is of course a spatial discretization implied by the

---

[1] Buckham and Nahon [9] have recently incorporated bending effects into a lumped parameter model for low tension ROV tethers.

numerical integration of the transformed governing equations. Sun *et al.* [86] point out the need for a method to suppress any spurious solution components that may grow as the spatial integrations proceed along the cable. Another alternative scheme is collocation which breaks the cable into a small number of segments and fits high order Chebyshev polynomials as a solution to the governing equations over each region [15].

1.4.2 Temporal discretization

For all spatial discretization methods the resulting equations are typically written as a non-linear matrix equation known as the semi-discrete equation of motion, because the time derivatives of the vector of dependent variables are left as continuous functions. The exception to this procedure is in finite difference based solutions which typically are differenced both in space and in time as part of the same process. This leads to yet another distinction between lumped parameter and finite difference approaches. The starting point for a finite difference method is typically a set of first-order hyperbolic partial differential equations. The equations of motion for lumped parameter schemes are most often presented in matrix form as a system of second-order ordinary differential equations – the semi-discrete equation of motion.

Most temporal integration schemes in use today have their roots in the method developed by Newmark [70]. Hughes and Belytschko [50] provide a summary of the development of these types of methods in the context of linear finite element structural dynamics. The methods typically employ temporal finite differences, with a variety of different schemes used to interpolate the solution over the time step. Most classical methods can now be cast into unified multi-parameter integration schemes where an adjustment in the parameters leads to one of several different methods with different numerical properties (e.g., [44, 100, 102]). Thomas [90] studied the three "classic" methods (Newmark, Houbolt, and Wilson-θ) and their applicability to the mooring dynamics problem. He concluded that Houbolt was the best choice. This is not a surprising result – earlier, Park [74] noted that Houbolt was a good choice for highly nonlinear problems. Thomas did not consider any of the more modern developments in time integration that are taken up in more detail in chapter 2.

In addition to Newmark and its variants which are popularly employed with finite element based models, researchers in the cable dynamics field have employed a variety of

different schemes for the temporal integration problem. Chiou and Leonard [17] use simple backward finite differences. Sun *et al.* [86] use the generalized trapezoidal rule which is a first-order variant of the Newmark method; it will be discussed in some detail in chapter 2. Garrett [33] and Paulling and Webster [78] use the Adams-Moulton method, which in first-order form reduces to the trapezoidal rule. Sanders [84] used a computationally expensive but fourth-order accurate Runge-Kutta procedure. This is unusual in that most researchers have accepted first- or second-order accuracy in order to reduce computational expense.

The most popular finite difference scheme is the box method, in which the governing equations are discretized on the half-grid point in both space and time. This method was first employed for the solution of tow cable dynamics by Ablow and Schechter [1]. Since then it has been employed in both towing and mooring applications by Milinazzo *et al.* [65], Howell [46], Tjavaras [93], and Chatjigeorgiou and Mavrakos [15] among others. As will be shown, the temporal portion of this discretization is a special form of the generalized-α method to be developed in chapter 2. That development will also demonstrate that the box method is seldom the best choice of temporal discretization schemes for the cable dynamics problem. In a recent paper, Koh *et al.* [60] came to this same conclusion and proposed a modified box method that used backward differences for the temporal discretization.

1.4.3 Forcing, boundary, and material effects

There is little disagreement in the proper method of incorporating fluid forces, including buoyancy, viscous drag, and added mass forces, into state-of-the-art numerical codes. As late as 1970, Casarella and Parsons [14] did choose to distinguish between models according to the treatment of drag and whether or not tangential drag was included, but there do not appear to be any significant differences between modern approaches. Likewise, Breslin [6] laid the groundwork for a consistent treatment of buoyancy and effective tension in modern codes. One significant source of hydrodynamic forcing that has not yet been fully incorporated into a nonlinear time domain code is vortex-induced vibrations. This is an area of active research [95].

The numerical treatment of the interaction of the cable with the sea bed is also an area of active research. Three basic approaches are prevalent in the literature. Frequency domain models (e.g., [94]) and some time domain models (e.g., [89]) cut the mooring off

at the touchdown point and attach an equivalent linear spring and/or dashpot. This approach is only valid for small dynamic motions about the static touchdown point. A second method is the lift-off and grounding approach described by Nakajima et al. [66] and Thomas [90]. In this method, the mass of the discrete nodes or elements is reduced to zero as they approach the bottom. This simulates a perfectly rigid bottom with no impact loads (a smooth rolling and unrolling of the cable, similar to the analytical calculations of Aranha et al. [2]). Thomas noted significant numerical difficulties associated with the implementation of lift-off and grounding. The third approach is to model the sea bed as an elastic foundation. This method has been used by Inoue and Surendran [56] and Webster [99]. It is relatively easy to implement and places few restrictions on the types of systems that can be modeled. The primary difficulty with this method is in determining appropriate elastic and damping constants to associate with a given type of soil. The elastic foundation approach is the basis for the bottom interaction model developed as part of this thesis.

For material effects, modern codes may or may not include the effects of material non-linearities or bending stiffness. There is little disagreement, however, on the conditions under which these effects should be included if an accurate response calculation is to be made. Most finite element codes, developed for riser systems that are built from relatively large diameter metal pipes, do include bending stiffness, but may neglect material non-linearities without a significant loss of accuracy. In the oceanographic community where small diameter synthetic mooring lines are common, material nonlinearities can be impor-tant and bending stiffness can often be neglected. Some codes employ a hybrid approach whereby bending stiffness is included only in low tension regions as a numerical smooth-ing effect (e.g., [87]). A general purpose code should allow for both linear and nonlinear materials and for materials with and without bending stiffness.

1.5   Overview of the thesis

Chapter 2 describes the development of the generalized-α method for the time integration of the cable equations. As an example, the governing continuous partial differential equa-tions for mooring lines in two dimensions are presented and the reduction to semi-discrete form, using spatial finite differences, is derived. The analysis of the stability of a time

31

integration scheme is introduced using the stability of the box method as an example. Potential problems with the box method are described and alternative methods are explored. The generalized-α method is introduced and the stability and accuracy of the method as applied to the cable equations are presented. Comparison is made between the new method and many of the previously used methods, including backward differences and the generalized trapezoidal family.

Additional details about the numerical program, including boundary conditions and the handling of bottom interaction effects, are described in chapter 3. The algorithms used for spatial mesh refinement and adaptive time stepping are also described. Details not provided in chapter 3 are given in the appendices.

The field experiment is described in chapter 4. The centerpiece of the experiment was a heavily instrumented all chain mooring. Mooring hardware and instrumentation are described. Calibration and data quality issues are also discussed.

The model is validated and the numerical parameters used in the model are studied in chapter 5. The validation is based on analytical and experimental results for a laboratory scale hanging chain problem and on full-scale mooring data from the experiments described in chapter 4.

Chapter 6 details a statistical and analytical study of the different contributions to the dynamic tension in geometrically compliant systems. These contributions are characterized as drag, stiffness (geometric and elastic), and inertia. The study is based on experimental data and extensive numerical runs. Statistical and spectral analyses are used along with parametric numerical studies to isolate each of the different tension mechanisms. The result of these analyses is a very simple model that can be used to predict dynamic tension given a basic characterization of mooring properties, steady state tension, and sea state parameters. The chapter concludes with an investigation of the effect of the directionality (vertical, horizontal, vertical and horizontal, fully three-dimensional) of the input motion.

A detailed examination of the interaction between the mooring line and the bottom is presented in chapter 7. This includes numerical and laboratory simulations of cases where there is significant buckling of the line in the region near the touchdown point. The implications of the shock condition at the touchdown point are also considered.

Conclusions and recommendations for follow-on study are presented in chapter 8.

1.6 Original contributions

The numerical program developed in this thesis is based on that of Tjavaras [93] and Howell [46]. In the thesis, the program is extended to include bottom interaction effects and adaptive discretizations in time step and mesh density. A new temporal integration scheme, the generalized-α method, is developed and placed in the context of the recent structural analysis literature. An analysis of the stability and accuracy of the overall procedure is presented and comparisons are made with other schemes. The new procedure has substantially improved stability properties when compared to the old method. The model validation detailed in chapter 5 is new for this particular numerical model.

The analysis of dynamic tension in geometrically compliant systems in chapter 6, using regular and random, vertical, horizontal and three-dimensional input motions, and a broad range of hydrodynamic and material parameters, is more extensive than any of the previous work in this area. The approach to and the development of the simple formula for predicting dynamic tension in these system is unique to this thesis.

Finally, the consideration of the extreme responses of the mooring line on the bottom is new. Previous authors [2,94] have limited their analyses to the subsonic case. This is the first time that the shock criterion has been experimentally verified and the implications of the tension shocks observed and discussed.

Chapter 2

Development of the Time Integration Algorithm

2.1 Governing partial differential equation

Detailed derivations of the three-dimensional dynamic governing equations for a cable with bending stiffness suspended in water are provided by Tjavaras [93]. For completeness, a derivation of the two-dimensional equations, upon which the analyses presented in this chapter are based, is provided in Appendix A. While the procedure developed below can be applied equally well to both two- and three-dimensional models (as will be illustrated through the use of both in subsequent chapters), the two-dimensional equations are used here for simplicity and succinctness; the two-dimensional model requires six equations where the three-dimensional model requires thirteen. The two-dimensional equations for

a nonlinearly elastic cable with bending stiffness in steady current are

$$T'(\epsilon)\frac{\partial e}{\partial s} - S_n\frac{\partial \phi}{\partial s} - m\frac{\partial u}{\partial t} + mv\frac{\partial \phi}{\partial t} - w_0\cos\phi$$

$$-\frac{1}{2}\rho_w d\pi C_{d_t} u_r\,|u_r|\,\sqrt{1+\epsilon} = 0, \tag{2.1}$$

$$\frac{\partial S_n}{\partial s} + T(\epsilon)\frac{\partial \phi}{\partial s} - (m+m_a)\frac{\partial v}{\partial t} - \left[mu + \left(\rho_w\frac{\pi d^2}{4}+m_a\right)(U\cos\phi + V\sin\phi)\right]\frac{\partial \phi}{\partial t}$$

$$+ w_0\sin\phi - \frac{1}{2}\rho_w d C_{d_n} v_r\,|v_r|\,\sqrt{1+\epsilon} = 0, \tag{2.2}$$

$$\frac{\partial u}{\partial s} - v\frac{\partial \phi}{\partial s} - \frac{\partial \epsilon}{\partial t} = 0, \tag{2.3}$$

$$\frac{\partial v}{\partial s} + u\frac{\partial \phi}{\partial s} - (1+\epsilon)\frac{\partial \phi}{\partial t} = 0, \tag{2.4}$$

$$\frac{\partial \phi}{\partial s} - \Omega_3 = 0, \tag{2.5}$$

$$EI\frac{\partial \Omega_3}{\partial s} + S_n\left(1+\epsilon\right)^3 = 0. \tag{2.6}$$

The cable properties are defined by the tension strain relationship, $T(\epsilon)$, wet weight, w_0, mass, m, and added mass, m_a, per unit length, diameter, d, and normal and tangential drag coefficients, C_{d_n} and C_{d_t}. The motion and force state of the cable is completely described by five degrees of freedom (DOF): tangential and normal velocity, u and v, strain, ϵ, shear force, S_n, and inclination, ϕ. A sixth DOF, the curvature of the cable, Ω_3, is introduced to remove higher order derivatives of ϕ. The current is given in the global vertical and horizontal coordinates by U and V, respectively. The relative velocities in local coordinates are given by

$$u_r = u - U\cos\phi - V\sin\phi, \tag{2.7}$$

$$v_r = v + U\sin\phi - V\cos\phi. \tag{2.8}$$

The independent variables are s, the Lagrangian coordinate measuring length along the unstretched cable and t, time. Equations 2.1 through 2.6 can be cast in matrix – vector

form as

$$\mathbf{M}\frac{\partial \mathsf{Y}}{\partial t} + \mathbf{K}\frac{\partial \mathsf{Y}}{\partial s} + \mathsf{F}\left(\mathsf{Y}, s, t\right) = 0 \qquad (2.9)$$

where $\mathsf{Y} = [\epsilon, S_n, u, v, \phi, \Omega_3]^{\mathrm{T}}$ and the mass and stiffness matrices, $\mathbf{M}$ and $\mathbf{K}$, and the forcing vector F are defined in appendix A.

2.2 Discretization of the governing equation

The discretization of the partial differential governing equation can proceed in several different ways. A straightforward method is to use finite differences in both space and time using the box method. This is the approach taken by Ablow and Schechter [1], Howell [46], Tjavaras [93], Chatjigeorgiou and Mavrakos [15], and others. With this scheme, the discrete equations are written using what look like traditional backward differences, but because the discretization is applied on

Figure 2-1: Stencil of the box method.

the half-grid points the method is second-order accurate (see appendix B). The stencil for the method is shown in figure 2-1. The result is a four point average centered around the half-grid point. Equation 2.9 becomes

$$\left(\mathbf{M}_j^i + \mathbf{M}_j^{i-1}\right)\left(\frac{\mathsf{Y}_j^i - \mathsf{Y}_j^{i-1}}{\Delta t}\right) + \left(\mathbf{M}_{j-1}^i + \mathbf{M}_{j-1}^{i-1}\right)\left(\frac{\mathsf{Y}_{j-1}^i - \mathsf{Y}_{j-1}^{i-1}}{\Delta t}\right)$$

$$+ \left(\mathbf{K}_{j-1}^i + \mathbf{K}_j^i\right)\left(\frac{\mathsf{Y}_j^i - \mathsf{Y}_{j-1}^i}{\Delta s}\right) + \left(\mathbf{K}_{j-1}^{i-1} + \mathbf{K}_j^{i-1}\right)\left(\frac{\mathsf{Y}_j^{i-1} - \mathsf{Y}_{j-1}^{i-1}}{\Delta s}\right)$$

$$+ \left(\mathsf{F}_j^i + \mathsf{F}_{j-1}^i + \mathsf{F}_j^{i-1} + \mathsf{F}_{j-1}^{i-1}\right) = 0.0 \quad (2.10)$$

The subscripts j define the spatial grid points (the nodes) and the superscripts i define the temporal grid points (the time steps). For n nodal points, equation 2.10 defines a system of $6(n-1)$ equations to be solved for the $6n$ dependent variables at time step i. The six equations needed to complete the problem are provided by boundary conditions.

2.3 Stability of the box method

The most convenient way to analyze the stability of the box method is to consider the stability of the method as applied to an equivalent linear, single DOF system in semi-discrete form. The first step is to apply the half-grid spatial discretization of the box method to equation 2.9. At each half-grid point we derive a set of six equations which we can write as

$$\tilde{\mathbf{M}}_{j-\frac{1}{2}} \begin{bmatrix} \dot{\mathbf{Y}}_{j-1} \\ \dot{\mathbf{Y}}_j \end{bmatrix} + \tilde{\mathbf{K}}_{j-\frac{1}{2}} \begin{bmatrix} \mathbf{Y}_{j-1} \\ \mathbf{Y}_j \end{bmatrix} + \tilde{\mathbf{F}}_{j-\frac{1}{2}} = 0 \qquad (2.11)$$

where the overdot signifies differentiation with respect to time. The nodal matrices $\tilde{\mathbf{M}}$ and $\tilde{\mathbf{K}}$, and vector $\tilde{\mathbf{F}}$ are defined by

$$\tilde{\mathbf{M}}_{j-\frac{1}{2}} =
\begin{bmatrix}
0 & 0 & -m_{j-1} & 0 & (mv)_{j-1} & 0 \\
0 & 0 & 0 & -(m+m_a)_{j-1} & -\left[mu + \left(\rho_w \frac{\pi d^2}{4} + m_a\right)(U\cos\phi + V\sin\phi)\right]_{j-1} & 0 \\
-1 & 0 & 0 & 0 & 0 & 0 \\
0 & 0 & 0 & 0 & -(1+\epsilon)_{j-1} & 0 \\
0 & 0 & 0 & 0 & 0 & 0 \\
0 & 0 & 0 & 0 & 0 & 0
\end{bmatrix}$$

$$\begin{bmatrix}
0 & 0 & -m_j & 0 & (mv)_j & 0 \\
0 & 0 & 0 & -(m+m_a)_j & -\left[mu + \left(\rho_w \frac{\pi d^2}{4} + m_a\right)(U\cos\phi + V\sin\phi)\right]_j & 0 \\
-1 & 0 & 0 & 0 & 0 & 0 \\
0 & 0 & 0 & 0 & -(1+\epsilon)_j & 0 \\
0 & 0 & 0 & 0 & 0 & 0 \\
0 & 0 & 0 & 0 & 0 & 0
\end{bmatrix}, \qquad (2.12)$$

$$\tilde{\mathbf{K}}_{j-\frac{1}{2}} = \begin{bmatrix} -(T'_j + T'_{j-1}) & 0 & 0 & 0 & S_{nj} + S_{nj-1} & 0 \\ 0 & -2 & 0 & 0 & -(T_j + T_{j-1}) & 0 \\ 0 & 0 & -2 & 0 & v_j + v_{j-1} & 0 \\ 0 & 0 & 0 & -2 & -(u_j + u_{j-1}) & 0 \\ 0 & 0 & 0 & 0 & -2 & 0 \\ 0 & 0 & 0 & 0 & 0 & -2EI \end{bmatrix}$$

$$\begin{bmatrix} T'_j + T'_{j-1} & 0 & 0 & 0 & -(S_{nj} + S_{nj-1}) & 0 \\ 0 & 2 & 0 & 0 & T_j + T_{j-1} & 0 \\ 0 & 0 & 2 & 0 & -(v_j + v_{j-1}) & 0 \\ 0 & 0 & 0 & 2 & u_j + u_{j-1} & 0 \\ 0 & 0 & 0 & 0 & 2 & 0 \\ 0 & 0 & 0 & 0 & 0 & 2EI \end{bmatrix}, \quad (2.13)$$

$$\tilde{\mathbf{F}}_{j-\frac{1}{2}} = \begin{bmatrix} -w_0 \left(\cos\phi_j + \cos\phi_{j-1}\right) - \frac{1}{2}\rho_w \pi dC_{d_t} \left[\left(u_r |u_r| \sqrt{1+\epsilon}\right)_j + \left(u_r |u_r| \sqrt{1+\epsilon}\right)_{j-1} \right] \\ w_0 \left(\sin\phi_j + \sin\phi_{j-1}\right) + \frac{1}{2}\rho_w dC_{d_n} \left[\left(v_r |v_r| \sqrt{1+\epsilon}\right)_j + \left(v_r |v_r| \sqrt{1+\epsilon}\right)_{j-1} \right] \\ 0 \\ 0 \\ -\Omega_{3j} - \Omega_{3j-1} \\ \left[S_n (1+\epsilon)^3 \right]_j + \left[S_n (1+\epsilon)^3 \right]_{j-1} \end{bmatrix}.$$

$$(2.14)$$

The shapes of the matrices and vectors in equation 2.11 are diagrammed in figure 2-2. If we assemble the blocks associated with the $n - 1$ nodal matrices and vectors (along with appropriate boundary conditions) according to the scheme shown in figure 2-3, then it is clear that we can write the semi-discrete equation of motion for all of the dependent variables at all of the nodes as

$$\tilde{\mathbf{M}}\dot{\mathbf{Y}} + \tilde{\mathbf{K}}\mathbf{Y} + \tilde{\mathbf{F}} = 0. \qquad (2.15)$$

This is similar to the assembly procedure common in finite element analysis [48]. From the semi-discrete equation of motion, then, we proceed to reduce the system to a single DOF,

$$\boxed{\tilde{M}_{3\frac{1}{2}}}\boxed{\begin{array}{c}\dot{Y}_3\\\dot{Y}_4\end{array}} + \boxed{\tilde{K}_{3\frac{1}{2}}}\boxed{\begin{array}{c}Y_3\\Y_4\end{array}} + \boxed{\begin{array}{c}\tilde{F}_3\\\tilde{F}_4\end{array}} = \boxed{0}$$

Figure 2-2: The shape of the matrices and vectors in equation 2.11.
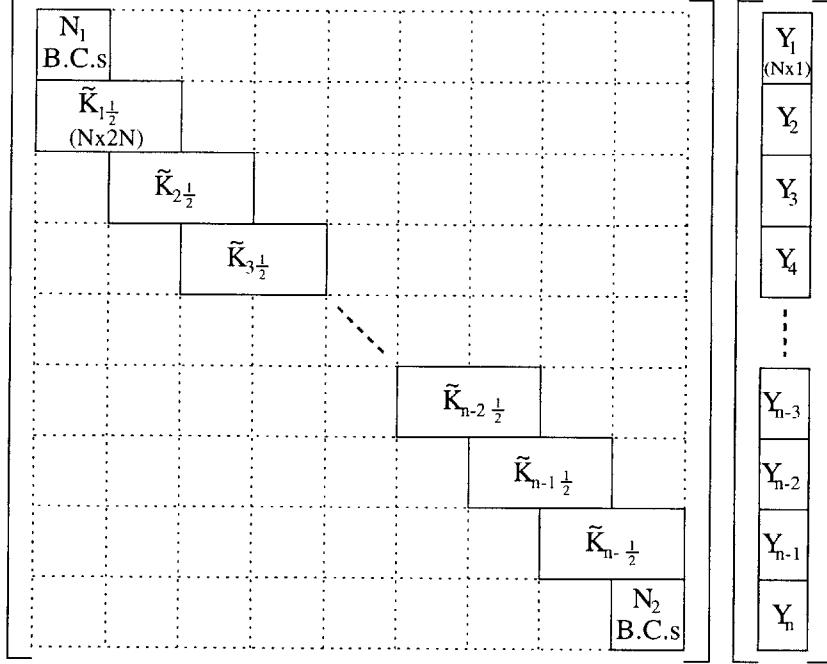
Figure 2-3: Assembly procedure for the nodal matrices and vectors into global form. With $N_1 + N_2 = N$ total boundary conditions the system is square. The procedure for the global mass matrix and force vector is similar.

linear, homogeneous problem to analyze the stability of the numerical time integration procedure. In general, the stability of equation 2.15 in full, nonlinear form, cannot be studied analytically. The usual practice is to study the same numerical procedure on a simplified model equation, and extrapolate stability properties from there [48, 100]. Numerical experiments can then be used to verify the analytical result on the full-scale problem.

The equivalent linear, homogeneous, single DOF problem is

$$\dot{y} + \omega y = 0. \tag{2.16}$$

Applying the box method's temporal discretization yields a second-order accurate approx-

imation for y^i

$$\ddot{y}^i + \ddot{y}^{i-1} + \omega \left(y^i + y^{i-1} \right) = 0, \tag{2.17}$$

where

$$\dot{y}^i + \dot{y}^{i-1} = 2 \left(\frac{y^i - y^{i-1}}{\Delta t} \right). \tag{2.18}$$

Rearranging equation 2.18 yields the recursion relationships

$$\dot{y}^i = 2 \left(\frac{y^i - y^{i-1}}{\Delta t} \right) - \dot{y}^{i-1}, \tag{2.19}$$

$$y^i = \frac{\Delta t}{2} \left(\dot{y}^i + \dot{y}^{i-1} \right) + y^{i-1}. \tag{2.20}$$

If we substitute each of the recursion relationships separately into equation 2.17 we can write equations for y^i and $\dot{y}^i$ in matrix form as

$$\begin{bmatrix} y^i \\ \dot{y}^i \end{bmatrix} = \begin{bmatrix} \frac{2-\omega\Delta t}{2+\omega\Delta t} & 0 \\ \frac{-4}{2+\omega\Delta t} & -1 \end{bmatrix} \begin{bmatrix} y^{i-1} \\ \dot{y}^{i-1} \end{bmatrix}. \tag{2.21}$$

The 2×2 matrix on the right hand side of equation 2.21 is the amplification matrix. The spectral radius, ρ, of this matrix, defined as

$$\rho = \max(|\lambda_1|, |\lambda_2|), \tag{2.22}$$

governs the growth or decay of the solution from one time step to the next [48]. $\lambda_{1,2}$ are the eigenvalues of the amplification matrix. For $\rho \leq 1$, the solution will remain steady or decay and is said to be stable. For $\rho > 1$, the solution will grow and is said to be unstable. For the time integration scheme defined by the box method,

$$\lambda_1 = \frac{2 - \omega\Delta t}{2 + \omega\Delta t}, \tag{2.23}$$

$$\lambda_2 = -1, \tag{2.24}$$

and the spectral radius is unity (and the scheme is stable) for all values of ω and Δt. When there are no conditions on stability, a procedure is called unconditionally stable.

41

An alternative analysis of the stability of the box method, using classical von Neumann stability analysis for finite difference methods, is provided in appendix B.

In spite of the unconditional stability of the box method, however, the scheme has significant problems. Because the update equation for y^i in equation 2.21 is decoupled from $\dot{y}^{i-1}$ we can simply write

$$y^i = \left(\frac{2 - \omega \Delta t}{2 + \omega \Delta t}\right) y^{i-1}.$$

(2.25)

As $\omega \Delta t$ goes to infinity this becomes

$$y^i = -y^{i-1}.$$

(2.26)

This is the phenomenon known as Crank-Nicolson noise [100], whereby the high frequency components of the solution oscillate with every time step. In a linear problem, this noise can be removed by computing step-to-step averages once the solution is completed. For a nonlinear problem, however, the noise can be a source of instability and hence should be eliminated as the solution progresses.

A second, related, problem is that the spectral radius is constant at unity. An artifact of the spatial discretization process is that at some point the high frequency (or equivalently, high spatial wave number) components of the solution are not well resolved and the numerical solution is inaccurate. For this reason it is desirous to have numerical dissipation in a scheme such that the spectral radius is less than unity for increasing values of $\omega \Delta t$ [48]. The box method has no numerical dissipation.

Finally, Wood [100] cites difficulties with averaging schemes in general as applied to nonlinear problems. For the nonlinear single DOF case, equation 2.17 can be written as

$$\dot{y}^i + \dot{y}^{i-1} + \omega^i y^i + \omega^{i-1} y^{i-1} = 0.$$

(2.27)

The update equation for y^i, equation 2.25, becomes

$$y^i = \left(\frac{2 - \omega^{i-1} \Delta t}{2 + \omega^i \Delta t}\right) y^{i-1}.$$

(2.28)

and the stability now becomes conditional as the parameter ω changes with time. The

practice suggested by Hughes [49], Wood [100] and others, for avoiding this problem is to use an averaged value of ω, such as

$$\ddot{y}^i + \ddot{y}^{i-1} + \left(\frac{\omega^i + \omega^{i-1}}{2} \right) \left(y^i + y^{i-1} \right) = 0. \tag{2.29}$$

2.4 Alternatives to the box method

Given the stability problems associated with the box method, a new solution method is sought. Hughes [48] cites the following desirable characteristics in a time-stepping algorithm:

1. Unconditional stability when applied to linear problems: Unconditional stability allows the time step to be chosen based on accuracy and resolution concerns, without regard for purely numerical issues.

2. No more than one set of implicit equations to be solved at each time step: This minimizes computational expense compared to schemes which may achieve a high order of accuracy at a significant computational cost.

3. At least second-order accuracy: This is a reflection of the constraints imposed by Dahlquist's theorem which states that a third-order accurate method with the most appropriate stability conditions does not exist [48]. Again, without a significant increase in computational effort, second-order accuracy is the best we can do.

4. Controllable algorithmic dissipation in the higher modes: In some cases with sufficiently small temporal and spatial discretizations, it may be desirable to have less high frequency numerical dissipation.

5. Self-starting, no information is needed prior to time step zero: Accuracy at time step zero (and thus accurate algorithm starting information) is critical in transient analysis applications. It is less important in cases where we can slowly ramp up a forcing scenario and are not concerned with start-up transients.

Hulbert [51] adds the following two desirable characteristics:

6. Single step, that is the solution at i depends only on information at i and $i - 1$: The advantage to a single step algorithm is that it facilitates the implementation

of an adaptive time-stepping scheme. If the time step is to be adjusted to Δt_1 in going from step $i - 1$ to step i, then the storage and computational requirement are significantly reduced if the solution at i does not also depend on information at $i - 2$ which is Δt_0 behind $i - 1$.

7. Asymptotically annihilating, or $\rho \to 0$ as $\omega \Delta t \to \infty$: Asymptotic annihilation is particularly beneficial in nonlinear problems where it is desirable to damp out high frequency noise in just one time step [19]. If the spectral radius at infinity is greater than zero, possibly destabilizing noise sources may take several time steps to decay completely.

Finally, based on the idea that nonlinear coefficients should be averaged as discussed above, we add that an algorithm should have:

8. A clear approach to the averaging of temporal coefficient matrices.

Of unconditionally stable single step algorithms, Thomas [90] compared three historically popular algorithms, Newmark, Houbolt, and Wilson-θ, as applied to mooring dynamics problems. His conclusion was that Houbolt was the best choice of the three. Other recent authors, however, have noted that Houbolt has an undesirable amount of low frequency dissipation [19, 48]. Also, while asymptotically annihilating, the numerical dissipation cannot be controlled (i.e., it can only be asymptotically annihilating). In work similar to that described here, Koh *et al.* [60] proposed a method that retained the box method's spatial discretization but replaced the temporal discretization with a backward difference scheme. This scheme is asymptotically annihilating, but only first-order accurate. Sun *et al.* [86] employ a generalized trapezoidal rule, which does allow for controllable dissipation, but is only first-order accurate when there is dissipation. Zueck [103] uses the Newmark method, which is the generalized trapezoidal rule for second-order problems, and as such also loses second-order accuracy when numerical dissipation is present.

In the structural dynamics literature, several different schemes have been proposed to satisfy the above outlined criteria. Most are developed to solve the second-order semi-discrete structural dynamics equations, but can be adapted to the first-order problem considered here. In fact, equation 2.15 has the same form as the semi-discrete equation for transient heat conduction finite element problems.

Some of the more recently proposed schemes include the HHT-α [42] and WBZ-α [101] methods which combine Newmark style difference formulas with some temporal averaging of the terms in the semi-discrete equation of motion. HHT-α averages stiffness, damping and force terms. WBZ-α averages the mass terms. Cornwell and Malkus [20] have applied the HHT-α method to the first-order semi-discrete heat conduction equation. Bazzi and Anderheggen [3] proposed a method whereby the spectral radius at infinity was directly set as the sole parameter of the scheme and no coefficient averaging was required. With dissipation, however, it is only $O(\Delta t)$ accurate. Several multi-parameter "unified" sets of algorithms have been published (e.g., [44, 71, 102]). Through appropriate choices in the parameters, these authors are able to implement many of the older methods in addition to new schemes. Hoff and Pahl [44, 45] developed what appears to be the most all-encompassing such scheme, based on six different parameters. Niemi [71] developed a set intended directly for the first-order problem. For our purposes, however, the large multi-parameter families in their most general forms do not offer a clear and direct approach to the temporal averaging of the nonlinear coefficient matrices. A reasonably complete family of algorithms that does offer such a clear approach is the generalized-α method proposed by Chung and Hulbert [18]. The method is a subset of Hoff and Pahl's [44] six parameter family and can be seen as a straightforward combination of the WBZ-α and HHT-α algorithms.

2.5 The Generalized-α method

Cornwell and Malkus [20] applied the HHT-α algorithm to the first-order problem. In this method the semi-discrete equation of motion is discretized with temporal averaging of the stiffness and force terms,

$$\tilde{\mathbf{M}}\dot{\mathbf{Y}}^i + (1 - \alpha)\tilde{\mathbf{K}}\mathbf{Y}^i + \alpha\tilde{\mathbf{K}}\mathbf{Y}^{i-1} + (1 - \alpha)\tilde{\mathbf{F}}^i + \alpha\tilde{\mathbf{F}}^{i-1} = 0. \tag{2.30}$$

The difference equation is the same as for the generalized trapezoidal rule [48],

$$\mathbf{Y}^i = \mathbf{Y}^{i-1} + \Delta t \left[(1 - \gamma)\dot{\mathbf{Y}}^{i-1} + \gamma\dot{\mathbf{Y}}^i \right]. \tag{2.31}$$

algorithm	γ	α_k	α_m	1st order problem	2nd order problem
box method	$\frac{1}{2}$	$\frac{1}{2}$	$\frac{1}{2}$	Ablow and Schechter [1]	
backward differences	1	0	0	Koh et al. [60]	
generalized trapezoidal	$[\frac{1}{2}, 1]$	0	0	Sun et al. [86]	Newmark [70]
Cornwell and Malkus	$\frac{1}{2} - \alpha$	α	0	Cornwell and Malkus [20]	HHT-α [42]
WBZ-α	$\frac{1}{2} + \alpha$	0	α		WBZ-α [101]

Table 2.1: Algorithms included in the generalized-α method. The box method and α methods are second-order accurate given the γ values as shown. The generalized trapezoidal rule is second-order accurate only for $\gamma = \frac{1}{2}$. Backward differences are always first-order accurate.

Following Chung and Hulbert's development of the generalized-α method for second-order equations, we add temporal averaging of the mass terms and equation 2.30 becomes

$$(1 - \alpha_m)\tilde{\mathbf{M}}\dot{\mathbf{Y}}^i + \alpha_m\tilde{\mathbf{M}}\dot{\mathbf{Y}}^{i-1} + (1 - \alpha_k)\tilde{\mathbf{K}}\mathbf{Y}^i + \alpha_k\tilde{\mathbf{K}}\mathbf{Y}^{i-1} + (1 - \alpha_k)\tilde{\mathbf{F}}^i + \alpha_k\tilde{\mathbf{F}}^{i-1} = 0.$$

$$(2.32)$$

The three parameter family of algorithms defined by equations 2.31 and 2.32 defines the generalized-α method for the first-order semi-discrete problem. Several of the algorithms that can be implemented through appropriate choices for γ, α_k, and α_m, are summarized in table 2.5.

2.5.1 Accuracy

As before we analyze the accuracy and stability of the method by studying a single DOF problem

$$(1 - \alpha_m)\ddot{y}^i + \alpha_m\ddot{y}^{i-1} + (1 - \alpha_k)\omega y^i + \alpha_k\omega y^{i-1} + (1 - \alpha_k)f^i + \alpha_k f^{i-1} = 0, \qquad (2.33)$$

$$y^i = y^{i-1} + \Delta t \left[(1 - \gamma)\dot{y}^{i-1} + \gamma\dot{y}^i\right]. \qquad (2.34)$$

The order of accuracy of the method is determined based on a multi-step (information at possibly more than just i and $i-1$), single-stage (only y or $\dot{y}$ appears, but not both) version of the recursion relationship defined by equations 2.33 and 2.34. If we write equation 2.33 at time step i, eliminate $\dot{y}^i$ using equation 2.34, and add the result to equation 2.33 written

at $i - 1$ and multiplied by $\Delta t(1 - \gamma)$, we find

$$[(1 - \alpha_m) + \gamma \omega \Delta t(1 - \alpha_k)] y^i$$

$$- [1 - 2\alpha_m - \omega \Delta t (1 - \gamma - \alpha_k + 2\gamma \alpha_k)] y^{i-1} - [\alpha_m - \omega \Delta t \alpha_k (1 - \gamma)] y^{i-2}$$

$$+ \Delta t \gamma (1 - \alpha_k) f^i + \Delta t (1 - \gamma - \alpha_k + 2\gamma \alpha_k) f^{i-1} + \Delta t \alpha_k (1 - \gamma) f^{i-2} = 0. \quad (2.35)$$

The local truncation error, τ, is the error associated with the use of the difference equation 2.35 instead of the exact ordinary differential equation

$$\dot{y}(t) + \omega y(t) + f(t) = 0. \tag{2.36}$$

If $y\left(t^i\right)$ is an exact solution to this ODE at time t^i, then the truncation error is defined by [48]

$$\tau(t^i) = \frac{1}{\Delta t} \sum_{n=0}^{2} \left[B_n y \left(t^{i-n} \right) + C_n f \left(t^{i-n} \right) \right], \tag{2.37}$$

where B_n and C_n are the coefficients of the y^i and f^i in equation 2.35. Expanding y and f terms in Taylor series about t^i and then eliminating forcing terms using the exact ODE, equation 2.36, yields after some algebraic manipulation

$$\tau \left(t^i \right) = \Delta t \left(\tfrac{1}{2} - \gamma - \alpha_m + \alpha_k \right) \ddot{y} \left(t^i \right) + O \left(\Delta t^2 \right). \tag{2.38}$$

Thus, the method is second-order accurate if

$$\gamma + \alpha_m - \alpha_k = \tfrac{1}{2}. \tag{2.39}$$

2.5.2 Stability

Following the same procedure as employed with the box method, the generalized-α method for first-order problems can be written in amplification matrix form as

$$\begin{bmatrix} y^i \\ \dot{y}^i \end{bmatrix} = \mathbf{A} \begin{bmatrix} y^{i-1} \\ \dot{y}^{i-1} \end{bmatrix} \tag{2.40}$$

47

where the amplification matrix is defined as

$$\mathbf{A} = \frac{1}{(1 - \alpha_m) + \gamma(1 - \alpha_k)\omega\Delta t} \begin{bmatrix} (1 - \alpha_m) - \gamma\alpha_k\omega\Delta t & \Delta t (1 - \gamma - \alpha_m) \\ -\omega & -\alpha_m - (1 - \gamma)(1 - \alpha_k)\omega\Delta t \end{bmatrix}$$

(2.41)

The eigenvalues of this matrix are

$$\lambda_{1,2} = \frac{1}{2\left[\gamma\omega\Delta t (\alpha_k - 1) + \alpha_m - 1\right]} \left[2\alpha_m - 1 + (1 - \gamma - \alpha_k + 2\gamma\alpha_k)\omega\Delta t \right.$$

$$\left. \pm\sqrt{\omega^2\Delta t^2 \left[(\gamma - 1)^2 + \alpha_k (\alpha_k + 2\gamma - 2)\right] + 2\omega\Delta t [\gamma + 2\alpha_m - \alpha_k - 1] + 1} \right]. \quad (2.42)$$

The method will be stable for all values of $\omega\Delta t$ provided that

$$\alpha_k \leq \tfrac{1}{2}, \qquad \alpha_m \leq \tfrac{1}{2}, \qquad \gamma \geq \tfrac{1}{2}. \tag{2.43}$$

Chung and Hulbert [18] suggested a procedure to reduce the scheme to a one parameter method. Taking the limit as $\omega\Delta t \to \infty$, the eigenvalues of the amplification matrix become

$$\lambda_{1,2}^{\infty} = \left\{ \frac{\alpha_k}{\alpha_k - 1}, \frac{\gamma - 1}{\gamma} \right\}. \tag{2.44}$$

Requiring second-order accuracy according to equation 2.39 yields λ^{∞} as a function of α_k and α_m only

$$\lambda_{1,2}^{\infty} = \left\{ \frac{\alpha_k}{\alpha_k - 1}, \frac{\alpha_k - \alpha_m - \frac{1}{2}}{\alpha_k - \alpha_m + \frac{1}{2}} \right\}. \tag{2.45}$$

Then, by forcing $\lambda_1^{\infty} = \lambda_2^{\infty}$ we can determine α_k and α_m such that the spectral radius at infinity takes on a specific value

$$\alpha_k = \frac{\lambda^{\infty}}{\lambda^{\infty} - 1}, \qquad \alpha_m = \frac{3\lambda^{\infty} + 1}{2\lambda^{\infty} - 2}. \tag{2.46}$$

This yields a second-order accurate algorithm in which the only parameter is the spectral radius at infinity, ρ^{∞}.

Spectral radii of some of the algorithms that are included in table 2.5 along with
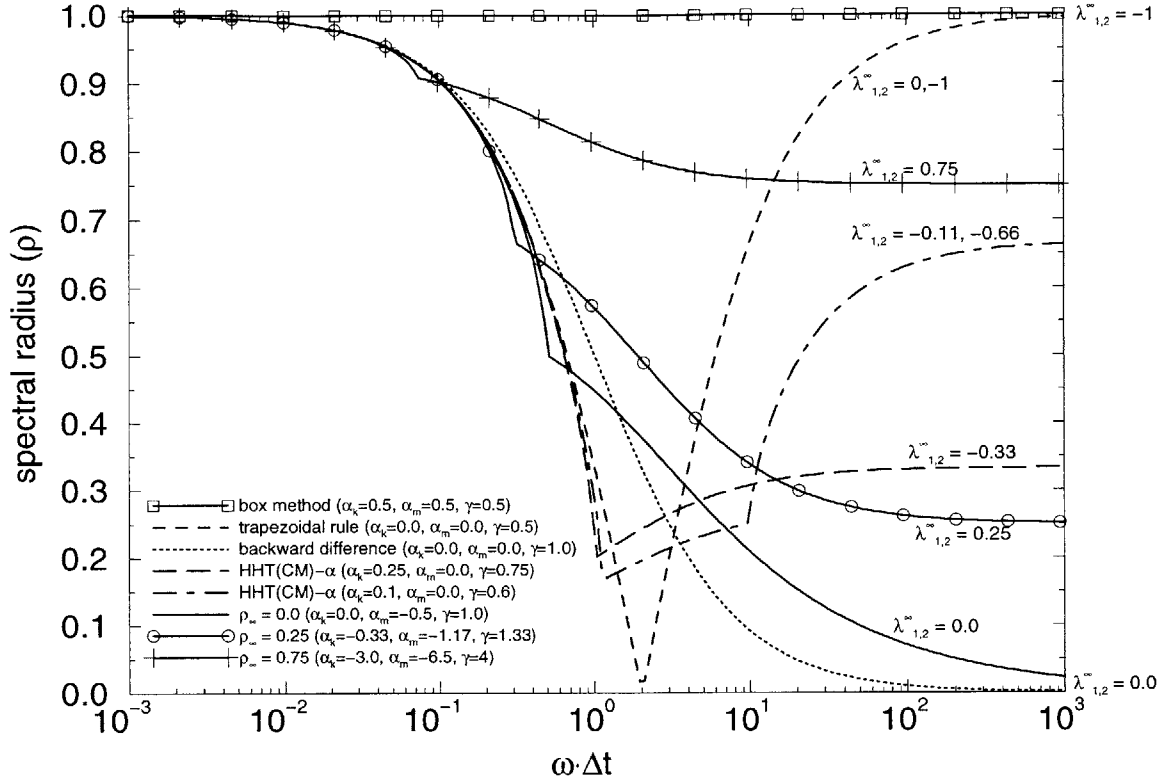
Figure 2-4: Spectral radii of the generalized-α family algorithms.

results for various values of ρ^∞ are shown in figure 2-4. Note that taking $\lambda^\infty \in [0,1)$ as the basis for the spectral radius results in a different set of algorithms than $\lambda^\infty \in [-1,0]$. For $\rho^\infty = 1$ the only option is the negative eigenvalue and this results in the box method. A non-dissipative algorithm with $\lambda^\infty = +1$ cannot be achieved. The asymptotically annihilating form of the algorithm is defined by $\alpha_k = 0$, $\alpha_m = -\frac{1}{2}$, and $\gamma = 1$.

The addition of averaging of the mass terms and the α_m parameter provides the extra degree of freedom that we need to control both the accuracy and the stability over the full frequency range. Equations 2.39 and 2.42 define a system of three equations and three unknowns. Without the third parameter, α_m, we would still have three equations but only the two unknowns, γ and α_k. The results from Cornwell and Malkus [20] reflect the fact that both λ_1 and λ_2 cannot be controlled while maintaining second-order accuracy. This leads to the bifurcations in the spectral radii, evident in figure 2-4, and at some point an increase in spectral radius with frequency. Their suggested algorithm is $\alpha_k = \frac{1}{4}$, $\gamma = \frac{3}{4}$. Without α_m, this is the only possible algorithm that drives the bifurcation point to ∞. It is the same algorithm that results from setting $\lambda^\infty = -\frac{1}{3}$ in equation 2.46.

2.6 Application to the nonlinear problem

In applying the generalized-α method to the nonlinear problem we must choose the time point at which we will evaluate $\tilde{\mathbf{M}}$, $\tilde{\mathbf{K}}$, and $\tilde{\mathbf{F}}$. A natural choice, consistent with the practice suggested by Hughes [49] for nonlinear first-order problems and exemplified by equation 2.29, is provided by the temporal averaging of terms that is already a part of the method. At time step i equation 2.32 becomes

$$
(1 - \alpha_m)\tilde{\mathbf{M}}^{i-\alpha_m}\dot{\mathbf{Y}}^i + \alpha_m\tilde{\mathbf{M}}^{i-\alpha_m}\dot{\mathbf{Y}}^{i-1}
$$
$$
+ (1 - \alpha_k)\tilde{\mathbf{K}}^{i-\alpha_k}\mathbf{Y}^i + \alpha_k\tilde{\mathbf{K}}^{i-\alpha_k}\mathbf{Y}^{i-1} + (1 - \alpha_k)\tilde{\mathbf{F}}^i + \alpha_k\tilde{\mathbf{F}}^{i-1} = 0, \quad (2.47)
$$

where the averaged coefficient matrices are defined as

$$
\tilde{\mathbf{M}}^{i-\alpha_m} = (1 - \alpha_m)\tilde{\mathbf{M}}^i + \alpha_m\tilde{\mathbf{M}}^{i-1}, \text{and} \tag{2.48}
$$
$$
\tilde{\mathbf{K}}^{i-\alpha_k} = (1 - \alpha_k)\tilde{\mathbf{K}}^i + \alpha_k\tilde{\mathbf{K}}^{i-1}. \tag{2.49}
$$

For use with the nonlinear solver described in appendix C, in which the global stiffness and mass matrices are never explicitly assembled, it is more convenient to expand equation 2.47 as

$$
(1 - \alpha_m)^2\tilde{\mathbf{M}}^i\dot{\mathbf{Y}}^i + \alpha_m(1 - \alpha_m)\left[\tilde{\mathbf{M}}^i\dot{\mathbf{Y}}^{i-1} + \tilde{\mathbf{M}}^{i-1}\dot{\mathbf{Y}}^i\right] + \alpha_m{}^2\tilde{\mathbf{M}}^{i-1}\dot{\mathbf{Y}}^{i-1}
$$
$$
+ (1 - \alpha_k)^2\tilde{\mathbf{K}}^i\mathbf{Y}^i + \alpha_k(1 - \alpha_k)\left[\tilde{\mathbf{K}}^i\mathbf{Y}^{i-1} + \tilde{\mathbf{K}}^{i-1}\mathbf{Y}^i\right] + \alpha_k{}^2\tilde{\mathbf{K}}^{i-1}\mathbf{Y}^{i-1}
$$
$$
+ (1 - \alpha_k)\tilde{\mathbf{F}}^i + \alpha_k\tilde{\mathbf{F}}^{i-1} = 0. \quad (2.50)
$$

Equation 2.50 represents the temporally and spatially discretized form of the two- or three-dimensional cable dynamics equations. The numerical program that implements this discretization is described in chapter 3. In chapter 5, this program is used to examine the stability of the generalized-α method as applied to the nonlinear cable dynamics equations, with particular emphasis on appropriate choices for α_k, α_m, and γ (or $\lambda_{1,2}^\infty$).

Chapter 3

Implementation of the Numerical Program

The time integration procedure described in chapter 2 is only one piece of the numerical program that was developed as part of this thesis. Other important pieces include the boundary conditions that round out the governing equations to form a fully determined system of equations and the static solution which serves as the initial condition for the dynamic solution. The entire solution procedure is diagrammed in figure 3-1. The more interesting blocks are described below. Details of the nonlinear solution procedure are presented in appendix C. The shooting method solution, which serves as the initial guess for the static solution, is described in appendix D. The calculation of coordinate positions is presented in appendix E. Details of the program interface and the procedure for model and environment description are given by Gobat *et al.* [35].

3.1   Boundary conditions

As mentioned in the derivation of the semi-discrete equation of motion in chapter 2, the governing equations provide only $N \times (n-1)$ equations for the N unknown DOF at each of the n nodes. The remaining N equations that are needed to completely determine the solution are provided by boundary conditions. The procedures for specifying the boundary conditions for the static and dynamic problems are described separately, below. Note that much of the complexity in the specification of the static boundary conditions arises from the fact that the coordinate positions of the boundaries are not explicitly included as
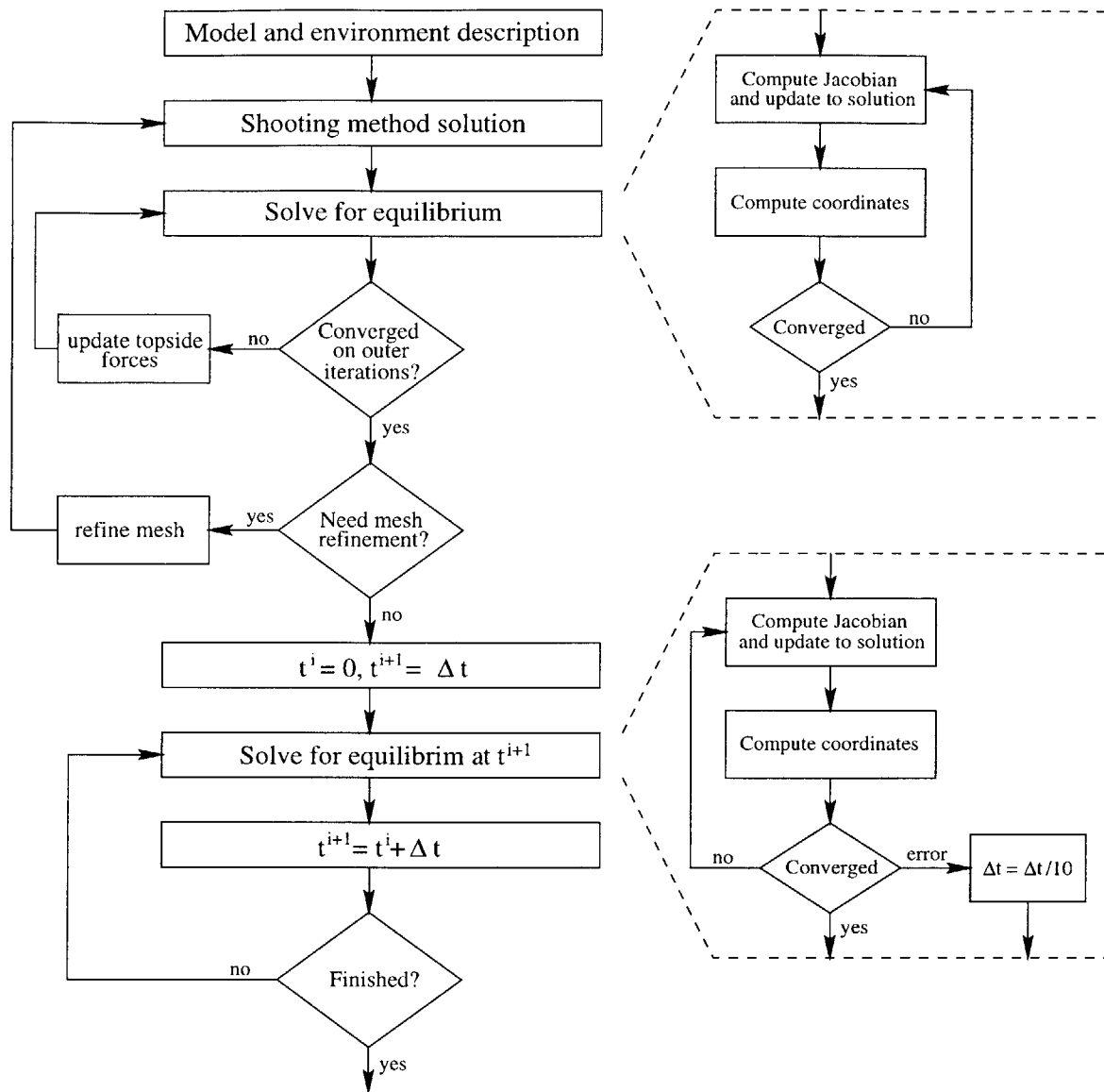
Figure 3-1: Flowchart of the complete numerical solution procedure. Details are given in the text and the appendices.

dependent variables in the governing equations. For a discussion about the merits of this formulation see appendix E.

3.1.1 Static problem

For the two-dimensional static problem there are four unknowns at each node ($N = 4$, see appendix A for details). The most common boundary conditions are based on specifying zero curvature at both ends and applying a known force at the top end. Zero curvature is realistic if the cable is attached top and bottom with a joint, shackle, or pivot that

releases the moment at the termination. The applied force at the top end comes from environmental and other applied forces (a tensioning winch for example) on the platform (buoy, ship, drill rig, etc.). The four additional equations are

$$\Omega_{31} = 0, \tag{3.1}$$

$$\Omega_{3n} = 0, \tag{3.2}$$

$$F_x - [T(\epsilon_n)\cos\phi_n - S_{nn}\sin\phi_n] = 0, \tag{3.3}$$

$$F_y + [T(\epsilon_n)\sin\phi_n + S_{nn}\cos\phi_n] = 0, \tag{3.4}$$

where F_x and F_y are the applied forces at node n in the global $\widehat{i}$ and $\widehat{j}$ directions, respectively.

In many cases, F_x and F_y are not known directly. For oceanographic surface moorings the interaction between mooring forces and buoy forces are coupled through the buoy draft. Thus, F_x and F_y cannot be known before the problem is solved. For offshore applications, the specified boundary condition is often the position of the platform relative to the anchor and the forces F_x and F_y are sought as part of the solution. To accommodate these conditions we must iteratively solve the static problem with consecutively better guesses at the top forces until the desired conditions are satisfied.

Solving for buoy draft

Vertical and horizontal forces applied by a surface buoy to the cable segment under the buoy are a function of the buoy draft and the known buoyancy and drag properties of the buoy. The solution begins with forces calculated from the draft found as part of the initial shooting solution, H_g^0. After solving the full nonlinear equilibrium problem, we then calculate the actual draft, H_s^0, for these forces based on the position of the top node. The absolute error is

$$e_H^0 = H_s^0 - H_g^0. \tag{3.5}$$

To bracket the solution we make a second guess

$$H_g^1 = \left(1 + \mu_d \frac{e_H^0}{|e_H^0|}\right) H_g^0, \tag{3.6}$$

that is some small percentage, μ_d, above or below the initial guess, depending on the sign of the error. μ_d expresses the confidence interval on the initial shooting solution. A value of $\mu_d = 0.1$ is typically conservative and works well. With the actual solution now bracketed between H_g^0 and H_g^1, we proceed to use a linear interpolation root finding technique [82] to calculate a final solution. This root finding procedure forms a second, outer loop of iterations. At each new guessed draft we must go through a new series of iterations within the nonlinear solution procedure to solve the problem. The inner loop of iterations calculates the equilibrium position for a given applied static force based on the current best guess at the draft. The outer iterations continue until the guessed draft coincides (to within some specified tolerance) with the calculated draft.

Resolving platform position

For the case where we know the position of the upper platform we can use a similar outer loop iteration procedure to change the topside applied force until the top end is brought into that position. The adjusted applied force at each outer iteration is calculated from

$$\vec{F}^{k+1} = \vec{F}^k - \mu_p \left(\vec{X}^k - \vec{X} \right) \tag{3.7}$$

where $\vec{F}^k$ and $\vec{X}^k$ are the applied force vector and calculated position of the platform at outer iteration k, and $\vec{X}$ is the desired position of the platform. μ_p is a numerical "stiffness" factor that can be used to accelerate or slow the procedure. These outer loop iterations continue until the calculated platform position is within some specified tolerance of the known position. The initial values for the forces are determined from the shooting method solution which uses this same procedure to bring the platform to the required coordinates.

A third situation requiring outer iterations arises from the inverse of the platform positioning problem. In this case, the tension is specified but the horizontal offset of the platform relative to the anchor is unknown. In this case we must iterate on the angle ϕ at the top node such that the specified tension produces forces F_x and F_y such that the platform is on the surface. Like the solution for buoy draft, we can take advantage of the fact that the initial shooting solution for ϕ at the top node should be reasonably accurate. Using that initial solution as the first guess, the final solution can be bracketed

with a second guess that is only some small distance away from the initial guess. Once ϕ is bracketed, it can be computed using either bisection or linear interpolation [82]. Again, the outer iterations proceed until the calculated vertical position of the platform is within some specified tolerance of the vertical coordinate of the surface.

3.1.2 Dynamic problem

For the two-dimensional dynamic problem with 6 degrees of freedom per node we need to formulate a total of six boundary conditions at the two ends. Like the static problem, two equations are provided by releasing moments at the two terminations. At the anchor we simply impose no motion by setting both normal and tangential velocities to zero. At the top we can impose either time varying forces or velocities in the two global directions. Velocities are the more common case, as we are typically interested in the response of the system to a specified environmentally induced motion of the top of the mooring. In this case, the six boundary equations are

$$\Omega_{3_1}^i = 0, \tag{3.8}$$

$$u_1^i = 0, \tag{3.9}$$

$$v_1^i = 0, \tag{3.10}$$

$$\Omega_{3_n}^i = 0, \tag{3.11}$$

$$U_f^i - \left(u_n^i \cos \phi_n^i - v_n \sin \phi_n^i\right) = 0, \tag{3.12}$$

$$V_f^i - \left(u_n^i \sin \phi_n^i + v_n \cos \phi_n^i\right) = 0, \tag{3.13}$$

where U_f^i and V_f^i are the specified velocities at time step i in the global vertical and horizontal directions, respectively.

Velocities are typically specified in one of three ways. The first case is a regular motion specified as displacements in the two global directions

$$x_f^i = A_x \sin\left(\omega_x t^i + \psi_x\right), \tag{3.14}$$

$$y_f^i = A_y \sin\left(\omega_y t^i + \psi_y\right). \tag{3.15}$$

The velocities for this case are

$$U_f^i = A_x \omega_x \cos \left(\omega_x t^i + \psi_x \right),$$ (3.16)

$$V_f^i = A_y \omega_y \cos \left(\omega_y t^i + \psi_y \right),$$ (3.17)

where $A_{x,y}$, $\omega_{x,y}$, and $\psi_{x,y}$ define the amplitude, period, and relative phase of the displacements in the two directions, respectively.

Secondly, we may specify a random motion profile for a given sea state by breaking the spectrum into a summation of individual frequency components with separate amplitudes and random phases [29]. For example, a Bretschneider spectrum, specified with a modal frequency, ω_m, and significant height, H_s,

$$S(\omega) = \frac{1.25}{4} \frac{\omega_m^4}{\omega^5} H_s^2 e^{-1.25 \left(\frac{\omega_m}{\omega} \right)^4}$$ (3.18)

can be discretized over m frequencies, ω_k, with a spacing of $\Delta \omega$. The amplitude of the kth component is

$$A_k = \sqrt{2 S(\omega_k) \Delta \omega}.$$ (3.19)

The displacement is the sum of all the discrete components

$$A^i = \sum_{k=1}^{m} A_k \sin \left(t^i + \psi_k \right).$$ (3.20)

The random phases, ψ_k, are generated as uniform random numbers on the interval $[-\pi, \pi]$. The total velocity is

$$U_f^i = \sum_{k=1}^{m} A_k \omega_k \cos \left(\omega_k t^i + \psi_k \right).$$ (3.21)

This procedure is not limited to spectra which are known analytically. It can easily be applied to wave spectra derived from field data gathered by such instruments as wave-following buoys and acoustic doppler current profilers.

Finally, for model validation purposes it is often convenient to impose an entire time series of motion onto the top of the mooring. These time series might be the integrated

motions from accelerometer data that were recorded during storm events. Given the known platform motion we can compare model predicted tensions to those actually recorded in the field. The velocity record necessary for this application can either be numerically integrated from acceleration or numerically differentiated from displacements, depending on the available data. If the velocity record consists of discretely sampled points, U_e^k, with a spacing between points of Δt_v then the velocity at time step i is interpolated by

$$U_f^i = \left(U_e^{k+1} - U_e^k \right) \left(\frac{t^i}{\Delta t_v} - k + 1 \right) + U_e^k, \tag{3.22}$$

where k defines the appropriate index into the zero-offset velocity record,

$$k = \text{int} \left(\frac{t^i}{\Delta t_v} \right) + 1. \tag{3.23}$$

3.2 Bottom interaction

Following the same basic approach as Webster [99], the unilateral boundary condition at the sea floor is modeled as an elastic foundation with linear stiffness and damping properties. Given the vertical coordinate of the bottom, which may vary with horizontal position, $x_{\text{bottom}}(y)$, the bottom exerts a force on node j if $x_j \leq x_{\text{bottom}}(y_j)$. For both static and dynamic problems the force is defined as

$$F_b = k \left| x_j \right|, \tag{3.24}$$

where k is the stiffness per unit length of the bottom. In static problems the force is constrained so that $F_b \leq w_0$. The force is always assumed to act in the global vertical direction and as such can be treated simply as a modification to the wet weight, w_0, in the governing equations. In the dynamic problem we also add a damping force,

$$F_d = -bv_j, \tag{3.25}$$

where b is the dashpot constant of the bottom and v_j is the normal velocity of node j.

One of the disadvantages of this approach is that appropriate values for k and b are difficult to calculate without extensive field and laboratory experimental testing of soils. For most problems, however, the gross response of the system is largely insensitive to the

choice of values. Typically, we specify k as the fraction of the line wet weight that will be supported with a deflection equal to one diameter. A non-dimensional form of the stiffness, $\tilde{k}$, can be defined as that fraction,

$$\tilde{k} = \frac{kd}{w_0}.$$ (3.26)

The damping constant b is calculated from a specified value of a damping ratio, ζ. Given ζ, the mass plus added mass of the grounded line, $m + m_a$, and the natural frequency of the elastic foundation/cable system, ω_n, the damping constant is [92]

$$b = 2\zeta \left(m + m_a \right) \omega_n.$$ (3.27)

The natural frequency of the system is calculated as

$$\omega_n = \sqrt{\frac{k}{m + m_a}}.$$ (3.28)

A damping ratio of 0.5 is typically sufficient to eliminate any spurious high frequency effects that result from the line impacting the bottom without significantly affecting overall system response.

The advantages to this treatment of the bottom are the simplicity with which it can be implemented and the generality which it allows. The approach places no restrictions on the number of touchdown points or where and how those points move during the dynamic problem because the entire mooring, including grounded line, is always "in play". This contrasts with approaches which may track a single touchdown point, adding or removing line from the problem to calculate a dynamic response only for line that is instantaneously above that point. The implementation described above has no difficulty handling cases in which positively buoyant portions of the line float above the bottom between heavier portions of line which remain on the bottom or in which a traveling wave of ungrounded line moves along a portion of grounded line.

3.3 Refinement of the spatial discretization

In many moorings with low flexural stiffness, the half grid spatial discretization can lead to undesirable spatial oscillations in the solution. This phenomenon can be easily understood by considering the equation relating shear force to curvature,

$$EI\frac{\partial \Omega_3}{\partial s} + S_n \left(1 + \epsilon\right)^3 = 0. \tag{3.29}$$

For a static solution this equation is discretized as

$$2EI\left[\frac{\Omega_{3j} - \Omega_{3j-1}}{\Delta s_j}\right] + S_{nj}\left(1 + \epsilon_j\right)^3 + S_{nj-1}\left(1 + \epsilon_{j-1}\right)^3 = 0. \tag{3.30}$$

If $EI \approx 0$ and $\epsilon << 1$ as is typical, the only solution (barring $\Delta s_j = 0$) is $S_{nj} \approx -S_{nj-1}$. If $|S_n| > 0$, the shear force will oscillate about zero from one node to the next. This error is particularly manifest in areas of high curvature and at the boundaries. The problem can be minimized by increasing the density of the spatial mesh [10].

Without a priori knowledge of the static solution the most easily applied spatial discretization is uniform,

$$\Delta s_j = \frac{L}{n-1}, \tag{3.31}$$

where L is the length of the cable segment and n is the number of nodes used in the discretization. Unfortunately, a uniform mesh with small Δs to reduce spatial oscillations can require large numbers of nodes. An alternative is to make the mesh finer only in problem areas: areas of high curvature and at the boundaries. To automate this allocation of nodes we can develop a procedure such that given a static solution based on a uniform mesh, we can optimize the mesh in some sense and then recalculate the static solution to take advantage of the refinement. The procedure outlined below is based on that described by Eggleton [27]. It is worth noting that Press et al. [82] describe a procedure, also based on Eggleton's approach, that adaptively refines the mesh as part of the nonlinear solution procedure. That procedure had significant problems with convergence when applied to the geometrically nonlinear problems considered here. It also requires that three equations and additional dependent variables be added into the problem.

The approach to mesh refinement can be understood by considering a minimization of the sum given by

$$\sum_{j=2}^{n} \left[c_w \left(\Omega_3(s_j) - \Omega_3(s_{j-1}) \right) + (s_j - s_{j-1}) \right]^2. \tag{3.32}$$

The s_j coordinates of the n nodes are unknown, but from our previous static solution we can provide a good estimate of $\Omega_3(s)$ for any value of s. The first term in the sum will keep nodes close together in areas of high variability in Ω_3. The second term will keep nodes from getting too far apart in areas with low variability in Ω_3. c_w is a constant that controls the weighting used to place nodes with respect to the two effects. $c_w \gg 1$ will result in a large proportion of the n available nodes being used in areas of high curvature with large spacing between the remaining nodes in other regions of the system. In contrast, $c_w \ll 1$ results in a nearly uniform mesh, with little emphasis placed on refining mesh density in high curvature regions.

Minimizing equation 3.32 requires that we solve an n degree of freedom nonlinear least squares problem. Alternatively, we can approximate the sum as an integral and cast the minimization as a variational problem. If we define the mesh control function

$$f(s) = c_w \Omega_3(s) + s, \tag{3.33}$$

then equation 3.32 is simply

$$\sum_{j=2}^{n} \left[f(s_j) - f(s_{j-1}) \right]^2. \tag{3.34}$$

Without affecting the solution of the minimization problem we can introduce a new independent variable, q, that varies uniformly throughout the mesh (Δq is a constant) and rewrite the summation as

$$\sum_{j=2}^{n} \left[\frac{f(s_j) - f(s_{j-1})}{s_j - s_{j-1}} \right]^2 \frac{(s_j - s_{j-1})^2}{\Delta q}. \tag{3.35}$$

We can approximate this sum as the integral given by

$$\int_0^L \left[\frac{df}{ds}\right]^2 \frac{ds}{dq} ds. = \int_0^L \left[c_w \frac{d\Omega_3}{ds} + 1\right]^2 \frac{ds}{dq} ds. \qquad (3.36)$$

The integral form can now be minimized by solving the variational problem

$$\delta \int_0^L \left[c_w \Omega_s'(s) + 1\right]^2 \frac{ds}{dq} ds = 0. \qquad (3.37)$$

In writing equation 3.37 we have substituted a normalized estimate of the curvature gradient, Ω_s', for the spatial derivative of Ω_3. Ω_s' is defined as

$$\Omega_{sj}' = \frac{|\Omega_{3j} - \Omega_{3j-1}|}{\max |\Omega_{3k} - \Omega_{3k-1}|}, k = 1 \ldots n - 1. \qquad (3.38)$$

This formulation normalizes the curvature to have a maximum value of one and a lower bound at zero. c_w can then be interpreted as the mesh density weight for curvature effects, relative to unity.

The solution to the variational problem in equation 3.37 can be written as [21, 27]

$$\frac{ds}{dq} = \frac{\beta}{c_w \Omega_s' + 1}, \qquad (3.39)$$

where β is a constant to be determined. Equation 3.39 is a boundary value problem for s with boundary conditions $s = 0$ at $q = 0$ and $s = L$ at $q = L$. We use the shooting method [82] and bisection to determine β such that all boundary conditions are satisfied. Bounds on β can be derived by considering the extreme cases $\Omega_s'(s) = 0$ and $\Omega_s'(s) = 1$; both conditions lead to a uniform mesh,

$$\Omega_s'(s) = 0 \quad \rightarrow \quad \frac{ds}{dq} = 1 \quad \rightarrow \quad \beta_{\min} = 1, \qquad (3.40)$$

$$\Omega_s'(s) = 1 \quad \rightarrow \quad \frac{ds}{dq} = 1 \quad \rightarrow \quad \beta_{\max} = 1 + c_w. \qquad (3.41)$$

With each trial β, we integrate from $q = 0$ to $q = L$ using fourth order Runge-Kutta integration. The error function for the bisection is simply $s(q = L) - L$, i.e., the difference between the integrated s coordinate of node n and its known coordinate, $s_n = L$.

The final step in the process it to recalculate the static solution on the refined mesh.

With some care, it is possible to minimize the computational expense associated with outer iterations during this second solution because the solution for the unknown boundary conditions is unlikely to vary significantly from the uniform mesh solution to the refined mesh solution.

3.4 Adaptive time-stepping

The stability analysis of the generalized-α method that was presented in chapter 2 can be strictly applied only to a linear form of the problem. In the nonlinear case the method cannot guarantee stability because the nonlinear solution procedure at each time step is not unconditionally convergent. Because the nonlinear solver uses the result from the previous time step as the initial guess at the solution for the current time step, the solution may not converge if those two solutions are significantly different. For this reason, there are limits to the maximum allowable time step that can successfully be used to propagate the solution in time without giving rise to numerical instabilities.

Typically, we choose a value of Δt based on factors such as the accurate resolution of the physics in the problem and the desired sampling rate of the numerical solution. Depending on the particular problem this value of Δt may not be small enough to avoid numerical instabilities that arise over the course of the simulation. This situation is common in cases where the cable goes slack for brief periods of time or when there is rapid lifting and lowering of cable to and from the bottom. A procedure for avoiding the numerical problems in these cases, without modifying the baseline time step for the whole problem, is adaptive time-stepping.

The adaptive time-stepping procedure that is implemented here is relatively simple. If an instability arises the time step will be reduced automatically to try to get through that portion of the simulation. At each time step where the baseline time increment is not small enough to accurately propagate the solution, Δt is reduced by a factor of ten. The solution then proceeds through ten steps at the smaller increment. The reduction can be recursive, with a practical limit set as four orders of magnitude below the base value of Δt. If the nonlinear solver fails even at this lowest increment, the solution is aborted. This procedure has the advantage that the simulation always produces results on the originally requested sampling grid.

Adaptive time-stepping is only of limited usefulness, however, without some care being taken in the choice of a baseline time increment. If the algorithm is deciding that it needs a smaller time increment at every step then it would be faster to have set a smaller time step in the first place.

Chapter 4

Description of the Field
Experiment

Numerical studies of complex mechanical systems, like the geometrically compliant moorings considered in this thesis, have the advantages that they place few constraints on the system under study and that they are relatively inexpensive to conduct. In contrast, experimental efforts are limited by practical and cost considerations. Nevertheless, a numerical study alone is seldom able to paint a complete picture of the physics that govern the responses of these kinds of systems. For this reason, both a field and a laboratory experiment were conducted as part of this thesis to provide an added level of detail and confidence. The field experiment described in this chapter offered the chance to collect full scale data that reflect a response to real environmental conditions. The results from the experiment are used in chapter 5 as part of the validation of the numerical program and in chapter 6, along with simulation results, to analyze the dynamic response of mooring systems. The laboratory experiments described in chapter 7 provide higher spatio-temporal resolution under more controlled conditions. These advantages facilitate the detailed analysis of the bottom interaction described in that chapter.

4.1   Location and climatology

The Shallow Water Engineering Experiment (SWEX) was conducted at an area known as the WHOI Buoy Farm. This is a one km^2 area approximately 40 km southwest of Woods Hole, Massachusetts or 18 km southwest of Gay Head on the island of Martha's Vineyard,
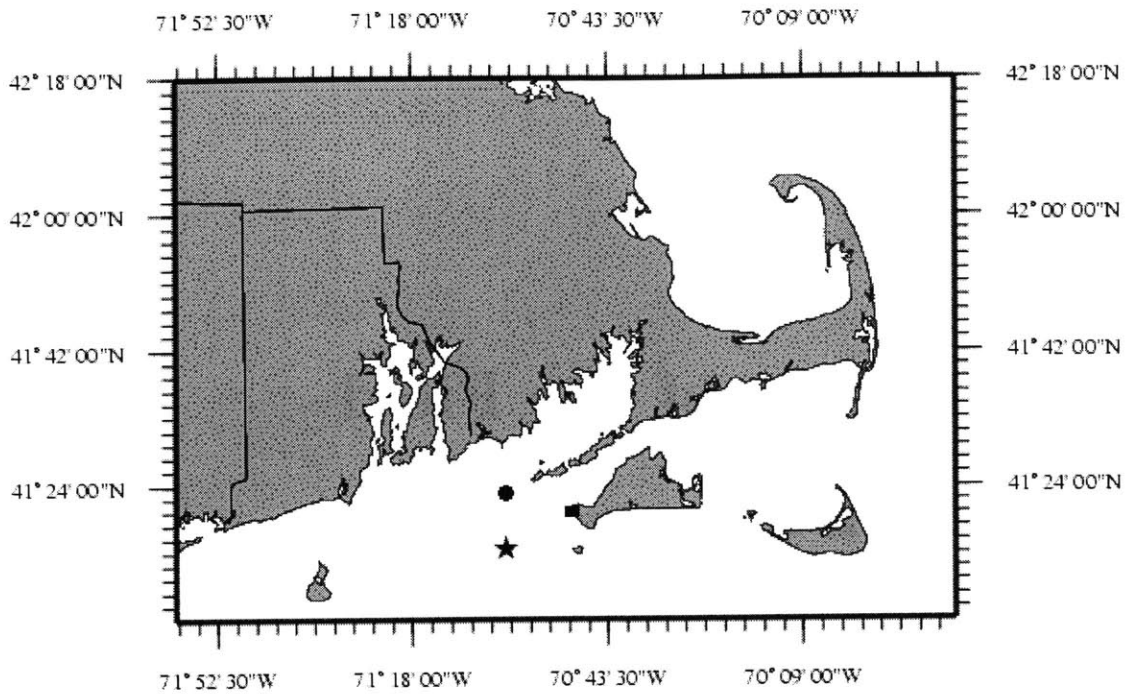
Figure 4-1: Geographic map of field experiment site. The star marks the WHOI Buoy Farm. The base GPS receiver station was located at the Gay Head lighthouse on the southwestern most tip of Martha's Vineyard, marked by the black square. The Buzzards Bay tower is marked by the black circle.

Massachusetts. The site location within Rhode Island Sound is shown in figure 4-1. The locations of the moorings within the Buoy Farm are shown in figure 4-2. Nominal water depth at the site is 42 m.

The experiment was deployed on 5 December 1998 and recovered on 20 January 1999 to coincide with a portion of the winter storm season. As shown in figure 4-1 the site is exposed with significant fetch to wind and storms from the south, southeast, and to a more limited degree the southwest. There is much less exposure to significant storms from the north and northeast due to limited fetch. Based on climatological records from the nearby Buzzards Bay C-MAN tower, the dominant winds blow from the southwest during this period. Figure 4-3 shows the hourly averaged wind records from the Buzzards Bay tower during the experiment. Through December and January the average wind direction was 224° (southwest) and average wind speed was 18.3 knots. There were several large storm events, however, with winds from the southeast. The largest of these occurred on 3 January 1999, with peak sustained winds of 50 knots.
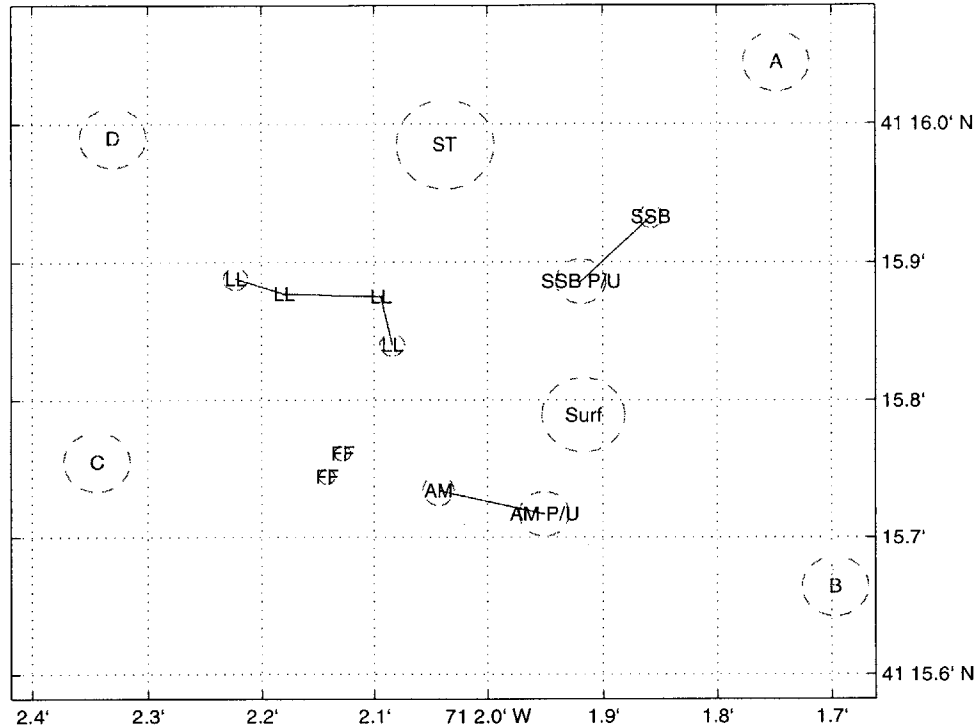
Figure 4-2: Location of the experimental moorings within the Buoy Farm during SWEX. Surf = surface mooring, ST = Seatex waverider buoy. The 600 kHz ADCP was located in a bottom mounted tripod that was on the groundline between SSB and SSB P/U. Dashed circles indicate the approximate watch circle of each mooring. A,B,C, and D mark the four corner guard buoys that delimit the Buoy Farm. Other markers indicate additional experiments and fishing floats that were deployed at the Buoy Farm during the field experiments.

4.2 Mooring hardware

The primary experimental mooring was an all chain catenary mooring. The mooring design is shown in figure 4-4. The system consisted of 80 m of $\frac{1}{2}$-inch galvanized steel trawler chain, broken only by three inline accelerometer instruments (AxPacks). The AxPacks were hose clamped onto stainless steel strongbacks and the strongbacks were shackled between shots of the chain. The surface buoy was a cylindrical block of Surlyn foam 1.27 m in diameter and 0.75 m high. An instrument well extended through the middle of the buoy and 1.4 m beyond the bottom of the foam. The well is approximately 24 cm in diameter. The properties for all of the mooring components are summarized in table 4.1.
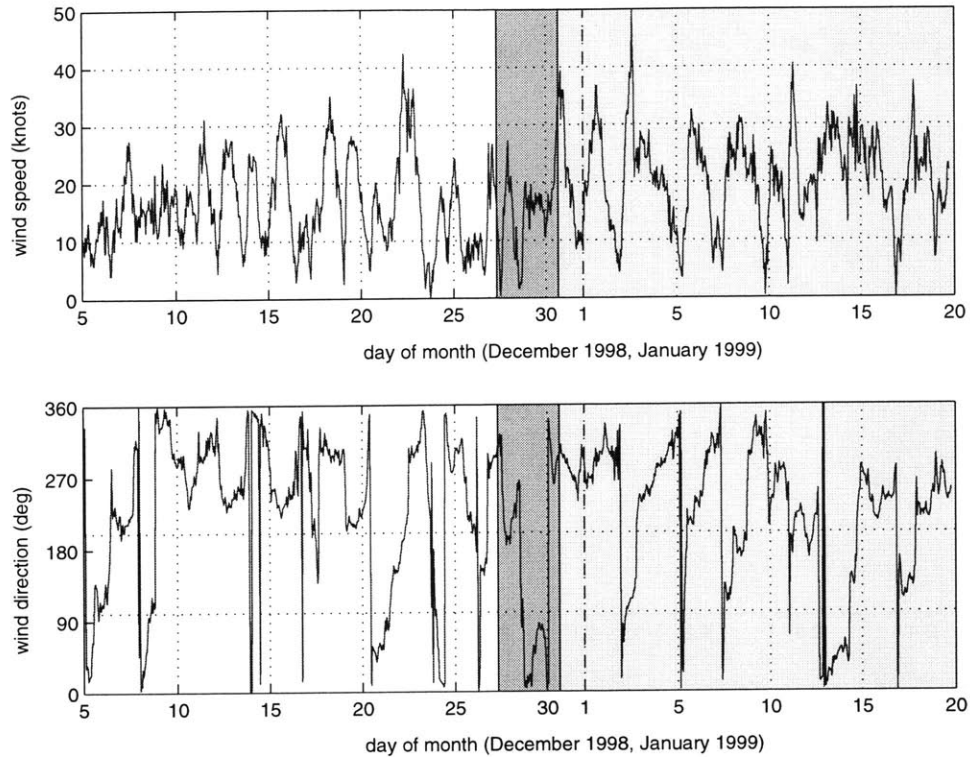
Figure 4-3: Winds during the field deployment. The data are hourly averaged results from the Buzzards Bay C-MAN tower maintained by the National Data Buoy Center (http://www.ndbc.noaa.gov). Shaded areas indicate dates where all channels (dark) or just the y accelerometer channel (light) of the surface buoy instrument had significant data errors.

material	length (m)	m (kg/m)	w_0 (N/m)	EA (N)
$\frac{1}{2}$-inch chain		3.73	31.85	6.4×10^7
AxPack	0.76	10.02	70.82	8.0×10^7
shackle/ring/shackle	0.22	16.22	81.23	8.0×10^7

Table 4.1: Properties of the components used in the experimental mooring. AxPack properties include two $\frac{5}{8}$-inch chain shackles and a $\frac{3}{4}$-inch pear ring at each end of the strongback. The axial stiffness of components that include a shackle are based on the stiffness of a shackle.
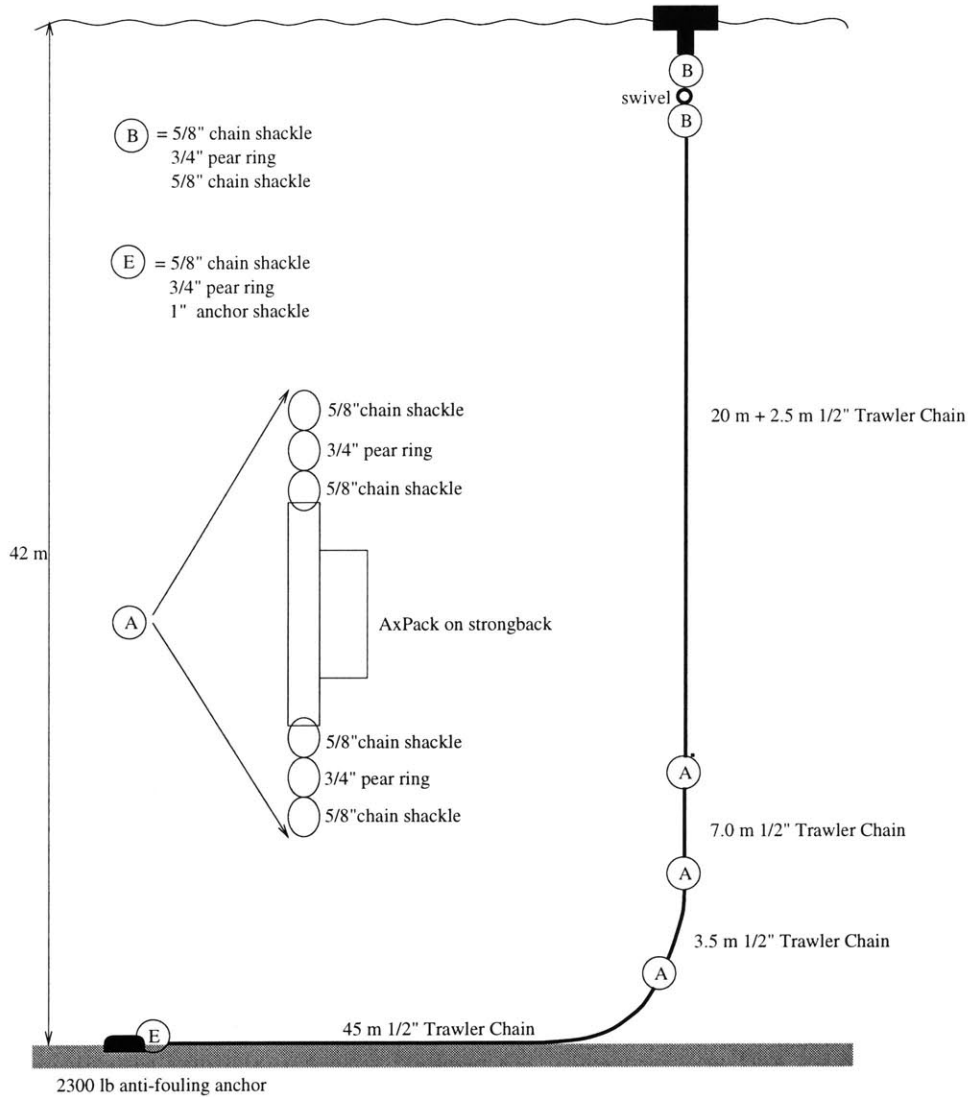
Figure 4-4: Schematic of the surface mooring used in the field experiments.

4.3 Instrumentation

4.3.1 Engineering instrumentation

Mooring line instrumentation

The mooring chain was instrumented with three AxPack self-contained accelerometer in-
struments as shown in figure 4-4. They were located so as to span the region of high
curvature near the touchdown point over the range of currents that were expected at the
site. The lowest instrument was placed so that it would be approximately 3 m off the
bottom at the lowest tide and slack current. The data indicate that it probably did hit

the bottom at various times during the deployment.

Each AxPack consists of Tattletale Model 8 microcontroller (with eight channels of 12-bit A/D) from Onset instruments mated to a Persistor CF8 compact flash board (with a 24 MB compact flash card) from Peripheral Issues. The accelerometer is a Summit Instruments model 34103A triaxial accelerometer with a 0 - 5V output scale over the range $\pm 1.5G$. The primary advantage to these accelerometers is that they are completely self-contained. Given a single +5V power supply they produce an amplified and filtered 0 - 5V signal. The internal filter is a single pole Butterworth filter with the 3 dB point at 4.6 Hz. The accelerometer is packaged in a small cube less than 2.5 cm on a side. Power is provided by three 3.6V lithium C cells (manufactured by Tadiran). All power conditioning is done on board the Tattletale.

The sample rate throughout the experiment was 10 Hz. The AxPack accelerometers were sampled for 20 minutes beginning on the hour at 0800, 1600, and 0000 hours localtime. Because there is no communication between the instruments during the experiment, each unit carries a separate battery backed real time clock (Dallas Semiconductor DS1302). These clocks were synchronized using an electronic trigger pulse prior to deployment. The crystals for these clock chips appear to have been cut from the same batch and exhibit similar drift characteristics, with each AxPack losing approximately 50 seconds in 30 days. These clocks retain the real time in case of a fault and reset in the Tattletale.

The electronics and accelerometer are secured into a machined aluminum rack and together with the batteries sealed into delrin pressure cases. The pressure cases are 21 cm long and 7.5 cm in diameter. A photo of the assembled and unassembled AxPack components is shown in figure 4-5. The driving factor in the AxPack design was to keep the size, mass, and wet weight of the units as consistent as possible with the rest of the mooring. However, on their strongbacks and taking into account the shackle/ring/shackle assemblies that are required to attach the AxPack inline with the rest of the mooring, the AxPacks have approximately twice the mass and wet weight per length of the $\frac{1}{2}$-inch trawler chain.

Buoy instrumentation

The buoy was instrumented with a six axis motion package: triaxial linear acceleration (Columbia Research Laboratories model SA-307-TX) and three Systron Donner single axis

70
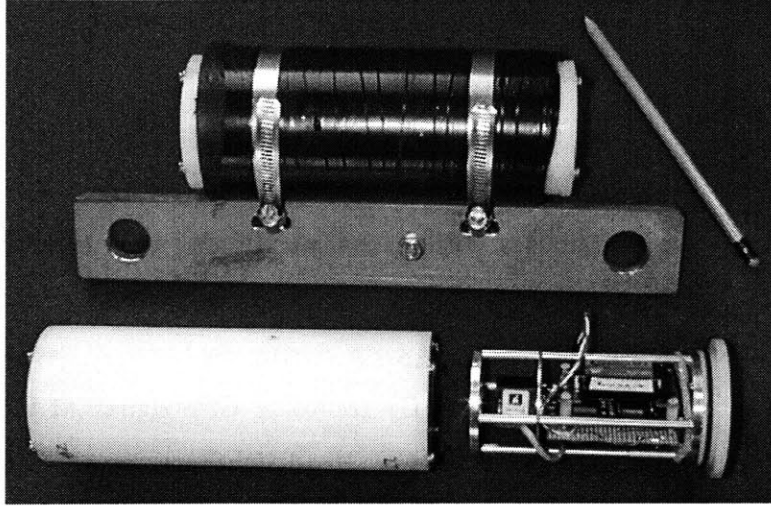
Figure 4-5: AxPack strongback, pressure case, and electronics.

gyro rate chips. The instruments were controlled and logged (at 12-bit resolution) by a Tattletale Model 6F controller. The surface package also included a Precision Navigation TCM2 electronic compass module. The digital signal from the compass was converted to an analog signal using the onboard 8-bit digital to analog converter. This analog signal was then sampled by the Tattletale for logging, providing 256 levels of heading around the $360°$ of the compass in the final dataset. The connection to the mooring chain was made through a 5000 pound capacity load cell. The load cell was also sampled by the Tattletale. All of these instruments were sampled at 12.5 Hz (though the effective update rate of the compass is only 1 Hz) three times a day for twenty minutes. Due to a programming error prior to deployment, the start time of each sample was delayed by five minutes relative to the AxPack sample periods; the three sample periods began at 0805, 1605, and 0005 localtime. No attempt was made to synchronize the surface instrument clock with the AxPacks beyond setting them within approximately one second of each other before sealing the instruments.

All of the instruments performed well for the first three weeks of the deployment. Data from the surface buoy instruments had significant drop-outs and obvious signal problems from 27 December through 31 December. After 31 December, the y accelerometer signal (one of the horizontal axes) was always bad, but the other channels appeared to be problem free. During a post-deployment analysis it was determined that the multiplexer channel for the y accelerometer had failed. Our speculation is that while it was in the process of

71

failing it caused problems with the other channels, but that once it had failed completely, the remaining channels were unaffected.

GPS instrument

The surface buoy also contained a GPS (global positioning system) receiver. The motivation for including this instrument was to verify the quasi-static position of the buoy within its watch circle. From the ship's GPS during deployment we knew the location of the anchor to within several meters. By recording GPS signals at the buoy and at a non-moving base station located at the Gay Head lighthouse on the island of Martha's Vineyard (figure 4-1) we hoped to resolve the motions of the buoy to within better than one meter [24]. The GPS receivers were Canadian Marconi Allstar units with 1 Hz position, velocity, and time output and 1 Hz carrier phase output. On the buoy the GPS receiver was controlled by a Tattletale Model 8 with logging to a Peripheral Issues Persistor AT8 with a 175 MB flash card. The base station GPS receiver was controlled by a standard PC. Unfortunately, the remote receiver failed. We feel confident, however, that the technique can provide an interesting and valuable dataset and thus the system will be redeployed on a future engineering test deployment.

4.3.2 Environmental instrumentation

In order to quantify the environmental forcing on the surface mooring, both waves and current were measured during the deployment. Current was measured using two acoustic doppler current profilers (ADCPs): a 600 kHz unit mounted in a tripod on the sea floor and a 1200 kHz unit mounted on top of a subsurface buoy that was tethered at 13 m depth. Directional wave spectra were measured by a Seatex Wavescan buoy (Seatex A/S). This buoy is moored such that it has a significant portion of its tether floating on the surface. This allows it to respond freely to the incident waves in heave, pitch, and roll. The motion of the buoy is measured using a six axis Hippy unit.

As part of a separate effort, the Wavescan data will be compared with the ADCP data to test the ability of the ADCP to resolve directional wave spectra. This comparison required relatively high frequency sampling of the ADCP. The ping rate was 3 Hz, with the velocity results averaged and stored at 1 Hz (i.e., each 1 Hz current sample represents the average current result from three pings over the previous second). The current data

is provided as a profile, with 75 cm between depth bins on the 600 kHz unit and 25 cm between bins on the 1200 kHz unit. Accounting for the tripod height above the bottom, the first current point is 1.95 m above the bottom. An overly conservative number of bins was used so that the last bin always fell beyond the surface. The ADCPs were sampled for 40 minutes (600 kHZ) and 26 minutes (1200 kHz) three times per day (0800, 1600, 0000).

4.3.3 Data telemetry

All of the instruments stored their data locally. The Wavescan buoy and the surface buoy both had ARGOS satellite transmitters that were used for location purposes only. This allowed remote monitoring of the location of the buoys to ensure that they had not failed and gone adrift.

4.4 Data processing

All accelerometer and gyro calibrations were performed using manufacturer supplied calibration coefficients. The validity of the accelerometer calibrations was verified both before and after the deployment through a check of each instrument's outputs in a variety of tilted positions. The 5000 pound load cell was sent to the manufacturer for a recalibration immediately prior to the experiment.

The motion of the buoy in earth referenced coordinates was computed using the approach outlined by Edson *et al.* [25]. In this procedure, the orientation of the local coordinate system is computed using a complementary filter in which the high frequency signal from the rate gyros is combined with low frequency tilt and heading information derived from the horizontal accelerometers and the compass.[1] The result of the complementary filter is a time series of buoy orientation which can be used to transform the recorded accelerometer signals into east, north, and vertical components. These earth referenced accelerations are then integrated into velocity and displacement, with a highpass filter at each step to remove any low frequency (greater than 30 second period) drift.

---

[1] Results after 27 December 1998 were processed with the assumption that the low frequency y accelerometer signal was identically zero, i.e., that there was no systematic tilt in that direction. The assumption is easily justified given the near zero mean y accelerometer signals prior to 27 December and it allowed us to compute an estimate of the vertical motion even after the loss of the y accelerometer. Motions in the horizontal plane (east and north) were not computed for data after 27 December.

For use with the numerical model it is convenient to determine an approximate orientation for the plane of the mooring and to project wind, current, and motion vectors into a coordinate system oriented with this plane. This approximation and projection allows us to apply forcing data derived from the three-dimensional experimental results in two-dimensional model simulations. Definitions for the procedure are shown in figure 4-6. We determine the direction of the plane of the mooring by considering the net force due to wind and current on the buoy only. We neglect for now any current drag on the chain because the currents tended to decay sharply away from the surface and thus drag forces on the chain were much smaller than the forces on the buoy due to current and wind. For a current profile $\vec{V}(z)$ with magnitude and direction at the surface V_H and θ_H, and wind with speed W and direction θ_w, the north and east components of the force, F_n and F_e, are

$$
\begin{bmatrix} F_n \\ F_e \end{bmatrix} = \begin{bmatrix} \cos\theta_H & \cos\theta_w \\ \sin\theta_H & \sin\theta_w \end{bmatrix} \begin{bmatrix} \frac{1}{2}\rho S_b C_{db} V_H^2 \\ \frac{1}{2}\rho_{\text{air}} S_w C_{dw} W^2 \end{bmatrix},
\tag{4.1}
$$

where S_w, C_{dw}, S_b and C_{db} are the projected area and drag coefficient above and below the buoy waterline, respectively. The resultant effective direction of the plane of the mooring is

$$
\theta_{\text{eff}} = \tan^{-1}\left(\frac{F_e}{F_n}\right).
\tag{4.2}
$$

Given the effective plane determined by θ_{eff}, we seek effective values of the wind, W_{eff}, and current profiles, $V_{\text{eff}}(z)$, which yield the same level of force as the true forces projected onto the effective plane

$$
F_c \cos\left(\theta_{\text{eff}} - \theta(z)\right) = \frac{1}{2}\rho S_b C_{db} V_{\text{eff}}(z)^2,
\tag{4.3}
$$

$$
F_w \cos\left(\theta_{\text{eff}} - \theta_w\right) = \frac{1}{2}\rho_{\text{air}} S_w C_{dw} W_{\text{eff}}^2.
\tag{4.4}
$$
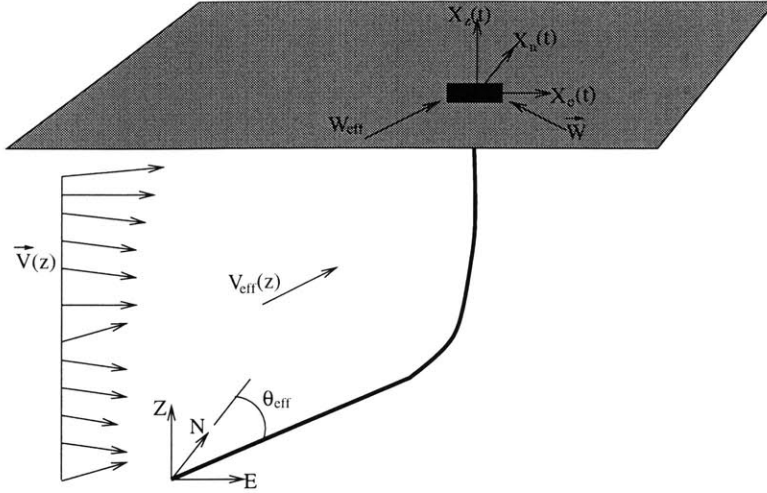
Figure 4-6: Definitions for the procedure to determine the approximate two-dimensional plane of the mooring.

Taking care of signs, we define the effective current and wind in this plane as

$$V_{\text{eff}}(z) = \text{sign}\left[\cos\left(\theta_{\text{eff}} - \theta(z)\right)\right] V(z) \sqrt{|\cos\left(\theta_{\text{eff}} - \theta(z)\right)|}, \tag{4.5}$$

$$W_{\text{eff}} = \text{sign}\left[\cos\left(\theta_{\text{eff}} - \theta_w\right)\right] W \sqrt{|\cos\left(\theta_{\text{eff}} - \theta_w\right)|}. \tag{4.6}$$

The north and east components of the buoy motion, $X_n(t)$ and $X_e(t)$, respectively, are converted into in-plane and out-of-plane components according to

$$X_{\text{ip}} = X_n \cos\theta_{\text{eff}} + X_e \sin\theta_{\text{eff}}, \tag{4.7}$$

$$X_{\text{op}} = -X_n \sin\theta_{\text{eff}} + X_e \cos\theta_{\text{eff}}. \tag{4.8}$$

Because the average water depth of 42 m was near the maximum range of the 600 kHz unit, the data from the 1200 kHz unit appear to be more accurate near the surface. As the near surface currents (along with the wind) dominate the steady-state response of the mooring, the profiles, $\vec{V}(z)$, used in the procedure outlined above are based on data from the 1200 kHz instrument, with extrapolated values below 13 m depth. While both instruments recorded three ping ensembles at 1 Hz, only temporally averaged profiles (over the 26 minute length of each sample period) were used.

Chapter 5

Validation and Parameterization of the Numerical Program

The numerical model described in chapters 2 and 3 and appendices C through E was validated using the data collected during the full scale field experiment and by comparison with two hanging chain problems with known solutions. The first step in the validation is to characterize those aspects of the model which are purely numerical, particularly the time integration and mesh refinement parameters. We do this by comparing simulation results to a known solution. This allows us to establish reasonable values for the numerical parameters which are then used in the comparison of model results with experimental results in order to establish the ability of the numerical program to accurately predict dynamic response under a variety of forcing conditions.

5.1   Response of a hanging chain

Figure 5-1 depicts the hanging chain system used for the first part of the validation. Two cases will be considered. In the first case we apply a very small initial displacement to the chain and then at time $t = 0$, release it. The dynamic response of the chain for $t > 0$ can be calculated analytically for the small motions that result. In the second case we impose a sinusoidally varying horizontal displacement to the top of the chain and analyze the forced response. This latter problem was studied both numerically and experimentally by Howell [46].

5.1.1 Free response to an initial displacement

For small motions and an inextensible chain, the equation of motion for the chain can be written as

$$m\frac{\partial^2 q}{\partial t^2} = \frac{\partial}{\partial s}\left[mgs\frac{\partial q}{\partial s}\right]. \tag{5.1}$$

Assuming a harmonic solution of the form

$$q(s,t) = q(s)\left[A\cos\omega t + B\sin\omega t\right] \tag{5.2}$$

the mode shapes, $q(s)$, are [97]

$$q(s) = c_1 J_0\left(2\omega\sqrt{\frac{s}{g}}\right) + c_2 Y_0\left(2\omega\sqrt{\frac{s}{g}}\right). \tag{5.3}$$

The requirement that the solution be finite at $s = 0$ leads to the elimination of the Y_0 term and the requirement that $q(L) = 0$ leads to the natural frequencies, ω. They are given by the roots of

$$J_0\left(2\omega\sqrt{\frac{L}{g}}\right) = 0. \tag{5.4}$$

The complete response is the sum of the response in each mode

$$q(s,t) = \sum_{n=1}^{\infty} J_0\left(2\omega_n\sqrt{\frac{s}{g}}\right)\left[A_n\cos\omega t + B_n\sin\omega t\right]. \tag{5.5}$$

The coefficients A_n and B_n are determined from the initial displacement, $q_0(s)$, and velocity, $\dot{q}_0(s)$. Given $\dot{q}_0(s) = 0$, we can immediately determine that $B_n = 0$. To determine A_n we first write

$$q(s,0) = \sum_{n=1}^{\infty} A_n J_0\left(2\omega_n\sqrt{\frac{s}{g}}\right) = q_0(s). \tag{5.6}$$

Multiplying both sides by $J_0\left(2\omega_n\sqrt{\frac{s}{g}}\right)$, integrating from $s = 0$ to $s = L$, and making use

of the fact that

$$\int_0^L J_0\left(2\omega_n\sqrt{\frac{s}{g}}\right) J_0\left(2\omega_m\sqrt{\frac{s}{g}}\right) ds = 0, \quad \text{for } n \neq m, \tag{5.7}$$

yields the following equation for A_n,

$$A_n = \frac{\int_0^L q_0(s) J_0\left(2\omega_n\sqrt{\frac{s}{g}}\right) ds}{\int_0^L J_0^2\left(2\omega_n\sqrt{\frac{s}{g}}\right) ds}. \tag{5.8}$$

For comparison with simulation results, the analytic solution was computed for a chain released from an initial catenary configuration. For simplicity all of the model parameters (mass per length, gravity, length) were set to unity. The horizontal force applied at $s = 0$ to create the initial deflection was set to 0.001. For simulation results EI was set to 10^{-6} and EA to 10^9. All of the integrals were computed using the trapezoidal rule with 10000 panels. A 400 second time series of the response at the free end was constructed using the first 20 modes

Figure 5-1: Definitions for the hanging chains problems.

of the analytic solution. The analytic result was sampled at 20 Hz; the natural frequency for mode 20 is approximately 5 Hz.

Because the primary distinction amongst the various algorithms contained within the the generalized-α method is the amount of numerical damping, all results are compared in the frequency domain. For each 400 second time series, power spectra of the response at the free end were computed using non-overlapping 256 point FFTs. As an example, figure 5-2 shows the power spectra for the analytic solution and for a numerical solution with $\lambda_{1,2}^{\infty} = -\frac{1}{2}$, $\Delta t = 0.01$ s, and 50 nodes. The circle and square markers indicate the spectral peaks as computed using a crude peak detection algorithm. In subsequent results only the peaks are plotted.

Figure 5-3 shows a comparison between the analytic solution and numerical solutions for six different parameterizations of the generalized-α method. At this time step, $\Delta t = 0.01$ s, most of the algorithms are accurate out to the fifth or sixth mode. The
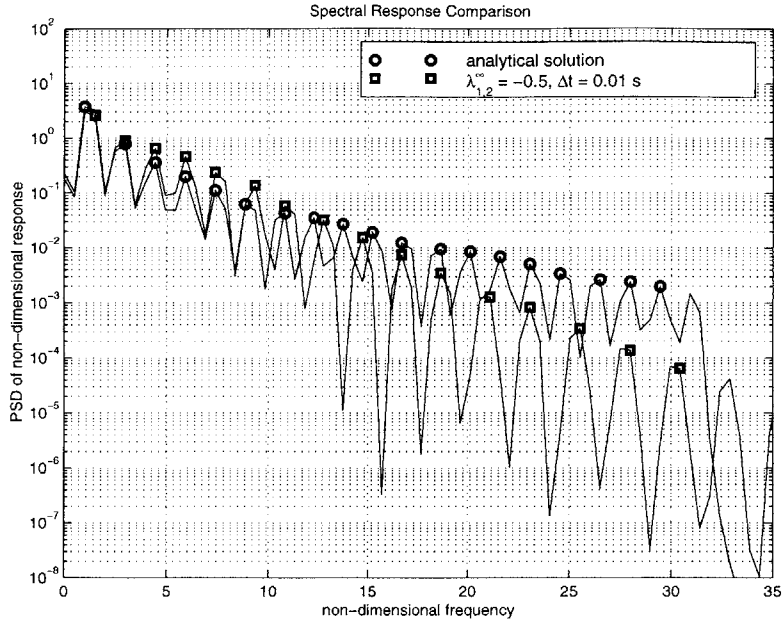
Figure 5-2: Power spectral density of the response of the free end of the chain for the analytic solution and for a numerical solution with $\lambda_{1,2}^{\infty} = -\frac{1}{2}$, $\Delta t = 0.01$ s, and $n = 50$.

notable exception is the first-order accurate backward differences, which substantially underestimates the response even in the first mode. All of the algorithms show a marked fall off from the analytic solution at higher frequencies, with the solutions for $\lambda_{1,2}^{\infty} \geq 0$ showing the most decay and the trapezoidal rule appearing to be the most accurate.

In figure 2-4, the numerical damping of the various algorithms varies with the product $\omega \Delta t$. The idea that we should see less numerical damping at a fixed frequency with a decrease in Δt is illustrated in figure 5-4 which shows the same results comparison as in figure 5-3 for a time step of $\Delta t = 0.001$ s. At this time step most algorithms are accurate out to the tenth mode. Only backward differences, which due to its first-order accuracy is again a poor solution even at very low frequencies, and $\lambda_{1,2}^{\infty} = 0$ (which like backward differences is asymptotically annihilating) are worse than this.

That the other algorithms, with their varying levels of dissipation, have converged to the same solution suggests that the remaining error is not due to numerical dissipation. Figure 5-5 shows the comparison for four cases with $\lambda_{1,2}^{\infty} = -\frac{1}{2}$ and $\Delta t = 0.001$ s, with a varying number of nodes. As the node density is increased, the numerical model is better able to resolve the mode shapes associated with the higher frequencies. At $n = 800$, the numerical solution is in agreement with the analytic solution over the full range of the

80
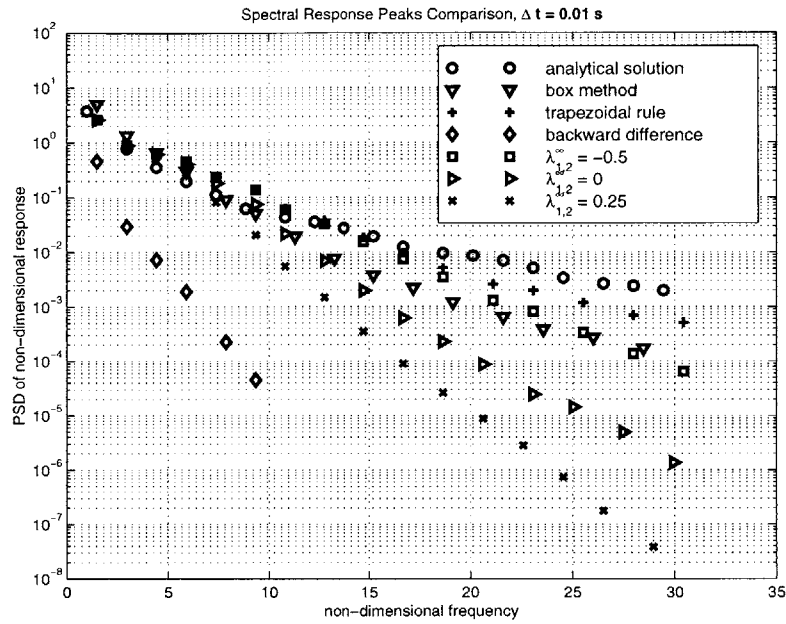
Figure 5-3: Power spectra peaks of the response of the free end of the chain for the analytic solution and for six variants of the generalized-α method with $\Delta t = 0.01s$, and $n = 50$.
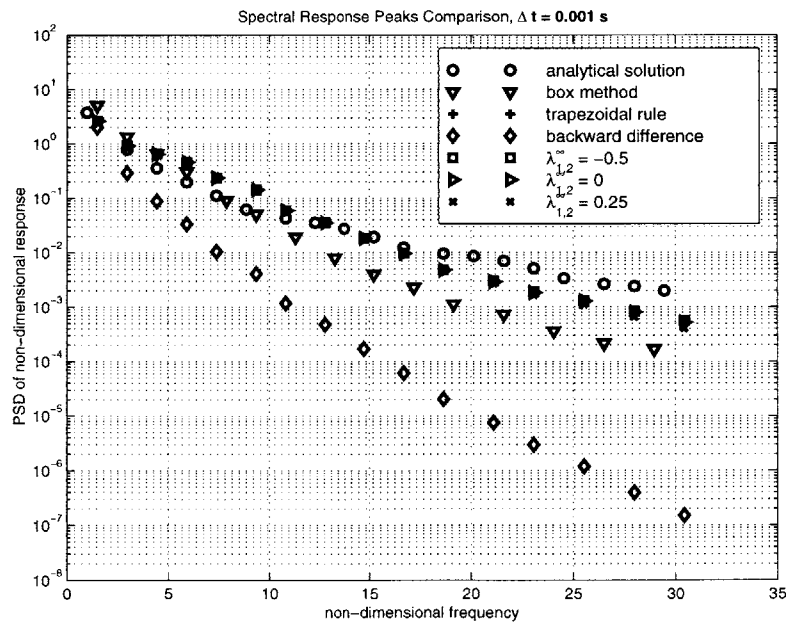
Figure 5-4: Power spectra peaks of the response of the free end of the chain for the analytic solution and for six variants of the generalized-α method with $\Delta t = 0.001s$, and $n = 50$.
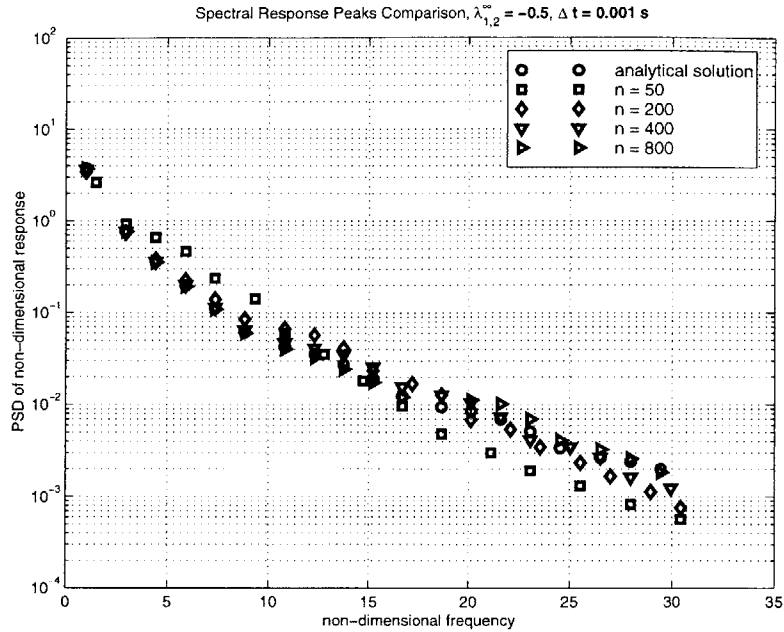
Figure 5-5: Power spectra peaks of the response of the free end of the chain for the analytic solution and for $\lambda_{1,2}^{\infty} = -\frac{1}{2}$, $\Delta t = 0.001$ s, with $n = 50, 200, 400, 800$. Note that the y axis scaling has changed from previous power spectra plots.

analytically computed response.

These results demonstrate that the ability of the model to accurately resolve high frequency response is dependent on temporal and spatial discretizations and on the numerical dissipation for a given algorithm. Given sufficient temporal and spatial resolution, all forms of the algorithm appear ultimately capable of accurately calculating the free response of the swinging chain. Based on its better accuracy at the larger time step, the best choice of algorithm for this problem appears to be the trapezoidal rule. As will be demonstrated, however, this may not always be the case, particularly in cases where numerical instabilities arise.

5.1.2 Forced response to an imposed motion

Two-dimensional simulations

The second hanging chain problem that we consider is the case studied by Howell [46]. In this problem, a 1.75 m long chain is suspended from an actuator which imposes a sinusoidally varying horizontal displacement, $Q(t)$, to the top of the chain (see figure 2-1). There is no analytic solution for this problem so we will compare numerical solution

Box: n=100, Δt = 0.01   Trapezoidal: n=100,Δt = 0.01   Backwards: n=100, Δt = 0.01

3.43 s
3.44 s
3.45 s
3.46 s

vert coordinate (m)

horiz coordinate (m)

$\lambda_{1,2}^{\infty}$ = –0.7: n=100, Δt = 0.01 $\lambda_{1,2}^{\infty}$ = –0.5: n=100, Δt = 0.01 $\lambda_{1,2}^{\infty}$ = 0.0: n=100, Δt = 0.01

vert coordinate (m)

horiz coordinate (m)
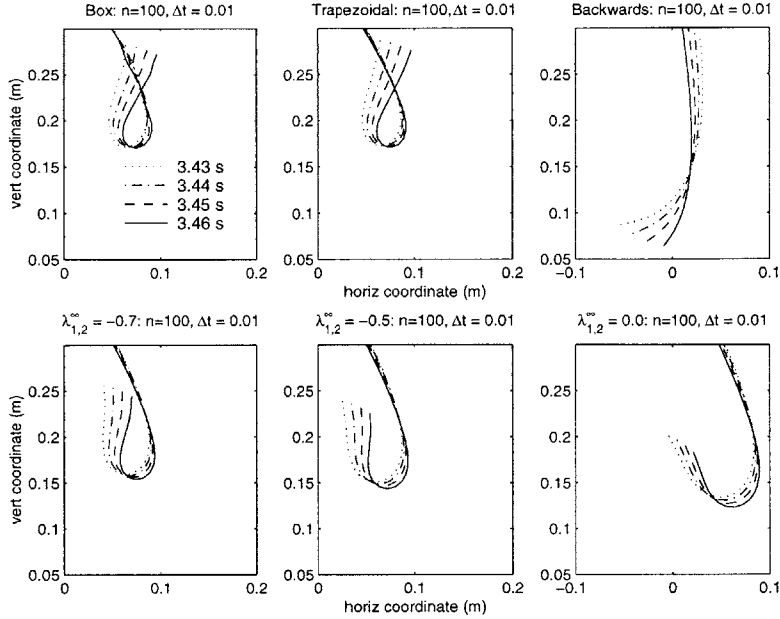
Figure 5-6: Snapshots of the chain configuration near the time of expected intersection for six variants of the generalized-α method.

results to snapshots of the chain configuration derived from experiments conducted by Howell. Figure 5-6 shows the configuration of the lower portion of the chain from 3.43 s to 3.46 s for six different algorithms, all with $n = 100$ and $\Delta t = 0.01$ s. Howell observed that the free end of the chain intersects the chain above it at approximately 3.4 seconds. The box method and trapezoidal rule most closely match this result, with intersection occurring by the 3.43 second mark. For the other algorithms, the delay in intersection is proportional to the amount of numerical dissipation in the algorithm. The solution for backward differences is again the worst; the chain never intersects itself. Likewise for $\lambda_{1,2}^{\infty} = 0$, though it comes closer to doing so. For $\lambda_{1,2}^{\infty} = -0.7$, intersection actually happens at 3.47 seconds and for $\lambda_{1,2}^{\infty} = -0.5$, at 3.5 seconds.

The situation changes somewhat if we consider the effect of temporal and spatial discretization. Figure 5-7 shows the same time points for versions of the box method with $n = 100, 200$ and $\Delta t = 0.01, 0.001, 0.0001$ s. In this case we see that increasing the number of nodes does not significantly effect the solution, suggesting that $n = 100$ is adequate to accurately capture the response. An increase in temporal resolution, however, from $\Delta t = 0.01$ s to $\Delta t = 0.001$ s, leads to a delay in the crossover to approximately 3.46 seconds. The result at the even smaller $\Delta t = 0.0001$ s confirms that the solution
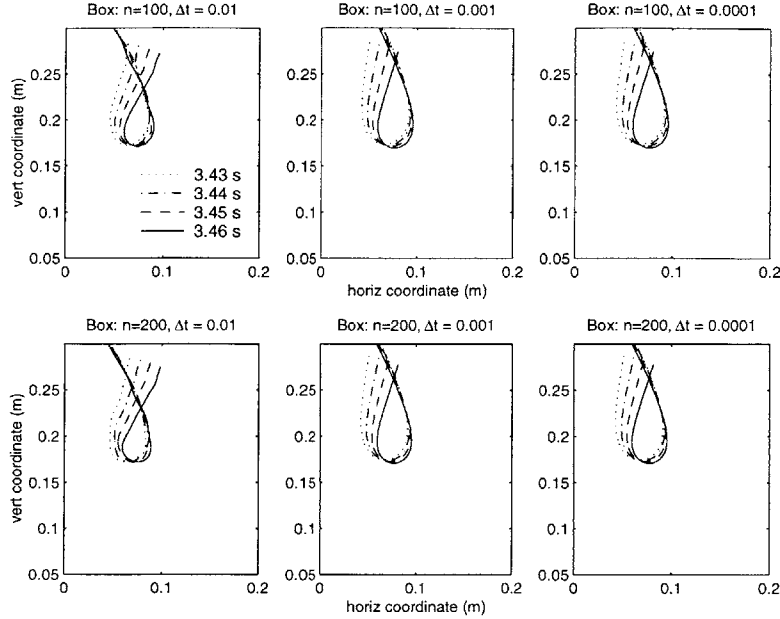
Figure 5-7: Snapshots of the chain configuration near the time of expected intersection for the box method with different spatial and temporal discretizations.

has converged at these smaller time steps. Figure 5-8 shows this same behavior for the trapezoidal rule. The only notable difference between trapezoidal rule and box method solutions is the better smoothness of the trapezoidal rule solutions at $\Delta t = 0.01$ s.

Similar results for $\lambda_{1,2}^{\infty} = -0.5$ are shown in figure 5-9. In this case, the solution at $\Delta t = 0.001$ s has not quite converged to the solutions from the trapezoidal rule and the box method at the 3.46 second point. The solutions for $\Delta t = 0.0001$ s are in good agreement with the similar solutions in figures 5-7 and 5-8. A notable difference in the solutions for the various algorithms does appear in the half second (solutions were only run for four seconds) following intersection. Both trapezoidal rule and box method solutions required significant adaptation of time step to get through the collapse of the lower portion of the chain following the crossover. The enhanced stability of solutions with $\lambda_{1,2}^{\infty} = -0.5$ allowed for a smooth numerical solution in this region, with no or very little adaptation. Without experimental verification, however, we cannot say if this numerically more easily obtained solution is accurate.

The basic accuracy of the solutions from all of the algorithms can be verified by comparison with Howell's [46] data for the chain configuration prior to intersection. The data points were recovered graphically from digitized versions of the hardcopy plots. Because

84
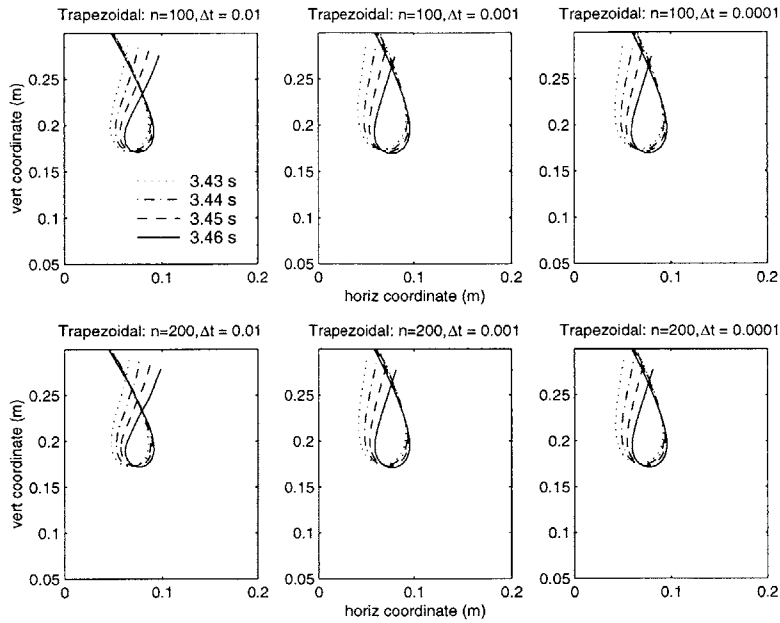
Figure 5-8: Snapshots of the chain configuration near the time of expected intersection for the trapezoidal rule with different spatial and temporal discretizations.
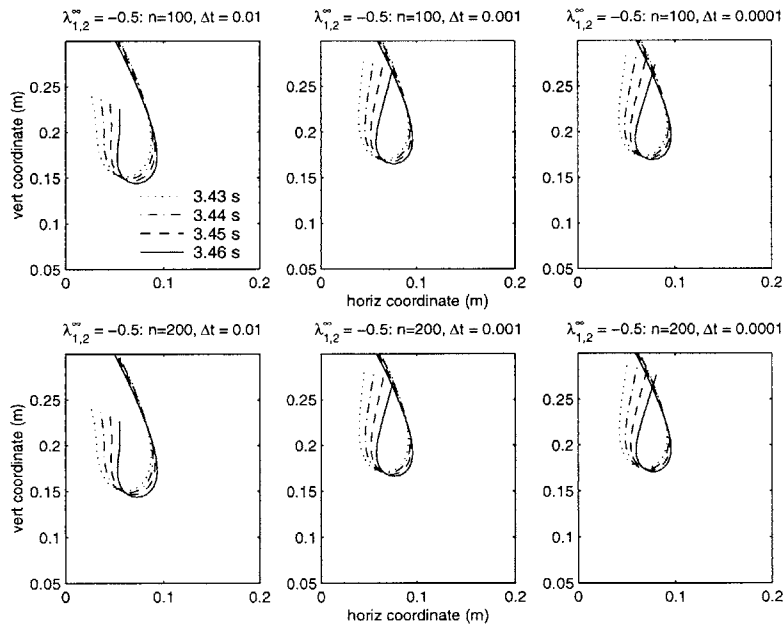
Figure 5-9: Snapshots of the chain configuration near the time of expected intersection for $\lambda_{1,2}^{\infty} = -\frac{1}{2}$ with different spatial and temporal discretizations.
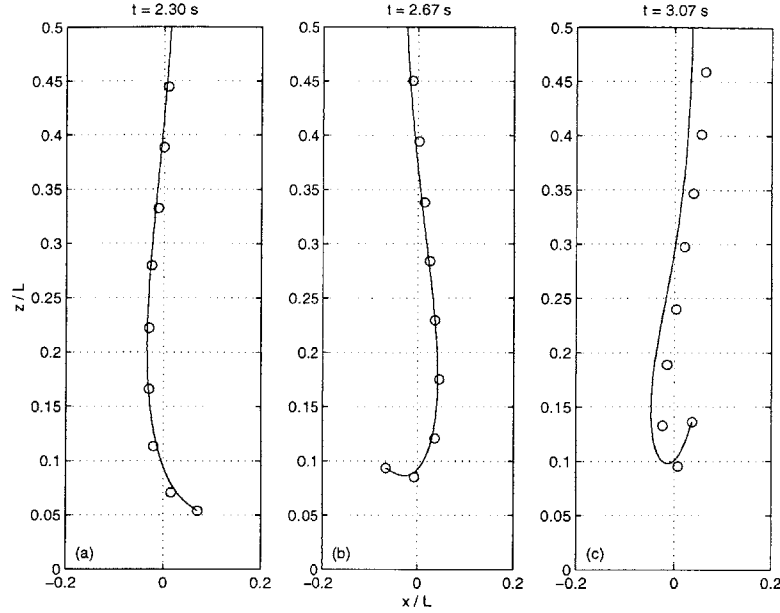
Figure 5-10: Comparison of simulation and experimental results from Howell [46], figure 5.29. Simulation results are for $\lambda_{1,2}^{\infty} = -0.5$ with $\Delta t = 0.0001$ s and $n = 200$.

the original plots did not contain absolute offset information for the points, the experimental points were aligned with the simulation snapshots by matching the first experimental point with the free end of the chain. The comparison for the lower half of the chain is shown in figure 5-10. The simulation results are for $\lambda_{1,2}^{\infty} = -0.5$ with $\Delta t = 0.0001$ s and $n = 200$. At this temporal and spatial resolution the solutions from all of the second-order accurate algorithms were essentially identical. The results at all three time points show good agreement. The comparison at $t = 3.07$ s improves with a slight adjustment to the horizontal offsets that were applied.

These results are in agreement with the observations drawn from the free response problem. At sufficiently small time steps and adequate spatial resolution, all three algorithms: box method, trapezoidal rule, and $\lambda_{1,2}^{\infty} \approx -0.5$, provide accurate solutions. Trapezoidal rule is the best choice in terms of the computational costs of accuracy, where cost is measured simply in terms of time step. As indicated, however, in regions where the solution becomes numerically unstable some numerical dissipation may be necessary to obtain a solution. This suggests a trade-off between optimizing the time step for accuracy and optimizing the algorithm for stability.

86

method	$\Delta t = 0.01$ s		$\Delta t = 0.001$ s	
	x-over (s)	run length (s)	x-over (s)	run length (s)
box	–	3.38	3.45	3.64
trapezoidal	3.41	3.78	3.45	3.60
$\lambda_{1,2}^\infty = -0.7$	–	3.40	–	3.40
$\lambda_{1,2}^\infty = -0.5$	–	3.42	–	3.40
$\lambda_{1,2}^\infty = -0.4$	3.49	3.56	3.46	10.0
$\lambda_{1,2}^\infty = -0.3$	3.51	10.0	3.46	10.0
$\lambda_{1,2}^\infty = -0.2$	3.52	10.0	3.47	10.0
$\lambda_{1,2}^\infty = -0.1$	–	3.60	–	3.40
$\lambda_{1,2}^\infty = 0.0$	–	10.0	–	3.42
$\lambda_{1,2}^\infty = 0.1$	–	10.0	–	3.42

Table 5.1: Comparison of the predicted cross-over time and total simulation time before failure for three-dimensional simulations of the forced hanging chain.

Three-dimensional simulations

In order to further explore these trade-offs, three-dimensional simulations were conducted to explore the behavior of the solutions beyond the time when the chain crosses over itself. Howell [46] noted that out-of-plane motions of the experimental chain only became significant after this point. The simulations were conducted with a small initial out-of-plane force applied at the free end to promote the initiation of out-of-plane motion. This models the inevitable presence of small disturbing forces which produce instabilities in the two-dimensional motion and eventually lead to a fully three-dimensional response.

Table 5.1 lists the observed time of the chain crossing over itself and the total running time (out of a possible ten second simulation) of the simulation before failure. Depending on time step, only solutions for $-0.4 \le \lambda_{1,2}^\infty \le -0.2$ ran for the full ten seconds and resulted in an accurate cross-over prediction. At $\Delta t = 0.01$ s, the stable solutions (at $\lambda_{1,2}^\infty = -0.3$ and $\lambda_{1,2}^\infty = -0.2$) were less accurate than the two-dimensional simulations for $\lambda_{1,2}^\infty = -0.5$ at this same time step. This is consistent with the observation that as damping increases the cross-over time is delayed, until with enough damping it does not occur at all. Also consistent with the two-dimensional results is the convergence to an accurate prediction of 3.46 s with an increase in temporal resolution to $\Delta t = 0.001$ s.

The stability of results for $\lambda_{1,2}^\infty = 0.0$ and $\lambda_{1,2}^\infty = 0.1$ at $\Delta t = 0.01$ s, but not at
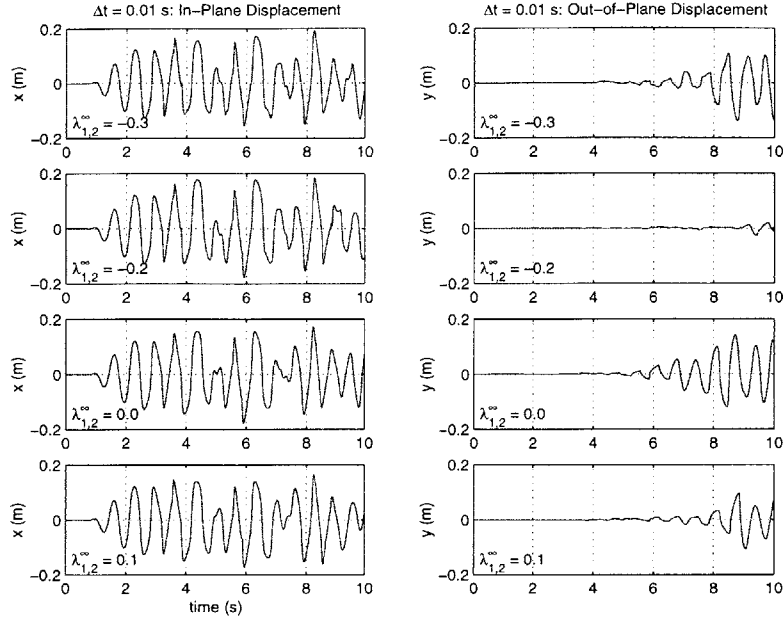
Figure 5-11: In-plane and out-of-plane motion of the free end of the hanging chain for the stable algorithms with $\Delta t = 0.01$ s.

$\Delta t = 0.001$ s, illustrates the dependence of the stability on the frequency content of the response, the time step, and the damping properties of the algorithm. Because the spectral radii in figure 2-4 all initially decrease with the product $\omega \Delta t$, at a fixed frequency a decrease in Δt will result in less damping. If the response at that frequency was responsible for the instability then the solution at the smaller time step may actually be less stable.

Figures 5-11 and 5-12 show the in-plane and out-of-plane motion of the free end of the chain for all simulations which ran for the full ten seconds. At $\Delta t = 0.01$ s there is little consistency between the levels of out-of-plane motion predicted by the different algorithms. For the solutions at $\Delta t = 0.001$ s the results for out-of-plane response appear roughly equivalent. A trace of the motion of the free end in the horizontal plane for $\Delta t = 0.001$ s and $\lambda_{1,2}^{\infty} = -0.3$ is shown in figure 5-13. The roughly circular whirling motion revealed by the trace after the three-dimensional motion is fully developed is the type of response that we expect for this problem [68].

5.2 Solutions for a full scale mooring

As a final study of the stability and accuracy of the time integration algorithm we consider a full scale mooring with an imposed sinusoidal vertical motion at the top node of the

88
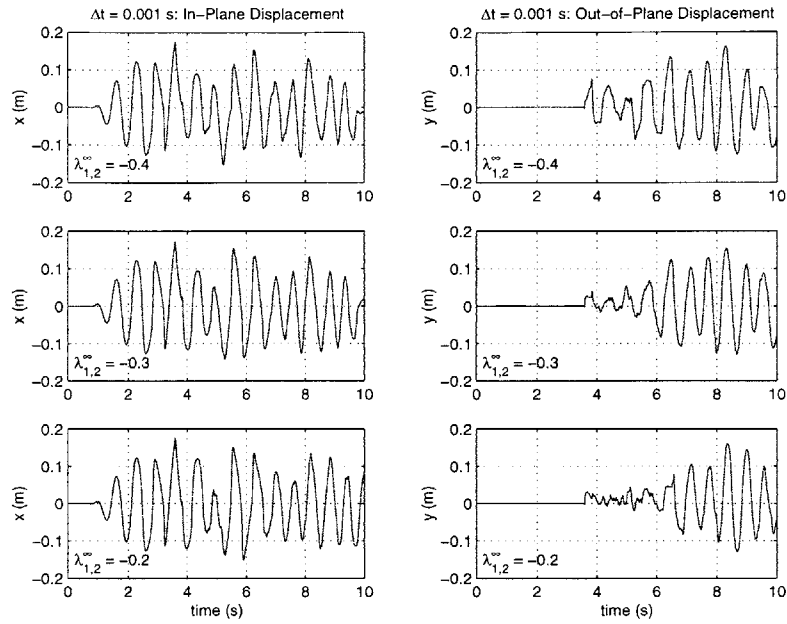
Figure 5-12: In-plane and out-of-plane motion of the free end of the hanging chain for the stable algorithms with $\Delta t = 0.001$ s.
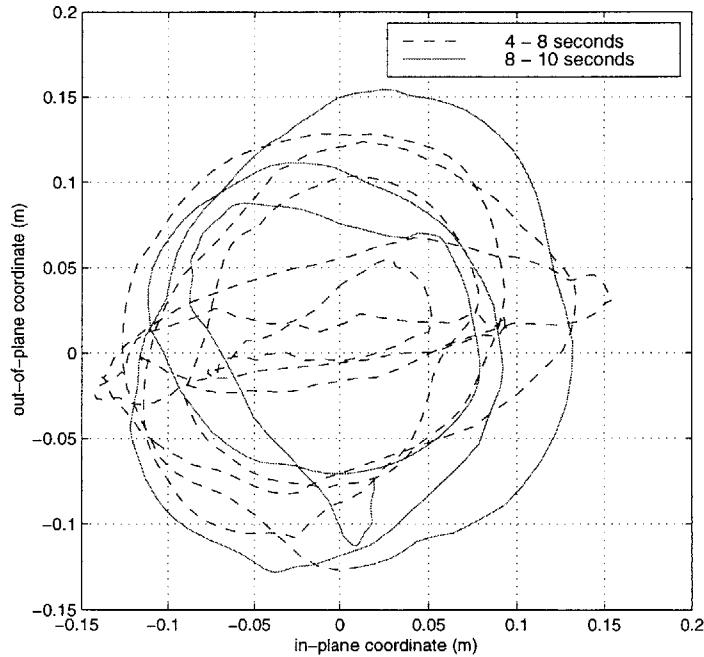
Figure 5-13: Trace of the horizontal motions of the free end of the hanging chain for $\lambda_{1,2}^{\infty} = -0.3$ and $\Delta t = 0.001$ s.

mooring. Given the coordinate integration procedure described in appendix E, errors in the overall solution will be evident based on the error in the computed coordinates of the top node. We can see this if we consider integrals for the top node position in continuous form. From equations E.1 and E.2 it is clear that we can write those positions as

$$x(L,t) = \int_0^L [1 + \epsilon(s,t)] \cos \phi(s,t) ds, \qquad (5.9)$$

$$y(L,t) = \int_0^L [1 + \epsilon(s,t)] \sin \phi(s,t) ds. \qquad (5.10)$$

If we had a perfect solution, the dynamic vertical motion at the top, $x(L,t)$ would always match the imposed vertical sinusoidal motion and the horizontal motion, $y(L,t)$, would always be zero. Ignoring any errors associated with the numerical integration of equations 5.9 and 5.10, any deviation away from the ideal solution represents error in the computed values of ϵ and ϕ along the entire mooring. Thus, comparing the time evolution of the computed horizontal displacement of the top node, when the imposed motion is purely vertical, provides a simple and convenient estimate of the error associated with a particular form of the time integration algorithm.

The physical characteristics of the trial mooring are the same as for the field experiment, as described in table 4.1 and figure 4-4. For each form of the algorithm under consideration, the model was run for 300 seconds of simulation time with a base time step of 0.1 seconds. To facilitate comparison with results from a previous version of the program, the spatial discretization was uniform over each segment. The flexural stiffness, EI, of the chain was set to 0.1 N m^2. The environmental forcing was chosen to simulate rather severe conditions with a uniform current of 2.0 m/s and an imposed vertical motion with amplitude 2.0 meters and period 8.0 seconds.

Figure 5-14 shows the computed top node horizontal position for four cases: the original box method without any averaging of the coefficient matrices, the box method that arises from the generalized-α method with $\alpha_k = 0.5$, $\alpha_m = 0.5$, $\gamma = 0.5$, the generalized trapezoidal rule, and backward differences. For all cases, the values of α_k, α_m, and γ are summarized in table 5.2. Note that for both box methods the solution failed before the full 300 second run was completed. A solution fails when the nonlinear solver cannot get a convergent solution even after adapting Δt down by a factor of 10^{-4}. For the original box method without any coefficient averaging this happened at 131 seconds. The box

90

algorithm	α_k	α_m	γ
box method w/o coefficient averaging	–	–	–
box method w/ coefficient averaging	0.5	0.5	0.5
trapezoidal rule	0.0	0.0	0.5
backward differences	0.0	0.0	1.0
$\lambda_{1,2}^{\infty} = 0.0$	0.0	-0.5	1.0
$\lambda_{1,2}^{\infty} = -0.33$ (Cornwell and Malkus [20])	0.25	0.0	0.75
$\lambda_{1,2}^{\infty} = -0.2$	0.167	-0.167	0.833
$\lambda_{1,2}^{\infty} = 0.1$	-0.111	-0.722	1.111

Table 5.2: α_k, α_m, and γ values for the tested algorithms. Solutions for the box method without averaging are based on an old version of the program and cannot be obtained within the newly developed generalized-α family of algorithms.

method with coefficient averaging (this is the box method that we can achieve within the generalized-α family derived in chapter 2) lasted somewhat longer, with failure at 260 seconds. In addition to those failures, it appears that the solution from the trapezoidal rule is beginning to exhibit the same type of behavior starting at around 250 seconds. This solution does indeed fail completely at 445 seconds when allowed to proceed beyond 300 seconds.

The failure of these three algorithms reinforces two of the important motivations that we gave in developing the generalized-α method for the cable dynamics equations. The difference in the box method solutions illustrates the improved stability characteristics of the algorithm with temporally averaged coefficient matrices. That all three eventually failed illustrates the importance of numerical dissipation in improving stability. Figure 5-15 illustrates the calculated shear force at the top node for these four trials. With $EI = 0.1$ for this chain mooring we expect very little shear force. Prior to failure, however, all three algorithms developed obvious Crank-Nicolson type noise in the shear force. The solution using backward differences has significant error in the calculated horizontal displacement and a slightly noticeable drift in the shear force, but remains stable. The numerical dissipation associated with backward differences eliminates the Crank-Nicolson noise and the solution proceeds with good stability (albeit with relatively poor accuracy).

Solutions with significantly improved stability and error properties are obtained from the one parameter form of the new generalized-α algorithm. Figure 5-16 shows the error
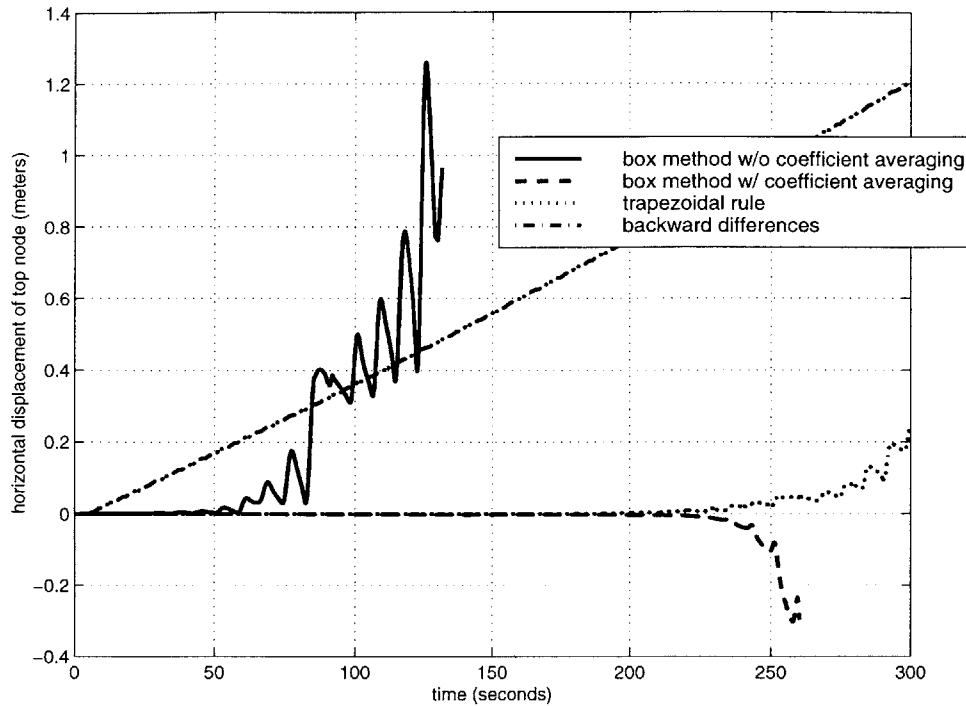
Figure 5-14: Calculated horizontal displacement of the top node of the trial mooring for the box, trapezoidal, and backward difference algorithms.

in calculated horizontal displacement for the trial mooring using four different values of $\lambda_{1,2}^{\infty}$. Noting the different vertical scales in figures 5-14 and 5-16 it is clear that the drift in the calculated horizontal displacement is substantially reduced for all four of these cases relative to backward differences. The worst case in figure 5-16 has approximately two orders of magnitude less error at 300 seconds. The best case is nearly four orders of magnitude better.

The rate of error growth, defined as the maximum absolute value of the horizontal displacement divided by the 300 second simulation time, is plotted (with circles) for a number of $\lambda_{1,2}^{\infty}$ values in figure 5-17. This error rate is essentially the slope of the trends represented by the four curves in figure 5-16. The error is minimized for $\lambda_{1,2}^{\infty} \approx -0.19$.

Unfortunately, as the additional curves in figure 5-17 illustrate, the optimum value of $\lambda_{1,2}^{\infty}$ is highly problem dependent. The first three curves reflect the error growth rate for the mooring in the 2.0 m/s current with three different dynamic excitation conditions. The second set of three curves shows the error growth rate for the mooring in 0.5 m/s current with the same three dynamic excitation conditions. The static shapes of the mooring in the two different current conditions are shown in figure 5-18.
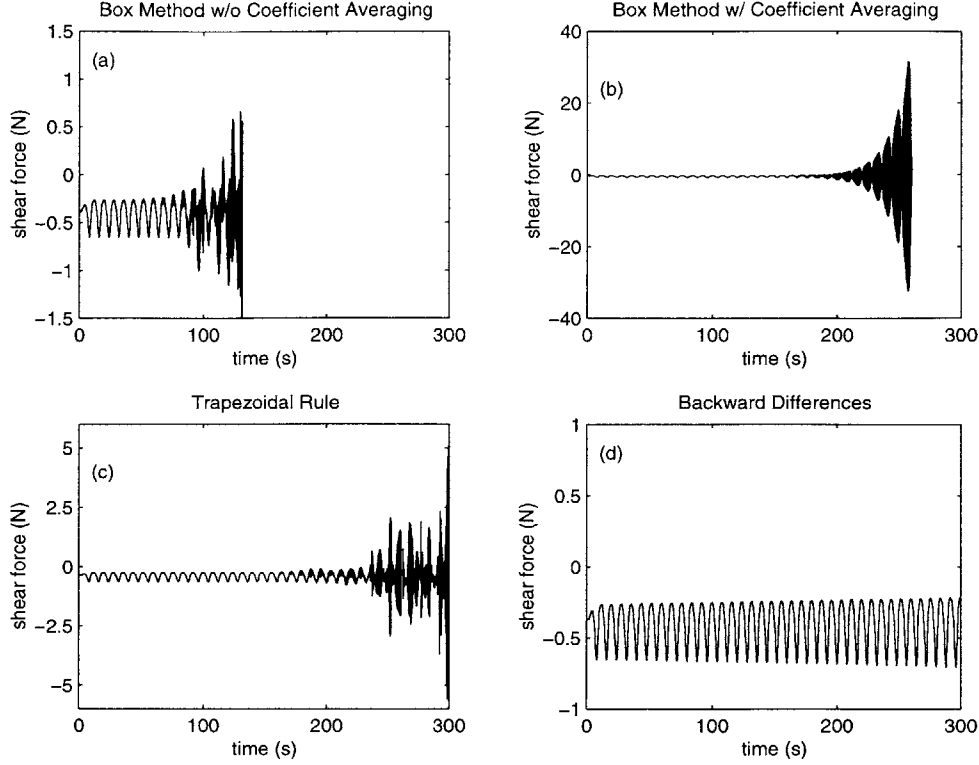
Figure 5-15: Shear force at the top node in the trial mooring for the three failed solution algorithms and backward differences. Note that the vertical axes on all four plots are different.

For the high current configurations, the location of the error minimum does not change significantly for excitations with the same period but differing amplitudes. When the period of the excitation is changed, the location of the minimum does shift. This behavior is consistent with the frequency response of the mooring not changing significantly with amplitude of excitation. This contrasts with the low current configurations for which the error maxima and minima are shifted most dramatically when the amplitude, not the excitation period, changes.

Such behavior makes it difficult to draw any general conclusions that would aid in choosing an appropriate value of $\lambda_{1,2}^{\infty}$ for a given problem. We can say that the overall level of error appears to be a direct function of the severity of the excitation, as measured by the amplitude of the imposed velocity, $A\frac{2\pi}{T}$, for example. The safest choices also seem to be $\lambda_{1,2}^{\infty} < 0$ to avoid the local maxima seen in the low current configuration.

Additional support for choosing $\lambda_{1,2}^{\infty} < 0$ comes from an examination of the stability of the solution as a function of $\lambda_{1,2}^{\infty}$. If we modify our adaptive time-stepping scheme

93
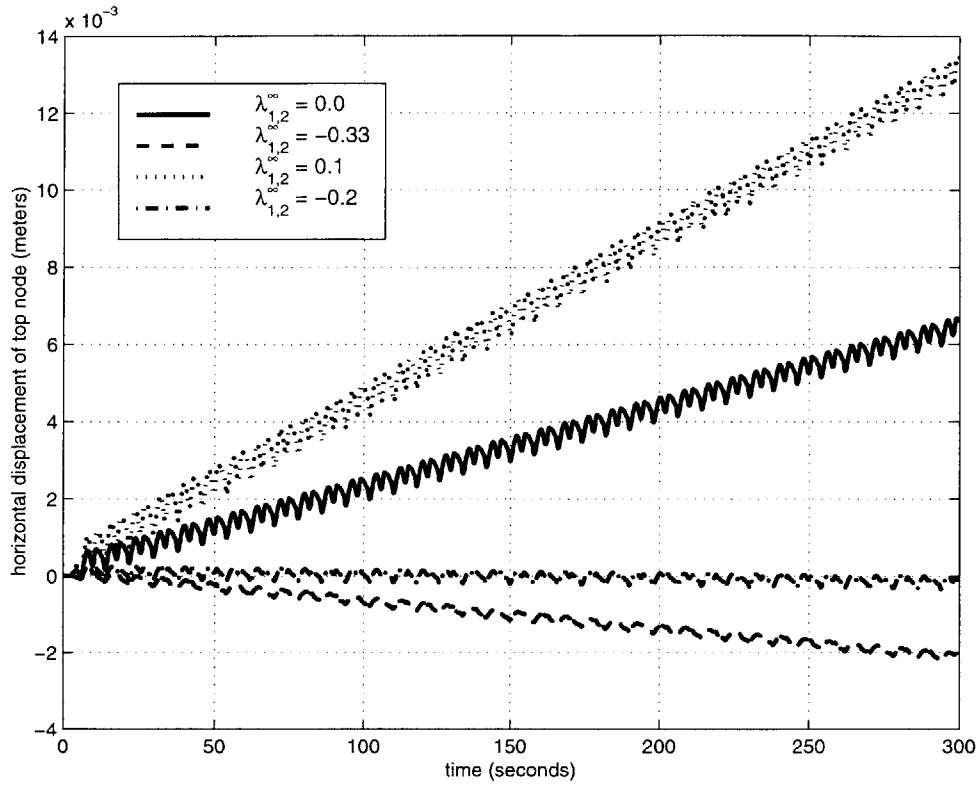
Figure 5-16: Calculated horizontal displacement of the top node of the trial mooring for $\lambda_{1,2}^{\infty}$ value of 0.0, -0.33, 0.1, and -0.2.
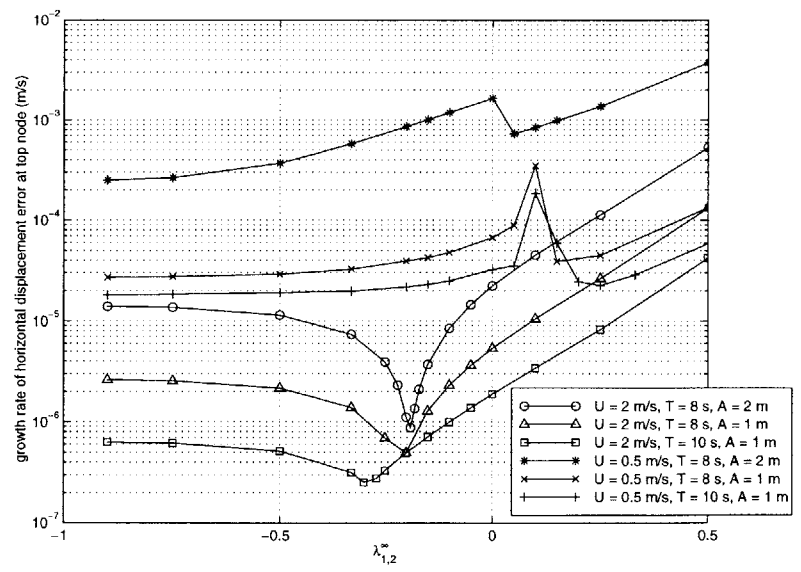
Figure 5-17: Time rate of growth of the error in the top node horizontal displacement of the trial mooring as a function of $\lambda_{1,2}^{\infty}$.
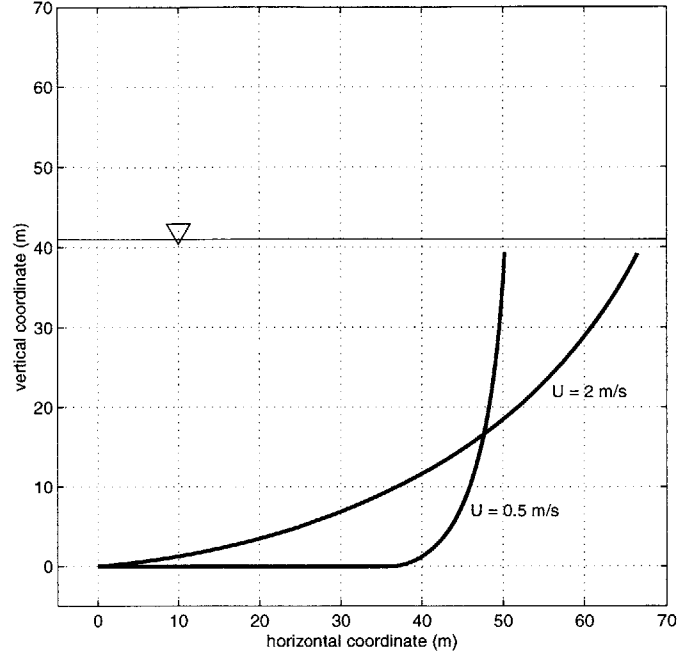
Figure 5-18: Static configuration of the trial mooring configurations in 0.5 m/s and 2.0 m/s uniform current.

such that it functions like the adaptive relaxation scheme described in appendix C, we can determine the largest Δt that can successfully and consistently be used to propagate a solution in time. At each time step, we either increase or decrease Δt by some small factor depending on the success of the solution at that step. Given

$$t^{i+1} = t^i + \Delta t^i, \tag{5.11}$$

if we can successfully solve the nonlinear problem for t^{i+1} then we increase the time step

$$\Delta t^{i+1} = R_2 \Delta t^i, \tag{5.12}$$

and try for the solution at $t^{i+2} = t^{i+1} + \Delta t^{i+1}$. If the solution at t^{i+1} is unsuccessful, then we decrease the time step

$$\Delta t^i = \frac{\Delta t^i}{R_1}, \tag{5.13}$$

and try again. R_1 and R_2 are constants slightly larger than unity with $1 \leq R_2 < R_1$ so that a failed step decreases Δt more than a successful step increases Δt. For these trials
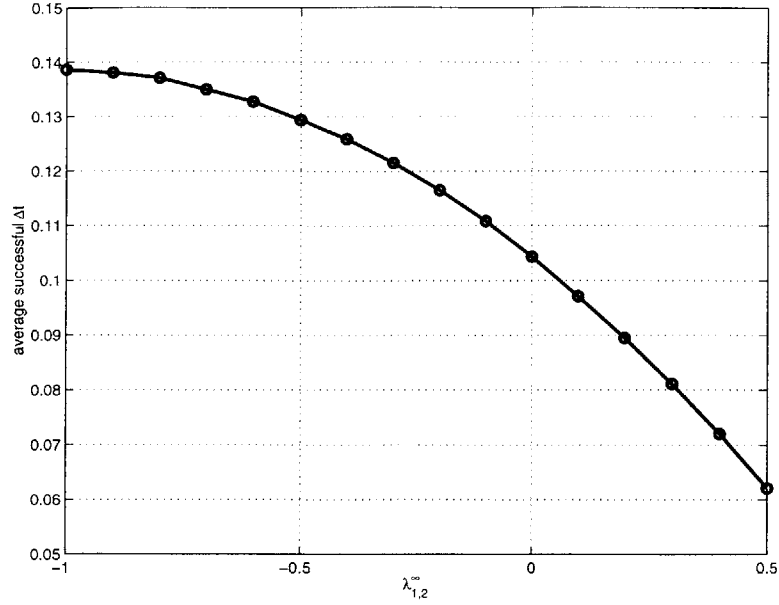
Figure 5-19: Average successfully adapted time step as a function of $\lambda_{1,2}^\infty$ over the course of a 100 second simulation for the low current configuration with 1.0 m amplitude and 8.0 second period excitation.

$R_2 = 1.02$ and $R_1 = 1.1$. This procedure tends to drive Δt to an optimum value in a relatively small number of time steps.

Figure 5-19 shows the average (over a 100 second simulation) successfully applied value of Δt as a function of $\lambda_{1,2}^\infty$ for the low current configuration with 1.0 m amplitude and 8.0 second period. This configuration was chosen because the simulations with $\lambda_{1,2}^\infty \geq 0$ in the latter three curves (the low current configurations) in figure 5-17 required base time steps of 0.05 seconds to proceed without constant adaptation[1]. Simulations with $\lambda_{1,2}^\infty < 0$ used a base time step of 0.1 seconds and proceeded successfully with little or no adaptation. This suggested, and figure 5-19 confirms, that the maximum time step value for these cases was dependent on $\lambda_{1,2}^\infty$. Data from the high current configurations shows a similar trend, with the maximum Δt decreasing sharply for $\lambda_{1,2}^\infty > 0$. There is more variability in the data for $\lambda_{1,2}^\infty < 0$, however, as the maximum Δt is significantly larger than for the low current configurations (between 0.5 and 1.0 second) and in each case shows more variability as the solution progresses.

Based on data in figures 5-17 and 5-19 then, we can conclude that a value for $\lambda_{1,2}^\infty$

---

[1] Adaptation in those simulations refers to the standard adaptive time-stepping algorithm which reduces Δt by factors of 10 to ensure that the solution remains on the original sample grid.

between -0.5 and -0.9 is reasonable in terms of maximizing stability (as measured by the largest allowable Δt) and minimizing the drift error in long time simulations. In this range both the error and stability properties appear to be relatively flat and near optimal for most of the cases considered. $\lambda_{1,2}^{\infty} = -1$ should clearly be avoided as it is the box method with no dissipation and is prone to the type of failures exemplified in figure 5-15. A trial using a value of $\lambda_{1,2}^{\infty} = -0.98$ demonstrated the same failure mechanism after approximately 2250 seconds of simulation. This suggests that even a small amount of numerical dissipation can significantly improve long term stability, but that for guaranteed stability there is a nominal level of dissipation which must be provided. A run with $\lambda_{1,2}^{\infty} = -0.9$ showed no signs of Crank-Nicolson noise build-up after 3000 seconds of simulation.

These results are consistent with the observations gleaned from the hanging chain problems, with the additional caveat that in the case of real moorings, solutions with $\lambda_{1,2}^{\infty} \approx -0.5$ are significantly more stable than trapezoidal rule solutions. That we might be able to use a slightly larger Δt to achieve the same level of accuracy with the trapezoidal rule is no consolation when we cannot in fact get a stable long-time solution at any reasonable Δt.

5.3   Mesh refinement

In studying the spatial discretization of a model mooring system there are three important factors to consider. At the most basic level we must choose how many nodes to use in discretizing each continuous segment of the mooring. The mesh refinement procedure described in chapter 3 also requires that we set c_w, the weighting factor used in assigning the available nodes. Finally, the value of the flexural stiffness, EI, for a given segment has an important effect on the static solution over that segment. For relatively high EI, oscillatory solutions for curvature and shear, described in section 3.3, are not typically a problem and uniform meshes with relatively low numbers of nodes are generally sufficient. For materials with zero EI or EI just large enough to prevent the singularities associated with zero tension, which is the typical situation for chain moorings, these oscillations can be quite significant and mesh refinement becomes important.

For the chain mooring deployed during the field experiment we arbitrarily set the value of EI to a value of 0.1. Experience has shown that this value is large enough to prevent

zero tension singularities in the dynamic solution. In practical terms this is the flexural stiffness of a steel wire that is 1.76 mm in diameter. Alternatively, if we take the diameter of the chain to be the shaft link diameter and consider that

$$EI \sim EA\frac{d^2}{16},$$ (5.14)

then our small value of EI is 1/6500 smaller than the value of EI for a circular rod of equivalent axial stiffness. Given that the refined mesh solutions with this value of EI are satisfactory, it seems reasonable to avoid any question that a larger artificial value of EI might begin to affect the dynamic solution in a non-negligible way.

To examine the effect of c_w on the static solution on the refined mesh we consider two mooring models. The first models the system as a single, continuous shot of chain, neglecting the presence of inline instruments. The second models the field experiment mooring as it was deployed, with the inline AxPack instruments between shots of chain. In both cases the current was uniform over the water column at 0.5 m/s. The static shape of the mooring (which is nearly the same for both configurations) for this current profile is shown in figure 5-18. For each trial static solution we compare the curvature to a baseline solution generated on a uniform mesh with twice as many nodes and EI increased to 10.0.

The static curvature solutions for the continuous chain model are shown in figure 5-20. The trial solutions used 162 nodes over the 80.78 m total length of the mooring. The solutions on the mesh refined with $c_w = 10$ and $c_w = 50$ appear to be a clear improvement over the unrefined uniform mesh ($c_w = 0$) with the same number of nodes and EI value. To quantify the improvement, the error in curvature for a range of c_w values is plotted in figure 5-21. The error is calculated as the root mean square difference between the baseline curvature solution (resampled on the trial solution mesh using cubic splines) and the curvature from the trial solution.

The error is minimized for a value of $c_w \approx 5$. Higher values of c_w give too much weight to curvature oscillations and produce a mesh which is too coarse in the interior portions of the system. This is clearly shown in the top half of the mooring for $c_w = 50$ in figure 5-20, where there are now oscillations in the solution where there were none in the uniform mesh trial solution. Figure 5-22 shows the mesh density (defined as the number of elements per meter) for the same three cases shown in figure 5-20. The solution with the lower weight
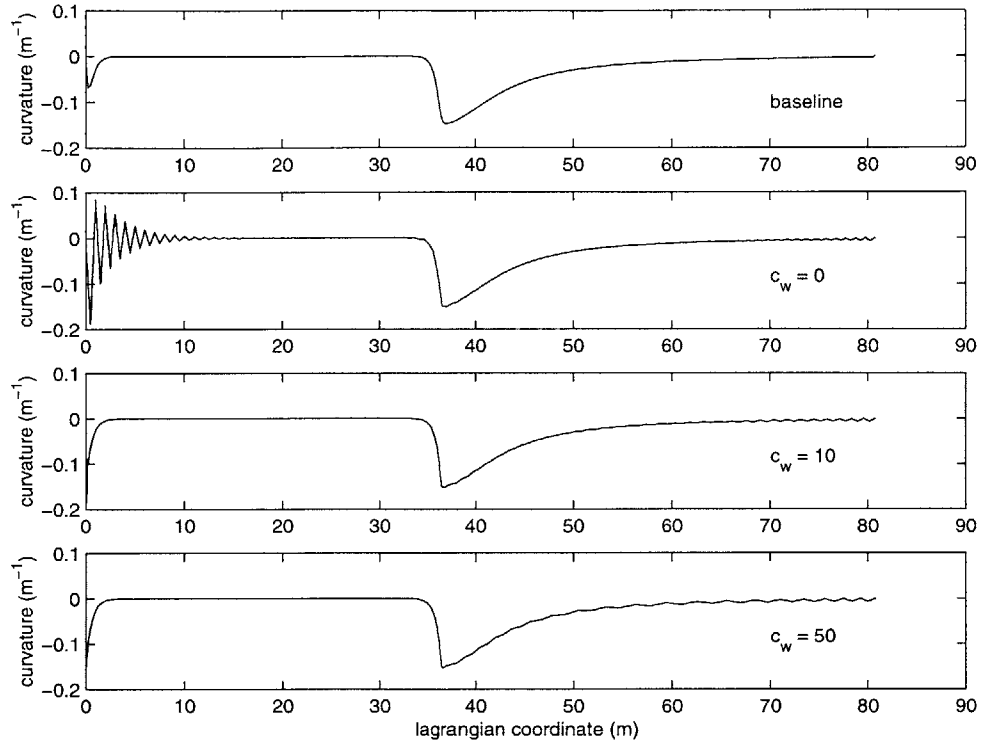
Figure 5-20: Curvature from the static solutions of the continuous all chain mooring.
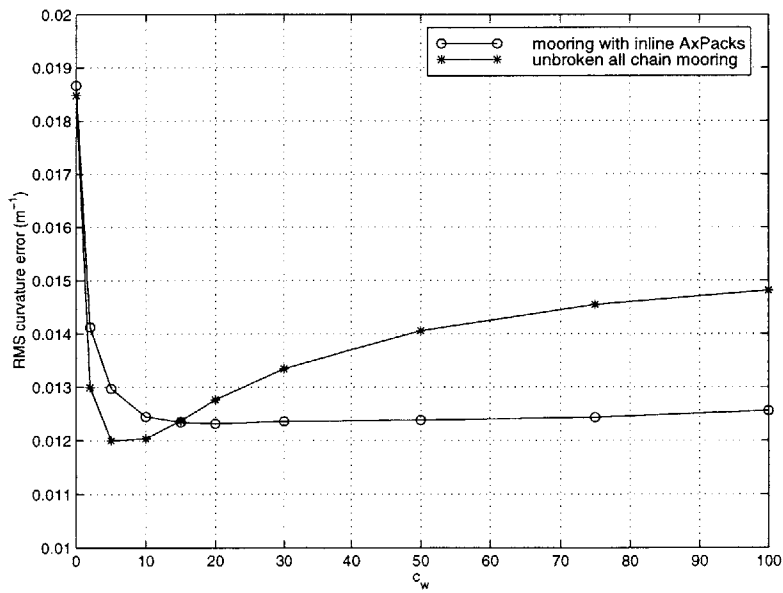
Figure 5-21: Root mean square error in the curvature of the trial solutions.
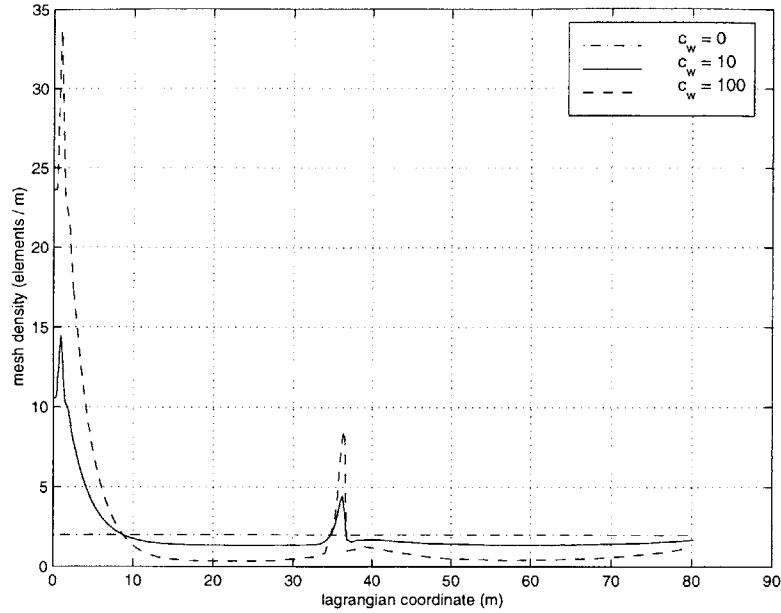
Figure 5-22: Mesh density after refinement of the all chain mooring.

is able to distribute sufficient density near the boundary while maintaining a density that is not significantly lower than the uniform mesh in the rest of the mooring. The higher weight solution devotes many more nodes to the area near the boundaries and as a result cannot provide enough density to other areas.

Figure 5-23 shows the baseline solution, the uniform mesh solution ($c_w = 0$), and two refined mesh solutions for the mooring with inline instruments. The locations of the instruments along the mooring are clearly visible as the flat spots in curvature at $s \approx 45$ m, $s \approx 50$ m, and $s \approx 57$ m. The number of nodes on each of the chain segments was 91 (over 45.0 m), 18 (over 3.5 m), 36 (over 7.0 m), and 47 (over 23.0 m). Each 0.76 m AxPack was modeled using 3 nodes. The baseline solution with uniform mesh had twice the number of nodes over each of the chain segments. The relatively larger number of nodes in the shorter chain segments reflects the fact that the length of the decay of oscillations in the curvature is related more to mesh density than to physical length. This means that comparable numbers of nodes must be employed near each segment boundary, regardless of the length of the segment.

For this case there is no striking minimum in the error shown in figure 5-21. A value of $c_w = 20$ appears to give the best solution, but values at least out to $c_w = 100$ also appear reasonable based on this measure of the error. In looking closely at figure 5-23 for $c_w = 50$,

100
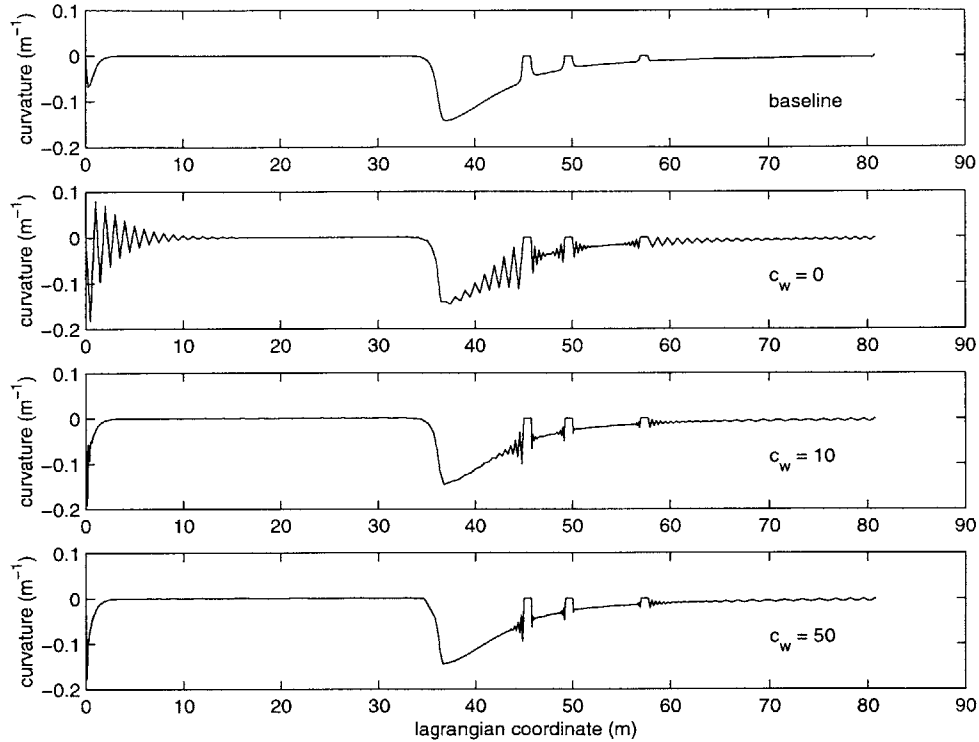
Figure 5-23: Curvature from the static solutions of the mooring with inline instruments.

however, the sharpness of the plot around the curvature maximum ($s \approx 35$) indicates that oscillations near the boundaries are being reduced at the expense of an overly coarse mesh elsewhere.

5.4 Comparison with experimental results

The final phase of the model validation process is a comparison of simulation results to data from the full-scale mooring described in chapter 4. For both the two- and three-dimensional models we make two types of comparison. In the first we compare time series and spectra from individual data sets to verify the ability of the model to accurately capture the detailed response of the mooring. In the second comparison we consider statistics of the response from all data sets. This analysis provides a check that our chosen hydrodynamic coefficients and environmental parameters yield accurate solutions over a wide range of forcing conditions.

The hydrodynamic coefficients for the chain and AxPacks in the validation runs are shown in table 5.3. The added mass can be calculated from the added mass coefficients,

material	d (m)	C_{d_n}	C_{d_t}	C_{a_n}	C_{a_t}
half-inch chain	0.0495	0.5	0.01	1.0	0.1
AxPack	0.075	0.8	0.069	1.0	0.5

Table 5.3: Mass and drag coefficients for the validation simulations.

C_{a_n} and C_{a_t}, according to

$$m_{a_n} = \rho_w \frac{\pi d^2}{4} C_{a_n},$$
(5.15)

$$m_{a_t} = \rho_w \frac{\pi d^2}{4} C_{a_t},$$
(5.16)

where d is the width of a link of chain. Coefficients for the chain are based on experimental results from Gopalkrishnan [37] and previous numerical studies (e.g., [8]). AxPack coefficients are approximations based on cylinder and flat plate coefficients. The bottom stiffness was set to 100 N/m^2 and the bottom damping ratio to 1.0. The buoy normal drag coefficients for the static solutions were 0.5 (in water) and 1.3 (in air). For the purposes of the validation, all of these values were chosen because they were physically reasonable and produced simulation results that matched experimental results over most data sets. Variations on these parameters and schemes for choosing parameters that best match the experimental data are studied in detail in chapter 6.

5.4.1 Two-dimensional model

For each of the experimental data sets, the effective values for wind and current in the two-dimensional plane and the time series of buoy vertical velocity are used as input to the model and a time series of mooring response is computed. The procedures for calculating these inputs are described in section 4.4. Because of the relatively low currents and winds that were observed during the experiment, static solutions for the simulations were obtained using the dynamic relaxation procedure described in section C.4.

Examples of the simulated tension beneath the buoy, along with the corresponding experimentally observed values are shown for two cases in figure 5-24. In both cases, the agreement between simulation and experiment is excellent. For the 6 December data with relatively moderate environmental conditions (approximately 15 knot winds), the mean

102
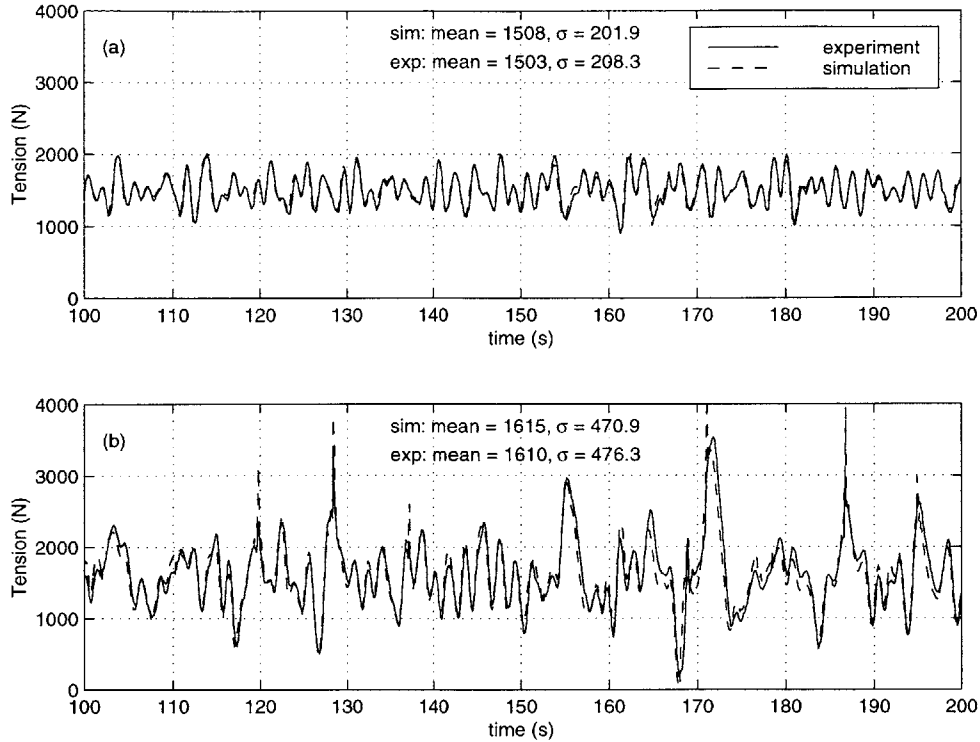
Figure 5-24: Comparison of experimental and two-dimensional model simulated tension. (a) 6 December 1998 at 0800 localtime. (b) 3 January 1999 at 1600 localtime.

and standard deviation of the simulated tension over the full 200 seconds of simulation time (excluding a 10 second initial ramp-up period) were 1503 N and 201 N, respectively. The corresponding statistics for the experimental data were 1503 N and 208 N. The statistics for the 3 January storm (with near 50 knot winds) also show close agreement: 1611 N and 471 N for the simulation compared to 1610 N and 476 N for the experiment. In this latter case a few of the tension peaks are higher in the simulation than in the experiment. Given the sharpness of these peaks, it is possible that the analog filtering in the buoy instrumentation attenuated the experimental signal.

Figure 5-25(a) shows the tangential acceleration signal recorded by the lowest AxPack for the 3 January 1999 storm. For comparison, we calculate the simulated acceleration, $a(t)$, at this point based on the tangential velocity, $u(t)$, and the inclination from the vertical, $\phi(t)$,

$$a(t) = \frac{du}{dt} + G \cos \phi(t), \tag{5.17}$$

103
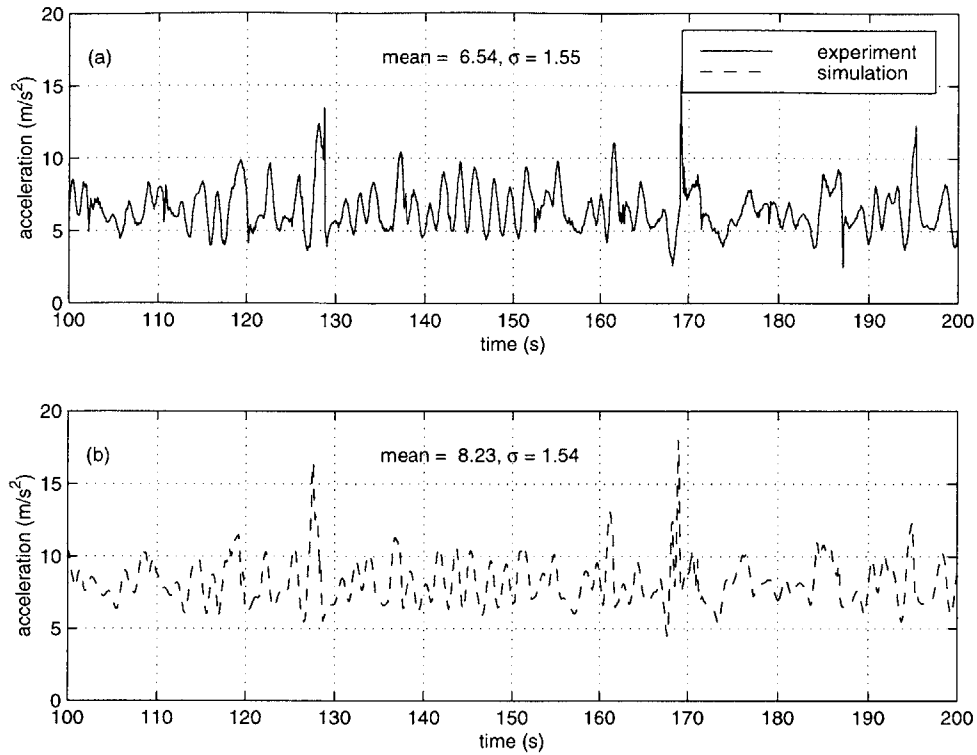
Figure 5-25: Comparison of experimental (a) and two-dimensional model simulated (b) acceleration signal at the lowest AxPack for the 3 January 1999 storm event.

where G is the acceleration due to gravity. This quantity is plotted in figure 5-25(b). After time aligning the two signals using the peak observed just before 170 seconds, the results look very similar. Based on a comparison of the spectra of the responses (figure 5-26) and the experimental standard deviation, 1.54 m/s^2, and simulation standard deviation, 1.55 m/s^2, the level and frequency content of the responses also show excellent agreement. The mean of the acceleration (which is an indication of the static tilt of the mooring chain at that point) is lower in the experiment than in the simulation (6.54 m/s^2 versus 8.23 m/s^2). This suggests that the AxPack may have been lower along the chain than expected. Given the predicted static shape for the mooring under these conditions, any error of two to three meters in the position of the lowest AxPack could produce this discrepancy in the mean accelerations.

For a more complete picture of the model performance, we consider the tension statistics for all 119 experimental and simulated data sets. The standard deviation and mean of the tension are plotted versus the standard deviation of heave acceleration (a measure of the severity of the dynamic forcing) in figure 5-27. The heave statistic is identical for
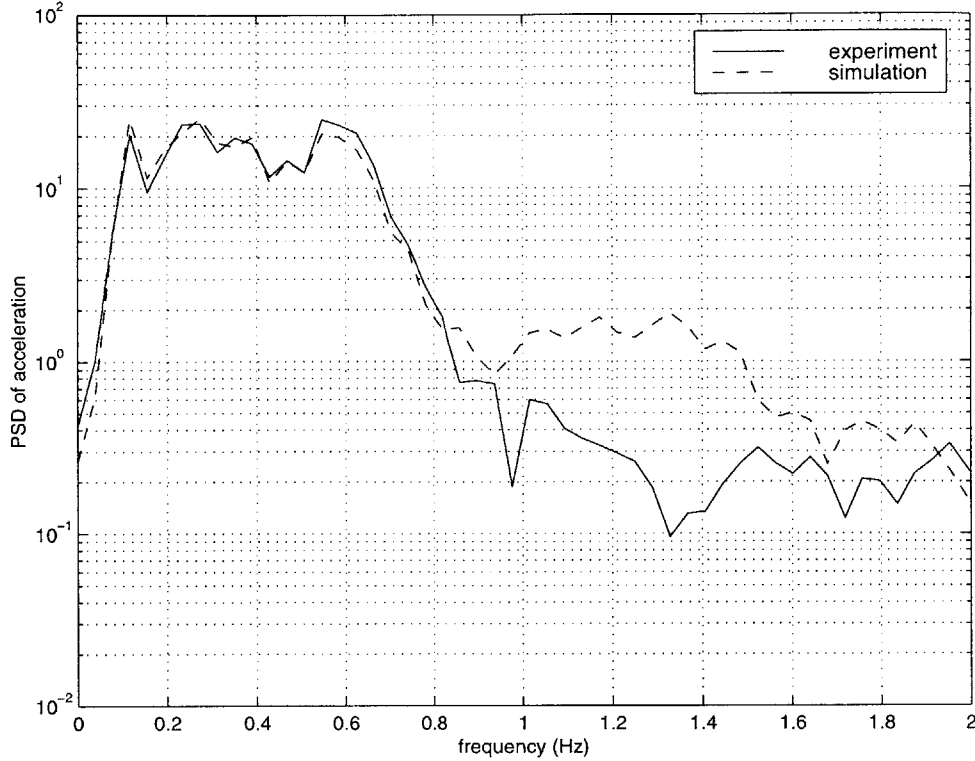
Figure 5-26: Spectral comparison of experimental and two-dimensional model simulated acceleration signal at the lowest AxPack for the 3 January 1999 storm event.

simulation and experiment because the experimental buoy motion is imposed as an input for the simulation. Overall, the agreement in the dynamic results (as measured by standard deviation of tension) is quite good, with nearly exact agreement in low sea states and good agreement in higher sea states. The root mean square difference between experiment and simulation is 16.1 N. The relative RMS difference, defined as

$$e = \sqrt{\frac{1}{n} \sum_{j=1}^{n} \left(\frac{\sigma_{T,\exp} - \sigma_{T,\text{sim}}}{\sigma_{T,\exp}} \right)_j^2}, \qquad (5.18)$$

is 5.8%.

The simulated mean tensions do not correspond quite as well with experimental results, but again the trend with sea state appears to be correct. The root mean square difference between simulation and experiment, 37.0 N, is less than 16% of the total observed variation in mean tension over the course of the experiment. Given the lack of collocation of the wind measurement, the heavy temporal averaging of both wind and current, and the assumptions made in projecting wind and current into a two-dimensional
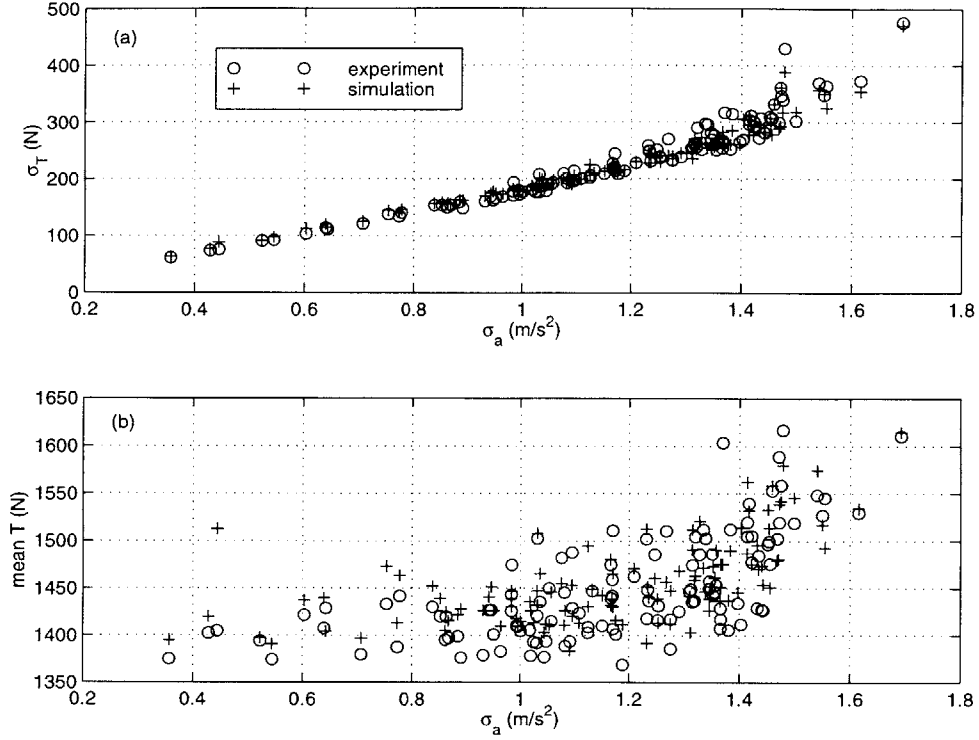
Figure 5-27: Comparison of experimental and two-dimensional model simulated tension statistics over all 119 data sets. (a) Dynamic response as measured by the standard deviation of the tension. (b) Steady-state response as measured by the mean of the tension.

plane, these larger discrepancies in steady-state results are not unexpected. Relative to dynamic results for which we have exact knowledge of the forcing (though we are neglecting the horizontal motions of the buoy), we do not have sufficient information to hope for an exact comparison.

Finally, for a frequency domain analog to the time domain comparisons above, we consider the errors in the simulated tension spectra. Because the standard deviation is a measure of the energy over the entire spectrum,

$$\sigma_T = \sqrt{\int_0^\infty S_T(\omega)d\omega},$$
(5.19)

it is possible for positive and negative errors at different frequency components to effectively cancel in a comparison of standard deviations. A spectral error metric that scales similarly to the RMS error in standard deviation, but prevents the cancellation of positive and negative errors can be derived by modifying the spectrum from the simulation so that

all errors have the same sign,

$$S_{T,\text{sim}}^*(\omega) = |S_{T,\text{sim}}(\omega) - S_{T,\text{exp}}(\omega)| + S_{T,\text{exp}}(\omega). \tag{5.20}$$

The standard deviation from the discrete form of this modified spectrum with N frequency components is

$$\sigma_{T,\text{sim}}^* = \sqrt{\frac{1}{N} \sum_{i=1}^{N} S_T^*(\omega_i)}. \tag{5.21}$$

Analogous to equation 5.18 then, the spectral error over n data sets is simply

$$e_* = \sqrt{\frac{1}{n} \sum_{j=1}^{n} \left(\frac{\sigma_{T,\text{exp}} - \sigma_{T,\text{sim}}^*}{\sigma_{T,\text{exp}}} \right)_j^2}. \tag{5.22}$$

Equation 5.22 applied to the full simulation data set produces an error result of 0.068. To better understand the magnitude of this error, figures 5-28 and 5-29 show the experimentally observed and simulated tension spectra for the 6 December and 3 January data sets. The spectral errors for these two individual cases are 0.040 and 0.074, respectively. Visually, the error in these two cases is quite small, indicating that the error value of 0.068 over the entire data set is quite reasonable.

5.4.2 Three-dimensional model

The validation process for the three-dimensional model is similar to that described above for the two-dimensional model. Only 60 experimental data sets are available for the validation, however, because of the loss of the y accelerometer channel after 27 December. For data sets before 27 December we are able to calculate the vertical, horizontal in-plane and horizontal out-of-plane velocities of the buoy to use as dynamic inputs into the three-dimensional model. Like the two-dimensional simulations, static solutions are obtained using the dynamic relaxation procedure. With the current and wind projected into the effective plane of the mooring and horizontal motions rotated into in-plane and out-of-plane components we can use the same high current static solution as the initial condition in all of the dynamic relaxation solutions, regardless of the orientation of the mooring in earth reference coordinates.
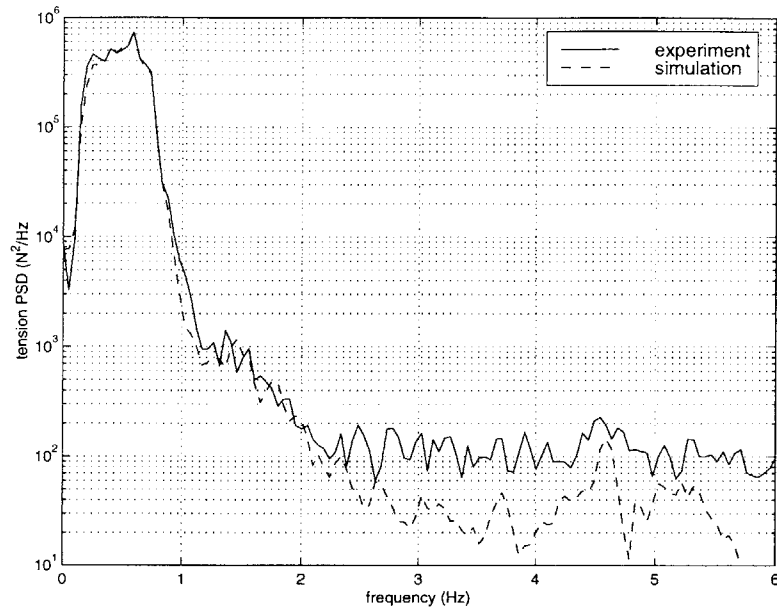
Figure 5-28: Comparison of simulated and experimental tension spectra for the 6 December 1998, 0800 data record.
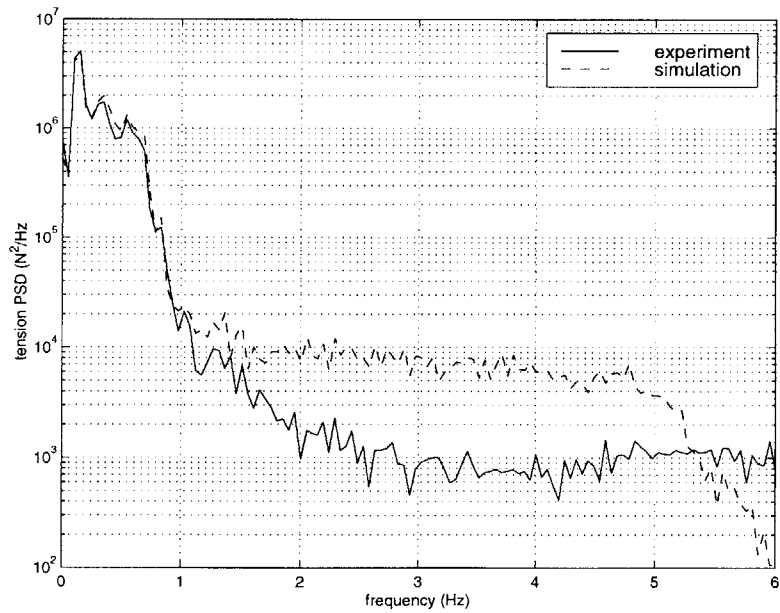
Figure 5-29: Comparison of simulated and experimental tension spectra for the 3 January 1999, 1600 data record.
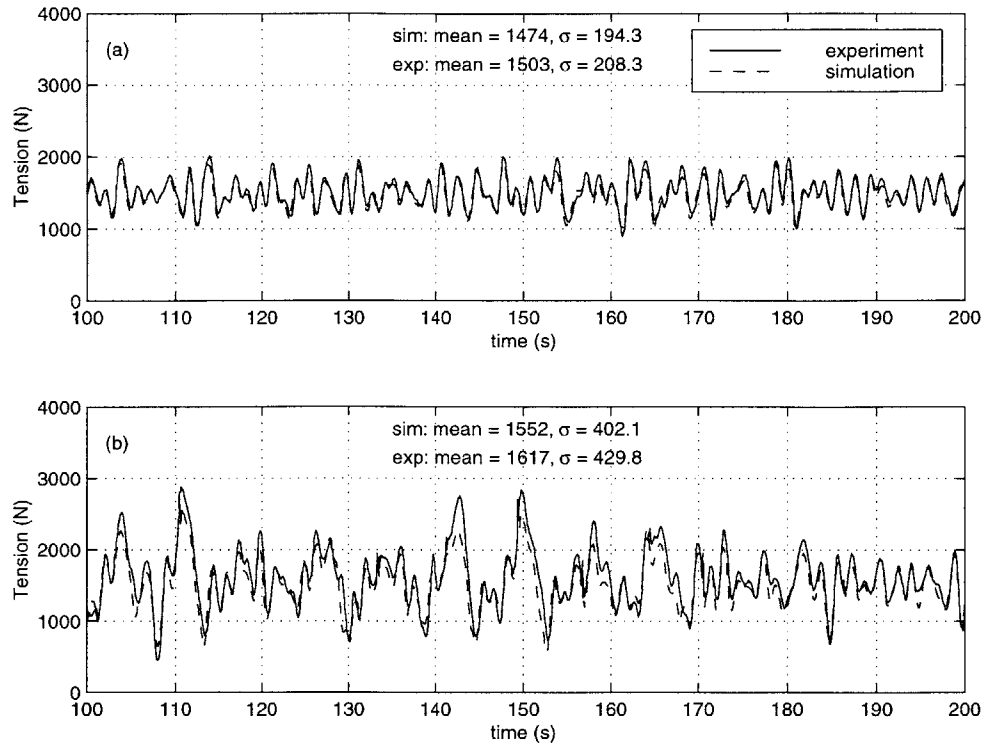
Figure 5-30: Comparison of experimental and three-dimensional model simulated tension. (a) 6 December 1998 at 0800 localtime. (b) 22 December 1998 at 0800 localtime.

A comparison of the experimental and three-dimensional model simulated tension beneath the buoy is shown in figure 5-30 for the same 6 December data set as in the two-dimensional validation and for a storm on 22 December with winds of 35 knots. In both cases the results agree well. For the 6 December data set the tension standard deviation from the two-dimensional simulation (201 N) better matches the experimental result (208 N). For the 22 December storm the tension standard deviation from a two-dimensional simulation is 392 N and the result from the three-dimensional simulation (405 N) is closer to the experimental result of 430 N. In both cases, the mean tension is less accurate in the three-dimensional simulation than in the corresponding two-dimensional simulation (the mean tension in a two-dimensional simulation of the 22 December data is 1571 N). Statistics for all of these cases are summarized in table 5.4.

Tension statistics for all 60 data sets prior to 27 December are plotted in figure 5-31. The root mean square difference between experimental and simulated standard deviations is 11.2 N. For the mean tensions it is 31.7 N. In the two-dimensional simulations of these same 60 data sets, the corresponding differences are 10.7 N and 29.6 N, respectively.

	6 December		22 December		3 January	
data set	σ_T(N)	$\bar{T}$(N)	σ_T(N)	$\bar{T}$(N)	σ_T(N)	$\bar{T}$(N)
experiment	208	1503	430	1617	476	1610
2D simulation	202	1508	389	1580	471	1615
3D simulation	194	1474	402	1552	-	-

Table 5.4: Tension statistics for the comparison data sets.
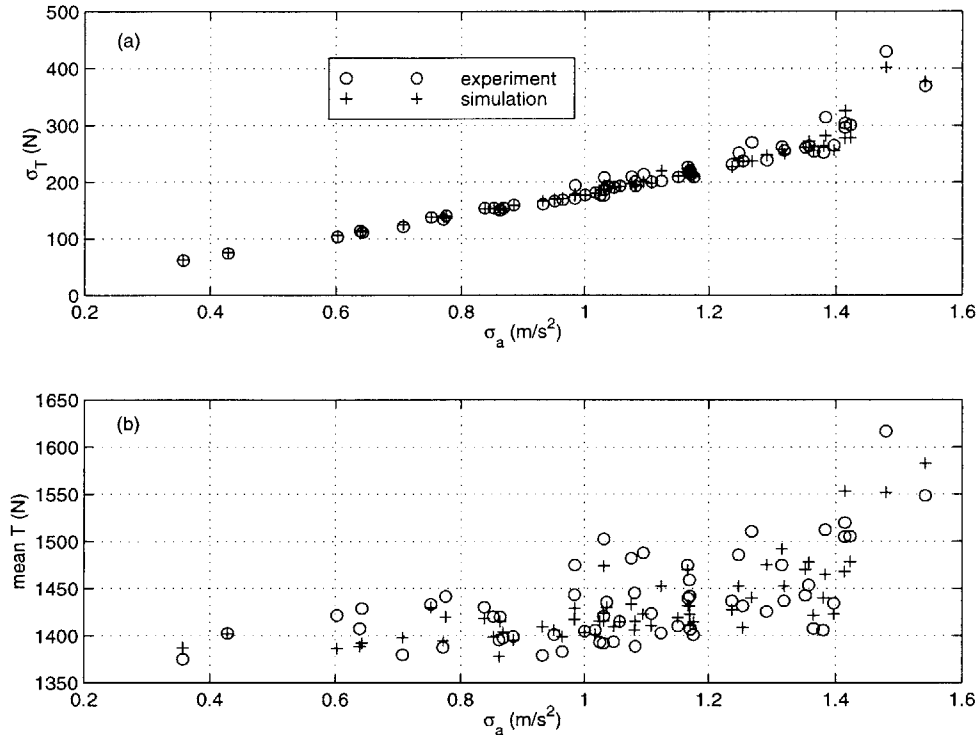
Figure 5-31: Comparison of experimental and three-dimensional model simulated tension statistics. (a) standard deviation of tension. (b) mean tension.

On average then, for the hydrodynamic coefficients and environmental parameters chosen for the validation runs, the two-dimensional results are marginally more accurate when compared to experimental data. However, for the purposes of the validation, both models appear to accurately simulate the mooring response over a wide range of forcing conditions. The primary reason for the different results from the two models is that the hydrodynamic coefficients for the simulations were originally chosen to produce reasonably accurate results with the two-dimensional numerical model. As discussed in section 6.11 the two-dimensional model can often give accurate results with purely vertical

110

input motion, even if the true input motion is three-dimensional, if the drag coefficients are adjusted slightly upwards from their true values. In a three-dimensional simulation these same values will be slightly too high. This is the situation here where for simplicity and consistency we have used the same set of hydrodynamic coefficients for both two- and three-dimensional results.

Chapter 6

A Simple Model for Dynamic Tension in Catenary Compliant Systems

In this chapter the validated numerical program and data from the field experiment are used to develop a simple model to predict dynamic tension in geometrically compliant moorings, particularly shallow water oceanographic moorings. Motivated by the strong correlation between the tension and acceleration standard deviations in figure 5-27, a model is sought that can predict the dynamic tension (as measured by σ_T, the standard deviation of tension) given only very simple inputs. Such a model can offer a significant reduction in computational cost and provide a framework for the understanding of the physics of these systems. While complete time domain simulations have the advantages of high accuracy and completeness in terms of resolving the motions and loads throughout the mooring, they are computationally expensive. The full set of two-dimensional simulations generated for the program validation in section 5.4.1 took approximately six hours to complete on a 533 MHz Alpha LX workstation (119 simulations at approximately three minutes per simulation). For analyses requiring long-term statistics of mooring response under a wide variety of forcing conditions, as in fatigue studies [39], such an expense can be burdensome. In other situations, such as response prediction for offshore floating structures, a simplified model could eliminate the need for a fully coupled mooring–structure interaction model.

In the past, analytical formulations for these types of models have been developed for the slow drift damping problem. Nakamura *et al.* [67] used catenary theory to calculate the quasi-steady vertical velocity and acceleration along the mooring. By integrating these quantities they were able to approximate the dynamic force at the top of the line due to low frequency motions in both the horizontal and vertical directions. When investigating the role of high frequency dynamics on the damping problem, however, previous investigators have relied on numerical simulation [55]. In the development that follows, analytical arguments are combined with statistical relationships gleaned from the experimental data to develop a model appropriate for wave frequency dynamics.

6.1 Physical motivation for a simple model

Previous authors have used a single degree of freedom (SDOF) spring-mass-dashpot system to model the dynamic effects in both taut [38] and geometrically compliant catenary moorings [34, 40]. The equation of motion for the SDOF system shown in figure 6-1 is

$$T(t) = M\ddot{z}(t) + B\dot{z}(t) + Kz(t),\qquad(6.1)$$

where the overdots signify differentiation with respect to time. Reversing the standard convention and treating $z(t)$ as the input and $T(t)$ as the output, the frequency domain transfer function, $H(\omega)$, for this system is

$$H(\omega) = -M\omega^2 + i\omega B + K.\qquad(6.2)$$

For a linear time-invariant system, the spectrum of T, $S_T(\omega)$, and the spectrum of z, $S_z(\omega)$, are related by

$$S_T(\omega) = |H(\omega)|^2 S_z(\omega).\qquad(6.3)$$

The spectra of the input velocity, $S_v(\omega)$, and acceleration $S_a(\omega)$, are related to the input displacement spectrum by

$$S_v(\omega) = \omega^2 S_z(\omega), \tag{6.4a}$$

$$S_a(\omega) = \omega^4 S_z(\omega). \tag{6.4b}$$

By substituting equation 6.2 into equation 6.3 and making use of equation 6.4, the spectrum for tension can be written as

$$S_T(\omega) = M^2 S_a(\omega) + \left(B^2 - 2MK\right) S_v(\omega) + K^2 S_z(\omega). \tag{6.5}$$

To apply this SDOF spring-mass-dashpot model to the data from the SWEX experiment, a nonlinear fitting procedure is used. For each time series from the experimental data, spectra of tension and heave displacement, velocity, and acceleration are computed. These spectra are then fitted to equation 6.5 using a minimization of the spectral error defined by equation 5.22 to determine individual values, M_i, B_i, and K_i for that data set. On these terms, and elsewhere in this chapter, the subscript i is used to reinforce the idea that the value in question relates to a single experimental data set. The resulting coefficients can be plotted against a non-dimensionalized form of the mean tension to observe how the coefficients change with the shape of the mooring. The non-dimensionalized mean tension, $\Delta\tau$, is defined as

Figure 6-1: An SDOF spring-mass-dashpot system.

$$\Delta\tau = \frac{\bar{T} - T_0}{T_0}. \tag{6.6}$$

This value serves as a convenient way to represent the amount that the system is pulled away from a purely vertical ($\Delta\tau = 0$) configuration. T_0 is the suspended weight of the mooring at slack current: $T_0 = w_0 H$, where w_0 is the wet weight per length of the mooring and H is the water depth.
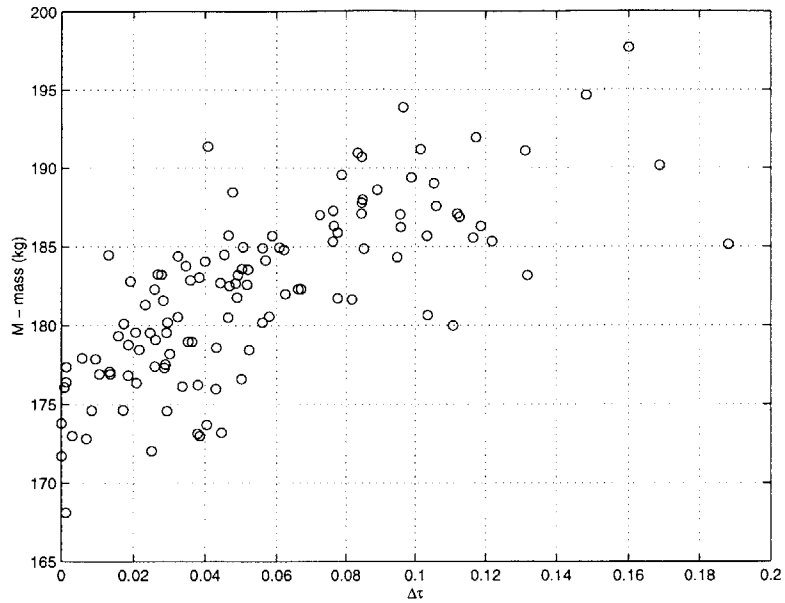
Figure 6-2: Mass values from each of the 119 spectral fits to equation 6.5.

Figures 6-2 through 6-4 show the coefficients from the fits to the 119 SWEX data sets. The overall quality of each individual fit is quite high. The spectral error over all data sets from equation 5.22 is 0.023. The maximum spectral error in any one data set is 0.055 and 89% of data sets have a spectral error of less than 0.03. There is a significant amount of scatter in the aggregated results, however. In spite of the scatter, trends are apparent in both the fitted mass and drag coefficients. The mass that participates in the response increases with increasing $\Delta\tau$. This is consistent with additional mooring line being pulled off the bottom as $\Delta\tau$ increases. The damping coefficient also increases with mean tension. This is a result of both the additional suspended line and the fact that the normal motion (and hence normal drag) over the entire mooring increases as the mooring is pulled into a more open configuration. There is no apparent trend in the fitted stiffness coefficients.

The very high scatter in the stiffness is likely due to the difficulty in determining a robust value when stiffness effects are relatively small. The scatter in the mass and drag coefficients is more interesting, however, as it may well be real. That is, it may reflect natural variation in the data that simply looks scattered given the presentation as a function of $\Delta\tau$ only. It may also be a reflection of the fact that the model is not capturing all of the relevant physics.

116
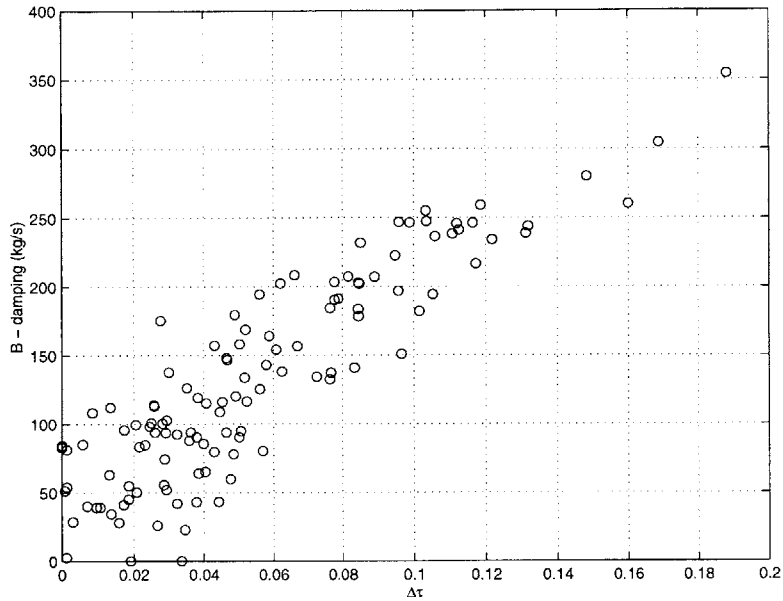
Figure 6-3: Damping values from each of the 119 spectral fits to equation 6.5.
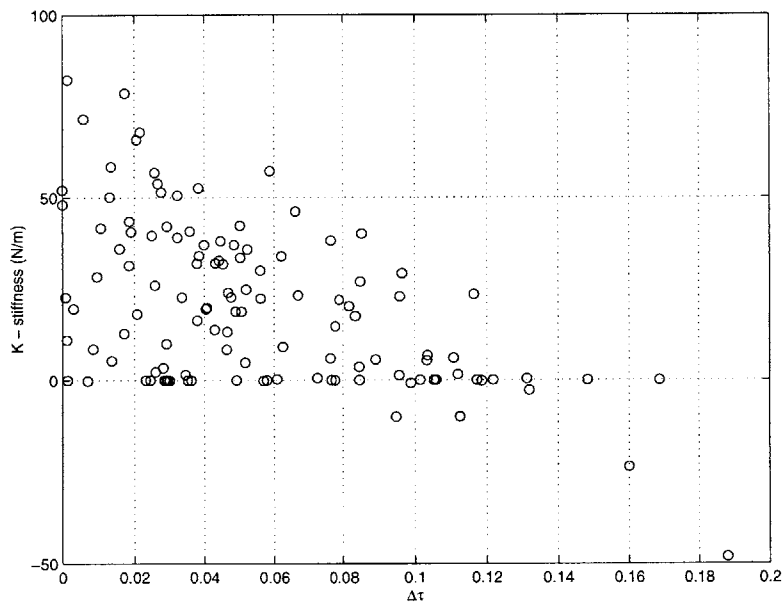
Figure 6-4: Stiffness values from each of the 119 spectral fits to equation 6.5. Negative values are not physically meaningful; they are an artifact of fitting to data sets with very small stiffness effects.

117
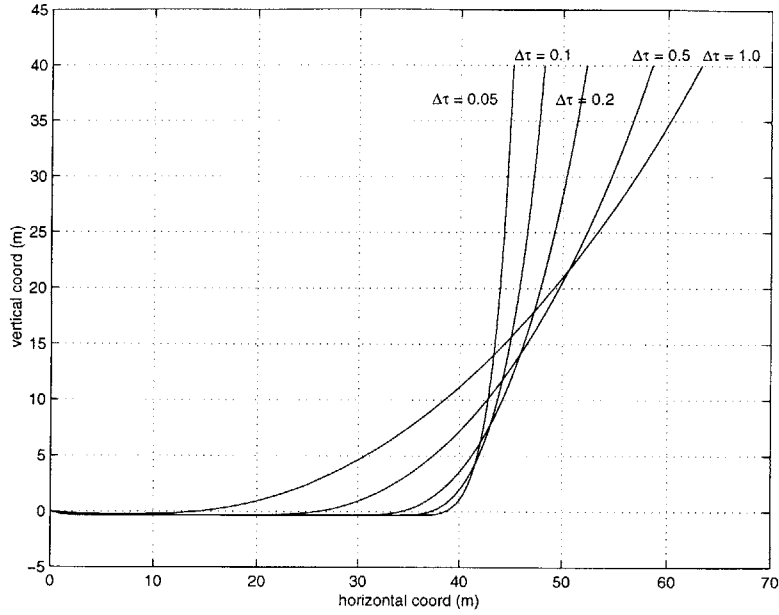
Figure 6-5: Static configurations of the simplified SWEX mooring used in the study to isolate tension mechanisms.

From the governing equations (equations A.44 through A.49) the four basic mechanisms that produce dynamic tension are inertia, drag, geometric stiffness, and elastic stiffness[1]. The spring-mass-dashpot model includes these same mechanisms, but given the highly coupled, nonlinear, multiple degree of freedom form of the full model there is no particular reason that it should be an accurate SDOF representation of the coupling between these mechanisms. To explore these ideas, simulations of a simplified version of the SWEX mooring were run with the mooring properties varied so as to isolate the various contributions to the dynamic tension. The mooring model consisted of a single continuous shot of chain (the AxPacks were removed) in a fixed water depth of 40 m.

Simulations were run for five levels of non-dimensional mean tension, ranging from $\Delta\tau = 0.05$ to $\Delta\tau = 1.0$. At each $\Delta\tau$ the static tension at the top of the mooring was specified and the static configuration of the mooring was determined using the second of the procedures described in section 3.1.1. The static configuration of the mooring at each $\Delta\tau$ is shown in figure 6-5. No current was present in the simulations. This procedure was used so that $\Delta\tau$ would remain fixed even with variations in the mooring drag coefficients. Dynamic excitation was sinusoidal with amplitudes ranging from 0.2 to 2.0 m and periods

---

[1] Elastic stiffness effects are negligible in most geometrically compliant systems.

118

variation	m (kg/m)	w_0 (N/m)	C_{d_t}	C_{d_n}
k	0.01	31.85	0.0	0.0
mk	3.73	31.85	0.0	0.0
tk	0.01	31.85	0.01	0.0
nk	0.01	31.85	0.0	0.5
mdk	3.73	31.85	0.01	0.5
dk	0.01	31.85	0.01	0.5

Table 6.1: Variations on the mooring properties used in the simulations to isolate individual tension mechanisms. Normal and tangential added mass were zero.

ranging from 4 to 15 seconds. The mooring configurations that were run are shown in table 6.1.

The first four versions can each be used to isolate a single contribution to the dynamic tension. For example, with negligible mass, and no drag, the only contribution to the dynamic tension in the first variant is stiffness. Because the wet weight cannot be varied without changing $\Delta\tau$, other effects are obtained by subtracting the known stiffness contribution. If $T_k(t)$ is the dynamic tension record from the simulation with stiffness only then the dynamic tension due to mass is

$$T_{\text{mass}} = T_{mk}(t) - T_k(t), \tag{6.7}$$

where $T_{mk}(t)$ is the dynamic tension record from the simulation with both mass and stiffness effects present. If σ_{mass}, σ_{tan}, σ_{nor}, and σ_{stiff}, are the standard deviations of the time series of the tension contributions due to mass, tangential drag, normal drag, and stiffness, then a convenient way to summarize the effect of each mechanism is to derive effective mass, drag, and stiffness coefficients using

$$M^* = \frac{\sigma_{\text{mass}}}{\sigma_a}, \tag{6.8}$$

$$C_{d_t}^* = \frac{\sigma_{\text{tan}}}{\frac{1}{2}\rho\pi dH\sigma_{v|v|}}, \tag{6.9}$$

$$C_{d_n}^* = \frac{\sigma_{\text{nor}}}{\frac{1}{2}\rho dH\sigma_{v|v|}}, \tag{6.10}$$

$$K^* = \frac{\sigma_{\text{stiff}}}{\sigma_z}. \tag{6.11}$$
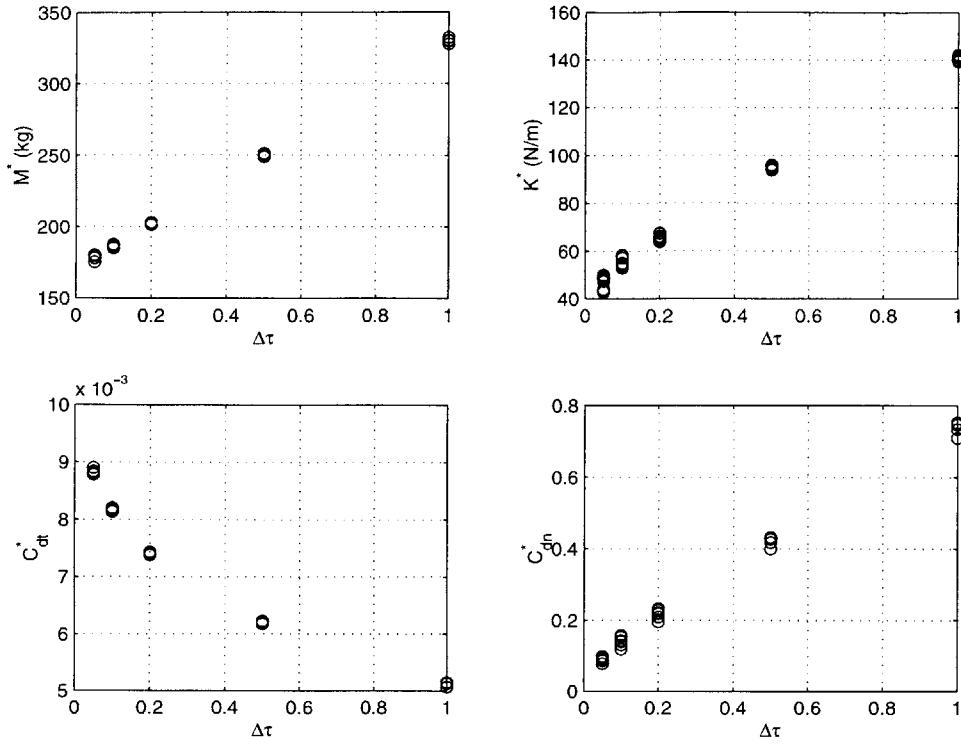
Figure 6-6: (a) Mass, (b) stiffness, (c) tangential drag, and (d) normal drag coefficients calculated from simulations with isolated tension contributions.

Note that for the drag coefficients in particular, these are effective calculated values, rather than the actual values assigned to mooring materials for the numerical simulation. Standard deviations are used because they are a convenient expression of the amplitude of a sinusoidal time series. σ_a, $\sigma_{v|v|}$, and σ_z are the standard deviations of the heave acceleration, quadratic velocity, and displacement.

Figure 6-6 shows the four calculated coefficients as a function of $\Delta \tau$. For each coefficient type, only simulations that had a symmetric, regular tension response were used to calculate coefficients. For the mass coefficients this means that only results for 15 second period simulations are used. Simulations with 4 and 8 second periods did not have a regular response because of impact loading at the bottom and the lack of damping. For the normal drag coefficients only results for amplitudes of 1 m or less and 8 and 15 second periods were used. With no inertial forces the tension response at high velocity was not symmetric. The full range of simulations were used for the tangential drag and stiffness coefficients.

All of the coefficients behave roughly as expected. Mass, stiffness, and normal drag coefficients all increase roughly linearly with $\Delta\tau$ as additional line is pulled off the bottom. The tangential drag coefficient, which at $\Delta\tau = 0$ is nearly equal to the actual tangential drag coefficient used in the simulations, decreases with $\Delta\tau$. This is because the amount of tangential motion along the chain decreases as the chain is pulled into more open configurations.

The coefficients in figure 6-6 represent the behavior of the mooring with little or no coupling between the tension mechanisms. The resulting mass and drag coefficients are affected by the presence of geometric stiffness, but because stiffness effects are small, the results are similar to those that would be obtained if pure isolation were possible. Variations mk, mdk, and dk in table 6.1 can be used to calculate mass and drag coefficients in the presence of more significant coupling. For these calculations a single effective drag coefficient,

$$C_d^* = \frac{\sigma_{\mathrm{drag}}}{\frac{1}{2}\rho dH\sigma_{v|v|}},\tag{6.12}$$

combining the effects of tangential and normal drag, is used.

Assuming that the time series of tension for variation mdk (with all effects present) can be written as

$$T(t) = T_{\mathrm{mass}}(t) + T_{\mathrm{drag}}(t) + T_{\mathrm{stiff}}(t),\tag{6.13}$$

then a drag coefficient in the presence of mass coupling can be calculated by subtracting the tension from variation mk (with mass and stiffness) from variation mdk (with mass, drag, and stiffness). Likewise, a mass coefficient in the presence of drag coupling can be calculated by subtracting variation dk (with drag and stiffness) from variation mdk. These results are presented, along with the uncoupled coefficients, in figures 6-7 and 6-8 for mass and drag, respectively.

The coupled drag coefficients differ from the more fully isolated results in that they represent the drag contribution to tension in the presence of motions which are enhanced by mass effects. In the fully isolated case, the drag contribution was calculated in a simulation that had no mass. The coupled drag coefficient is calculated by subtracting the mass and stiffness contributions to tension from the tension in a simulation with all
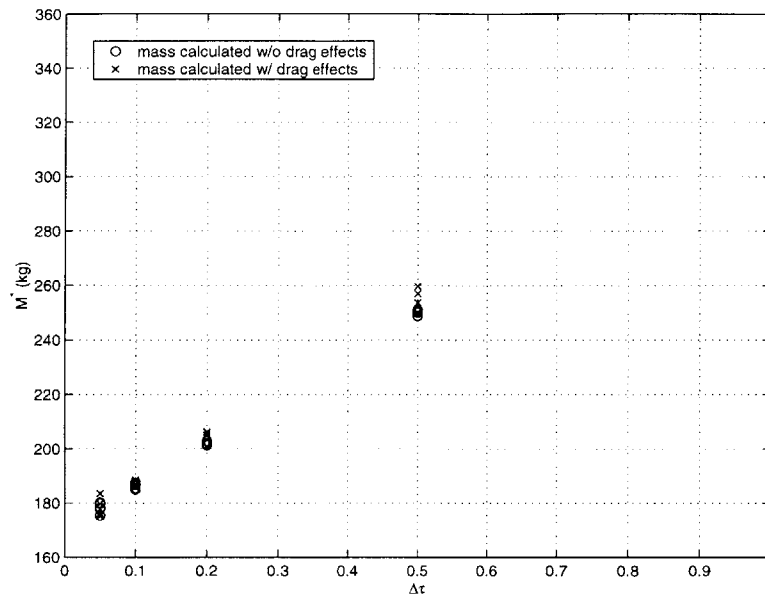
Figure 6-7: Fully isolated mass coefficient (circles) and mass coefficient when drag is present (x).
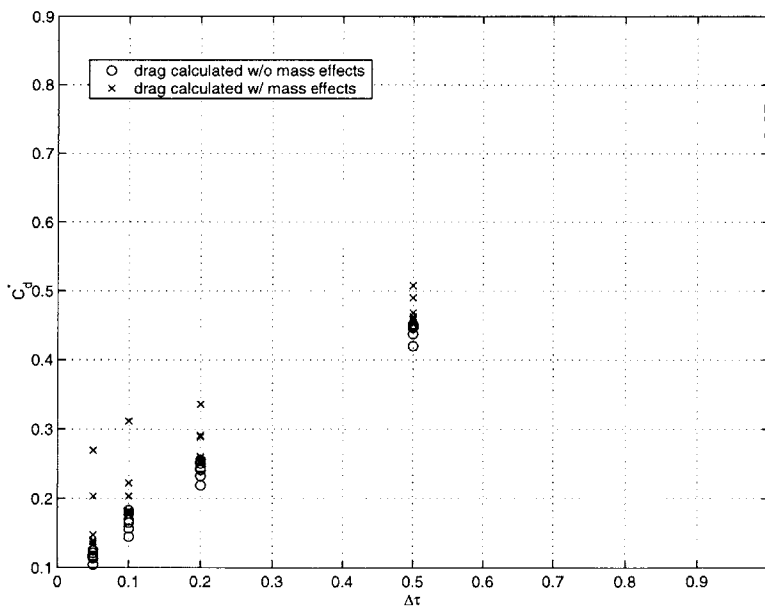
Figure 6-8: Fully isolated drag coefficient (circles) and drag coefficient when mass is present (x).

effects present. The effects of mass on the motion in this latter simulation are not removed and thus the effect of that motion on the drag coefficient is reflected in the final result. This same reasoning applies to the coupled mass coefficient as well.

In both of figures 6-7 and 6-8, the motion effects due to the coupling lead to increases in coefficient values. For drag coefficients the presence of mass leads to increased levels of motion along the length of the mooring. This increased motion leads in turn to increases in the drag forces. Because the calculated drag coefficient is normalized by the motion at the top of the mooring only, the increase in the drag contribution to tension is reflected by an increase in the drag coefficient. For the coupled mass coefficients, the presence of drag restricts the ability of the mooring to deform, in effect increasing the overall stiffness of the mooring. To comply with the topside motion then, the amount of mooring line pulled off the bottom increases relative to the simulations in which no drag is present. This increase in line off the bottom results in a slight increase in the mass.

The coupling of mass effects into the drag coefficient is clearly the most significant of these relationships, particularly at low values of $\Delta\tau$. This coupling could explain much of the scatter that is apparent in the fitted mass and damping coefficients for the experimental SWEX data in figures 6-2 and 6-3. Using the the individual coefficients in those figures the spring-mass-dashpot model accurately captures the tension response in any single data set. This is clear from the good quality of any one of the spectral fits described above. However, the coupling between mass and drag means that the coefficients are a function both of the steady state configuration and of the excitation frequency and amplitude. Thus, when the coefficients are plotted as a function of the configuration (as measured by $\Delta\tau$) they show significant scatter. This scatter, and the underlying dependence on both static configuration and input excitation, make it difficult to formulate analytical relationships for the coefficients.

One approach to developing a simple model then is to find representations of the data that have low scatter. If the scatter in the data can be minimized, such representations could lead to a model that naturally expresses some of the coupling in the system. In such a model the coupling is expressed within the form of the model rather than in the individual coefficients. This makes mass and drag effects easier to isolate and thus facilitates analytic prediction of model mass and drag coefficients.
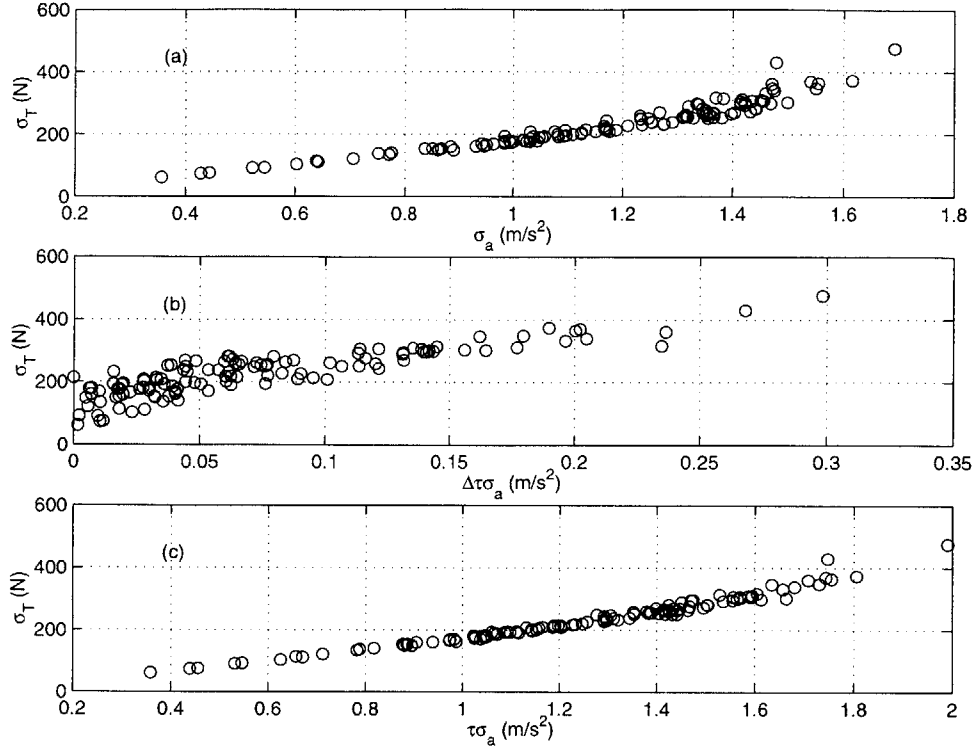
Figure 6-9: Comparison of scatter in the relationship between σ_T and various function of σ_a: (a) as a function of σ_a, (b) as a function of $\Delta\tau\sigma_a$, and (c) as a function of $\tau\sigma_a$.

6.2 Development of the simple model

Figure 6-9 shows three presentations of σ_T. In the first, σ_T is plotted against σ_a as in figure 5-27(a). In the second it is plotted against the product $\Delta\tau\sigma_a$. The third panel presents σ_T as a function of the product $\tau\sigma_a$, where τ is defined as

$$\tau = \frac{\bar{T}}{T_0}. \tag{6.14}$$

There is a marked reduction in the scatter in this presentation compared to the first panel.

Motivated by figure 6-9(c) a proposal for the model is

$$\sigma_T = M\tau\sigma_a + f(\sigma_{v|v|}), \tag{6.15}$$

where M is a single coefficient that, together with τ, expresses the model mass effect for any configuration. The simple linear form of the inertia term reflects the trend apparent in figure 6-9(c) for values of $\tau\sigma_a < 1.0$. This is the inertia dominated regime [40,99]. Beyond
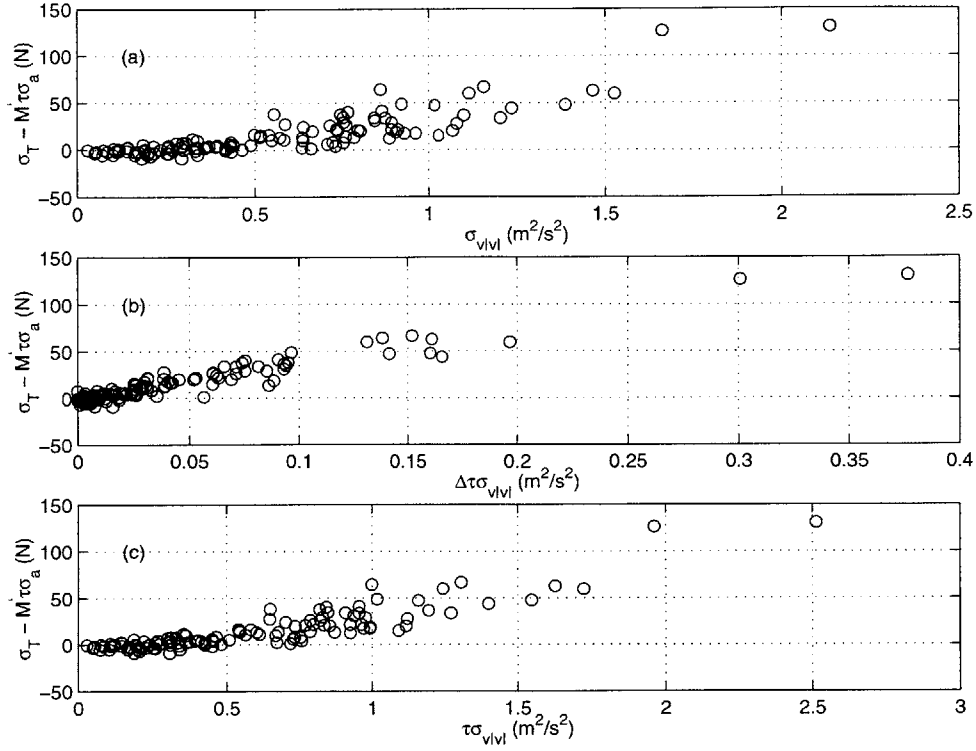
Figure 6-10: Comparison of scatter in the relationship between the portion of σ_T attributable to drag and various functions of $\sigma_{v|v|}$. The preliminary value for M, M' is 173.7 kg. (a) As a function of $\sigma_{v|v|}$; (b) as a function of $\Delta\tau\sigma_{v|v|}$; (c) as a function of $\tau\sigma_{v|v|}$.

this regime drag $(f(\sigma_{v|v|}))$ becomes important and σ_T varies away from the straight line trend.

Various forms for $f(\sigma_{v|v|})$ can be examined by subtracting a preliminary estimate of the inertia contribution from σ_T. An initial estimate, M', for the value of M is computed based on the slope of a line fitted to the data for which $\tau\sigma_a < 1.0$ in figure 6-9(c). Figure 6-10 shows the resulting estimated values for $f(\sigma_{v|v|})$ in the same three presentations as in figure 6-9, with σ_a replaced by $\sigma_{v|v|}$.

The scatter in the velocity plots is greater than for the best acceleration case, but the relationship in figure 6-10(b), drag as a function of the product $\Delta\tau\sigma_{v|v|}$, appears to have the least scatter. It also offers the possibility that a simple linear form can be used to model the drag contribution. This form does have the disadvantage that drag disappears as $\Delta\tau$ goes to zero. This limitation is addressed more fully in section 6.10.

With the same type of linear form as the inertia term and the different non-dimensionalized

mean tension, the model equation becomes

$$\sigma_T = M\tau\sigma_a + \frac{1}{2}\rho C_d \Delta\tau dH \sigma_{v|v|}. \tag{6.16}$$

Like M, C_d is a single coefficient for drag in any configuration. The two model coefficients, M and C_d can be determined from a linear least squares fit using experimentally observed values of σ_T, σ_a, $\sigma_{v|v|}$, τ, and $\Delta\tau$. For n data sets, the formula for the coefficients is

$$\begin{bmatrix} M \\ \frac{1}{2}\rho dH C_d \end{bmatrix} = \begin{bmatrix} \sum\limits_{i=1}^{n} (\tau\sigma_a)_i^2 & \sum\limits_{i=1}^{n} (\tau\sigma_a\Delta\tau\sigma_{v|v|})_i \\ \sum\limits_{i=1}^{n} (\tau\sigma_a\Delta\tau\sigma_{v|v|})_i & \sum\limits_{i=1}^{n} (\Delta\tau\sigma_{v|v|})_i^2 \end{bmatrix}^{-1} \begin{bmatrix} \sum\limits_{i=1}^{n} (\sigma_T\sigma_a)_i \\ \sum\limits_{i=1}^{n} (\sigma_T\sigma_{v|v|})_i \end{bmatrix}. \tag{6.17}$$

For the 119 data sets from the SWEX experiment, the fitted values are $M = 172.8$ kg and $C_d = 0.375$.

6.3 Physical interpretation of the simple model

The variance of tension in the new model is

$$\sigma_T^2 = (M\tau)^2\, \sigma_a^2 + \left(\frac{1}{2}\rho C_d \Delta\tau dH\right)^2 \sigma_{v|v|}^2 + \rho M\tau C_d \Delta\tau dH \sigma_a \sigma_{v|v|}. \tag{6.18}$$

Using the linearizing approximation $\sigma_{v|v|}^2 = 3\sigma_v^4$ [4] this can be written as

$$\sigma_T^2 = (M\tau)^2 \sigma_a^2 + \left[3\left(\frac{1}{2}\rho C_d \Delta\tau dH\right)^2 \sigma_v^2 + \sqrt{3}\rho M\tau C_d \Delta\tau dH \sigma_a\right]\sigma_v^2. \tag{6.19}$$

Neglecting the relatively small covariance between acceleration and velocity to make use of the fact that the variance of a sum of independent random variables is the sum of the variances, the governing equation for the corresponding physical system is

$$T(t) = Ma(t) + v(t)\sqrt{3\left(\frac{1}{2}\rho C_D dH\right)^2 \sigma_v^2 + \sqrt{3}\rho M C_D dH \sigma_a}. \tag{6.20}$$

It is clear from this result that the proposed model can be understood to represent a mass-damper system with a linearized damping coefficient that depends on both the quadratic drag and inertia.

126

Casting the simple model in the variance form given by equation 6.19 allows for a comparison with the terms in the physically motivated SDOF spring-mass-dashpot model. For that model, integrating equation 6.5 yields the variance of the tension in data set i as

$$\sigma_{T_i}^2 = M_i^2 \sigma_{a_i}^2 + \left(B_i^2 - 2M_i K_i\right) \sigma_{v_i}^2 + K_i^2 \sigma_{z_i}^2. \tag{6.21}$$

Both models represent the dynamic tension as a weighted sum of motion statistics. They differ in the coefficient of the velocity term and in the inclusion or absence of the stiffness term.

The qualitative form of the mass term is the same in both models. From figures 6-2 and 6-7 it is clear that a mass term that grows linearly with non-dimensional mean tension is reasonable. Linear fits to either of those results would be of the form $M_0 + M_1 \Delta \tau$. From a comparison with the model mass term, $M\tau$, it is clear that the implicit assumption in the model is that the mass initial value and growth rate are equal. To first order this is a reasonable assumption. If the total suspended mass is taken as the mass per length times the suspended length, then the τ form of the non-dimensionalized mean tension is equal to the scope of the mooring,

$$\tau = \frac{\bar{T}}{T_0} \approx \frac{mgL}{mgH} = \frac{L}{H}. \tag{6.22}$$

Assuming that the model mass coefficient is equal to the mass per length times the suspended length and that the mass coefficient at $\Delta \tau = 0$, M_0, is equal to mH then for

$$M = M_0 + M_1 \Delta \tau = mH + M_1 \left(\frac{L}{H} - 1\right) = mL \tag{6.23}$$

to be true, M_1 must equal M_0.

In the variance form of the model, the coefficient of σ_v^2 is

$$3 \left(\frac{1}{2}\rho C_d \Delta \tau dH\right)^2 \sigma_v^2 + \sqrt{3}\rho M \tau C_d \Delta \tau dH \sigma_a. \tag{6.24}$$

From the time domain form of the simple model, equation 6.20, it can be seen that this entire coefficient represents a linearized damping constant. This damping constant can be compared to the velocity coefficient $B_i^2 - 2M_i K_i$, in equation 6.21 for the spring-mass-
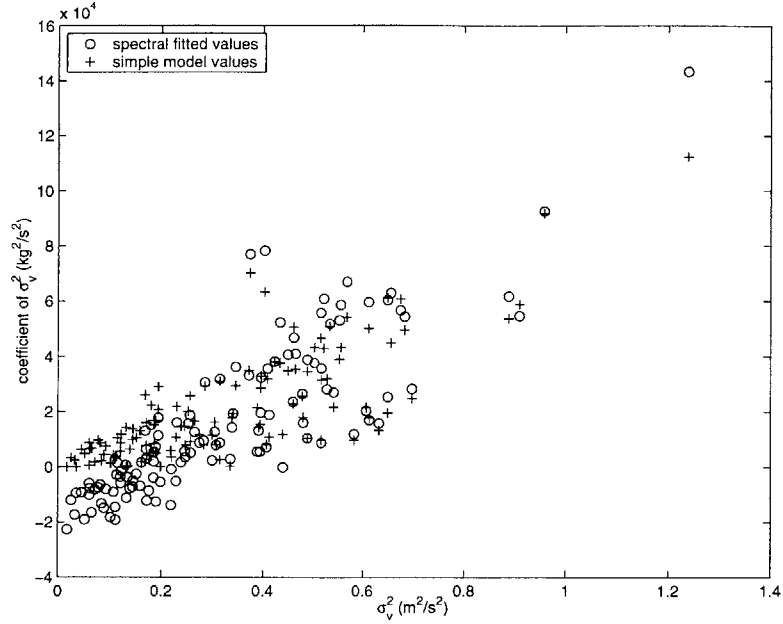
Figure 6-11: Total effective damping constant for the experimental spectral data, $B_i^2 - 2M_iK_i$, and the simple model total damping coefficient from equation 6.24.

dashpot model. That term represents both a damping and a stiffness effect.

Figure 6-11 shows the term $B_i^2 - 2M_iK_i$ for each of the 119 individual fits to the SWEX spectral results for the spring-mass-dashpot model along with the total damping coefficient for the simple model for each data set calculated from equation 6.24. With mass and drag coefficients calculated from a linear fit to the standard deviation form of the model, the model total damping coefficient is able to reproduce the nonlinear shape and much of the scatter of the spectrally fitted values. With no stiffness, however, the simple model does not capture the negative coefficients at low σ_v^2. For linearized quadratic drag in the spring-mass-dashpot model, $B^2 \propto \sigma_v^2$ [29]. Thus, as the velocity goes to zero in this model the intercept of the σ_v^2 coefficient is $-2MK$. This term is only important at low frequencies and amplitudes where there is little damping. At higher frequencies and amplitudes the B^2 term dominates. This higher velocity region is where the simple model total damping constant, with its inherent expression of coupling between inertia and drag, is accurately reproducing the shape and scatter of the individually fitted values.

In an undamped spring-mass model, the $-2MK$ term governs the response near resonance. For frequencies above resonance, inertia dominates the response. By neglecting this term the simple model is sacrificing accuracy at these lower frequencies. Given the re-

versed notions of input and output in the definition of the transfer function in equation 6.2, the undamped resonance is defined as the frequency at which infinite wave amplitude produces zero tension. Thus, neglecting this term is conservative. Additionally, any loss in accuracy will be tempered in real situations because there is always some damping present. At the very lowest frequencies, the simple model also loses accuracy because it does not include a stiffness term like the spring-mass-dashpot model's $K^2\sigma_z^2$. This term governs the response near zero frequency.

The relative importance of the two stiffness effects, mass, and damping in the SWEX data can be calculated using the coefficients fitted to the spectra of individual data sets in section 6.1. The relative magnitude of each of the terms on the right side of equation 6.21 in comparison with the total tension energy are

$$f_i^a = \frac{M_i^2 \sigma_{a_i}^2}{\sigma_{T_i}^2},$$ (6.25)

$$f_i^{vB} = \frac{B_i^2 \sigma_{v_i}^2}{\sigma_{T_i}^2},$$ (6.26)

$$f_i^{vK} = \frac{2M_i K_i \sigma_{v_i}^2}{\sigma_{T_i}^2},$$ (6.27)

$$f_i^z = \frac{K_i^2 \sigma_{z_i}^2}{\sigma_{T_i}^2}.$$ (6.28)

These response fractions are plotted together in figure 6-12. From these fractions it is clear that the stiffness term f_i^{vK} has little effect over the full range of conditions encountered during the SWEX experiment. For low $\Delta\tau$ the relative magnitude of this term approaches 20%, but the total dynamic tension in these configurations is relatively low. At higher sea states, this term does not contribute significantly to the dynamic tension. f_i^{vK}, the contribution from the stiffness dependent portion of the velocity coefficient is also quite small. This explains why the simple model is able to represent the SWEX data without any reference to stiffness. The small stiffness effect also explains the high scatter in the fitted stiffness coefficients in figure 6-4.

6.4 Model performance

To examine the performance of the simple model, three types of analyses are made:

- Accuracy of the model predicted σ_T values compared to the experimentally observed

129
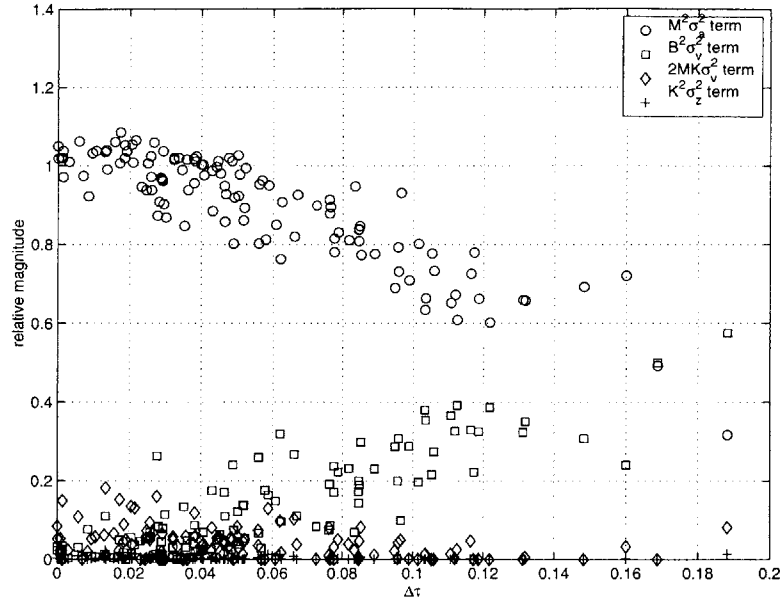
Figure 6-12: Portion of the total tension energy attributable to each of the terms in the variance form of the spring-mass-dashpot model, equation 6.21.

values in terms of RMS error, max error, and the number of predictions with error less than five percent.

- Accuracy of tension spectra calculated using a formula derived from the simple model. Detailed comparisons are presented for the 3 January 1999 storm data set and 6 December 1998 data set. The spectral error over all data sets is also presented.

- Bootstrap confidence intervals on the fitted model coefficients.

For the error analysis, the fractional error in the predicted value of σ_T for data set i is defined as

$$e_i = \left| \frac{\sigma_T - \sigma_T^{\text{model}}}{\sigma_T} \right|_i.$$ (6.29)

The root mean square error over all data sets is

$$e = \sqrt{\frac{1}{119} \sum_{i=1}^{119} e_i^2}.$$ (6.30)

Using these metrics, the RMS error between model fitted and experimentally observed values of σ_T is 2.7%. The maximum error in any one data set is 8.3%. 93% of data sets

130
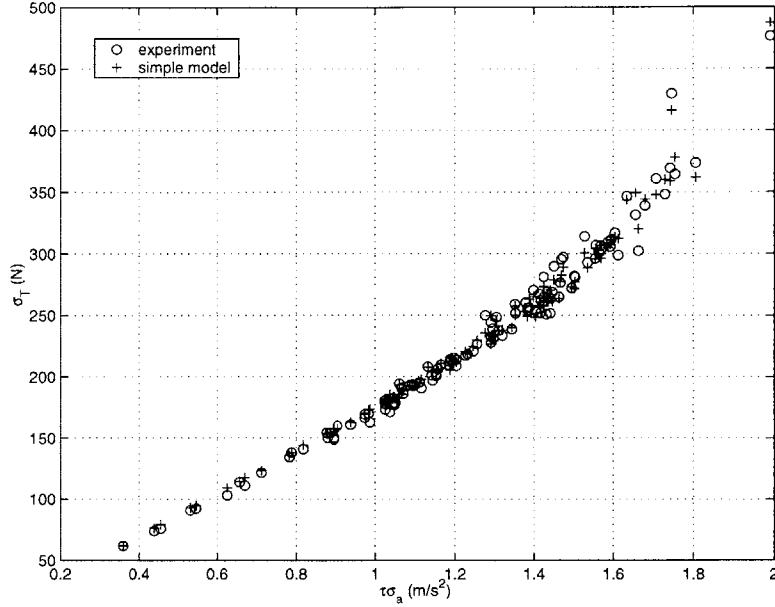
Figure 6-13: Comparison of model predicted and experimentally observed standard deviation of tension.

have an error less than 5%. Figure 6-13 shows the model and experimental tension as a function of $\tau\sigma_a$.

Casting the statistical relationship into the form given by equation 6.19 facilitates the prediction of the tension spectrum based on quantities that are easily obtained from an input wave spectrum:

$$S_T = (M\tau)^2 S_a + \left[3 \left(\frac{1}{2} \rho C_d \Delta \tau dH \right)^2 \sigma_v^2 + \sqrt{3} \rho M\tau C_d \Delta \tau dH \sigma_a \right] S_v. \qquad (6.31)$$

Comparisons of model predicted spectra calculated using the fitted coefficients and equation 6.31 with the experimental spectra for the 6 December and 3 January data sets are shown in figures 6-14 and 6-15, respectively. For the low sea state case (figure 6-14) the response is inertia dominated and the model result agrees well with the experimental spectrum across the full range of frequencies. In the high sea state case the basic agreement is good, but the model over predicts the spectral peak by 12.5%. Beyond the spectral peak, the velocity spectrum falls away quickly while the acceleration spectrum has the same basic shape as the tension spectrum; that the predicted tension spectrum is too high suggests that the model is over predicting the mass effect for this configuration.

131
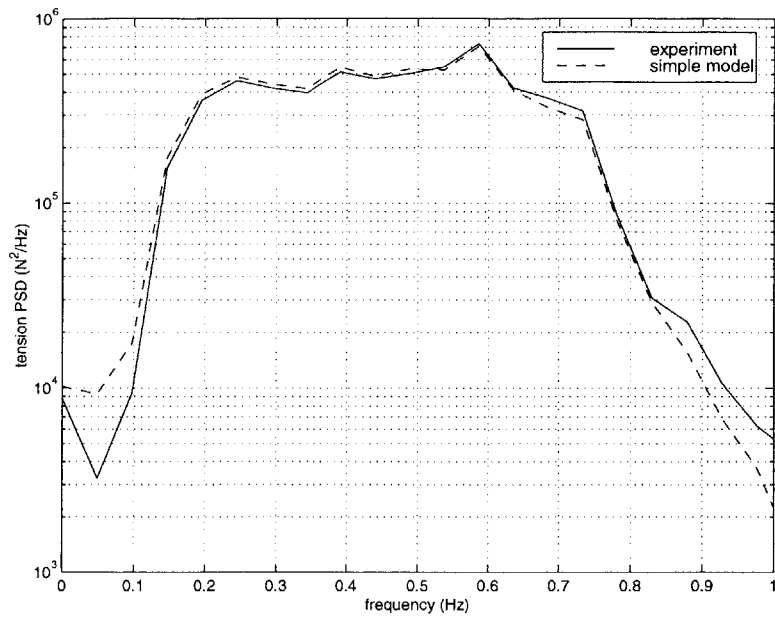
Figure 6-14: Comparison of model predicted tension spectra with the experimentally observed tension spectrum for the 6 December 1998, 0800 data set.
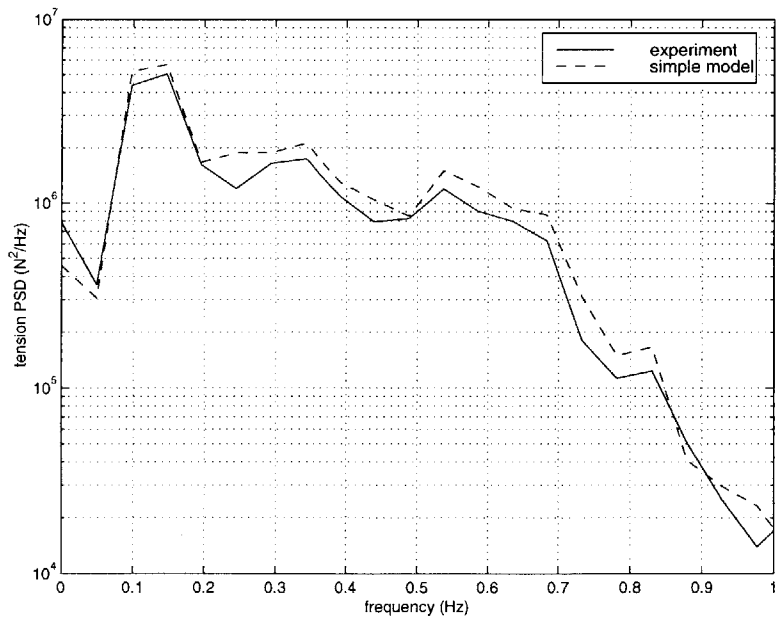
Figure 6-15: Comparison of model predicted tension spectra with the experimentally observed tension spectrum for the 3 January 1999, 1600 data set.

To more fully quantify the spectral performance of the model, the spectral error metric defined by equation 5.22 was applied to model predicted spectra for all 119 experimental data sets. For each data set, equation 6.31 was used to calculate a model tension spectrum for comparison with the experimentally observed tension spectrum. The RMS spectral error for all data sets is $e_* = 0.043$. The maximum spectral error in any one data set is 0.10. These errors are lower than those for the tension spectra which were calculated from the results of the full time domain numerical simulations in the validation in section 5.4.1 (e_* = 0.068, maximum error of 0.176). They are also not markedly higher than the errors for the spectra calculated using the individually fitted coefficients in section 6.1 ($e_* = 0.023$, maximum error of 0.055). This is significant because each of those individual fits was actually based on a minimization of this same error. Thus, the error for those spectra represents a best case which requires the calculation of 119 sets of coefficients. With just two parameters for the entire data set, the simple model is able to reproduce the tension responses over the entire frequency range with only slightly less accuracy.

In addition to producing accurate tension results, the fitted coefficients are very robust. With their 95% confidence intervals (calculated using the bootstrap method described in appendix F) the fitted mass and drag coefficients are 172.8 ± 2.0 kg and 0.375 ± 0.045, respectively. The confidence intervals on these fitted coefficients are 1% and 12% of the nominal value. These small confidence intervals are important because they support the idea that meaningful model coefficients can be calculated using a priori knowledge of mooring properties. Large uncertainties on the fitted coefficients would indicate that the model was not capturing the scatter in the data.

These values can be compared to intervals for coefficients for a model based purely on the spectrally derived mass and damping coefficients in figures 6-2 and 6-3. In such a model, the mass and damping coefficients as functions of $\Delta\tau$ are derived using fits to the individual spectrally fitted values. A straightforward example of this type of model is [40]

$$M = M_0 + M_1 \Delta\tau, \tag{6.32}$$

$$B = (B_0 + B_1 \Delta\tau)\,\sigma_v. \tag{6.33}$$

Linear fits to these forms yield $M_0 = 176.5 \pm 1.3$ kg, $M_1 = 102.4 \pm 21.7$ kg, $B_0 = 161.3 \pm 27.8$ kg/s, and $B_1 = 1255 \pm 426$ kg/s. At the highest value of $\Delta\tau$, the confidence

133

intervals for M, and B are 2.8% and 27% of the nominal value. These intervals only take into account the uncertainty in the linear fits to the individual coefficients. The actual intervals are even larger than this because of the uncertainties in the individual fits that are not accounted for in this analysis. These large uncertainties are a result of the highly scattered coefficients derived from the individual spectral fits.

6.5 Model coefficient dependence on physical parameters

With a validated numerical simulation program it is possible to simulate the entire experimental data set. This capability permits the calculation of model coefficients for parametric variations of the system that was actually deployed. By simulating a large number of variations, the dependence of the model coefficients on the system parameters can easily be determined. Parameters considered here are the chain normal and tangential drag coefficients, C_{d_n} and C_{d_t}, chain normal and tangential added mass coefficients, C_{a_n} and C_{a_t}, and bottom stiffness and damping constants.

The total explored parameter space is shown in table 6.2. In most cases only one parameter is varied relative to the baseline case defined in the first line of the table. The baseline values are the same as those used for the validation simulations in section 5.4. For each set of parameters, the full time domain numerical model is run for the environmental conditions in the 119 experimental data sets. Simulations are two-dimensional with only vertical (heave) input. Statistics of the tension responses are then computed and a least squares fit is used to calculate the model coefficients M and C_d for that parameter set. Curves showing the variation in both coefficients while a single parameter is varied are shown in figures 6-16 through 6-18.

Figure 6-16 shows a strong linear dependence of the mass coefficient on both tangential and normal added mass. The model drag coefficient also varies with the added mass parameters: very slightly with the tangential parameter and a bit more substantially for the normal parameter. This dependency indicates that the model form by itself is not completely capturing the coupling between inertia and drag. The increase in normal motion along the chain that accompanies the increase in mass is causing an increase in drag beyond the level accounted for by the coupling term in equation 6.19. Because the model input velocity is the same in both cases, the increase in drag must be reflected by

134

variation	drag C_{d_n}	C_{d_t}	mass C_{a_n}	C_{a_t}	bottom $\tilde{k}$	ζ
baseline	0.5	0.01	1.0	0.1	0.155	1.0
1	0.5	0.01	**0.0**	0.1	0.155	1.0
2	0.5	0.01	**0.2**	0.1	0.155	1.0
3	0.5	0.01	**0.5**	0.1	0.155	1.0
4	0.5	0.01	**1.5**	0.1	0.155	1.0
5	0.5	0.01	**2.0**	0.1	0.155	1.0
6	0.5	0.01	**0.0**	**0.0**	0.155	1.0
7	0.5	0.01	**0.5**	**0.0**	0.155	1.0
8	0.5	0.01	1.0	**0.0**	0.155	1.0
9	0.5	0.01	1.0	**0.05**	0.155	1.0
10	0.5	0.01	1.0	**0.2**	0.155	1.0
11	0.5	0.01	**0.0**	**0.2**	0.155	1.0
12	0.5	0.01	**0.0**	0.1	0.155	1.0
13	**0.0**	0.01	1.0	0.1	0.155	1.0
14	**0.2**	0.01	1.0	0.1	0.155	1.0
15	**0.4**	0.01	1.0	0.1	0.155	1.0
16	**0.45**	0.01	1.0	0.1	0.155	1.0
17	**0.55**	0.01	1.0	0.1	0.155	1.0
18	**0.6**	0.01	1.0	0.1	0.155	1.0
19	**0.7**	0.01	1.0	0.1	0.155	1.0
20	**0.45**	**0.003**	1.0	0.1	0.155	1.0
21	**0.55**	**0.003**	1.0	0.1	0.155	1.0
22	**0.6**	**0.003**	1.0	0.1	0.155	1.0
23	**0.7**	**0.003**	1.0	0.1	0.155	1.0
24	0.5	**0.0**	1.0	0.1	0.155	1.0
25	0.5	**0.003**	1.0	0.1	0.155	1.0
26	0.5	**0.007**	1.0	0.1	0.155	1.0
27	0.5	**0.015**	1.0	0.1	0.155	1.0
28	0.5	**0.03**	1.0	0.1	0.155	1.0
29	**0.4**	**0.0**	1.0	0.1	0.155	1.0
29	**0.6**	**0.0**	1.0	0.1	0.155	1.0
31	**0.6**	**0.007**	1.0	0.1	0.155	1.0
32	**0.6**	**0.015**	1.0	0.1	0.155	1.0
33	**0.6**	**0.03**	1.0	0.1	0.155	1.0
34	0.5	0.01	1.0	0.1	**0.078**	1.0
35	0.5	0.01	1.0	0.1	**0.311**	1.0
36	0.5	0.01	1.0	0.1	**0.622**	1.0
37	0.5	0.01	1.0	0.1	0.155	**0.0**
38	0.5	0.01	1.0	0.1	0.155	**0.5**
39	0.5	0.01	1.0	0.1	0.155	**2.0**
40	0.5	0.01	1.0	0.1	0.155	**4.0**

Table 6.2: Parameter variations considered in the model coefficient functional dependence study. Bold entries indicate a variation in the parameter relative to the baseline value.
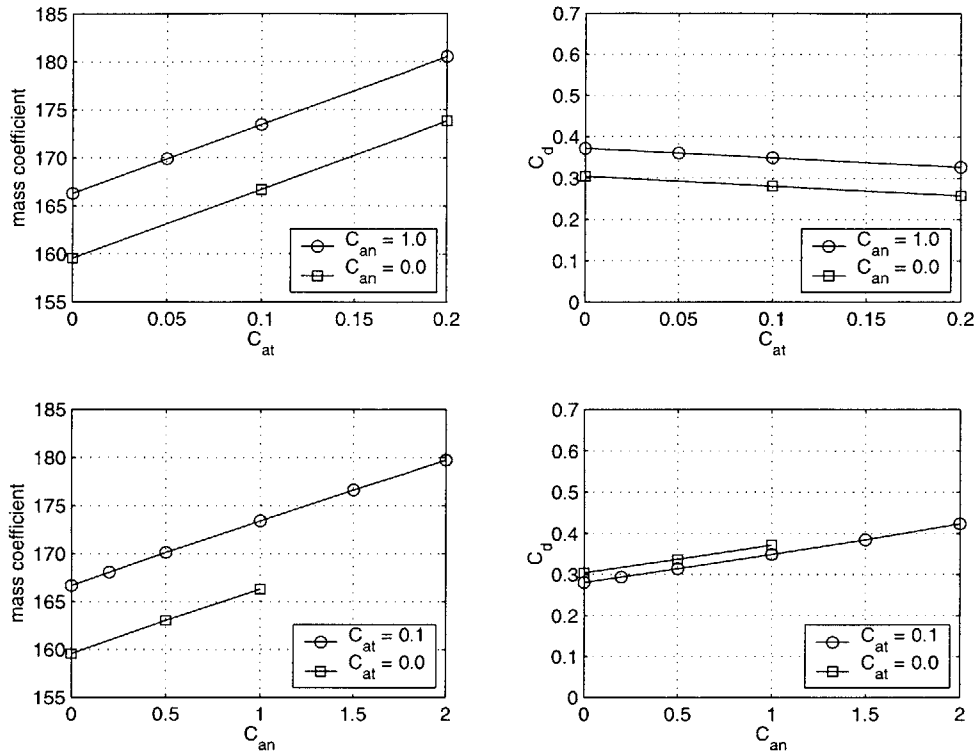
Figure 6-16: Variation of the model mass and drag coefficient with changes to the system normal and tangential added mass coefficients. Unless otherwise indicated, all other system parameters are at baseline values. For reference, the suspended mass of chain and AxPacks at slack current ($\Delta\tau = 0$) is 161.6 kg.

an increase in the model drag coefficient.

A similar effect is evident in figure 6-17 for the model drag coefficients as functions of normal and tangential drag parameters. There are clear linear relationships between the model drag coefficient and normal and tangential drag. There is also some dependence of the mass coefficient on the system drag coefficients. The effect is quite small, however, as expected from the earlier analysis of the effect of drag on mass (figure 6-7).

The dependencies of the model coefficients on the sea bottom parameters are shown in figure 6-18. The smallest effect is that of bottom stiffness on model drag coefficient. Over a broad range of stiffness levels, the model drag coefficient is nearly constant. There is a slight linear increase in drag coefficient with increasing bottom damping. The most significant effects of the bottom parameters are on the mass coefficient. As the bottom stiffness increases more of the mooring is supported by the bottom, reducing the mass of the mooring suspended beneath the buoy. This leads directly to a reduction in the model mass coefficient. That the model mass coefficient increases with increasing bottom

136
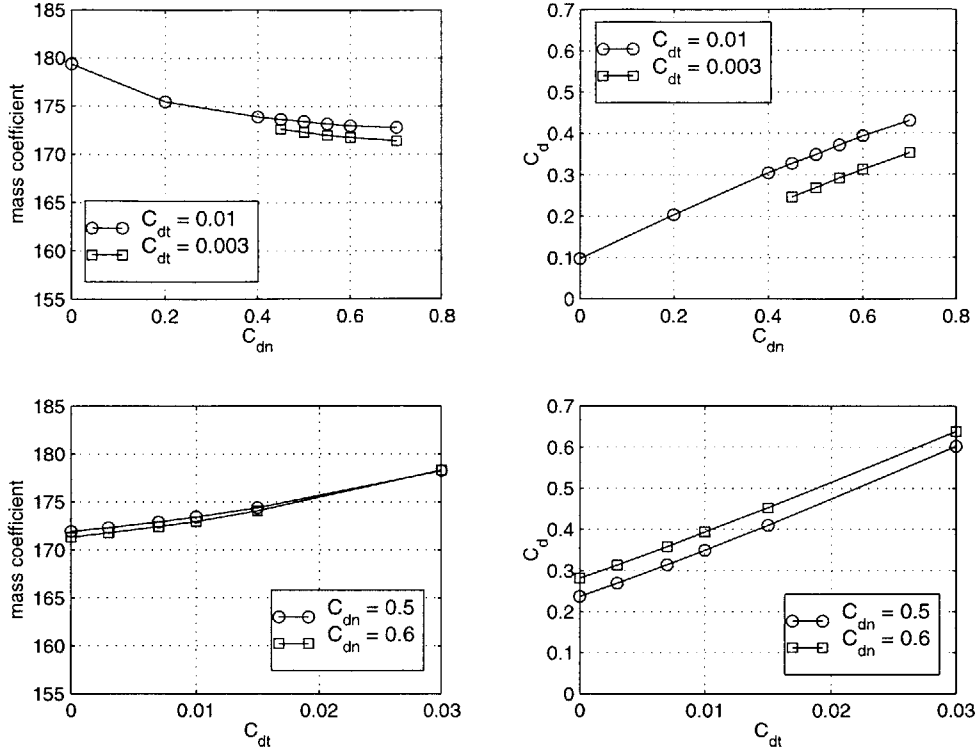
Figure 6-17: Variation of the model mass and drag coefficient with changes to the system normal and tangential drag coefficients. Unless otherwise indicated, all other system parameters are at baseline values. For reference, the equivalent tangential drag coefficient of suspended chain and AxPacks at $\Delta\tau = 0$ is 0.015, or $\pi C_{d_t}^{\text{equiv}} = 0.048$.

damping is a result of large accelerations (actually decelerations in this case) of the chain near the bottom in the presence of high bottom damping. The resulting increase in inertial force is once again reflected in the mass coefficient because of the constant acceleration input in the model.

6.6 Parameter validation using model coefficients

One potential use of the model coefficients from the parametric studies is to validate the choice of system parameters in the time domain simulations. In the validation in section 5.4, simulation results were checked against experimental results to ensure that the simulation results were correct. Given the numerous parameters in the simulations, however, it is conceivable that the right answers could be obtained with several different combinations of those parameters. Comparing the model coefficients derived from a simulated data set to coefficients derived from the experimental data is one way to check
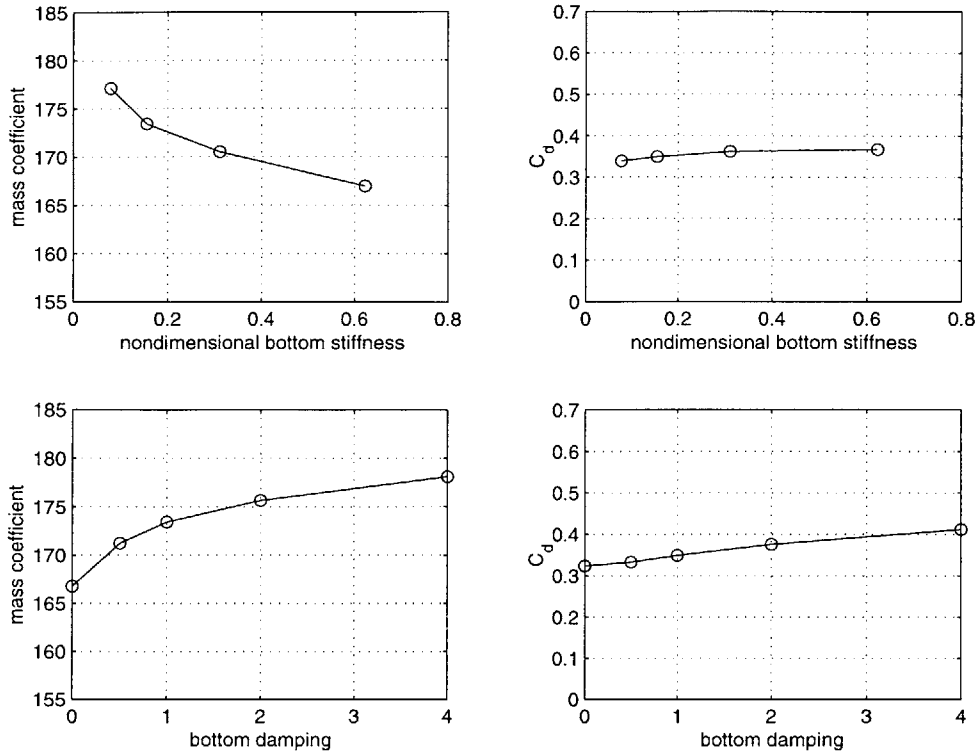
Figure 6-18: Variation of the model mass and drag coefficient with changes to the system bottom stiffness and damping parameters. Unless otherwise indicated, all other system parameters are at baseline values.

whether the simulation parameters are actually correct. In a sense this process checks not only that the simulation answers are correct, but that they are correct for the right reasons.

Figure 6-19 shows the fitted model mass and drag coefficients for the forty variations plus baseline simulation data sets relative to the model coefficients from the experimental data set. The small distance between the experimental result and the coefficients for variations 17, 18, and 31 suggests that the parameters in those variations more closely approximate the true parameters than those in the baseline simulation. Variations 17 and 18 represent an increase in the normal drag coefficient to 0.55 or 0.6. Variation 31 increases normal drag to 0.6, but reduces tangential drag to 0.007. Based on this analysis, the remaining baseline parameters (for added mass and the sea bottom) all appear to be physically reasonable.

This type of validation cannot be obtained simply by comparing statistical results: the RMS difference in tension standard deviation between simulation and experiment was
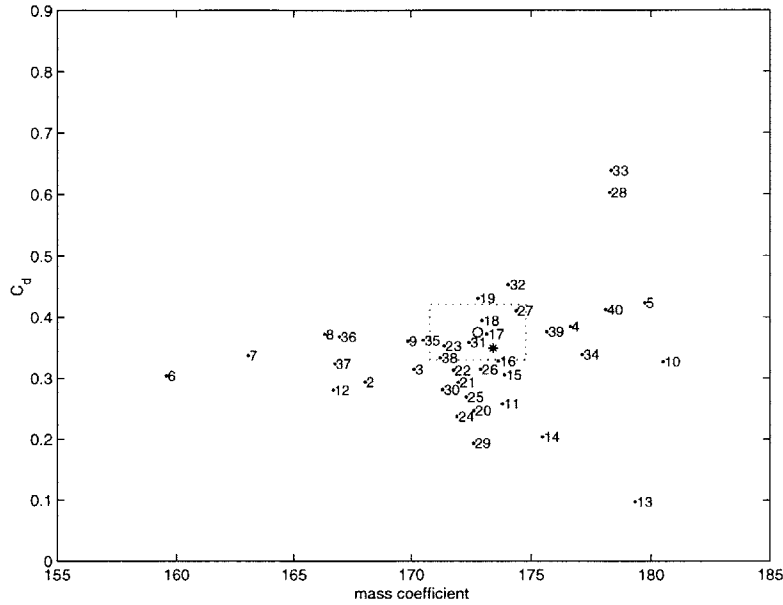
Figure 6-19: Model mass and drag coefficients for the simulation and experimental data sets. Numbers refer to the variation in table 6.2. The experiment result, with confidence intervals, is marked by the circle and the dotted box. The baseline simulation result is marked by the *.

5.7% for variations 17 and 18, and 5.8% for the baseline and variation 31. Variation 19, the coefficients for which actually fall outside the experimental result confidence intervals, also has an RMS error of 5.7%. While this error is minimum for all the simulation data sets, analysis of the model coefficients indicates that the normal drag coefficient of 0.7 in this variation is too high.

While this procedure can validate a parameter set as being a reasonable approximation to the true parameters, it cannot reveal the true values for those parameters. With an exhaustive search of the parameter space, which even for this simple mooring would be computationally very expensive[2], it would be possible to determine the parameter set which best matched the experimental results. Given the overlapping confidence intervals of all the fitted coefficients, however, the only result that could be accurately reported would be the possible ranges of the parameters.

---

[2] The forty variations in table 6.2, which by no means represent an exhaustive search of the space, took approximately eight days to complete on a 533 MHz Alpha LX workstation.

6.7 Empirical relationships for the model coefficients

The strong linear dependence of the model mass and drag coefficients on the system normal and tangential added mass and drag parameters suggests the possibility of constructing empirical functions which could be used to calculate model coefficients using only the known hydrodynamic and material properties of the mooring. Particularly revealing are the relationships exemplified in figure 6-17 for the model drag as a function of system tangential drag. That the two lines for different normal drag coefficients are separated by a constant offset indicates that the model drag coefficient is simply a linear combination of the system normal and tangential drag coefficients.

Ignoring any dependence of the model drag coefficient on system mass or bottom parameters, a formula for the model coefficient as a function of system parameters can be written as

$$C_d = \beta_{d_t} \pi C_{d_t} + \beta_{d_n} C_{d_n}.$$ (6.34)

β_{d_t} and β_{d_n} express the relative weighting of normal and tangential drag in the composite model drag coefficient. The factor of π on the tangential term accounts for the definition of the tangential drag coefficient based on material circumference, rather than diameter as for the normal drag coefficient. The two weights, β_{d_t} and β_{d_n}, can be determined by a least squares fit to the model results from variations 13 through 33 (in which only the drag coefficients were varied) plus the baseline case in table 6.2. The results from the fit are

$$\beta_{d_t} = 3.79,$$ (6.35a)

$$\beta_{d_n} = 0.46.$$ (6.35b)

Given validated values $C_{d_t} = 0.01$ and $C_{d_n} = 0.55$ from the previous section, these weights lead to proportions for tangential and normal effects in the composite model coefficient of approximately one-third and two-thirds, respectively. The quality of the fit is quite high. The root mean square difference between the actual model drag coefficients and those calculated from equation 6.34 with the weights from equation 6.35 is 5.1%.

The linear dependence of the model mass coefficient on the system added mass co-

140

efficients suggests that a formula similar to equation 6.34 can be derived for mass. The dimensional nature of the mass coefficient leads to a more complicated form, however. Taking into account the nominal mass that hangs under the buoy in a slack configuration, and the rate of increase of suspended chain length with static tension (the slope of the line in figure 6-20, φ), a formula for the mass coefficient is

$$M = M_{T_0} + \varphi \left[\beta_{m_t} \left(m + \rho \frac{\pi d^2}{4} C_{a_t} \right) + \beta_{m_n} \left(m + \rho \frac{\pi d^2}{4} C_{a_n} \right) \right]. \tag{6.36}$$

The nominal mass, M_{T_0}, is defined as the mass plus tangential added mass of all of the components hanging beneath the buoy in a slack (purely vertical) configuration. The model mass coefficient, M, is a combination of this nominal mass and a weighted sum of the virtual tangential and normal mass of additional material that is pulled off the bottom as steady state tension increases. The weights, β_{m_t} and β_{m_n}, are again determined using a least squares fit to simulation results: variations 1 to 12 plus the baseline in this case. The fitted weights are

$$\beta_{m_t} = -0.156, \tag{6.37a}$$

$$\beta_{m_n} = 0.102. \tag{6.37b}$$

The RMS difference between the actual mass coefficients and the results from equation 6.36 using these weights is less than one percent.

To understand the meaning of the various terms in equation 6.36 and the importance of the fitted weights, it is useful to consider a uniform mooring in water depth H. Defining

$$m_{a_t} = \rho \frac{\pi d^2}{4} C_{a_t}, \tag{6.38}$$

$$m_{a_n} = \rho \frac{\pi d^2}{4} C_{a_n}, \tag{6.39}$$

the nominal mass can be written as

$$M_{T_0} = H \left(m + m_{a_t} \right), \tag{6.40}$$

141
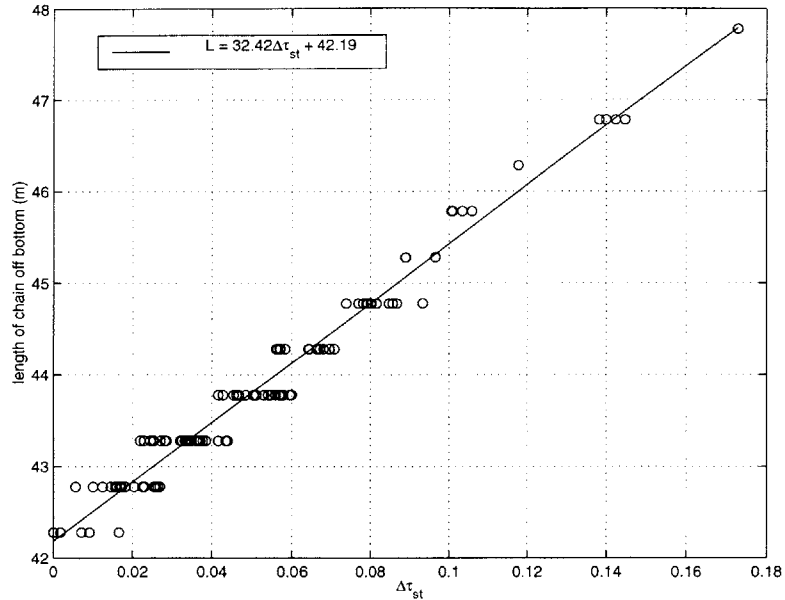
Figure 6-20: Total length of mooring components suspended below the surface buoy as a function of static tension. Data are from the two dimensional validation simulations presented in section 5.4.1.

and equation 6.36 becomes

$$M = (H + \varphi\beta_{m_t})(m + m_{a_t}) + \varphi\beta_{m_n}(m + m_{a_n}).$$ (6.41)

With this representation, the weights specify or modify the length of mooring material that contributes to the tangential or normal mass. This explains why β_{m_t} is negative. The composite model mass is made up of the tangential mass evaluated over some length slightly less than the total length of the mooring plus the normal mass evaluated over some small length.

6.8 A priori response prediction

The primary motivation for developing equations 6.34 and 6.36 is the hope that these formulae can be used to calculate the coefficients for a given mooring design based only on the known (or estimated) material and hydrodynamic properties of that system. Such a facility would permit dynamic response prediction without the costly construction and execution of time- or frequency-domain numerical simulations. In cases where the detailed information available from such simulations is a necessary part of the design process,

142

response prediction based on the simple model and a priori coefficients could still facilitate the early design iteration stages.

6.8.1 Specifying the steady state tension

A critical piece of information in the dynamic tension model is the non-dimensional steady state tension, τ (and $\Delta\tau$). In early design studies it is probably sufficient to estimate the mean tension using catenary formulae. For more refined predictions a static nonlinear model, such as the one described in chapter 3 and appendix D, could be run. Easiest of all for predicting the response in survivability conditions would be to specify a value for τ directly. Experience with oceanographic catenary moorings in 40 m or greater water depth suggests that a reasonable maximum value for τ in similar systems is about 1.3.

Calculating the mass coefficient (equation 6.36) also requires knowledge of the rate of change of the length of the mooring with steady state tension, φ. From the inextensible catenary results in appendix G, the rate of increase of suspended length with increasing $\Delta\tau$ is

$$\varphi = \frac{dL}{d\tau} = \frac{H^2}{L}. \tag{6.42}$$

This formula must be employed with some care for non-uniform moorings. More refined calculations of φ could be made by running several non-linear static simulations and estimating the slope of the resulting (τ, L) line, as in figure 6-20.

6.8.2 Calculating model coefficients

For the basically uniform all chain experimental mooring, application of equations 6.34 and 6.36 to calculate model mass and drag coefficients is straightforward – simply input the mass and drag properties of the chain. More complicated moorings require some pre-processing to calculate the input variables for equations 6.34 and 6.36. For a slack mooring composed of p segments (chain shots, instrument cages, strongbacks, etc.), equivalent normal and tangential drag coefficients are calculated as

$$C_{d_{n,t}}^{\text{equiv}} = \frac{1}{dH} \sum_{i=1}^{p} d_i L_i C_{d_{n,t}}^i. \tag{6.43}$$

d_i, L_i, and $C_{d_{n,t}}^i$ are the diameter, length, and drag coefficients of segment i, respectively. d is the diameter of the mooring material that includes the grounded portion of the mooring. The assumptions behind this approach to averaging the drag coefficients are that the mooring is uniform below a certain depth and that the mooring drag coefficients can always be characterized by the drag properties of that portion of the mooring that is suspended in a slack configuration. The first of these assumptions is not very restrictive. Instrumentation is seldom placed below the mud line. The second assumption implies that for heavily instrumented large scope moorings at high static tensions, the model prediction would be overly conservative. There is no mechanism in the model to account for the fact that the long length of ungrounded bottom line in this situation has lower drag coefficients than those calculated from the instrumented portion of the mooring.

For the mass coefficient the process is somewhat easier because there is no averaging involved. The nominal mass is calculated from

$$M_{T_0} = \sum_{i=1}^{p} (m + m_{a_t})_i L_i, \qquad (6.44)$$

where $(m + m_{a_t})_i$ is the mass plus tangential added mass per length of segment i. Appropriate values for m, C_{a_n}, and C_{a_t} in equation 6.36 are simply those for the lower uniform portion of the mooring.

6.9   Validation of a priori response prediction

In order to test the idea that formulae for the model coefficients derived using a data set from a single experiment are broadly applicable, three test moorings are considered. The first is the shallow water chain catenary mooring from the Coastal Mixing and Optics (CMO) experiment, for which experimental results are available. In this case the model predictions are compared directly to the experimental results. The remaining test cases are contrived examples of an offshore riser in four different configurations: three catenary shapes and a lazy wave shape. The lazy wave configuration is the same as that considered in Larsen's [61] comparative study of different numerical programs. Because no experimental results are available for these cases the model predictions are compared to simulation results.

144

6.9.1 CMO mooring

The central discus mooring of the CMO experiment was an instrumented chain mooring deployed in 70 m of water off the northeast coast of the United States from July 1996 through June 1997 [40]. The central discus buoy contained the same motion package as in the SWEX experiment, with a 10,000 pound load cell at the top of the mooring chain. The primary difference in the two moorings is the instrument load. In 70 m of water the CMO mooring had a nominal virtual mass of approximately 1570 kg of chain and instruments suspended below the buoy. The field experiment mooring had approximately 165 kg of chain and instruments in 40 m of water. Instrumentation included five vector measuring current meters (VMCMs) and four Seacat conductivity and temperature probes.

The data set from the Coastal Mixing and Optics experiment comprises 634 time series of tension and motion. Composite normal and tangential drag coefficients, calculated according to equation 6.43, are

$$C_{d_t}^{\text{equiv}} = 0.025, \tag{6.45}$$

$$C_{d_n}^{\text{equiv}} = 0.97. \tag{6.46}$$

The nominal mass is 1570 kg and the outside width and mass per length of the bottom chain are 0.066 m and 7.98 kg/m, respectively. Applying the weights from equations 6.35 and 6.37 yields model coefficients of $C_d = 0.75$ and $m = 1553$ kg.

These results are very close to the coefficients calculated from a model fit to the 564 experimental data sets for which wind data was readily available. From that fit, $M = 1557 \pm 7$ kg and $C_d = 0.79 \pm 0.05$. A plot of σ_T versus $\tau \sigma_a$ for the experimental and model results with the a priori calculated coefficients is shown in figure 6-21. Because the purpose of the comparison is to validate the a priori coefficients rather than the usefulness of the model as an a priori design tool, the model results were calculated using the experimental mean tension and a value for φ calculated from 564 static simulations. The root mean square difference between the model prediction and experimental result is 2.1%. This error is the same as that from a comparison of experimental and model results with the above mentioned fitted coefficients.
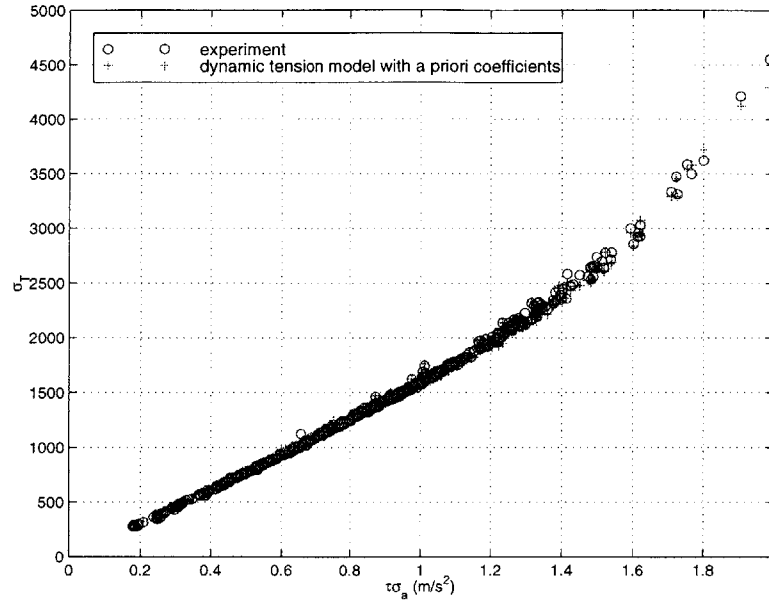
Figure 6-21: Comparison of experimental and model predicted σ_T for the CMO mooring using a priori calculated model coefficients. RMS error between experiment and model result is 2.1%.

6.9.2 Catenary riser

The steel catenary riser (SCR) problem tests the predictive capabilities of the model on a problem with a scale typical of offshore energy production systems rather than oceanographic applications. The validation baseline in this case is derived from simulations. The simulated system consists of 1500 m of 0.21 m diameter pipe deployed in three different configurations. The pipe has a mass per length of 89 kg/m, axial stiffness of 5×10^9 N, and bending stiffness of 6.6×10^3 Nm^2. Hydrodynamic and bottom parameters in the simulation were set to $C_{a_t} = 0$, $C_{a_n} = 1$, $C_{d_t} = 0.05$, $C_{d_n} = 1.0$, $\tilde{k} = 0.42$ and $\zeta = 1.0$. The simulations were run for vertically imposed motions equal to sea states two through nine. Two configurations were run in 600 m water depth with the steady state horizontal position of the top node at 1000 m and 1200 m. A third configuration was run in 300 m of water with the horizontal position of the top at 1450 m. The current profile in all cases was constant at $+1.0$ m/s (left to right) from the surface to one-third the water depth and then decreased linearly to zero at the bottom. The modeled static configurations are shown in figure 6-22. These configurations provide working scopes (ratio of suspended length to water depth) of approximately 1.1, 1.5, and 3.8.

For illustrative purposes and because only simulation results are available for compar-

146
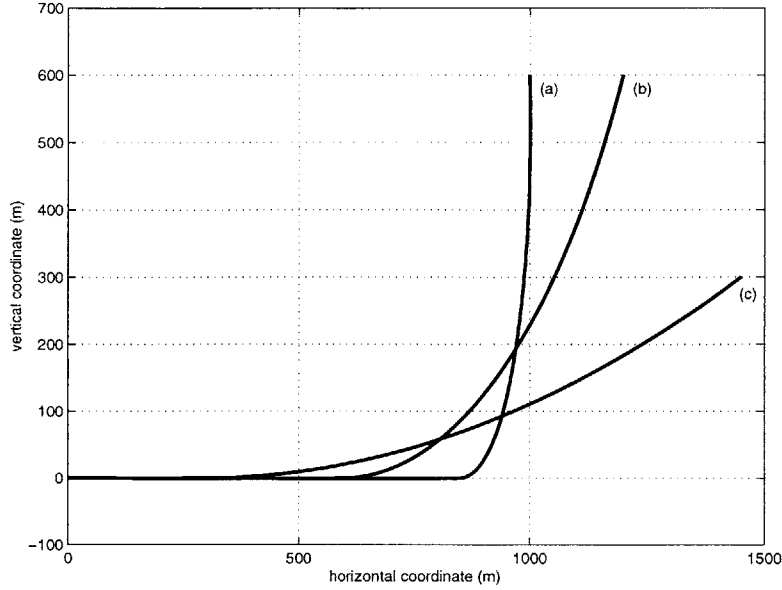
Figure 6-22: Static configurations of the catenary riser for the simulation results.

ison, this example also employs estimates for τ and φ based on catenary formulae rather than detailed static simulations or experimental results. Thus, the model calculations in this case demonstrate the process that a designer might follow in using the simple model in the early stages of the design process. Given estimates for the working scopes of 1.1, 1.5, and 3.8 for the three configurations, equations G.4 and G.6 were used to calculate values for τ and φ in each configuration. The results of these calculations are shown in table 6.3. Because the model mass coefficient, M, depends on φ, a different mass coefficient was calculated for each configuration. Substituting the known pipe properties, the weights for the mass coefficient given by equation 6.37, and the different values for φ into equation 6.36 yields for M of 52527 kg, 52760 kg, and 26574 kg, for the three cases, respectively. Similarly, substituting the pipe drag parameters into equation 6.34 with weights given by equation 6.35 yields $C_d = 1.055$, independent of the configuration.

Motion statistics for the model were calculated from the same Bretschneider spectrum, $S(\omega)$, that was used in generating the input time series for the simulation in each sea state,

$$\sigma_{v|v|} = \sqrt{3} \int_0^\infty \omega^2 S(\omega) d\omega, \tag{6.47}$$

$$\sigma_a = \left[\int_0^\infty \omega^4 S(\omega) d\omega \right]^{\frac{1}{2}}. \tag{6.48}$$

Configuration	scope	τ	φ (m)
SCR a	1.10	1.1	545.5
SCR b	1.50	1.63	400.0
SCR c	3.80	7.72	78.9
Lazy wave	1.07	1.07	290.7

Table 6.3: Non-dimensional mean tension and φ values for the catenary riser and lazy wave riser systems.

sea state	significant height (m)	peak period (s)	% error in model predicted σ_T		
			config (a)	config (b)	config (c)
2	0.3	7.5	-15.1	-48.6	-61.5
3	0.9	7.5	-14.3	-41.1	-43.8
4	1.9	8.8	-11.4	-29.9	-27.0
5	3.3	9.7	-8.3	-16.3	-9.0
6	5.0	12.4	-4.6	-7.0	0.9
7	7.5	15.0	-1.3	3.7	12.5
8	11.5	16.4	3.1	17.2	39.2
8+	16.0	20.0	0.9	15.8	38.7

Table 6.4: Error in the model predicted σ_T for the catenary riser using a priori model coefficients. Model coefficients were calculated using approximate steady state tension results from equations G.4 and G.6. Sea state parameters are based on the North Atlantic data from Faltinsen [29], Table 2.3.

Results of the comparisons are shown in table 6.4 and figure 6-23. The largest relative errors occur for the low sea states in all three configurations. At sea states two and three in the higher scope configurations the model under predicts the response by 50% or more. This represents a much smaller error in the total tension, however, as the static tension is very high in these configuration. At higher sea states the agreement between model and simulation improves. In the lowest scope case (a) the errors for sea states six and above are less than 5%. While the same holds true for the high scope configurations in sea states six and seven, the model over predicts σ_T by approximately 17% in both sea states eight and nine for case (b) and by nearly 40% in case (c). As described in section 6.10, the model increasingly over predicts the tension with increasing sea state because the coupling of mass into drag actually becomes less at these high sea states. Overall, however, the close

148
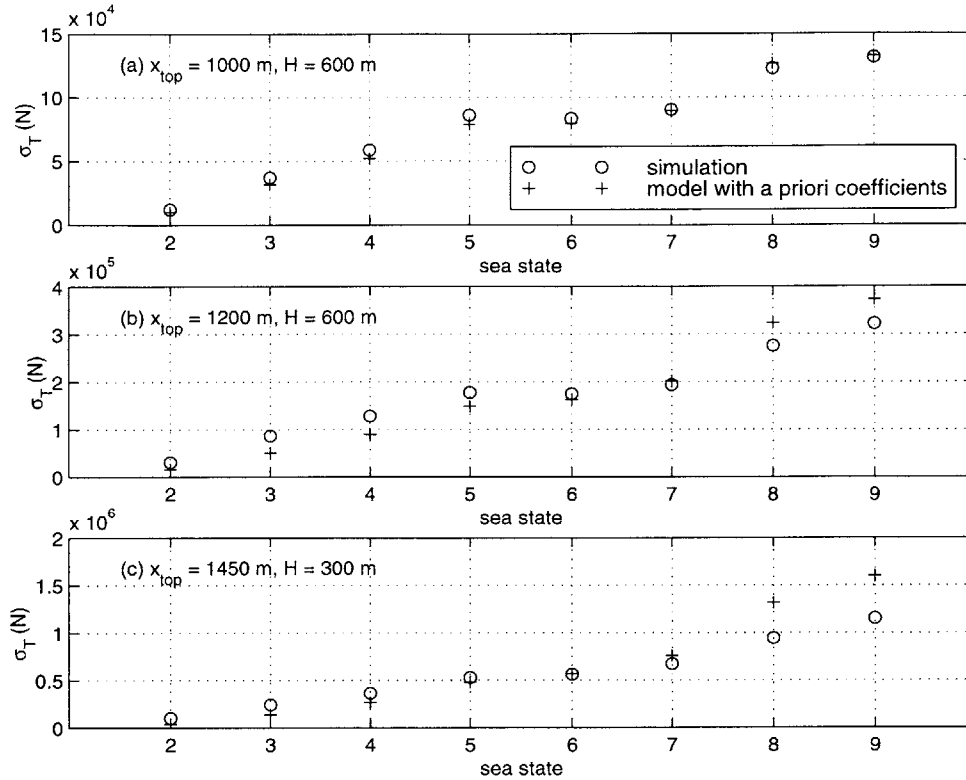
Figure 6-23: Comparison of simulation and model σ_T for the catenary riser. (a) Top node at $x = 1000$ m and water depth of 600 m in the simulation; estimated working scope of 1.1 for model calculations. (b) Top node at $x = 1200$ m and water depth of 600 m in the simulation; estimated working scope of 1.5 for model calculations. (c) Top node at $x = 1450$ m with water depth of 300 m in the simulation; estimated working scope of 3.8 for the model calculations.

agreement in both the quantitative and qualitative way in which the model results predict the response as a function of sea state suggest that the model can be applied successfully to moorings with very different scales than those considered previously.

6.9.3 Lazy wave riser

The lazy wave riser problem is based on the configuration described by Larsen [61]. The pipe and bottom parameters are the same as for the catenary riser. The water depth is 355 m and the static position of the top of the riser is $x = 350$ m, $z = 375$ m (20 m above the water surface). The current flows from right to left ($-x$ direction) with a constant value of 1.0 m/s from the surface to mid-depth and a linear decrease from mid-depth to the bottom. The top of the riser is held in place against the current with an applied pre-tension. The simulated static configuration is shown in figure 6-24.

149
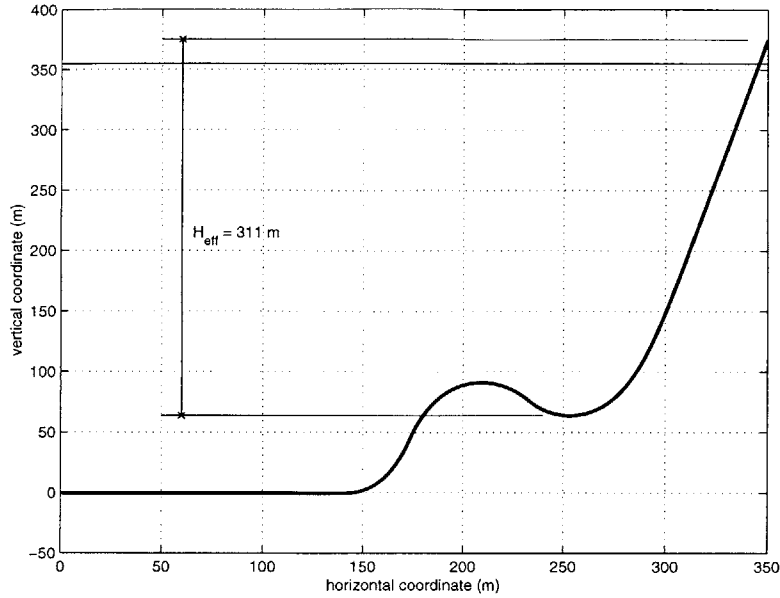
Figure 6-24: Static configuration of the lazy wave riser for the simulation results. The effective working scope for the model predictions was also determined from this result.

Because of the different shape, the model must be applied with some care in this case. The water depth is taken to be the distance from the bottom of the sagged section to the top of the riser (above the surface). Likewise, the suspended length is measured from the bottom of the sagged section upwards. With these caveats, equations G.4 and G.6 can be used to calculate τ and φ as for the catenary riser. Results of these calculations are given in the last line of table 6.3. The calculated model coefficients are $M = 36267$ kg and $C_d = 1.055$.

A comparison between simulation and model predicted σ_T for the same eight sea states as for the catenary riser is shown in figure 6-25. The largest relative errors in this case occur at the highest sea states, but none of the errors exceed 11%. For sea states six and lower the errors are all less than 5%. The good agreement between model and simulation in this comparison reinforces the idea that the model is applicable on a range of scales, and also suggests that it can be applied to geometrically compliant shapes other than the simple catenary mooring.

150
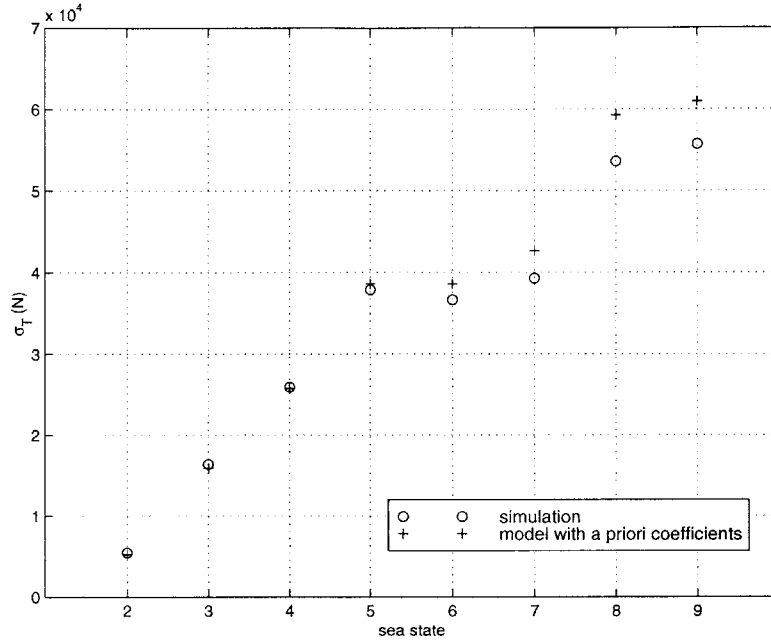
Figure 6-25: Comparison of simulation and model σ_T for the lazy wave riser.

6.10 Conditions under which the model breaks down

While the comparisons above all showed reasonably good agreement between model predictions and simulation results, there are conditions under which the accuracy of the model becomes degraded, such as at the highest sea states in the riser response. To explore these conditions the simplified version of the SWEX mooring first introduced in section 6.1 to study scatter in the response statistics was subjected to a wide range of forcing conditions. In this study, the mooring properties and hydrodynamic parameters were set to their baseline values. The a priori model coefficients given these properties are $M = 156.3$ kg and $C_d = 0.349$. Three hundred simulations were run with $\Delta \tau$ values of 0.05, 0.1, 0.2, 0.5, and 1.0, ten excitation amplitudes ranging from 0.1 m to 2.0 m, and six excitation periods (4, 6, 8, 10, 12, and 15 seconds).

Figure 6-26 shows the simulated and model predicted values of σ_T as a function of σ_a for four values of $\Delta \tau$. In each case the model prediction agrees reasonably well with the simulation for lower values of σ_a. At all four $\Delta \tau$ values, however, the model over predicts the dynamic tension at the highest acceleration levels. The critical acceleration at which the model accuracy is significantly degraded increases with $\Delta \tau$. Thus, both steady state configuration and excitation level determine when the model breaks down. In figure 6-

151
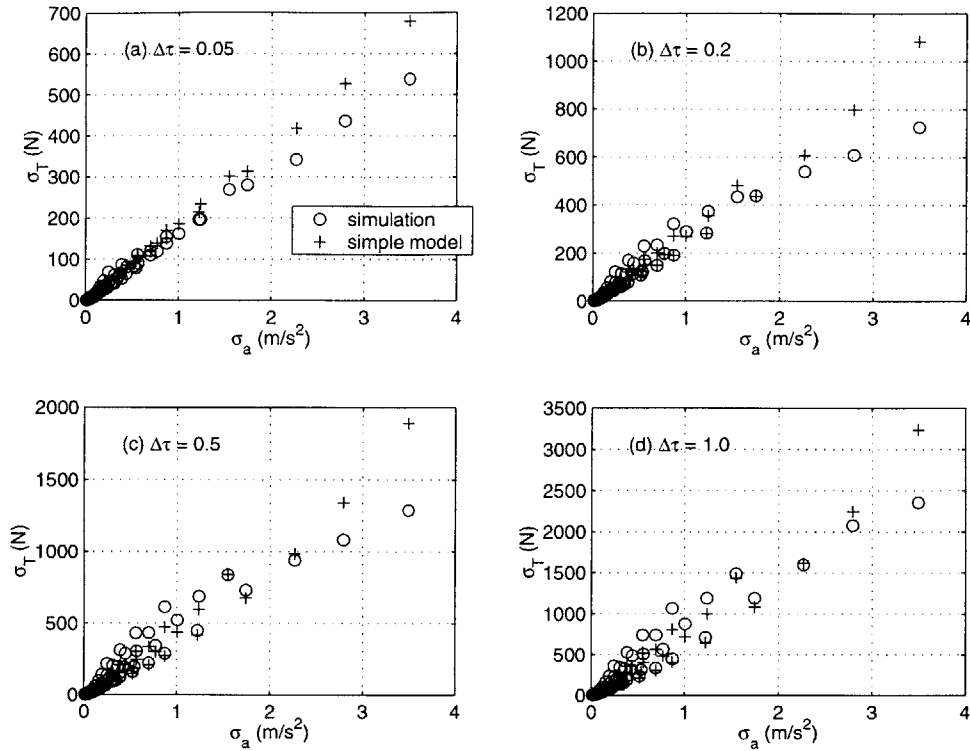
Figure 6-26: Simulation and model predicted values for σ_T in a study using a broad range of sinusoidal excitation conditions.

26(a) for $\Delta\tau = 0.05$ the model predictions for $\sigma_a > 2$ m/s^2 have relatively large errors. For $\Delta\tau = 1.0$ in figure 6-26(d), only the result at the highest value of σ_a (approximately 3.5 m/s^2) has a large error.

The over prediction of the tension is likely due to the presence of the coupling between mass and drag in the model. As shown in figure 6-8, the relative importance of the coupling on the drag coefficient decreases with increasing $\Delta\tau$. The model has no way to account for this decrease and thus the presence of the coupling leads to an over prediction of the tension in severe conditions. That the effect of the coupling should be reduced in severe conditions makes sense in that the process whereby an increase in inertially induced motions leads to an increase in drag forces should be self-limiting. At some point the motion will reach a speed at which quadratic drag, which is proportional to $A^2\omega^2$, will restrict any additional line motions that might be caused by inertia, which is proportional to $A\omega^2$. The point at which this occurs increases with increasing mean tension because as the mooring is pulled open the coupling between inertia and drag is important over a broader range of excitation conditions.

152

In addition to this over prediction of tension in severe conditions there are several remaining circumstances in which the model cannot accurately predict the dynamic response. The two most interesting are both related to elastic stiffness. For moorings with inadequate scope, the geometric compliance mechanism can fail and elastic stretching of the mooring line becomes important. In these cases, the model would likely under predict the tension. The model essentially assumes that there will always be sufficient geometric compliance.

In contrast, for moorings that are basically geometrically compliant, but also relatively elastically flexible, the model over predicts the tension. For example, the sea state 8 simulation result for σ_T for the higher scope catenary riser problem with the axial stiffness reduced by a factor of 100 is $\sigma_T = 1.05 \times 10^5$ N. This is nearly three times less than the result calculated using the original stiffness. The model has no mechanism to account for this reduction. The implicit assumption in ignoring stiffness effects in the development of the model is that the mooring line is inextensible. The validity of the inextensibility assumption can be checked using the ratio of elastic to catenary stiffness [94],

$$\left(\frac{w_0 L}{F_h}\right)^2 \frac{EA}{F_h}, \tag{6.49}$$

where F_h is the horizontal component of tension at the top of the mooring. Results from Irvine and Caughey [58] suggest that inextensibility is a reasonable assumption if this ratio exceeds $100 - 1000$.

Other failure modes for the model include cases where the mooring is near vertical ($\Delta\tau \approx 0$) and $\sigma_{v|v|}$ is large or tangential drag effects are substantial. In both of these cases, the model mass term will accurately predict the inertial response but the inclusion of $\Delta\tau$ in the drag term means that the drag response will be neglected. Also, in cases where tangential drag is very large and normal drag is very small, figure 6-6(c) makes clear that the total drag coefficient should decrease with $\Delta\tau$. The model drag coefficient always increases. Finally, because geometric stiffness induced dynamic tension is proportional to the dynamic length of material off the bottom and steady state forces acting on that material, strong bottom currents or very heavy bottom line can increase geometric stiffness effects to the point where they become non-negligible.

153

6.11 Effect of horizontal motions on the model coefficients

All of the simulations used in developing the simple model thus far have used purely vertical input. This approach was based on the derivation of the model using only heave statistics. Given the comparisons to simulation results of a wide range of configurations, the model is clearly successful at predicting the dynamic tension response to vertical motions. Furthermore, given the model's derivation from and success with the experimental results from the SWEX and CMO chain catenary moorings, for which the topside motion had components in three dimensions, it can be concluded that in these configurations the dynamic tension is dominated by the system response to vertical motions. Clearly, however, the horizontal motions must produce some contribution to the tension response.

To explore what effect horizontal motions have on the model coefficients, three-dimensional simulations of the experimental mooring were run for the same baseline plus 40 variations of the hydrodynamic coefficients listed in table 6.2. Because of the loss of the y accelerometer channel during the experiment there are only 60 available data sets to be simulated for each variation. Figure 6-27 shows the fitted model mass and drag coefficients as a function of the simulation tangential and normal added mass and drag coefficients for both the original two-dimensional vertical only simulations and the new three-dimensional simulations.

The obvious effect of the horizontal motions is an increase in the model drag coefficient and a decrease in the model mass coefficient. Based on the convergence to nearly identical mass coefficients at zero normal added mass, the change in model mass coefficient appears to be due entirely to an effect in the normal direction. In contrast, both tangential and normal effects contribute to the increase in model drag coefficient with the addition of horizontal motions. Qualitatively, however, there are no significant differences in the coefficients derived from the three-dimensional simulations with both vertical and horizontal topside motions. What this indicates is that the model, which uses statistics of vertical motion as the only input, can be successfully applied to some systems with horizontal motions because the horizontal motions in these systems can be accounted for by changes to the model mass and drag coefficients.

Because of this, figure 6-19, which compared model mass and drag coefficients for the vertical motion simulations to coefficients derived from the experimental data set, is not a
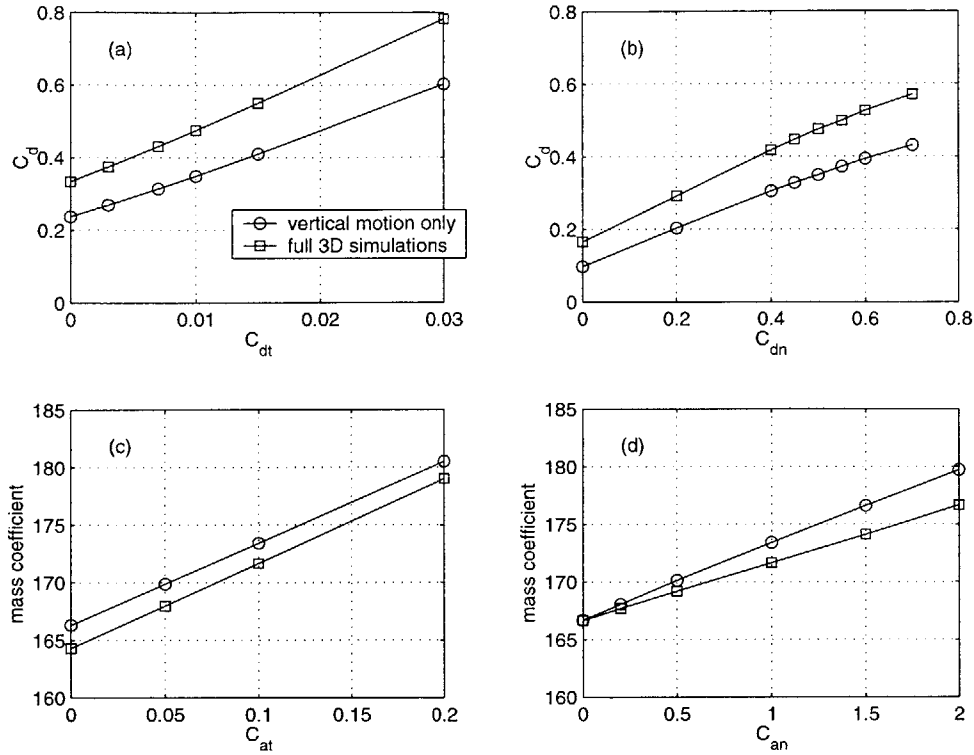
Figure 6-27: Variation of the model mass and drag coefficient with changes to the system normal and tangential added mass and drag coefficients for both vertical and fully three-dimensional topside motion input in the simulations. The parameters not under study in each panel remain at baseline values.

good indicator of the true value of the system hydrodynamic coefficients. Rather, it is an indicator of the coefficient sets which when used with a vertical motion only simulation produce good matches to the experimental results, which are three-dimensional. The best choices for drag parameters from that figure were $C_{d_t} = 0.01$ and $C_{d_n} = 0.55$. It is now clear that these values must be too high. They had to be artificially large to match the experimental results to make up for the fact that there was no horizontal motion in the simulations. Figure 6-28 shows the mapping of the model mass and drag coefficients from the three-dimensional simulations. The best choice in this case is $C_{d_t} = 0.003$, $C_{d_n} = 0.5$, and added mass coefficients at baseline values. This is variation 25 in table 6.2.
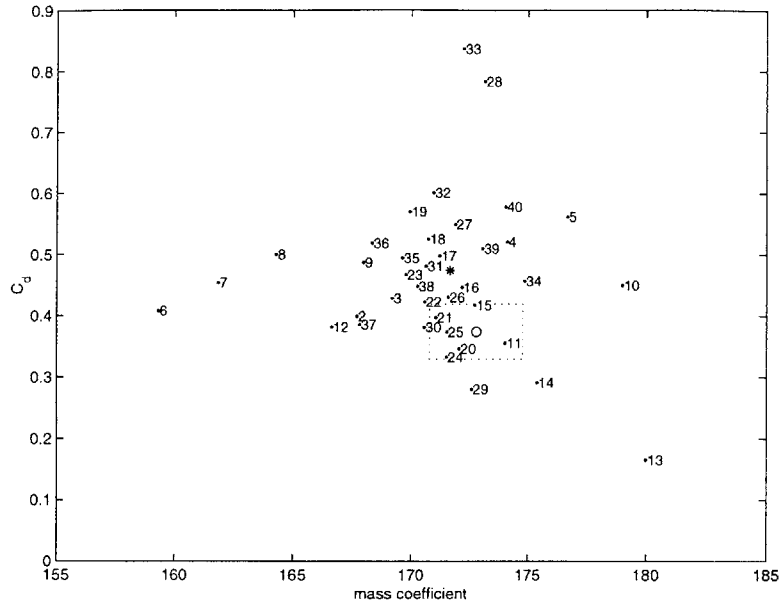
Figure 6-28: Model mass and drag coefficients for the three-dimensional simulation and experimental data sets. Numbers refer to the variation in table 6.2. The experiment result, with confidence intervals, is marked by the circle and the dotted box. The baseline simulation result is marked by the *.

6.12 Horizontal motion effects in very shallow water

Horizontal motions have a more significant effect on the dynamic tension as the water depth decreases. This conclusion became clear during analysis of an experimental data set from a 17 m deep National Data Buoy Center (NDBC) test mooring at Duck Pier, North Carolina. For that experiment, an instrumented 3-meter discus buoy was deployed from July 1997 through January 1998 [88] (due to an instrumentation failure, data is only available for the first two months of this period). The buoy contained a six axis motion package, current meter, and meteorological sensors. Two load cells and an S4 current meter were deployed on the mooring line immediately beneath the buoy. The current meter was deployed in the middle of a 7.1 m length consisting of shackle and short shots of 1-inch and $\frac{3}{4}$-inch chain. The remainder of the mooring line consisted of 41 m of $1\frac{1}{4}$-inch chain.

During the analysis of the data from this mooring two things became apparent. First, simulation results could not be made to match experimental results without the inclusion of the horizontal surge motion at the top of the mooring. There was no choice of hydrodynamic parameters which produced an accurate response given only vertical input.

156
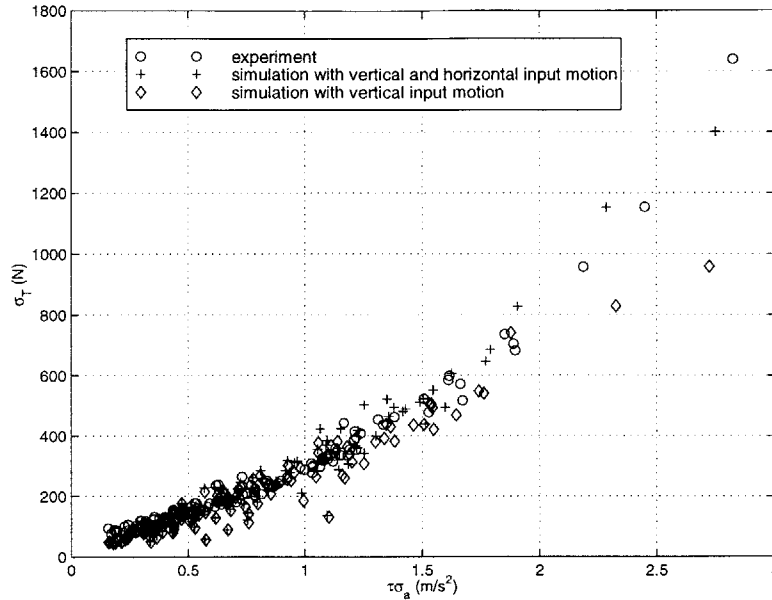
Figure 6-29: Experimental and simulated dynamic tension statistics for 126 of the data sets from the NDBC Duck mooring.

Statistical evidence of this inability is shown in figure 6-29. This situation contrasts with that for the deeper (40 m) SWEX experiment described above for which the hydrodynamic parameters could be increased in conjunction with vertical input to produce a simulation that compared well to the three-dimensional experimental result. The second observation was that while the dynamic tension model could be fitted to the experimental results the fitted drag coefficient was approximately three times greater than that predicted from the a priori coefficient prediction procedures outlined in section 6.8 These two observations indicate that the presence of horizontal motions in this very shallow water mooring lead to a dynamic tension response that is qualitatively different than the response to vertical motions that can be characterized by the simple model.

6.12.1 A model for the dynamic tension response to horizontal motion

To separate the effects of horizontal and vertical motions as a function of depth, simulations of the NDBC mooring were run with horizontal only, vertical only, and combined horizontal and vertical input motion at a series of depths from 10 to 40 m. The length of the bottom chain was increased at the higher depths so that the touchdown point was always away from the anchor. The simulations were two-dimensional, horizontal motion in the surge direction only, to minimize the computation time. Tension statistics at six depths

157

are shown in figure 6-30. Three results are presented for each depth: σ_T^{v+h}, dynamic tension in the simulations with both horizontal and vertical input, σ_T^v, dynamic tension in the simulation with vertical input, and $\sigma_T^v + \sigma_T^h$, the sum of the dynamic tension in the simulations with horizontal only and vertical only input. An important observation to draw from figure 6-30 is that as the depth increases the results from the vertical only and vertical+horizontal simulations appear to converge. This is consistent with the small difference between vertical and fully three-dimensional results from the SWEX mooring. A second observation is that at lower depths the sum of the dynamic tension from the vertical only and horizontal only simulations appear to sum to the results from the simulation with both horizontal and vertical input. This is important because it suggests that the effects of vertical and horizontal motion on dynamic tension are linearly separable.

Based on this latter observation then, a modification to the dynamic tension model can be proposed as follows:

$$\sigma_T = M\tau\sigma_a + \frac{1}{2}\rho C_d \Delta \tau dH \sigma_{v|v|} + f \text{ (horizontal motion statistics, depth)} . \qquad (6.50)$$

Figure 6-31(a) shows the dynamic tension statistics as a function of horizontal acceleration for the simulations with horizontal only input in 15 m depth. The qualitative similarity between this response and the typical response to vertical motions (e.g., figure 5-27(a)) suggests a form similar to the model for vertical motions for the horizontal terms,

$$\sigma_T^h = M^h \tau \sigma_{a_x} + \frac{1}{2}\rho C_d^h \Delta \tau S \sigma_{v_x|v_x|} . \qquad (6.51)$$

The superscripts h indicate terms specific to horizontal motion, subscripts x refer to statistics of the motion in the horizontal direction, and S is a projected area because it is not immediately clear that non-dimensionalizing the drag coefficient using the full water depth is appropriate. For that reason it is more convenient to express the model with a dimensional drag coefficient as

$$\sigma_T^h = M^h \tau \sigma_{a_x} + b^h \Delta \tau \sigma_{v_x|v_x|} . \qquad (6.52)$$

Figure 6-31(b) which shows a linear trend with quadratic velocity for the initial guess at the non-inertial portion of the tension response provides further evidence that this same

158
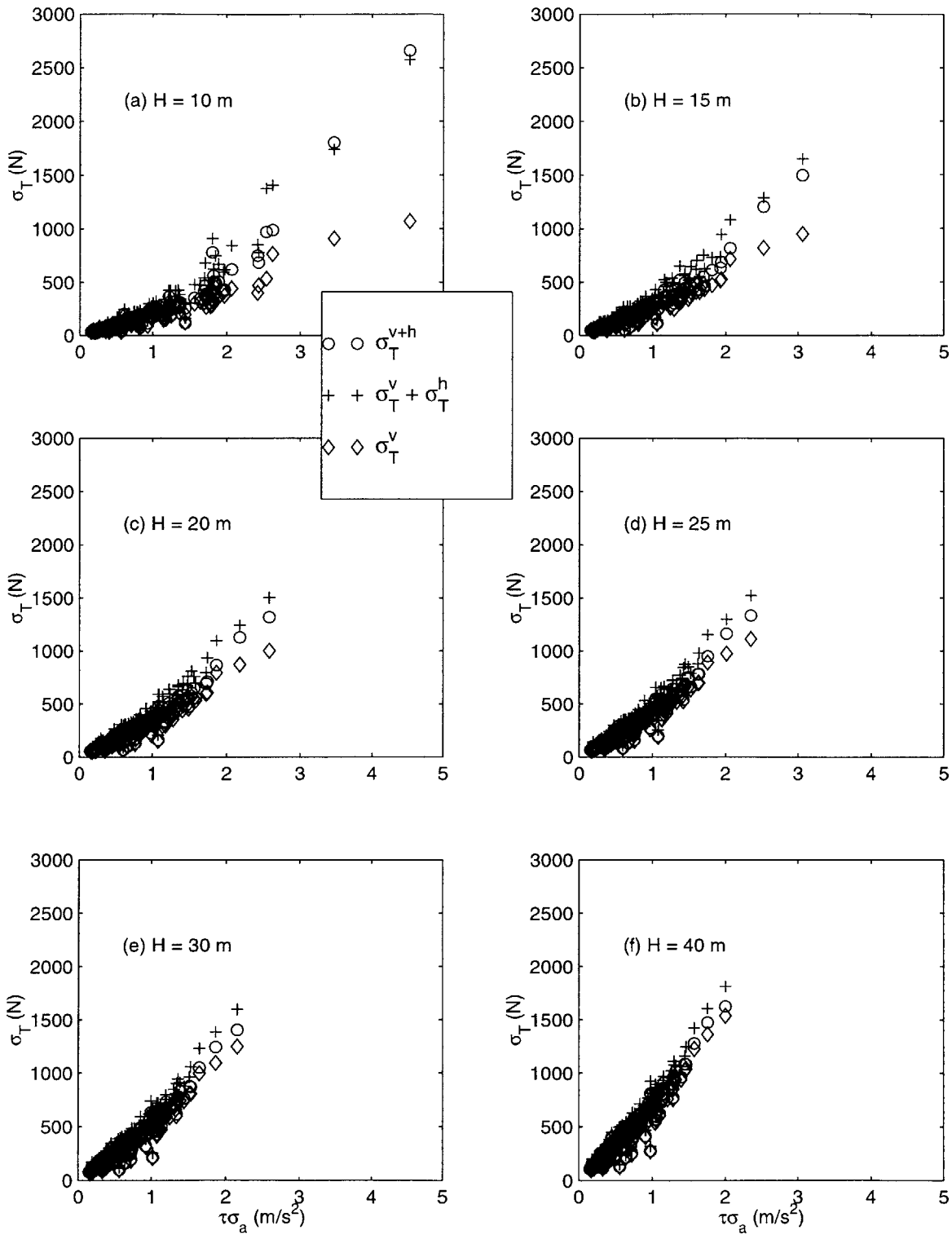
Figure 6-30: Simulated dynamic tension in the NDBC Duck mooring at six depths given vertical+horizontal, vertical only, and horizontal only motion input.
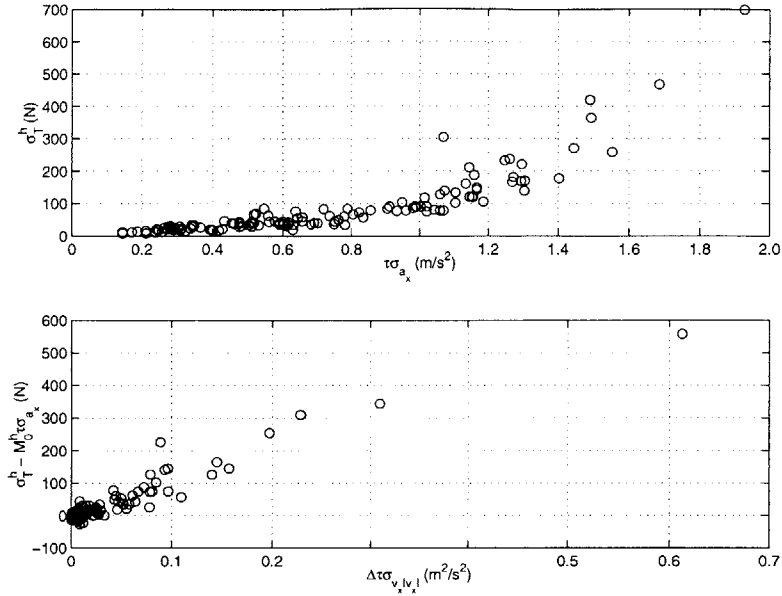
Figure 6-31: (a) Simulated dynamic tension in the NDBC Duck mooring in 15 m depth given horizontal only input motion. (b) Portion of dynamic tension attributable to drag with an initial mass estimate based on the slope of the points in (a) with $\tau\sigma_{a_x} < 0.8$.

form of model may be appropriate for horizontal motions.

When the fitted coefficients for this model are mapped over a range of simulation parameters, however, the fitted dimensional drag coefficient is insensitive to the value of the simulation normal and tangential drag coefficients. For example, at baseline values of $C_{d_n} = 0.3$ and $C_{d_t} = 0.003$, the fitted dimensional drag coefficient is $b^h = 1041$ kg/m. Doubling the normal drag coefficient to 0.6 results in only a slight increase in b^h, to 1080 kg/m. Likewise, increasing the tangential drag coefficient to 0.01 in the simulations produces a fitted value for b^h of 1044 kg/m. The fitted mass coefficients vary significantly with changes to the simulation normal added mass parameter; there does not appear to be any sensitivity of the model mass coefficient to tangential added mass. Parameter variations were also run with a range of bottom damping and bottom stiffness coefficients. The fitted mass and dimensional drag coefficients for some of these variations are listed in table 6.5.

The vertical model form for the horizontal motions, equation 6.52, is only superficially appropriate. That the dynamic tension response to purely horizontal motions is not dependent on the drag coefficients or bottom damping suggests that there is no significant drag contribution to the tension response. In fact, the only parameter variations that

160

variation	M^h (kg)	b^h (kg/m)
baseline	69.3	1041
$C_{d_n} = 0.6$	60.9	1080
$C_{d_t} = 0.01$	69.3	1044
$\zeta = 0.0$	68.0	1026
$\tilde{k} = 0.056$	67.9	1180
$C_{a_n} = 2.0$	84.9	1022
$C_{a_t} = 0.0$	69.1	1045

Table 6.5: Fitted coefficients for the dynamic tension response to horizontal motions using the same model form as for vertical motions. Baseline values are $C_{d_n} = 0.3$, $C_{d_t} = 0.003$, $C_{a_n} = 1.0$, $C_{a_t} = 0.1$, $\zeta = 2.0$, $\tilde{k} = 0.22$. Variations were run for the 15 m depth case.

produce a significant change in the fitted drag coefficient are changes to the mooring line wet weight. Doubling the wet weight (without changing the mass) of all the mooring components yields fitted mass and damping coefficients of 97 kg and 2204 kg/m, respectively. A better model then is one in which the non-inertial portion of the tension response is attributable to a geometric stiffness effect rather than a drag effect. Such a mechanism would explain this correlation between the non-inertial portion of the tension and the mooring wet weight. A model that makes use of this insight is,

$$\sigma_T^h = M^h \tau \sigma_{a_x} + k^h \Delta \tau \sigma_x. \tag{6.53}$$

The form of the stiffness term was chosen because of the strong linearity apparent in figure 6-32 for the non-inertial portion of the dynamic tension as a function of $\Delta \tau \sigma_x$. σ_x is the standard deviation of the surge motion.

Table 6.6 lists the fitted coefficients for the model described by equation 6.53 for the same variations as in table 6.5 plus variations on the wet weight. As expected the stiffness coefficient is largely insensitive to changes in any parameter except mooring wet weight. There is a slight dependence on the bottom stiffness: a factor of four decrease in $\tilde{k}$ results in a twelve percent increase in the fitted stiffness coefficient. The mass coefficient also shows a strong dependence on the wet weight. The quality of the fits is not as high and the confidence intervals are not as small as for the vertical model applied to the SWEX or CMO experimental data. The errors are not unreasonable, however: RMS error between the standard deviation of dynamic tension from the baseline simulations and the fitted

161
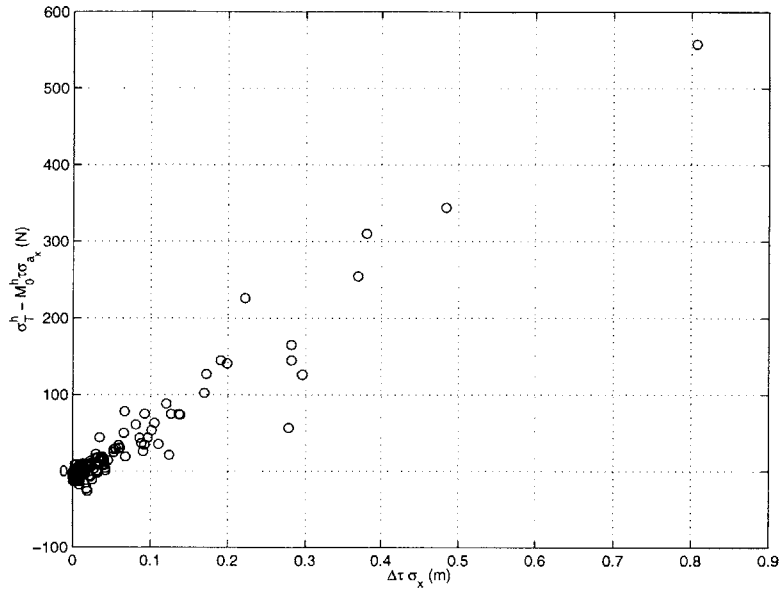
Figure 6-32: Portion of dynamic tension attributable to a stiffness effect with an initial mass estimate based on the slope of the points in figure 6-31(a) with $\tau\sigma_{a_x} < 0.8$.

variation	M^h (kg)	k^h (N/m)
baseline	56.5 ± 6.2	724 ± 100
$C_{d_n} = 0.6$	47.0 ± 6.2	753 ± 100
$C_{d_t} = 0.01$	56.3 ± 6.3	726 ± 100
$\zeta = 0.0$	55.0 ± 6.3	718 ± 99
$\tilde{k} = 0.056$	55.3 ± 6.0	815 ± 107
$C_{a_n} = 2.0$	72.3 ± 6.5	711 ± 98
$C_{a_t} = 0.0$	56.3 ± 6.3	727 ± 100
$w_0/w_0^* = 0.5$	51.3 ± 7.7	493 ± 66
$w_0/w_0^* = 1.5$	67.6 ± 6.8	1099 ± 159
$w_0/w_0^* = 2.0$	82.4 ± 7.9	1528 ± 83

Table 6.6: Fitted coefficients with 95% confidence intervals for the dynamic tension response to horizontal motions using the model described by equation 6.53. Baseline values for the parameters are given in table 6.5. The wet weight variations are specified as a ratio of the specified wet weight to the nominal wet weight in the baseline case. The variation is made to the wet weight of all mooring components.
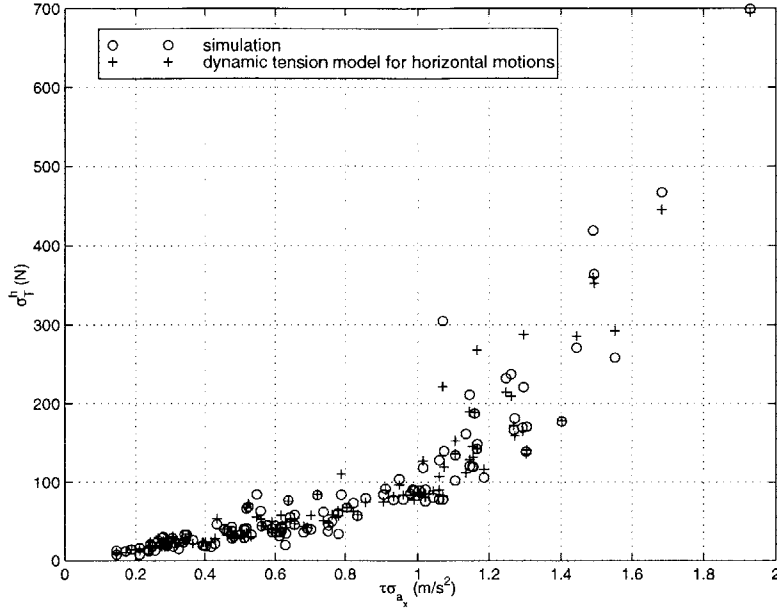
Figure 6-33: Simulated and model fitted (equation 6.53) values for the standard deviation of tension in response to horizontal input motion.

results is 25%; 74% of points have an error of less than 10%. Figure 6-33 shows the simulated and fitted values for σ_T^h for the baseline case in 15 m depth.

Equation 6.53 and the strong dependence of the stiffness coefficient on the wet weight explain why the horizontal motions in the deeper SWEX mooring contributed so little to the total dynamic tension. First, the stiffness term in equation 6.53 scales with non-dimensional mean tension, $\Delta\tau$. The average value of this parameter decreases with increasing depth. The maximum value of $\Delta\tau$ during SWEX was 0.17. In the NDBC experiment it was 0.99. Secondly, the weight of chain in the SWEX mooring was approximately five times lower than the depth averaged wet weight of components in the NDBC mooring. With model stiffness roughly proportional to wet weight, these two factors combine to produce a horizontal motion stiffness effect that is as much as 25 times lower in the SWEX mooring than in the NDBC mooring given similar topside motion.

6.12.2 Parametric dependence of the model coefficients

A practical benefit to choosing equation 6.53 as the form of the model for horizontal motions is that the fitted stiffness coefficients are relatively constant with depth. Figure 6-34 shows the fitted stiffness coefficient over a range of wet weight values for depths from 15 to 40 m. The upward trend in k^h is roughly linear with increasing weight, though the

163
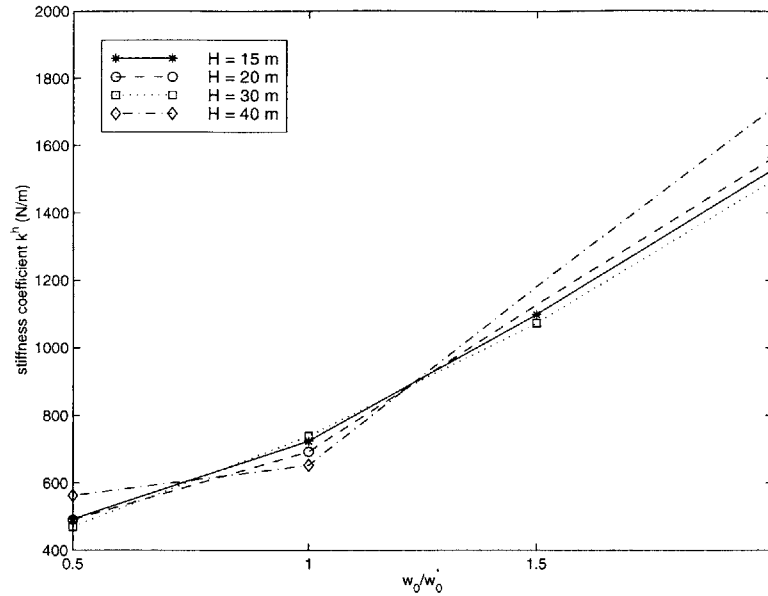
Figure 6-34: Fitted stiffness coefficient for the horizontal motion model in 15, 20, 30, and 40 m water depth. The x-axis is the scaling factor applied to the wet weight of all mooring components.

slope does steepen somewhat as the weight increases. It is difficult to quantify the exact relationship between the fitted value of k^h and the wet weight in the simulation because of the variation in weight over the length of the mooring[3]. Counterintuitively, perhaps, the appropriate value is not simply that for the bottom chain. In 15 m depth simulations with half the wet weight of the bottom chain, but nominal values for the rest of the mooring, the fitted stiffness value was 645 N/m. This value is higher than the 493 N/m stiffness from figure 6-34 calculated when all of the mooring component weights were halved, indicating that the weights of the components above the bottom chain do effect the stiffness.

In a simulation with a uniform mooring consisting only of heavy bottom chain with a wet weight of 188 N/m, the fitted stiffness coefficient was 850 ± 119 N/m. This leads to a ratio $k^h/w_0 = 4.5$. Applying this ratio to the actual mooring with a wet weight averaged over a length of 15 m yields a prediction for k^h of 693 N/m. This value is slightly low compared to the fitted result of 724 N/m in figure 6-34. In 40 m of water, the average wet weight increases because of the increased length of heavy bottom chain, and the predicted result using the ratio of 4.5 is 788 N/m, which is too high compared to the fitted result of 653 ± 173 N/m. All of these values, however, fall within the 95% confidence regions of

---

[3] The NDBC test mooring consisted of four distinct segments, with heavier segments nearer the bottom.
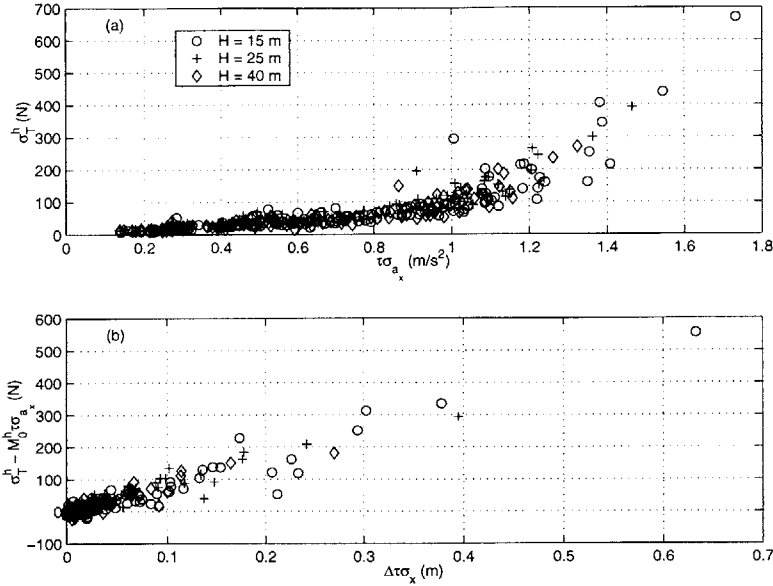
Figure 6-35: (a) Dynamic tension response to horizontal motion in the uniform NDBC mooring at 15, 25, and 40 m depths. (b) Portion of the dynamic tension attributable to stiffness. The initial mass estimate, M_0^h, is based on a linear fit to the data in (a) for $\tau\sigma_{a_x} < 0.8$.

one another.

To eliminate the difficulty associated with the variation in mooring properties with depth and to explore the interdependence of the mass and stiffness coefficients, simulations with only horizontal input were run with the uniform version of the NDBC mooring in water depths from 15 to 40 m. Because the mass and wet weight properties of a mooring line are related through a proportionality constant in most practical situations only the mooring mass was varied in these simulations. The wet weight was defined as

$$w_0 = mg \left(1 - \frac{\rho_{\text{water}}}{\rho_{\text{mooring}}} \right). \tag{6.54}$$

Both tangential and normal added mass coefficients were zero.

With a uniform mooring, the effective wet weight per length and mass per length are constant with depth. Under these conditions, there is virtually no depth dependence in the fitted coefficients. Figure 6-35 shows the dynamic tension response in the usual way for three different depths overlaid upon one another. That the response across depths can be plotted meaningfully in the same way as the response at a single depth suggests that a fit to the combined data from all depths will yield coefficients that are valid at any depth.
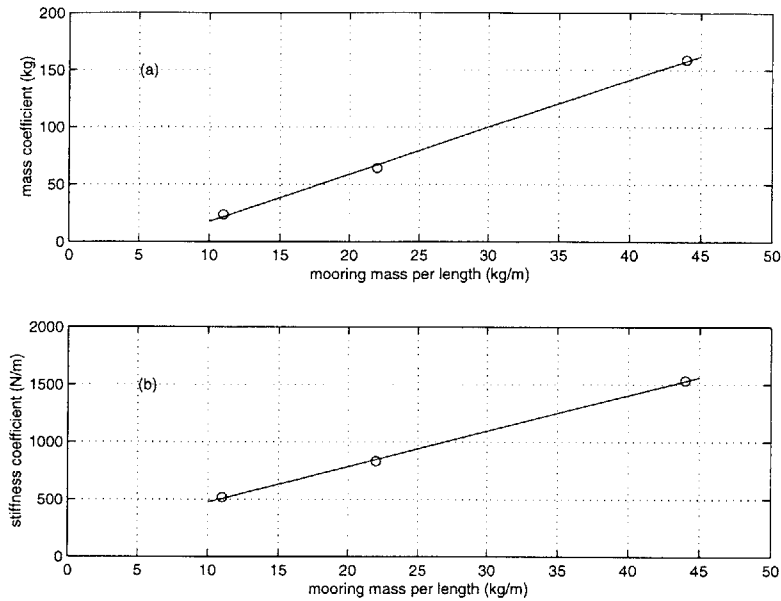
Figure 6-36: (a) Mass coefficient fitted to the tension response data in figure 6-35(a) for the uniform NDBC mooring at 15, 25, and 40 m depths plus additional results for 20, 30, and 35 m depths. (b) Fitted stiffness coefficient for the same data.

Figure 6-36 shows the fitted mass and stiffness coefficients for the combined data at 15, 20, 25, 30, 35, and 40 m depths with the mass per length set to 0.5, 1.0, and 2.0 times the nominal value of 22 kg/m. The fitted coefficients vary linearly with the mooring line mass. The average ratio of model mass coefficient to mooring mass is 2.89 m. The average ratio of model stiffness coefficient to mooring wet weight is 4.68.

The slope of the fitted mass coefficient as a function of mooring mass in figure 6-36(a) has units of length. This length is the amount of mooring chain over which there is an inertial response to horizontal motions. Typically, for wave frequency excitation and low values of non-dimensional mean tension, only a small region near the touchdown point responds with significant acceleration to horizontal motion. The dimensionality of the length of this region complicates any attempt to develop a formula for calculating the model mass coefficient in an arbitrary system. In the vertical model, the appropriate length scale was the water depth. For the horizontal model, the same mass coefficient can be applied across depths and thus depth does not provide the appropriate scaling.

A length scale, l, can be calculated from the ratio of stiffness and inertial effects,

$$l = \frac{w_0 \sigma_x}{m \sigma_{a_x}}. \tag{6.55}$$

166
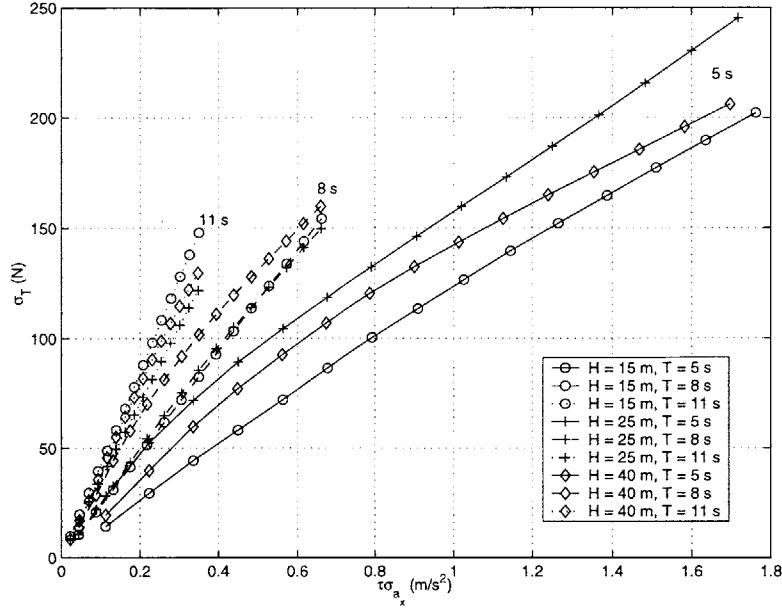
Figure 6-37: Dynamic tension response of the uniform NDBC mooring to purely sinusoidal horizontal input motion as a function of depth and excitation period.

With the wet weight proportional to mg and $\sigma_{a_x} \propto \omega_p^2 \sigma_x$,

$$l \propto \frac{g}{\omega_p^2}, \tag{6.56}$$

where ω_p is the peak frequency of the spectrum of horizontal motion. Though this dependence on excitation frequency could cause some of the scatter in the response statistics, the variation in excitation frequency over the course of the experiment was not great. To verify the dependence on frequency then, simulations were run with purely sinusoidal input motion. Figure 6-37 shows the dynamic tension for the uniform mooring in 15 m, 25 m, and 40 m depth with excitation periods of 5 s, 8 s, and 11 s. Excitation amplitude ranged from 0.1 m to 1.5 m. For each excitation period, the slope of the response is roughly the same, independent of depth. As the excitation period increases, acceleration level decreases, and the slope of the response increases. This increasing slope represents an increase in the total mass that is needed to keep inertia in balance with stiffness effects.

The slopes from these results can be compared to values calculated using equation 6.55. Given sinusoidal input, $\sigma_{a_x} = \omega_p^2 \sigma_x$ (rather than just being proportional) and the total

167

mass coefficient, ml, becomes

$$ml = \frac{w_0}{\omega_p^2}.$$

(6.57)

This formula yields predicted slopes of 575 kg, 304 kg, and 119 kg for 11 s, 8 s, and 5 s excitation periods, respectively. These values compare to average slopes for the results in figure 6-37 of 385 kg, 234 kg, and 126 kg. Even within the simulation results in figure 6-37 the correspondence between frequency and length scale is not exact. The ratio between the average slope of the results for 11 s and 5 s cases is 385/126 or 3.06. From equation 6.56 the expected ratio is $(11/5)^2$ or 4.84. The conclusion from both comparisons is that the calculated length scale becomes too large as the excitation period increases. At the highest frequency, where inertia is most dominant, the calculated length scale appears to be accurate. As the frequency decreases and stiffness effects begin to dominate, the calculated length scale becomes too large.

With the model mass coefficient written as $M^h = ml$, the length scale l given by equation 6.55, and the wet weight and mass related according to equation 6.54, the horizontal model for a uniform mooring with negligible or no added mass can be written in terms of standard deviation of motion only as

$$\sigma_T^h = w_0 \sigma_x \left(\tau + \Delta \tau \beta_k^h \right),$$

(6.58)

where β_k^h is a constant that relates the stiffness coefficient k^h to the mooring wet weight. Figure 6-38(a) shows the simulation results for 15 m, 25 m, and 40 m depth as in figure 6-35 along with σ_T^h calculated from equation 6.58 using a value for β_k^h of 4.68 from figure 6-36(b). At low values of $\tau \sigma_{a_x}$ the response is inertia dominated and the model predictions agree reasonably well with the simulation results. As $\tau \sigma_{a_x}$ increases, however, the model prediction becomes larger than the simulation result. This is a consequence of overestimating the mass length scale as the response becomes more stiffness dominated.

While a length scale based on the ratio of stiffness and inertial effects offers a generalized procedure for calculating the model mass coefficient, it is not applicable over a broad range of conditions. Figure 6-38(b) shows values for σ_T^h calculated from equation 6.53 with fitted mass and stiffness coefficients. At high $\tau \sigma_{a_x}$ these results are significantly more accurate than those based on equation 6.58. The process of calculating model coefficients
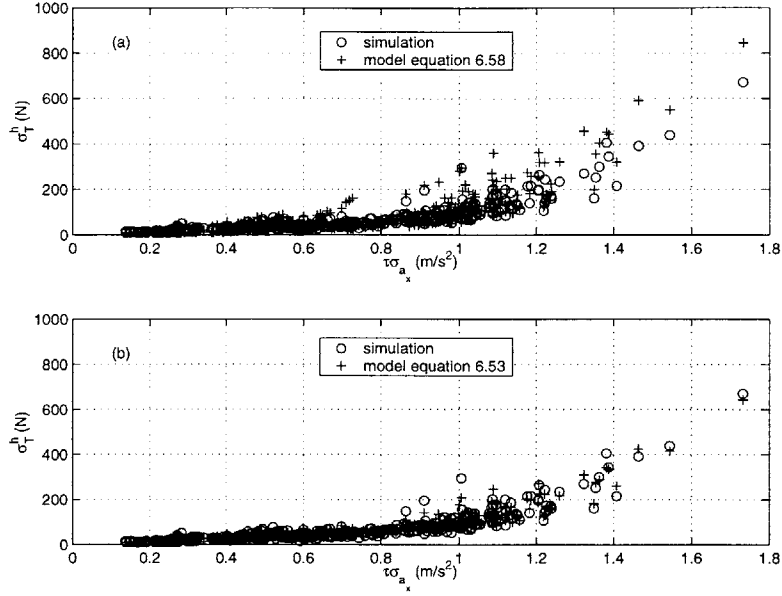
Figure 6-38: (a) Comparison of simulated and model calculated σ_T^h from equation 6.58. The simulation results are the same as those shown in figure 6-35. (b) Simulated and model calculated σ_T^h from the original model equation 6.53 with fitted coefficients ($M^h = 61.4$ kg, $k^h = 848$ N/m).

by fitting to experimental or simulation results is much harder to generalize, however, and is therefore much less useful in practical applications.

6.12.3 Practical application of the horizontal model

Given appropriate coefficients for both the vertical and horizontal models, the separate predictions for response to vertical (equation 6.16) and horizontal (equation 6.53 or 6.58) motions can be summed to calculate the total dynamic tension response in the presence of both vertical and horizontal topside buoy motions. The validity of this approach is supported by the linear separability (in a statistical sense) of the response to vertical and horizontal motions in figure 6-30. Additional work is required, however, to determine the limits of applicability of this approach.

For the analysis of experimental results, it would be desirable to fit the experimental data to a model which combined equations 6.16 and 6.53. The results from such a fit would immediately reveal the relative importance of vertical and horizontal effects in a given data set. Because of the typically strong correlation between vertical and horizontal motion statistics, however, such a fit does not produce reliable results. There are simply

too many degrees of freedom in the fit (four) and too little discrimination amongst the input parameters.

6.13 Summary

While the model for horizontal motions needs to be more fully studied, the overall results from the above analyses of simple models for dynamic tension are quite encouraging. For the response to pure vertical motion, or for cases with low values of $\Delta\tau$ in which horizontal effects can be neglected, the simple model given by equation 6.16 is quite accurate over a broad range of conditions. In the analyses above it was applied to a variety of chain catenary moorings and steel riser configurations with good success. When combined with a validated model for horizontal response effects the range of applicability will be even greater.

As a data analysis tool or as a design tool with a priori predicted coefficients, the simplicity of the model is a compelling advantage. In fact, in the latter application, the simplicity of the model greatly facilitated the analysis that yielded the rules for a priori coefficient prediction. Despite the model's simplicity, however, it has features which make it physically, as well as practically, compelling. In the analysis of these physics, many of the important features of the dynamic response of geometrically compliant moorings were highlighted:

- The dependence of the mass term on τ and the drag term on $\Delta\tau$ reflects the inertia dominated response regime in low to moderate excitation conditions.

- The presence of the coupling between mass and drag in the model is important in the transition between inertia dominated and drag dominated responses.

- At some excitation level which is dependent on both steady state configuration and quadratic velocity, the drag forces overwhelm the inertially induced motions of the chain. Under these conditions the coupling term in the model leads to an over prediction of the tension.

- Stiffness effects can typically be neglected at low non-dimensional mean tension, except perhaps for very low frequency, large amplitude excitations in which velocity

and acceleration are small. Stiffness effects are more important in the response to horizontal motions than to vertical motions.

Unstudied in this chapter is the elastic dominated regime which exists beyond the drag regime for cases where the non-dimensional mean tension is high enough to pull all of the available line off the bottom. Webster [99] studied this regime in some detail. In these cases the system is no longer geometrically compliant and deforms elastically in response to dynamic forcing. For the rigid, stiff materials typically used in these systems this can be a dangerous regime. This situation can be avoided by designing the mooring with sufficient scope given accurate specification of the environmental conditions.

Chapter 7

Bottom Interaction

In the previous chapter the focus of the analyses was the dynamic tension at the top of the mooring. For the most part, the stiffness and damping properties of the bottom played little role in determining that response. Previous authors [79] have shown that the bottom properties do play a role in governing the response, particularly the bending response, of the mooring in the immediate vicinity of the touchdown point (TDP). In this chapter, laboratory experiments are used to investigate whether there are excitation conditions under which bottom interaction effects do play a role in other aspects of the mooring response. Under these conditions, the suitability of the elastic foundation approach in the numerical simulations is also investigated.

7.1 Description of the laboratory experiment

The laboratory experiments were conducted in the Iselin flume at the Woods Hole Oceanographic Institution. The flume is 20 m long and has a cross-section approximately 1.2 m square. It is equipped both with a tow carriage and recirculation pumps, neither of which were used for these experiments. The experiments used a section of mooring chain deployed at a fixed position in the flume. Various configurations of the chain were excited using a linear servo actuation mechanism. Data was collected from load cells and a digital video camera.
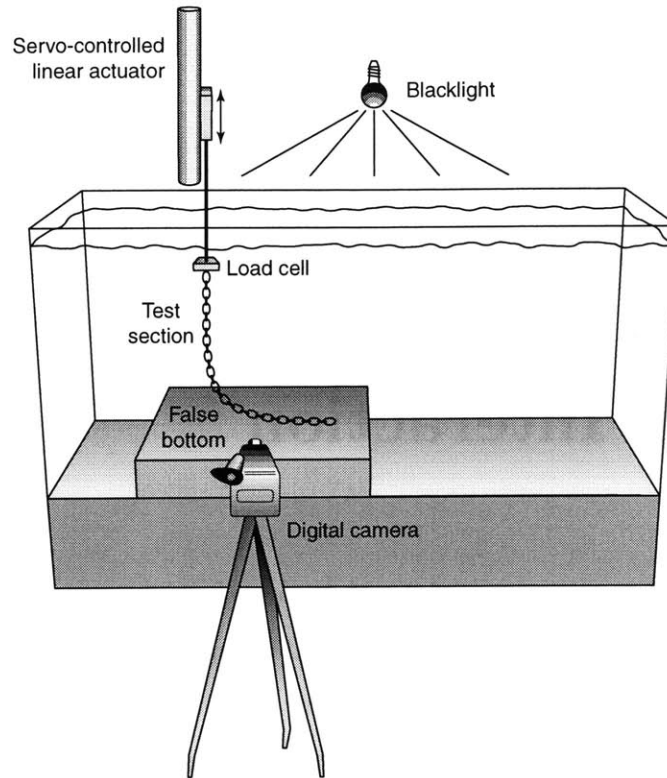
Figure 7-1: The basic setup for the laboratory experiments.

7.1.1 Physical layout of the experiment

The test specimen was a length of $\frac{3}{16}$-inch galvanized steel chain with an outside link width of 1.95 cm and a shaft diameter of 0.57 cm. The mass and wet weight of the chain were 0.57 kg/m and 4.84 N/m, respectively. The test chain was suspended from the linear actuator and run along a bottom platform to an anchor position. The anchor end of the chain was held in place using lead weights placed on top of the chain immediately beyond the end of the platform. Pretension and excitation levels were constrained so that the chain at the anchor end of the platform never lifted off the bottom. Water depth during the experiments was 1.1 m. With a bottom platform height of 10 cm, the effective depth was 1.0 m.

A schematic overview of the experiment is shown in figure 7-1. A photograph of the physical arrangement of the actuator, lighting, and test specimen is shown in figure 7-2. The 10 cm high bottom platform lifts the chain above the tank bottom so that the entire chain is in view of the video instrumentation. The platform, a section of wide aluminum channel stock, was used with four different surfaces. The basic hard bottom is simply the

174
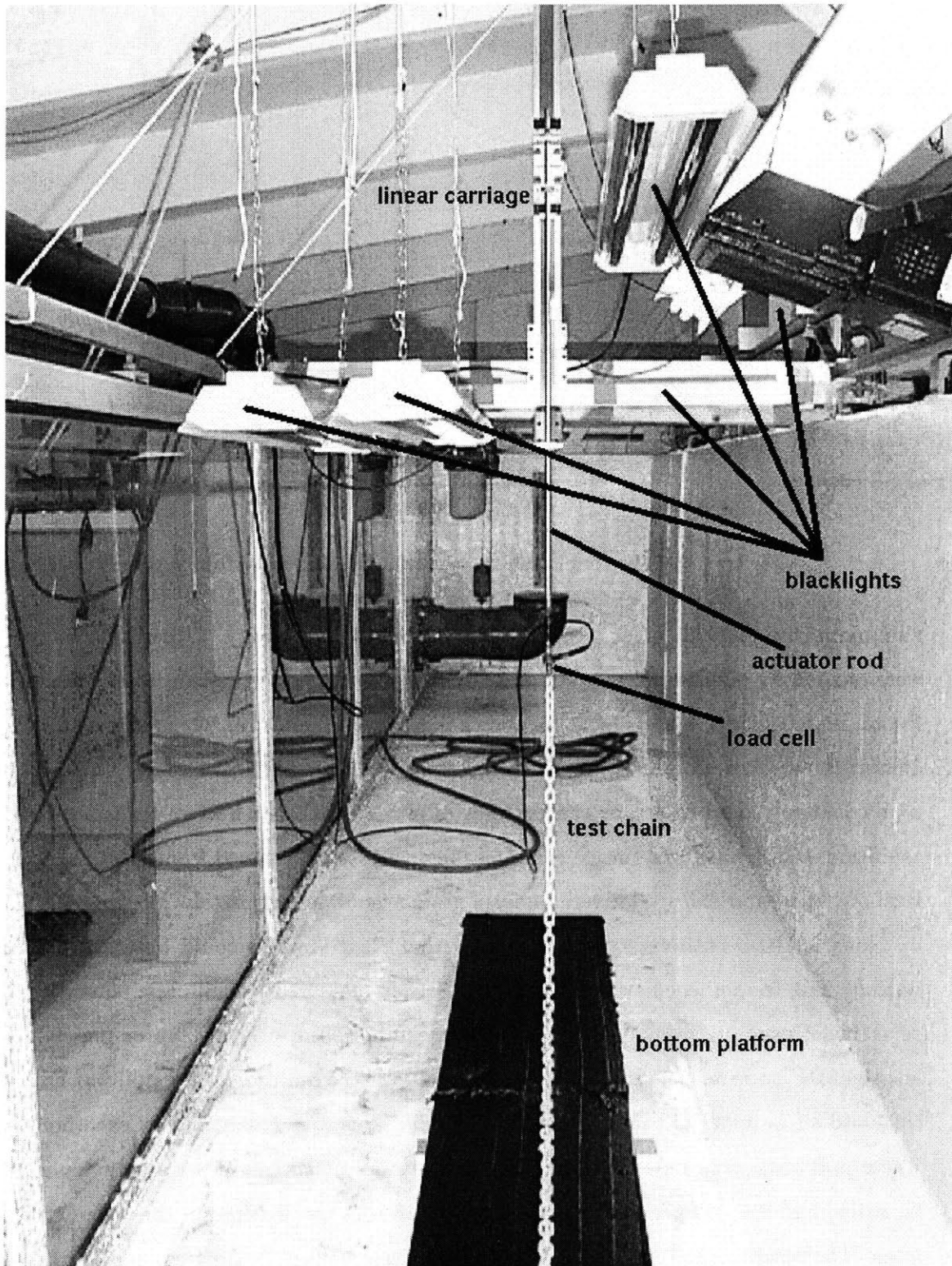
Figure 7-2: View of the actuator shaft, load cell, test specimen, and lighting arrangement looking down the flume from the anchor towards the top of the chain.
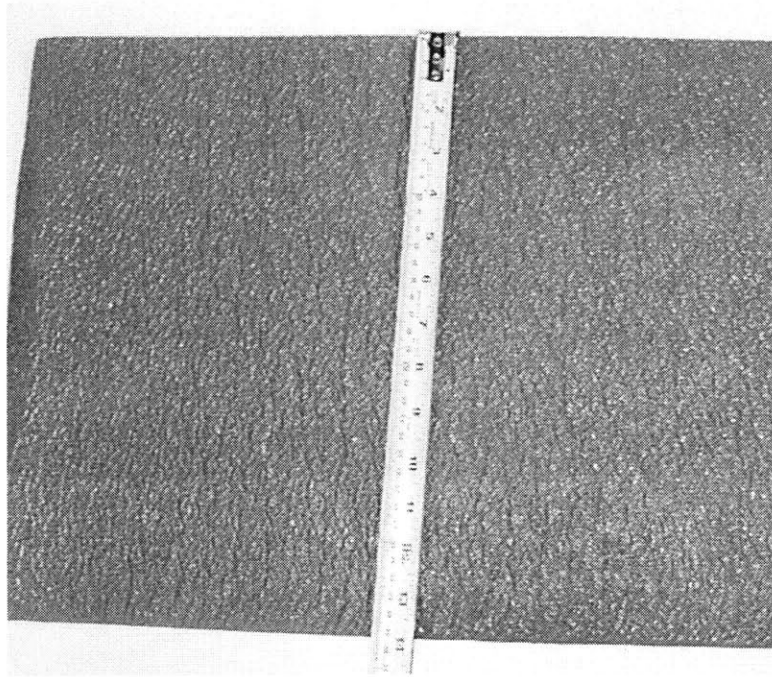
Figure 7-3: The foam anti-fatigue mat used as a bottom type.

aluminum covered with black electrical tape to reduce reflectivity. Other bottom types were created by placing either a stippled foam or artificial grass mat on top of the tape. Photographs of these two surfaces are shown in figures 7-3 and 7-4. The foam material is an anti-fatigue standing mat. The artificial grass mat is a green plastic door mat of the type commonly used to scrape the bottoms of shoes clean. For a more realistic bottom condition, the channel was turned over and filled with sand obtained from West Falmouth Harbor. This sand has a relatively uniform grain size of approximately 290 μm [30].

None of these bottoms were soft enough that their stiffness could be easily characterized. The friction coefficient of each bottom was measured by pulling a 90 cm length of chain horizontally by hand, at a roughly constant speed, over an approximately 1 m length of the bottom. The average of the tension over the duration of the pull was used to calculate an estimate of the drag coefficient. Four runs were conducted on each bottom. These pull tests were conducted in air; the results are not necessarily directly applicable in water, but they do provide a relative comparison of the friction on the different bottoms. The results of the four runs, and their average, for each bottom are summarized in table 7.1. The hard bottom has approximately one-third less friction than the two mat bottoms, which appear to have very similar friction properties within the context of this
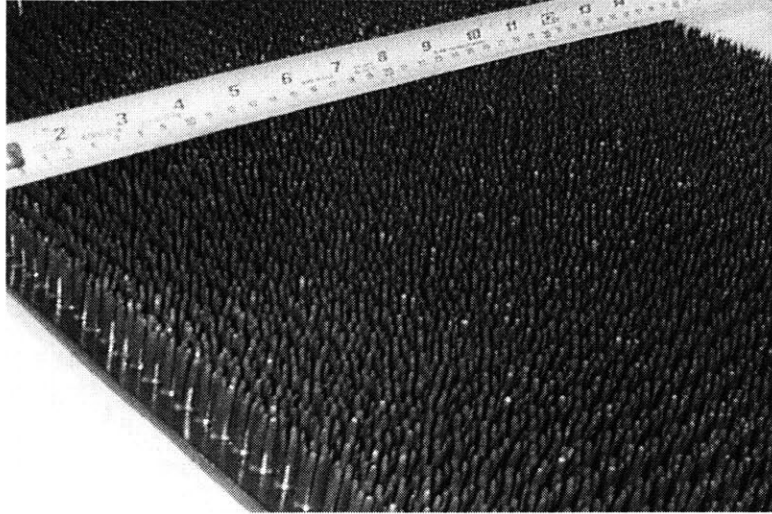
Figure 7-4: The artificial grass door mat used as a bottom type.

bottom	Run 1	Run 2	Run 3	Run 4	Average
hard	0.49	0.40	0.45	0.51	0.46
foam	0.55	0.78	0.75	0.74	0.71
grass	0.61	0.80	0.69	0.75	0.71
sand	1.25	1.20	1.39	1.01	1.21

Table 7.1: Friction coefficients, in air, of the various bottom types.

test. The sand has a high coefficient in this test partly because the chain tends to become partially buried over its length as each pull progresses.

7.1.2 Actuator mechanism

The actuator is a Parker Hauser HLE-60 with approximately 60 cm of usable throw. The actuator is driven through a 4:1 planetary gear box by a Parker Compumotor SM233 brushless servo motor. The motor is driven by a Parker Compumotor APEX 10 servo drive. The test specimen is attached to the actuator carriage via a hardened steel shaft that runs through a guide plate at the end of the linear stage. The system is controlled by a PC equipped with a Delta Tau PMAC-Lite servo controller card. The PC runs a custom designed program which generates the motion profiles, simulating either regular or random waves, and downloads them onto the controller card. Once the motion profile is started, the process is entirely under the control of the PMAC card which employs a

hardware based PID algorithm to command the drive/motor/actuator system. Feedback is provided by a 4000 line optical encoder on the motor. Home and limit switches on the actuator allow for repeatability to within approximately one millimeter from one run to the next.

7.1.3 Video instrumentation

One of the significant advantages of working in the laboratory versus working in the field is the opportunity to gather data along the whole mooring. The AxPacks on the field mooring provide valuable data, but it is impractical to use many more than the three that were employed. Also, they only provide relative motion. By using a video system we are able to capture the absolute motion of the entire system in a relatively compact and easy to interpret data set.

The video instrumentation system consists of a Pulnix TM-9701 camera and a MuTech MV-1500 frame grabber in a 200 MHz Pentium PC equipped with 192 MB of RAM. The camera is a progressive scan monochrome CCD camera with electronic shuttering and digital 8-bit output via RS-422. It has a resolution of 484 lines and 768 pixels. The camera and frame grabber are controlled by a custom written acquisition program that runs on the PC. With a relatively simplistic interrupt driven capture algorithm the maximum frame rate for full size frames is approximately 15 Hz. With half size frames, which are more convenient for processing and storage reasons, the frame rate can be 30 Hz. The frame grabber is triggered by a pulse that comes from the servo control computer.

The post-processing of the imagery is simplified by the use of blacklight and fluorescent paint. The mooring chain is painted white and coated with ultraviolet lacquer that fluoresces well under black light. During an experimental run all standard lighting is turned off and the windows are blacked out. Illumination is provided by six 40 watt blacklight fluorescent tubes hanging immediately above the free surface, parallel to the plan view of the chain, two 40 watt blacklight fluorescent tubes positioned across the width of the tank just above the top of the chain, and a 400 watt theatrical blacklight flood positioned behind and above the chain.

7.1.4 Force instrumentation

In addition to the video instrumentation, the model system is instrumented with a small waterproof load cell between the actuator arm and the top of the chain. The load cell is a Sensotech Model 34 miniature underwater load cell with a 4 - 20 mA output over the zero to five pound range of the cell. The current output is dropped across a 500Ω termination resistor to produce a 2 - 10V output signal. This output signal is fed through an analog six pole Tschebyscheff anti-aliasing filter with a 20 Hz corner frequency before being digitized (100 Hz, 16-bits) and stored. The data capture routine runs on the servo control computer as a background process while the motion profile is executing.

The load cell is attached to the test specimen and the actuator rod using loops of 26 AWG wire. The top and bottom studs on the load cell have small holes drilled through them to accommodate this wiring. The bottom of the actuator shaft also has such a hole. A photograph of this arrangement is shown in figure 7-5. The idea behind this attachment scheme is to measure the inline tension at the top of the chain. A rigid, vertical connection of the load cell to the bottom of the shaft would provide a measurement of the vertical component of tension only.

7.2 Video processing algorithm

During each experimental run 384 × 242 pixel, 8-bit grayscale video images are captured to RAM at 30 Hz. Each image is electronically shuttered at $1/60^{\text{th}}$ of a second. At the end of each run, every second frame is written to a compressed disk file, yielding a final sample rate of 15 Hz. An example of a single raw image is shown in figure 7-6. Because of the fast shuttering the contrast of the image is relatively low. For presentation purposes, the image in figure 7-6 was brightened and sharpened using image processing software.

The raw images are then convolved with a 3 × 3 vertical gradient filter defined as

$$\begin{bmatrix} 1 & 2 & 1 \\ 0 & 0 & 0 \\ -1 & -2 & -1 \end{bmatrix} \tag{7.1}$$

Edges are extracted from the gradient images using a simple threshold. The edge image corresponding to the raw image in figure 7-6 is shown in figure 7-7. At any given horizontal

179
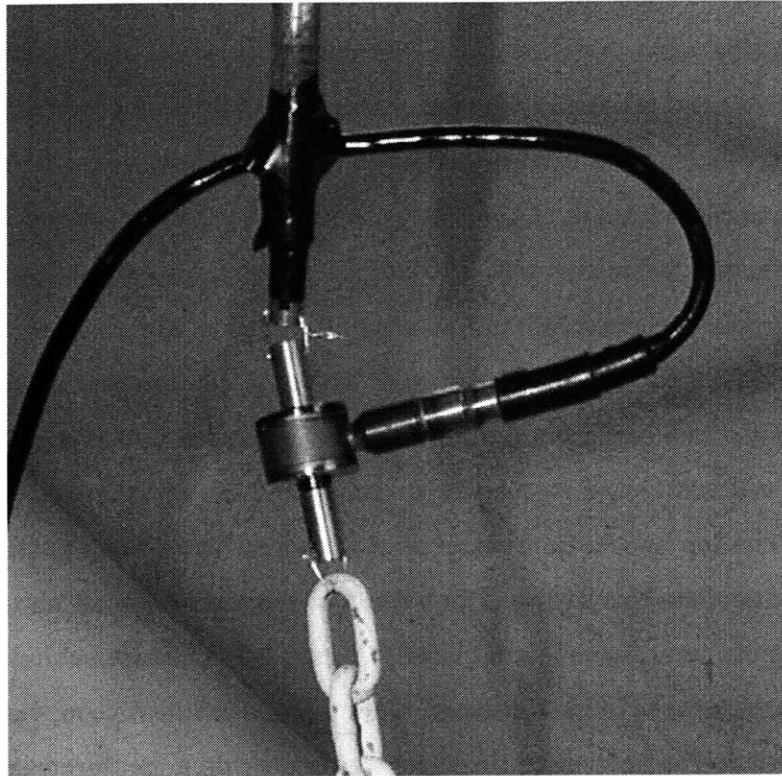
Figure 7-5: View of the actuator shaft, load cell, test specimen, and bottom platform through the glass wall of the flume.
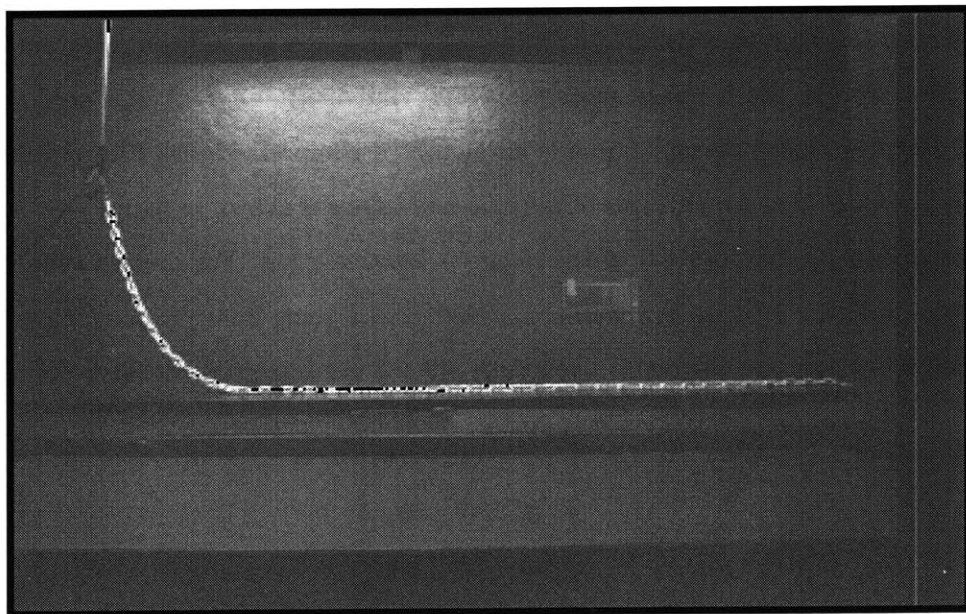
Figure 7-6: Example of a raw image from the video capture system.
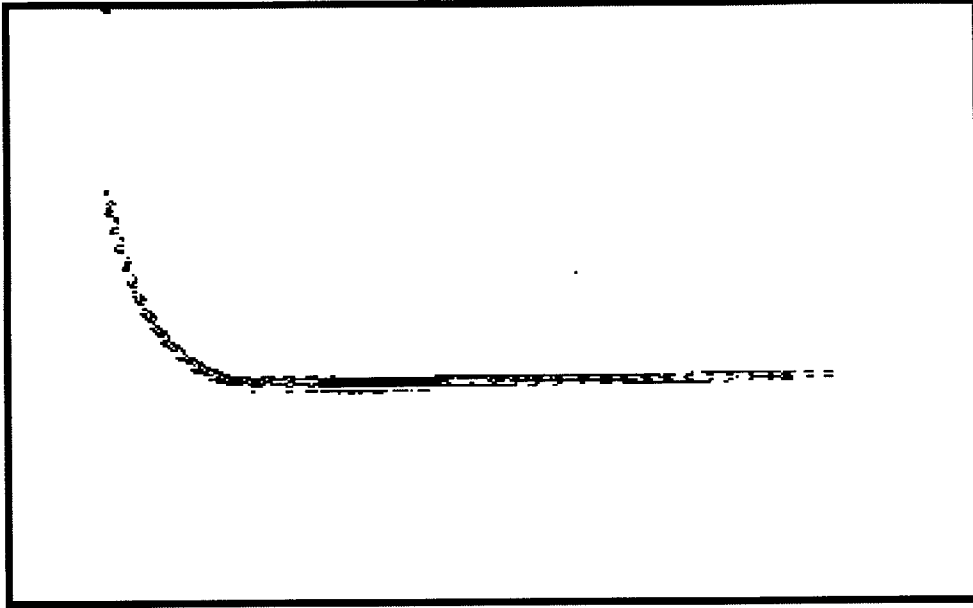
Figure 7-7: Edges extracted from the raw image in figure 7-6.

position, the vertical centerline of the chain at that position is calculated as the median location of all points along a vertical line. This procedure reduces the edge image to an image with no more than one pixel illuminated per horizontal coordinate. These pixels are turned into a line through a simple connection of adjacent points. The result of this final processing stage on the example image is shown in figure 7-8.

7.3 Mooring dynamics in the touchdown region

The initial series of experiments were all conducted on the basic hard bottom described in section 7.1.1. Each experimental run lasted twenty seconds, with a two second linear ramp of the excitation amplitude at the beginning and end. Excitation amplitudes were 0.1, 0.15, 0.2, or 0.25 m. Excitation periods were 1.25, 1.5, 2.0, and 3.0 seconds. These 16 excitation conditions were run at non-dimensional mean tensions, $\Delta\tau$, of approximately 0.16, 0.37, and 0.80. $\Delta\tau$ is defined by equation 6.6,

For reasons of brevity, only results for 0.25 m excitation amplitude and the highest and lowest mean tensions are presented. All of the different qualitative dynamic features are evident in this subset of the results. Time series of tension for the highest $\Delta\tau$ and lowest $\Delta\tau$ values are shown in figures 7-9 and 7-10, respectively, for excitation periods 3.0, 2.0, and 1.25 seconds. In both cases there is a marked difference in the tension response
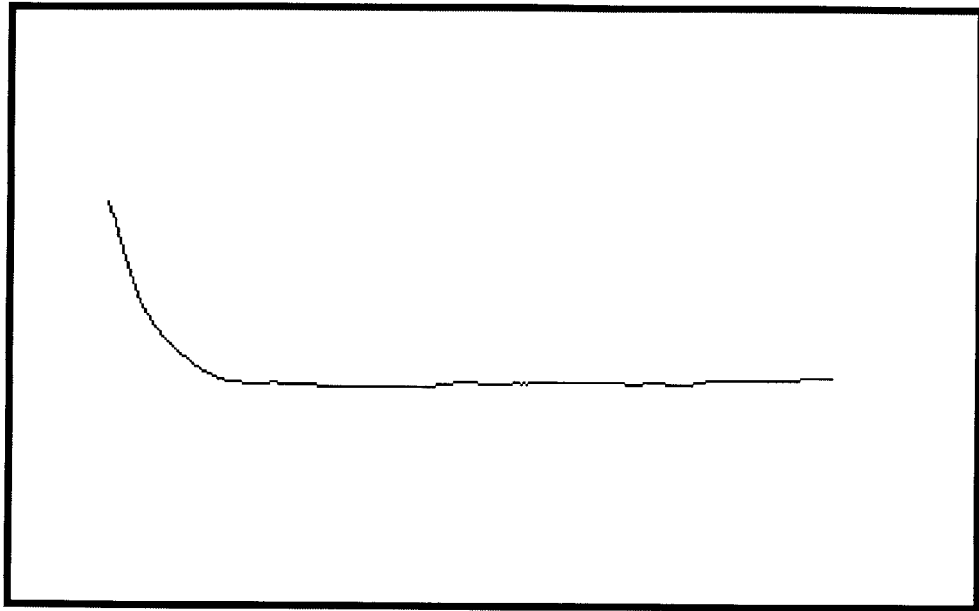
Figure 7-8: Line representing the center of the model chain extracted from the edge image in figure 7-7.
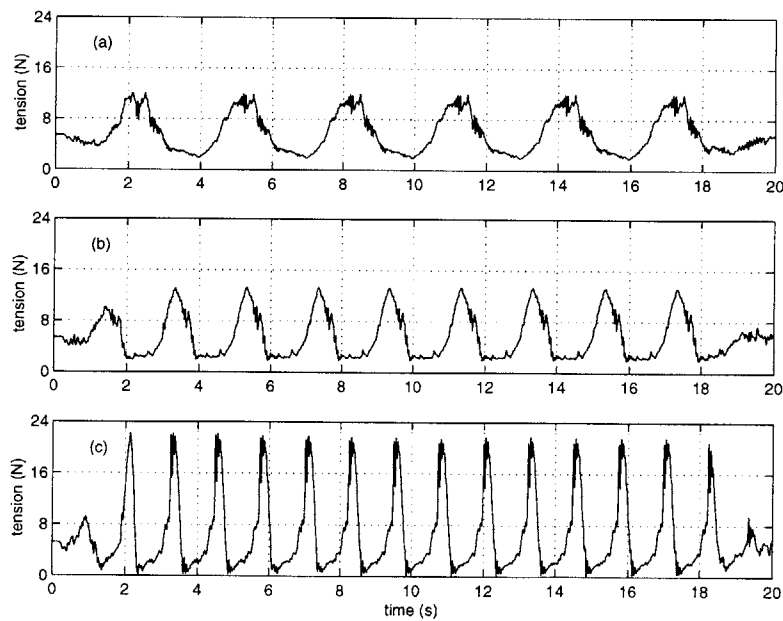
Figure 7-9: Tension time series for the hard bottom at $\Delta\tau \approx 0.80$ for excitation amplitude 0.25 m and excitation periods (a) 3.0 s, (b) 2.0 s, and (c) 1.25 s.
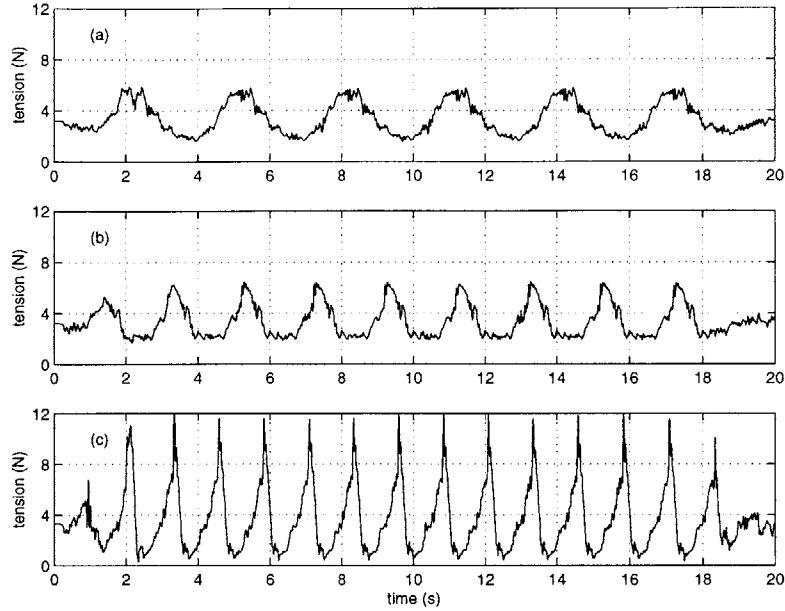
Figure 7-10: Tension time series for the hard bottom at $\Delta \tau \approx 0.16$ for excitation amplitude 0.25 m and excitation periods (a) 3.0 s, (b) 2.0 s, and (c) 1.25 s.

between the slowest and fastest excitation levels. For the 3 second excitation cases, the response is roughly sinusoidal, matching the regular input motion. As the excitation period decreases, however, the tension response becomes more and more asymmetrical.

To more fully understand what is happening in the high frequency excitation cases it is instructive to consider the motion and tension of the chain over a single cycle. Figure 7-11 shows the positions of the chain extracted from the video and the corresponding tension record for a single cycle of motion starting at 13 seconds for $\Delta \tau \approx 0.80$. The top left panel shows the chain positions while the motion of the top of the chain is upwards (vertical velocity greater than zero) with the starting position drawn in bold. The top right panel shows the chain positions during the downward motion, with the first downward position drawn in bold. In the tension plot, time points marked with circles correspond to the timing of the upward moving position snapshots; squares correspond to downward moving snapshots. Starting from the lowest point in the motion, the tension very gradually increases until approximately 13.2 seconds at which point it increases very rapidly. The tension remains relatively high for approximately 0.15 seconds before falling gradually until 13.6 seconds. After that point the tension increases very slowly for the remaining 0.6 seconds (nearly half) of the cycle.

At the beginning of the cycle the input velocity is zero and the chain top is at its

183
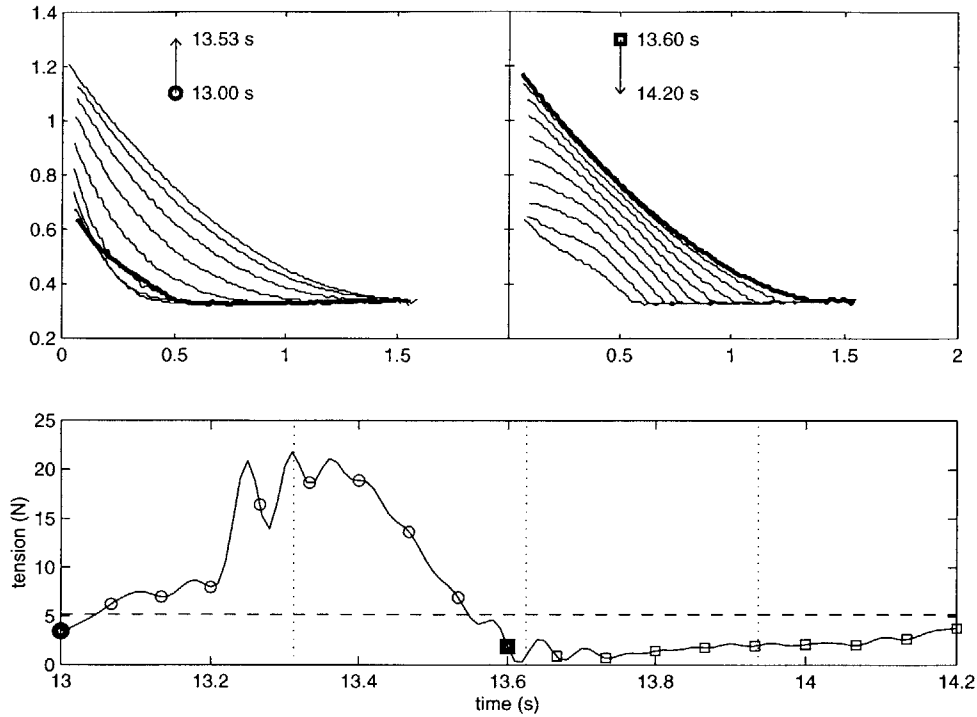
Figure 7-11: Chain response on the hard bottom over one cycle at 1.25 s excitation period, 0.25 m excitation amplitude, and $\Delta\tau \approx 0.80$ The bold line in each of the top panels marks the first profile of that panel. The arrow indicates the direction of motion of the top of the chain. In the tension plot, circles correspond to the time points of the upward moving profiles, squares to downward moving profiles. The dashed line is the static tension level. Dotted vertical lines mark the $T_p/4$, $T_p/2$, and $3T_p/4$ points.

lowest point. As the chain moves upwards, drag increases as velocity increases. The large jump in tension just after 13.2 seconds is due not to drag, however, but to a snap load that occurs when the slack, grounded chain suddenly retensions. This phenomenon can be seen clearly in close-up video of the touchdown region in figure 7-12. This imagery was actually taken for a slightly different case (artificial grass bottom which was held in place by a light coating of sand), but the features and timing are nearly the same as in the hard bottom case. As the chain moves downward in the moments preceding the cycle under consideration, the chain that is being grounded is slack. By the 13.14 second image the input motion has started moving upwards again and it is clear that the slack in the grounded chain is beginning to be pulled out. When it is fully pulled out, the tension spike occurs. Drag keeps the tension relatively high for a time because the bulk of the chain is moving very fast, as evidenced by the large separation between profiles in the upward moving panel in figure 7-11. As the chain slows in its upward motion, drag decreases and

184

t = 12.74   t = 12.87

t = 13.00   t = 13.14

t = 13.28   t = 13.41
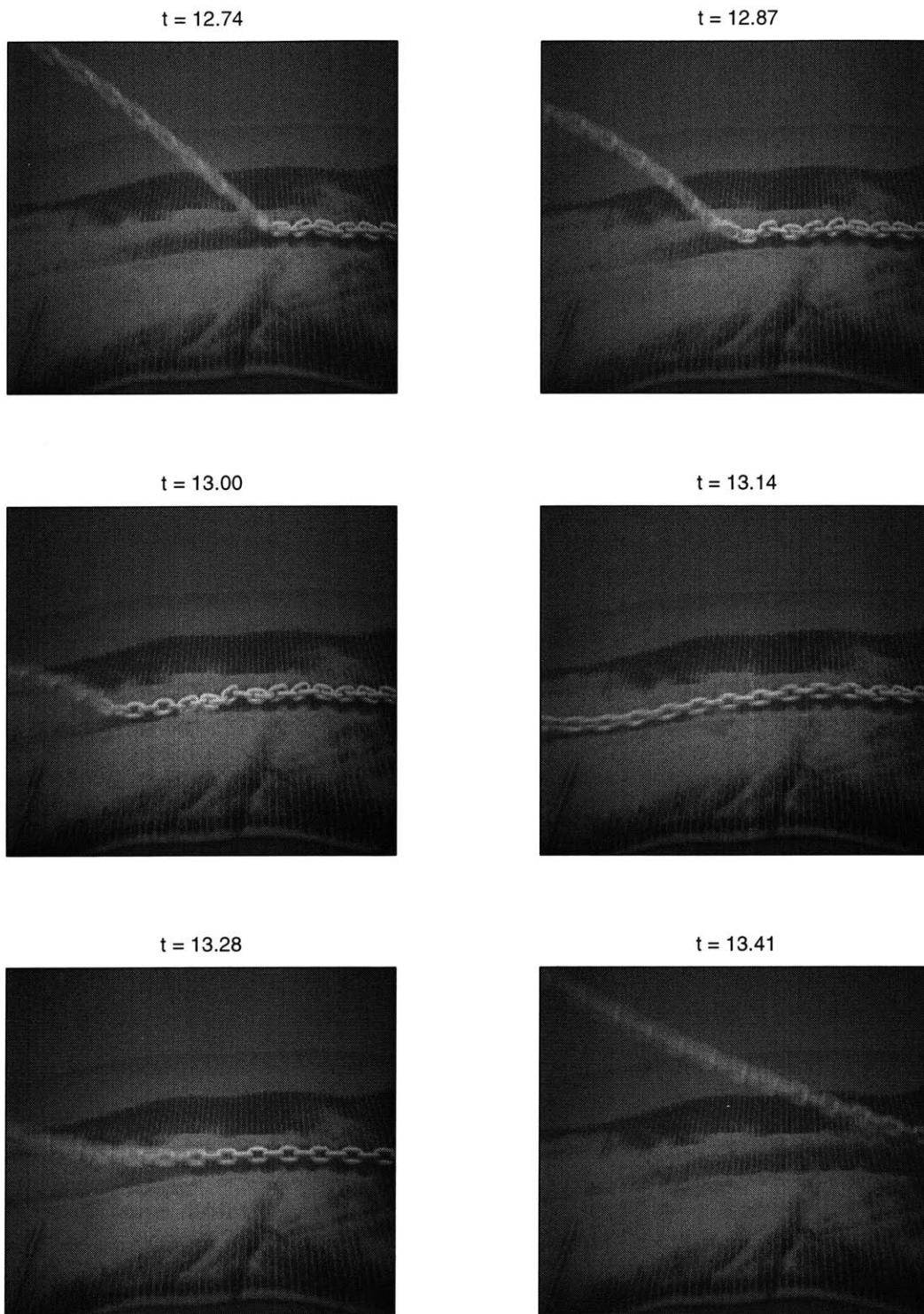
Figure 7-12: Closeup view of the touchdown region showing a sequence in which the chain is laid down with slack and then pulled taut. For practical reasons, the bottom in this case was the artificial grass mat with a light coating of sand to hold it in place. As will be shown in section 7.4, the results for this bottom are nearly identical to those on the hard bottom.

tension decreases.

At the transition from upwards to downwards motion near 13.6 seconds, the velocity is zero and the displacement and acceleration have maximum magnitude with opposite signs. Given an acceleration of nearly two-thirds the acceleration due to gravity, the inertial effect greatly reduces the increased tension attributable to the weight of the additional line that is pulled off the bottom. Thus, with little drag, the tension at this mid-point in the cycle is very low. The tension remains low after this point because at this point the chain that is being grounded is laid down slack. With no tension at the bottom of the chain, the curvature near the top of the chain reverses as the downward motion progresses. With the chain top more horizontal and the mid-section of the chain moving relatively slowly (as evidenced by the close spacing of profiles in the downward profiles of figure 7-11) due to this curvature reversal, there is little dynamic contribution to the tension during this part of the cycle.

Both tension discontinuities, the spike just after 13.2 seconds, and the slack at the touchdown point starting at 13.6 seconds, are the result of a shock in the tension. Using an analytical result for the interaction of string and bridge in a sitar by Burridge et $al.$ [12], Triantayllou et $al.$ [94] predicted that for the cable bottom interaction problem, shocks will occur when the velocity of the TDP exceeds the speed of transverse waves in the cable. Essentially, the transverse wave speed governs the ability of the mooring line to comply geometrically with a smooth rolling and unrolling motion. When the touchdown point moves faster than this speed during loading (upward motion) snap loads occur. A shock during unloading (downward motion) produces a slack condition at the touchdown point. Both of these conditions can be seen quantitatively in the experimental results.
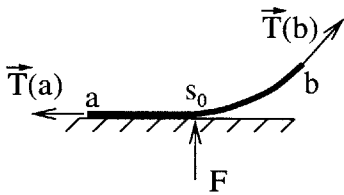
Figure 7-13: Definitions for the derivation of the shock criterion.

Following a result from Burridge and Keller [11], this shock criterion can be derived by considering the integral form of the momentum equation for the situation diagrammed in figure 7-13,

$$\frac{\partial}{\partial t} \int_a^b m \frac{\partial \vec{x}}{\partial t} ds = \vec{T}(b, t) - \vec{T}(a, t) + \vec{F} + \int_a^b \vec{f}(s) ds.$$

(7.2)

The limits a and b define a small region that contains

186

the instantaneous TDP which is located at $s = s_0(t)$. $\vec{T}$ is the line tension, $\vec{x}(s,t) = [x(s,t), z(s,t)]^{\mathrm{T}}$ describes the position of a point on the line, $\vec{f}$ is the force density due to weight and buoyancy, and $\vec{F}$ is a reaction force exerted on the line by the bottom at the TDP. Using Leibnitz's rule [43] the integral on the left side of equation 7.2 can be evaluated as

$$\frac{\partial}{\partial t} \int_a^b m \frac{\partial \vec{x}}{\partial t} ds = \frac{\partial}{\partial t} \int_a^{s_0^-(t)} m \frac{\partial \vec{x}}{\partial t} ds + \frac{\partial}{\partial t} \int_{s_0^+(t)}^b m \frac{\partial \vec{x}}{\partial t} ds$$

$$= \int_a^b \frac{\partial}{\partial t} \left[m \frac{\partial \vec{x}}{\partial t} \right] ds + m \frac{ds_0}{dt} \left[\frac{\partial}{\partial t} \vec{x} \left(s_0^-, t \right) - \frac{\partial}{\partial t} \vec{x} \left(s_0^+, t \right) \right]. \qquad (7.3)$$

Assuming that the line comes instantaneously to rest after being grounded, the velocity of the line immediately to the left of the TDP is zero and

$$\frac{\partial}{\partial t} \vec{x} \left(s_0^-, t \right) = 0. \qquad (7.4)$$

Furthermore, letting a and b approach s_0 from below and above, integral terms go to zero and equation 7.2 becomes

$$-m \frac{ds_0}{dt} \frac{\partial}{\partial t} \vec{x} \left(s_0, t \right) = \vec{T} \left(s_0^+ \right) - \vec{T} \left(s_0^- \right) + \vec{F}. \qquad (7.5)$$

Finally, noting that there is no vertical component of tension to the left of the TDP, and that for small vertical displacements

$$x \approx s, \qquad (7.6)$$

$$\cos \phi = \frac{\partial z}{\partial s}, \qquad (7.7)$$

the force balance in the vertical direction is

$$-m \frac{dx_0}{dt} \frac{\partial}{\partial t} z \left(x_0, t \right) = T_0 \frac{\partial}{\partial x} z \left(x_0, t \right) + F. \qquad (7.8)$$

Because $z(x_0(t), t)$ is zero for all t, the total derivative of z at the TDP must also be zero,

$$\frac{\partial}{\partial t} z \left(x_0, t \right) + \frac{dx_0}{dt} \frac{\partial}{\partial x} z \left(x_0, t \right) = 0. \qquad (7.9)$$

Substituting this geometric constraint into equation 7.8 yields

$$\left[m \left(\frac{dx_0}{dt} \right)^2 - T_0 \right] \frac{\partial}{\partial x} z \left(x_0, t \right) = F. \tag{7.10}$$

From geometric considerations and the assumption that F is an upwards directed reaction force, all of the terms in this equation are positive or zero. This leads to two possible scenarios:

$$m \left(\frac{dx_0}{dt} \right)^2 \geq T_0 \quad \Longrightarrow \quad \frac{\partial}{\partial x} z \left(x_0, t \right) \geq 0, \quad F \geq 0, \tag{7.11}$$

$$m \left(\frac{dx_0}{dt} \right)^2 < T_0 \quad \Longrightarrow \quad \frac{\partial}{\partial x} z \left(x_0, t \right) = 0, \quad F = 0. \tag{7.12}$$

In the second scenario, the line leaves the bottom tangentially and there is no impact force. The first scenario is the case in which a tension discontinuity forms. The condition for this case can be re-written as

$$\left| \frac{dx_0}{dt} \right| \geq \sqrt{\frac{T_0}{m}}. \tag{7.13}$$

The quantity on the right in equation 7.13 is the transverse wave speed in the line. When this condition is true, there is an impact from the bottom and the line does not leave the ground tangentially. This impact force and the loss of tangency introduce the tension discontinuity that is the most obvious consequence of the shock. It is important to note that while the impact force in this derivation is not itself evident in the topside tension record, it does have direct implications for the numerical simulations, as discussed in section 7.5.

Both the transverse wave speed and the TDP speed can be calculated for the experimental results. For the wave speed, T_0 can be estimated by the horizontal component of the top tension. The TDP speed is calculated by numerically differentiating the horizontal TDP coordinates, x_0, extracted from consecutive chain profiles. Figure 7-14 shows these two results for the same high frequency, high $\Delta \tau$ case as in figure 7-11. The exceedance of the shock criterion, equation 7.13, is clear at both the 13.2 and 13.6 second time points.

The utility of this criterion in predicting these tension discontinuities is further supported by the data from the the 2.0 and 3.0 second excitation period cases. In figure 7-15

188
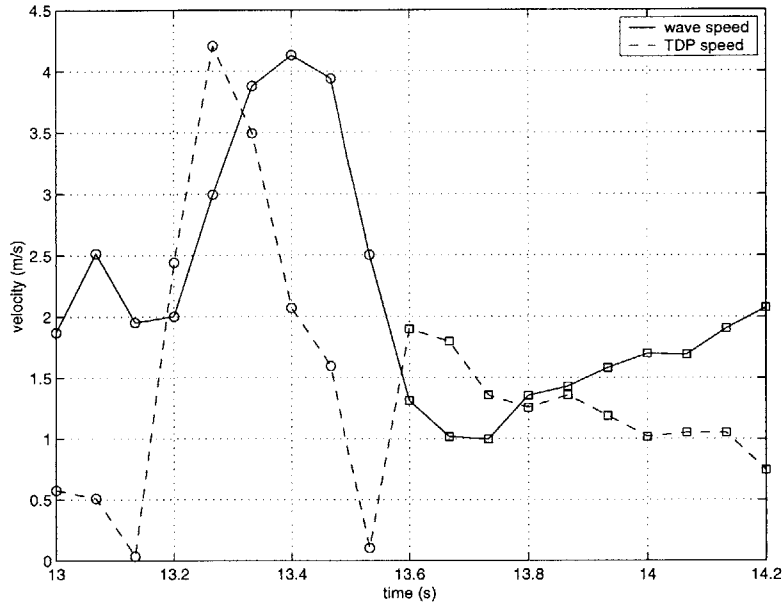
Figure 7-14: Transverse wave (solid line) and TDP (dashed line) speed over one cycle at 1.25 s excitation period, 0.25 m excitation amplitude, and $\Delta\tau \approx 0.80$. Circles and squares indicate upwards and downwards input motion as in figure 7-11.

for $T_p = 2.0$ s there is no snap load during the upwards motion but the tension does exhibit the slacking response during a portion of the unloading half of the cycle. Correspondingly, in figure 7-16 the TDP speed exceeds the estimated wave speed during unloading, but not during loading. Note that with slack in the grounded chain, the horizontal component of the top tension overestimates T_0 and the TDP speed likely exceeds the wave speed for some length of time beyond the brief exceedance shown in figure 7-16. This estimate is valid up to the point of the criterion being met, making it useful for the predictive purpose shown here, but is not accurate once the tension discontinuity has formed. The response in this case also differs from the $T_p = 1.25$ s case because the lower frequency excitation leads to a basic tension response that is not simply drag dominated, with weight and inertia effects largely canceling one another.

For 3.0 s period excitation, neither snapping nor slacking behavior is evident in figure 7-17. This is expected as the TDP speed in figure 7-18 never exceeds the transverse wave speed. At this lowest frequency the tension response is dominated by geometric stiffness. The phase of the tension in figure 7-17 very nearly matches the phase of the displacement of the chain top.

The results for 1.25 s excitation period and $\Delta\tau \approx 0.16$ (the lowest non-dimensional

189
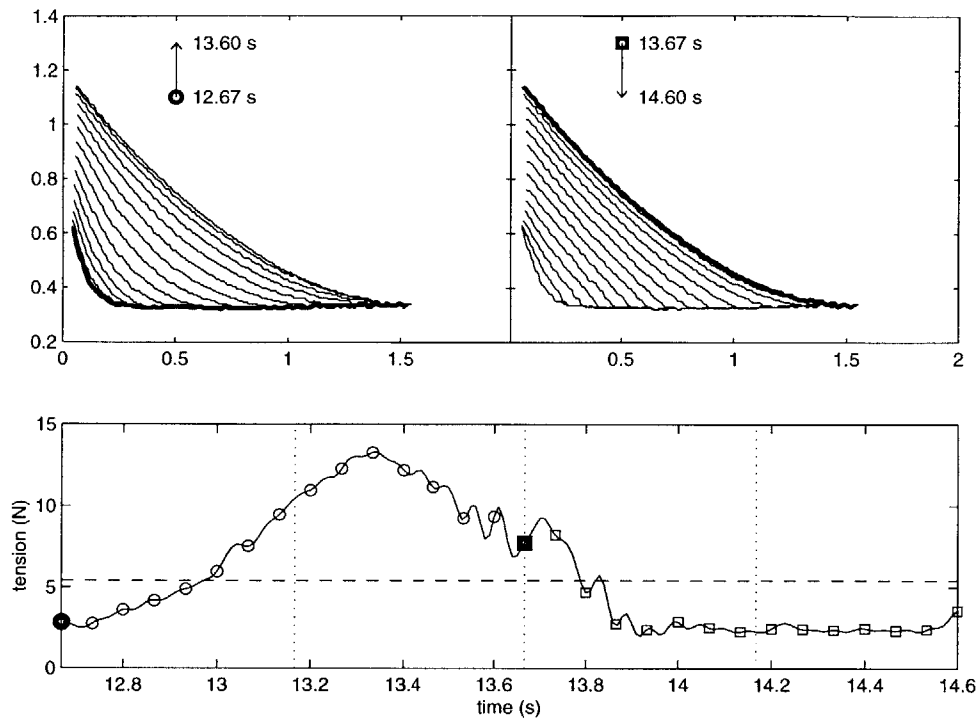
Figure 7-15: Chain response on the hard bottom over one cycle at 2.0 s excitation period, 0.25 m excitation amplitude, and $\Delta\tau \approx 0.80$.
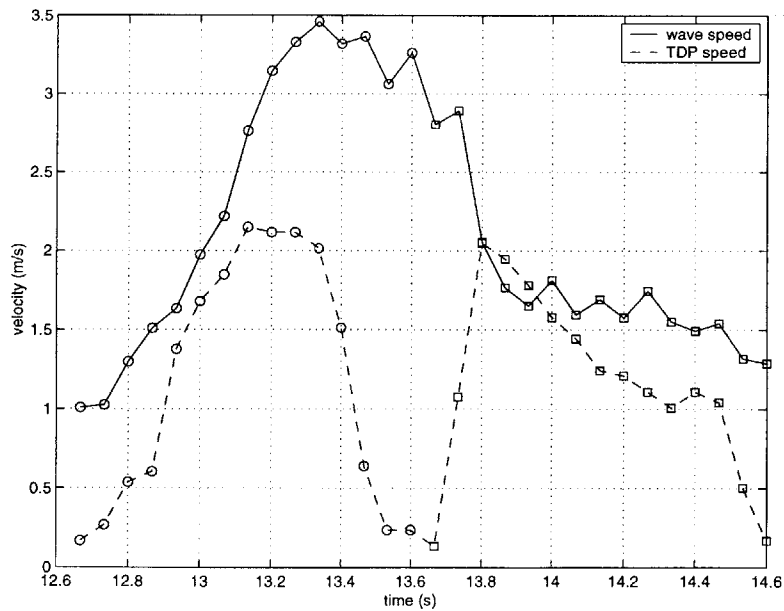
Figure 7-16: Transverse wave and TDP speed over one cycle at 2.0 s excitation period, 0.25 m excitation amplitude, and $\Delta\tau \approx 0.80$.
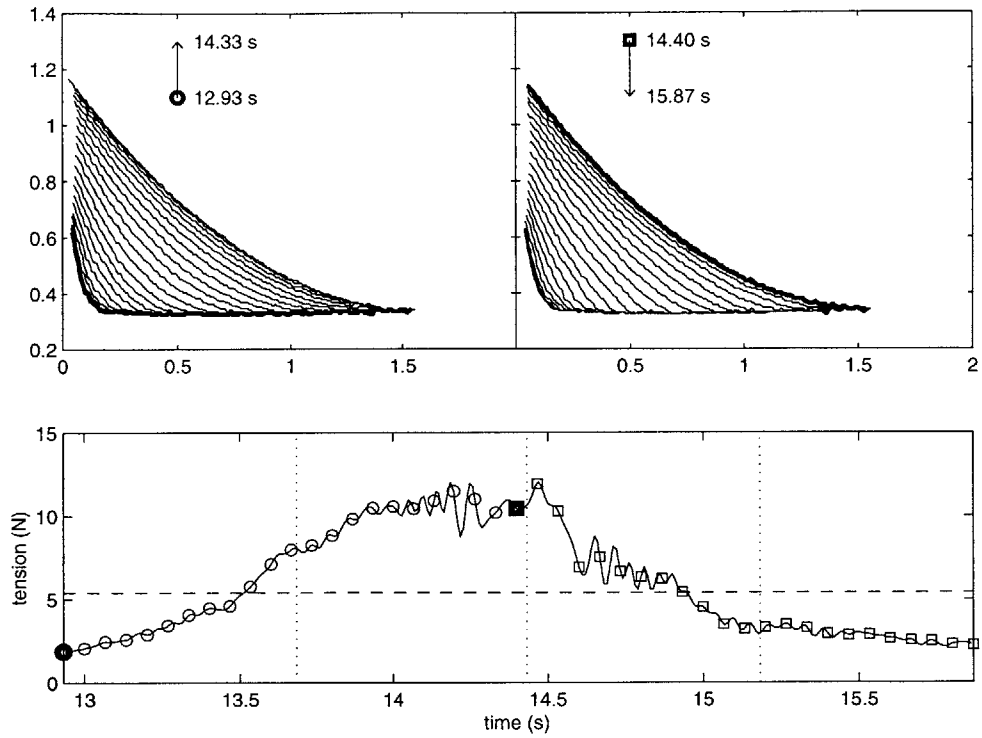
Figure 7-17: Chain response on the hard bottom over one cycle at 3.0 s excitation period, 0.25 m excitation amplitude, and $\Delta\tau \approx 0.80$.
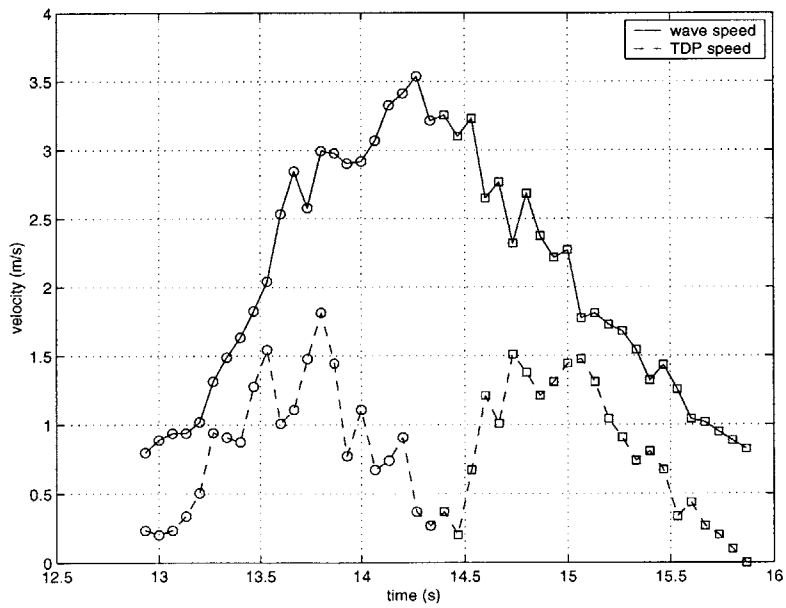
Figure 7-18: Transverse wave and TDP speed over one cycle at 3.0 s excitation period, 0.25 m excitation amplitude, and $\Delta\tau \approx 0.80$.
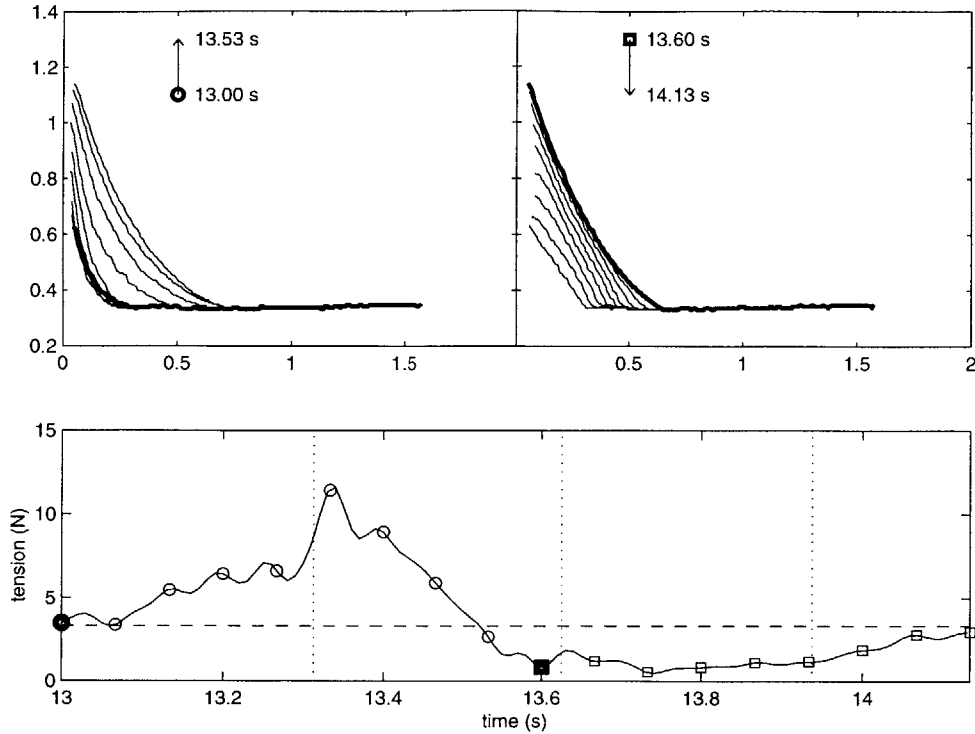
Figure 7-19: Chain response on the hard bottom over one cycle at 1.25 s excitation period, 0.25 m excitation amplitude, and $\Delta \tau \approx 0.16$.

mean tension) are shown in figures 7-19 and 7-20. Qualitatively, the response in figure 7-19 is similar to that for the $\Delta \tau \approx 0.80$ case in figure 7-11. The onset of the snap load is delayed relative to that case because the higher initial curvature of the low tension configuration at its lowest point results in the TDP speed reaching its maximum more slowly. The slack discontinuity occurs at the same time in the two cases because that shock is more dependent on a low wave speed than on a high TDP speed and the phase of the wave speed is similar in the two cases.

7.4   Effect of bottom conditions on mooring response

7.4.1   Artificial bottoms

In addition to the hard bottom tests described above, tests were run on the artificial bottom types described in section 7.1.1. The artificial mats have higher friction than the hard bottom and some unquantified differences in their stiffness properties. Based on the results, however, these properties are only weakly relevant (a conclusion supported
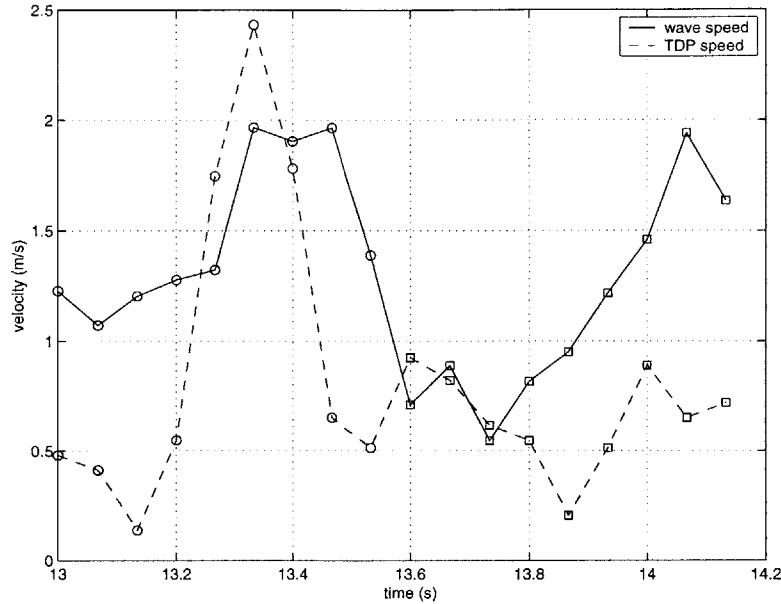
Figure 7-20: Transverse wave and TDP speed over one cycle at 1.25 s excitation period, 0.25 m excitation amplitude, and $\Delta\tau \approx 0.16$.

by the full scale experimental and simulation results in chapter 6) or the differences were not significant enough to produce a marked change in the response. Figures 7-21 and 7-22 show the tension time series for the runs on foam and artificial grass bottoms at $\Delta\tau \approx 0.80$ with excitation period 1.25 seconds and excitation amplitude 25 cm. There are no significant differences between these results and those shown in figure 7-9 for the hard bottom case. The mean values are slightly different due to the added height of the bottom mats and the accompanying small variations in the shape of the chain.

7.4.2 Sand bottom

A more interesting response was observed in the runs on the sand bottom. Like the artificial bottoms, the tension records for these runs do not look markedly different from those obtained on the hard bottom. The interesting feature of the response on sand is the trenching and digging action of the cycling chain. Because of this action, the chain was often below the plane of the bottom and thus was not visible to the camera. For this reason, the standard high speed video and associated processing were not used for runs on sand. Instead, the camera was repositioned to look down at an angle on the touchdown region (this is the position from which the closeup video in figure 7-12 was taken). To document the trenching behavior, time lapse video was then taken every ten seconds over

193
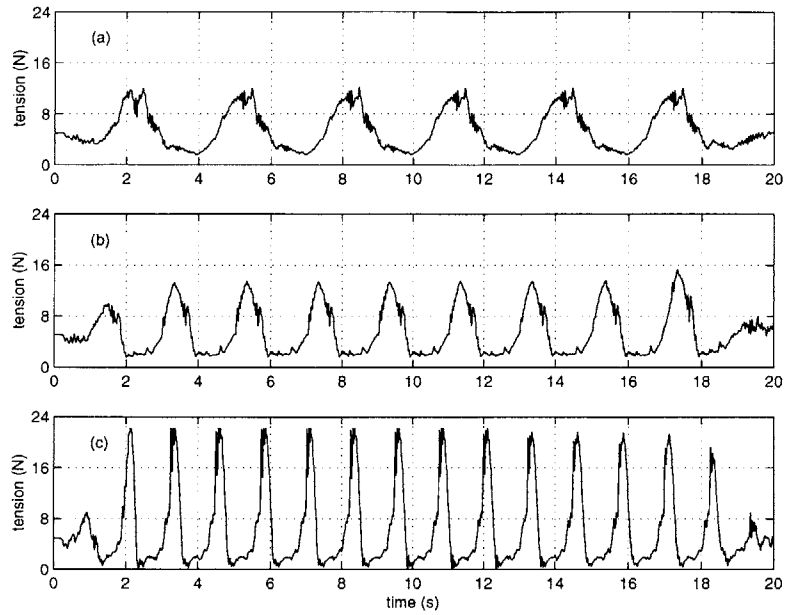
Figure 7-21: Tension time series for the foam bottom at $\Delta\tau \approx 0.80$ for excitation amplitude 0.25 m and excitation periods (a) 3.0 s, (b) 2.0 s, and (c) 1.25 s.
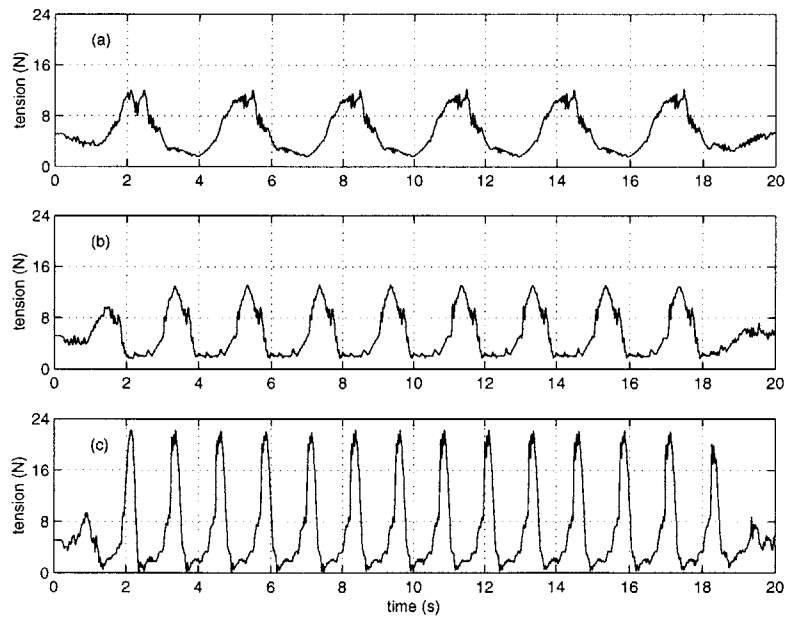
Figure 7-22: Tension time series for the grass bottom at $\Delta\tau \approx 0.80$ for excitation amplitude 0.25 m and excitation periods (a) 3.0 s, (b) 2.0 s, and (c) 1.25 s.
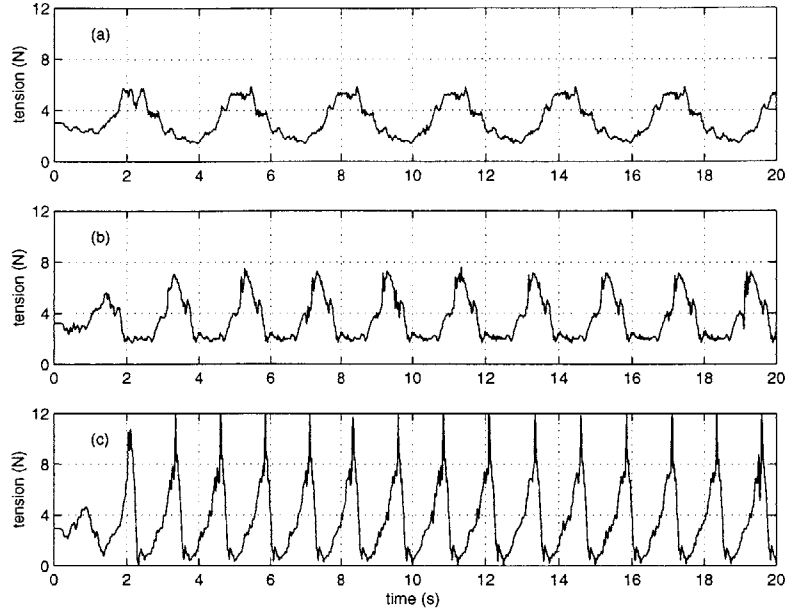
Figure 7-23: Tension time series of the initial twenty seconds for the sand bottom with $\Delta \tau \approx 0.16$, excitation amplitude 0.25 m, and excitation periods (a) 3.0 s, (b) 2.0 s, and (c) 1.25 s.

the course of two consecutive three minute runs. The sand was restored to its original, flat condition after every six minute run (between each change in excitation period or non-dimensional mean tension). Because this process was more time consuming than the runs on the artificial bottoms, only 25 cm excitation amplitude cases were performed. Tension data was captured as before at 100 Hz.

Figure 7-23 shows the first twenty seconds of the tension record for the runs on sand at $\Delta \tau \approx 0.16$. In the high $\Delta \tau$ runs, the lowering of the bottom as the trench deepened over time, and the subsequent rise in steady state tension, led to tension spikes in the 1.25 s excitation period case which were clipped in the data acquisition system (over 5 lbs). For this reason, the low $\Delta \tau$ runs are used to facilitate a direct comparison with the results already presented for the hard bottom runs in figure 7-10. As mentioned previously, these results are not significantly different than the hard bottom results.

Even after significant trenching has occurred for the 1.25 and 2.0 second excitation period cases, the tension results are not significantly different. The evolution of the trenching over the first 120 cycles for the 1.25 s case is shown in figure 7-24. The state of the bottom after 120 cycles is shown for each of the 1.25, 2.0, and 3.0 s cases in figure 7-25. Corresponding twenty second time series of tension, from the time immediately preceding the

t = 0 s	t = 30 s	t = 60 s

t = 90 s	t = 120 s	t = 150 s
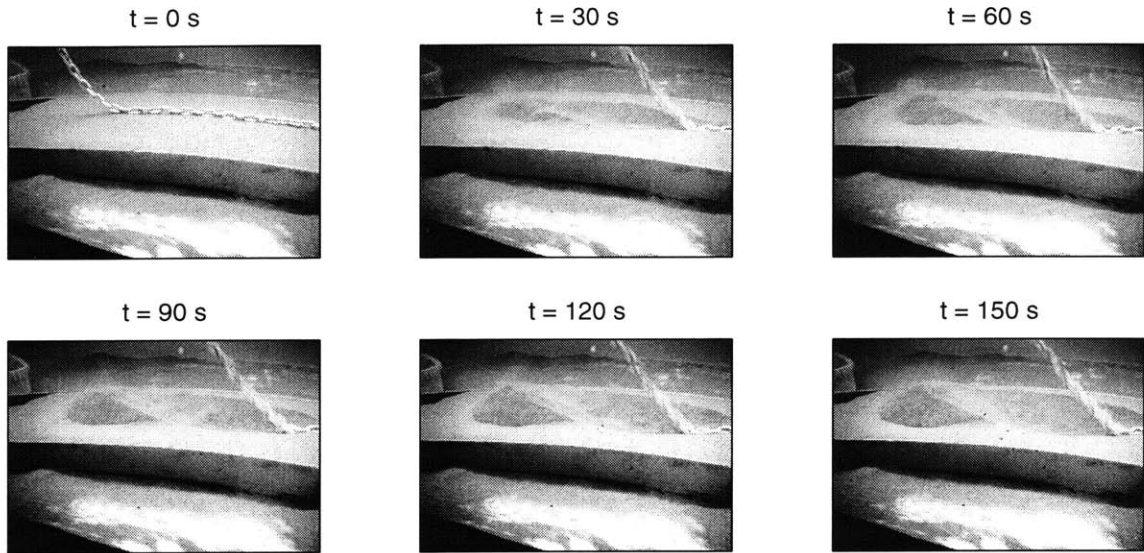
Figure 7-24: Changes in the sand bottom over the first 120 cycles of the 1.25 s excitation case at $\Delta\tau \approx 0.16$.

(a) T_p = 3.0 s, after 120 cycles   (b) T_p = 2.0 s, after 120 cycles   (c) T_p = 1.25 s, after 120 cycles
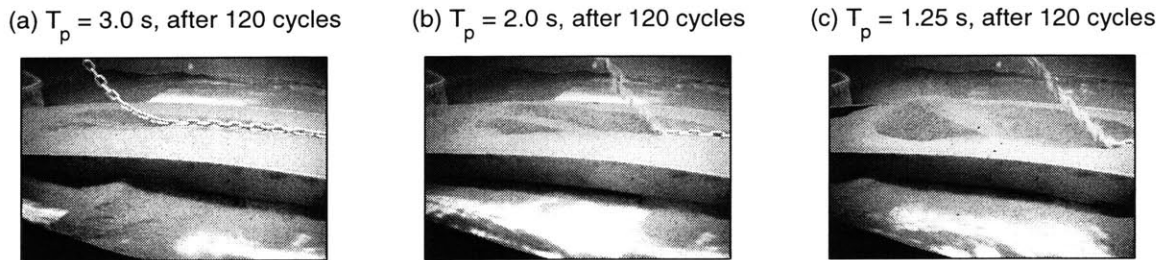
Figure 7-25: State of the sand bottom after 120 cycles for the (a) 3.0, (b) 2.0, and (c) 1.25 s excitation cases at $\Delta\tau \approx 0.16$.

120 cycle mark, are shown in figure 7-26. The presence of the trench increases the mean tension level, but it does not change the basic dynamic response.

The trenching action is a result of the slacking and re-tensioning of the chain following a shock discontinuity during the unloading phase of the motion. As the chain re-tensions, links on the ground move laterally forward (in the direction of the chain top), carrying sand with them. This relationship between the trench and the tension discontinuity explains why a trench forms for the 1.25, and 2.0 s cases, but not for the 3.0 s case. In both of the higher frequency cases a large pile of sand accumulates at the forward end of the trench. In the 3.0 s case, the chain does settle into the sand somewhat, but no pile forms because there is no lateral transport of sand by the links.

These results may have important implications for chain wear in long term deploy-
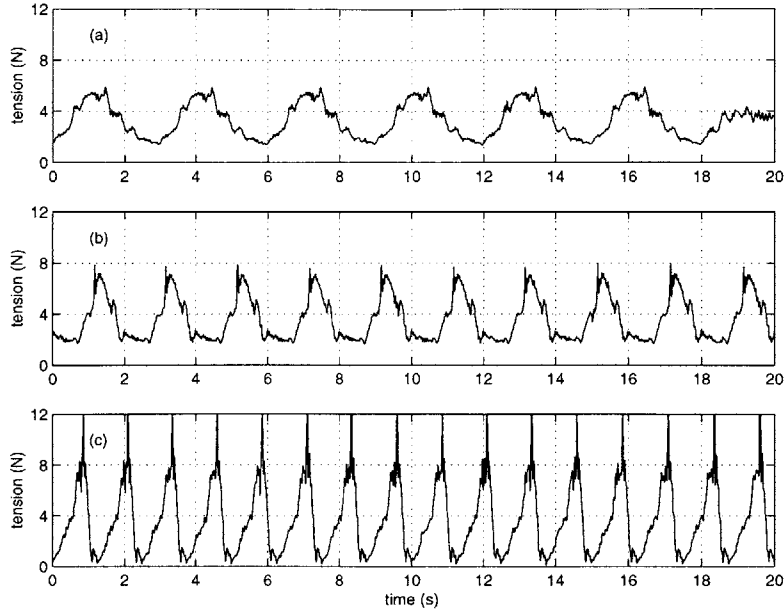
Figure 7-26: Tension time series for the twenty seconds preceding the 120 cycle mark on the sand bottom at $\Delta\tau \approx 0.16$, excitation amplitude 0.25 m, and excitation periods (a) 3.0 s, (b) 2.0 s, and (c) 1.25 s.

ments. The lateral motion of the chain along the bottom that is associated with the tension shocks may significantly enhance abrasion. If that is the case then wear might be reduced by designing moorings so that exceedances of the shock criterion are minimized.

7.5 Comparison with numerical simulations

The numerical program described in chapter 3 uses an elastic foundation with linear stiffness and damping to model the interaction of the mooring line with the sea floor. With the controlled bottom conditions and the importance of the bottom interaction in the dynamic response, the laboratory experiments provide an opportunity to investigate the limits of the elastic foundation approach in the numerical model. This analysis was not possible with the full scale experiment because detailed information about the response of the mooring in the touchdown region was not available.

In searching for a baseline simulation configuration that approximately matched the experimental results, it became clear that given correct input for the easily measured parameters (mass, weight, static tension), the important parameters in the validation were the bottom stiffness and damping, and the chain bending stiffness. Interestingly,

197

none of these three parameters played an important role in the simulations of the full scale experiment. The values for these parameters were chosen so that the baseline simulation result was in reasonably good agreement with the experimental result. The baseline values for these three parameters are $k = 10000$ N/m^2, $\zeta = 0.1$, and $EI = 10^{-6}$ Nm^2. This stiffness gives a non-dimensional bottom stiffness, $\tilde{k}$, of 40.3, 260 times greater than the baseline non-dimensional stiffness used for the field experiment. Stiffnesses significantly beyond this value made static solutions difficult to obtain. The bottom damping ratio chosen was low enough that impact on the tension response is small, but high enough that oscillations of the grounded chain are relatively low. The bending stiffness was set very low to minimize any possible effect on the response. Hydrodynamic parameters were similar to those used for the full scale mooring: $C_{d_n} = 0.5$, $C_{d_t} = 0.01$, $C_{a_n} = 0.5$, and $C_{a_t} = 0.05$.

Figures 7-27 and 7-28 show the simulated response with these parameters for one cycle at 1.25 and 3.0 s excitation periods, respectively. In both cases the basic agreement with the experimental results on the hard bottom (figures 7-11 and 7-17) is quite good[1]. For the high frequency excitation the same snapping and slacking behavior is evident as in the experimental result. The magnitude of the tension spike following the snap is higher in the simulation, but this may be an artifact of the analog filtering having attenuated the impulse in the experimental data. The most significant qualitative difference between the simulation and experiment is in the motion of the grounded chain during the downward half of the cycle. In the simulation the chain from the rightmost TDP to the current TDP at each step is bowed upwards because the model cannot properly resolve the slack in the chain along this length. The configuration of the suspended chain (to the left of the TDP) does accurately show the reversal in curvature that results from the slack tension (or in the simulation, very low tension) in the grounded chain. This discrepancy does not appear in the lower frequency excitation case because the tension discontinuity does not occur and the grounded chain is not slack. As a result, the simulated profiles in this case match the experiment very closely over the entire motion cycle.

The height of the buckled chain above the bottom during the downward motion can be reduced by increasing the damping ratio. Figure 7-29 shows the simulation result for

---

[1] The experimental results have a small temporal lag relative to the simulation results because of a delay in the start of the actuator motion after the video and analog instrumentation is triggered.
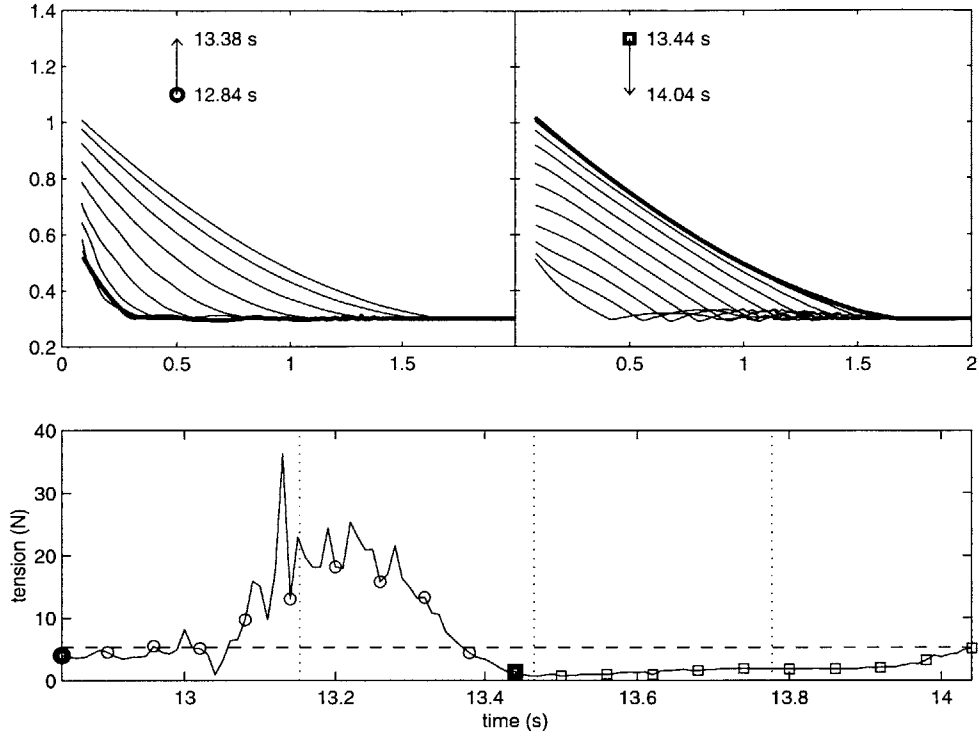
Figure 7-27: Simulated response with baseline parameters over one cycle at 1.25 s excitation period, 0.25 m excitation amplitude, and $\Delta\tau \approx 0.80$.
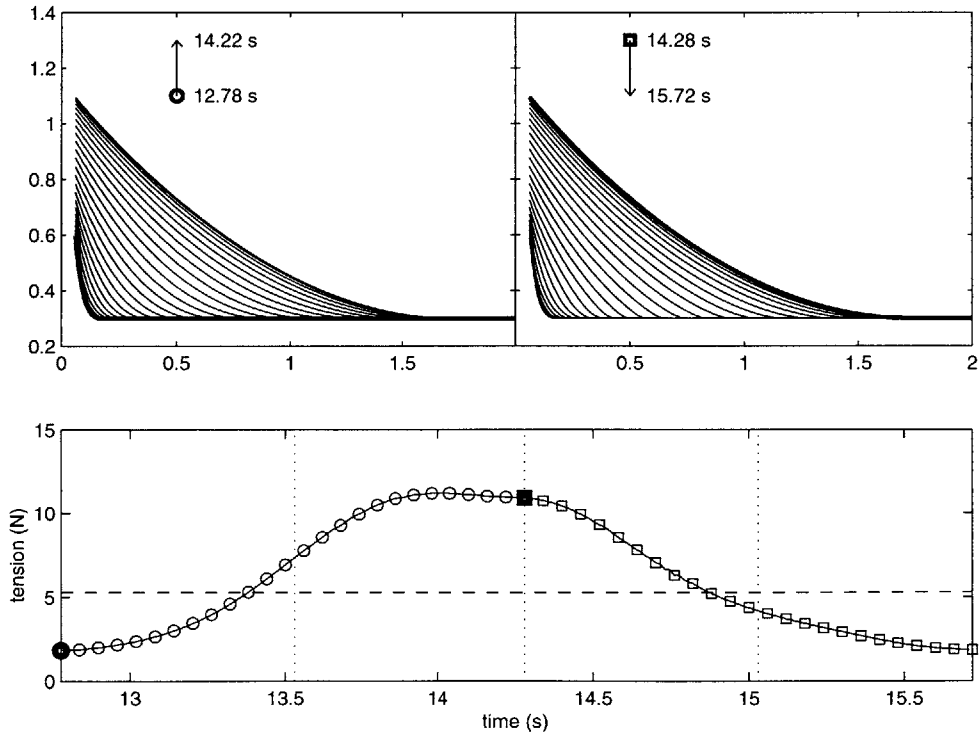
Figure 7-28: Simulated response with baseline parameters over one cycle at 3.0 s excitation period, 0.25 m excitation amplitude, and $\Delta\tau \approx 0.80$.
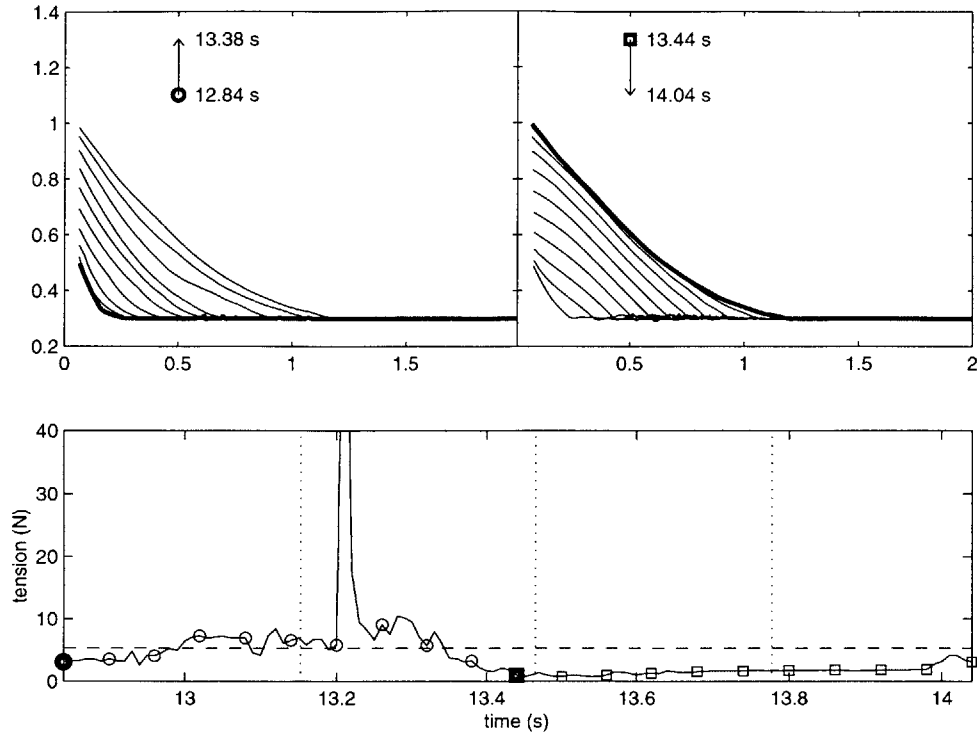
Figure 7-29: Simulated response with $\zeta = 0.3$ over one cycle at 1.25 s excitation period, 0.25 m excitation amplitude, and $\Delta\tau \approx 0.80$.

$\zeta = 0.3$ for the 1.25 s excitation case. The motion of the grounded chain is reduced, but so are the spatial extent of the motion and the overall tension level. A better alternative is to increase the damping ratio to 0.3, but at the same time decrease the bottom stiffness to 1000 N/m^2, so that the damping constant, $b = 2\zeta\sqrt{k\,(m + m_a)}$, remains approximately the same as in the baseline configuration. Results for this case, shown in figure 7-30, illustrate that lowering the stiffness reduces the height of the buckled chain above the bottom while preserving the tension level. This suggests that the bottom damping constant is the most important of the bottom parameters in determining the tension and that the motion of the chain on the bottom can be largely controlled with stiffness.

These same parametric variations in the 3.0 s excitation case do not produce significant changes in the simulation results. For simulations with $\zeta = 0.3$ the maximum tension in the cycle changed by a barely detectable 0.08% relative to the baseline simulation. This contrasts with the marked decrease in tension and increase in range of motion for the 1.25 s case. The simulation with $\zeta = 0.3$ and $k = 1000$ N/m^2 at this excitation period had similarly small changes. In cases where the shock criterion is never met, the bottom

200
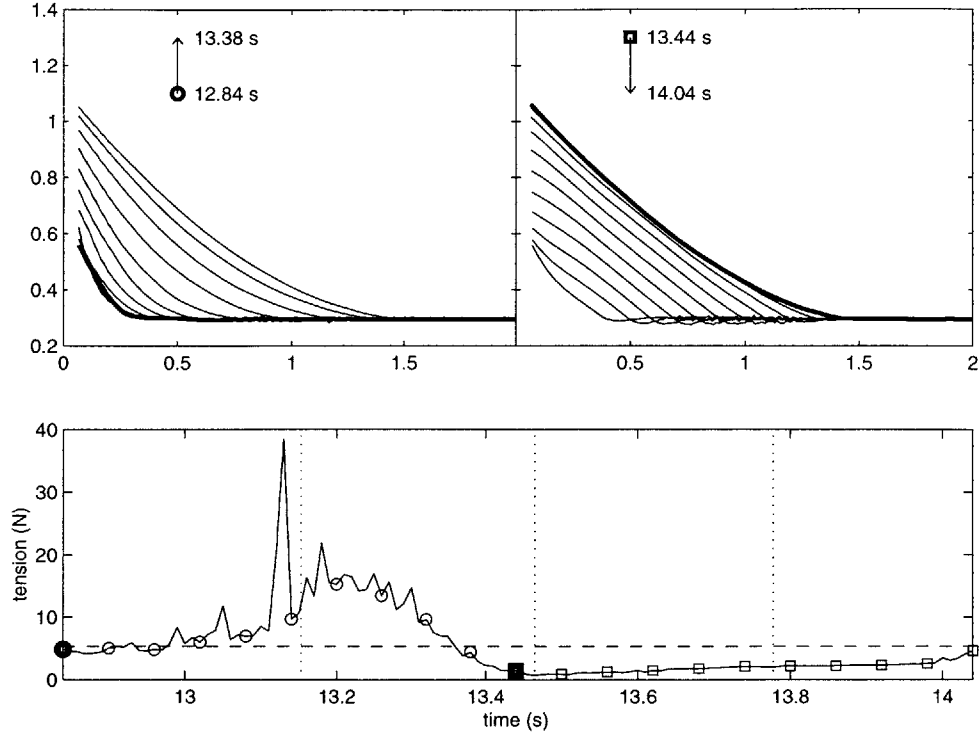
Figure 7-30: Simulated response with $\zeta = 0.3$ and $k = 1000$ N/m^2 over one cycle at 1.25 s excitation period, 0.25 m excitation amplitude, and $\Delta\tau \approx 0.80$.

properties do not appear to play any significant role in the dynamic response. This statement comes with the caveat that bottom stiffness always plays a role in the static response and thus, to the extent that the dynamic response depends on the steady state configuration, the importance of bottom stiffness can never be completely neglected.

This same situation in which simulation results are much less sensitive to parameter variation in the absence of tension shocks is evident in the results with increased bending stiffness. With EI increased by four orders of magnitude to 0.01 Nm^2, the results for the 3.0 s case again only changed very marginally: the maximum tension increased by 1.6%. The result for the 1.25 s case is shown in figure 7-31. Both the tension and motion are significantly different than for the baseline simulation. The increased bending stiffness allows the wave in the grounded chain to propagate upwards into the suspended chain, thus altering the response over the entire length.

The grounded chain buckles because there is an extended period and region of zero tension. With no mechanism to model the collapsing of individual chain links, the chain must deform by bending, no matter how low the EI value. Providing a means to prop-

201
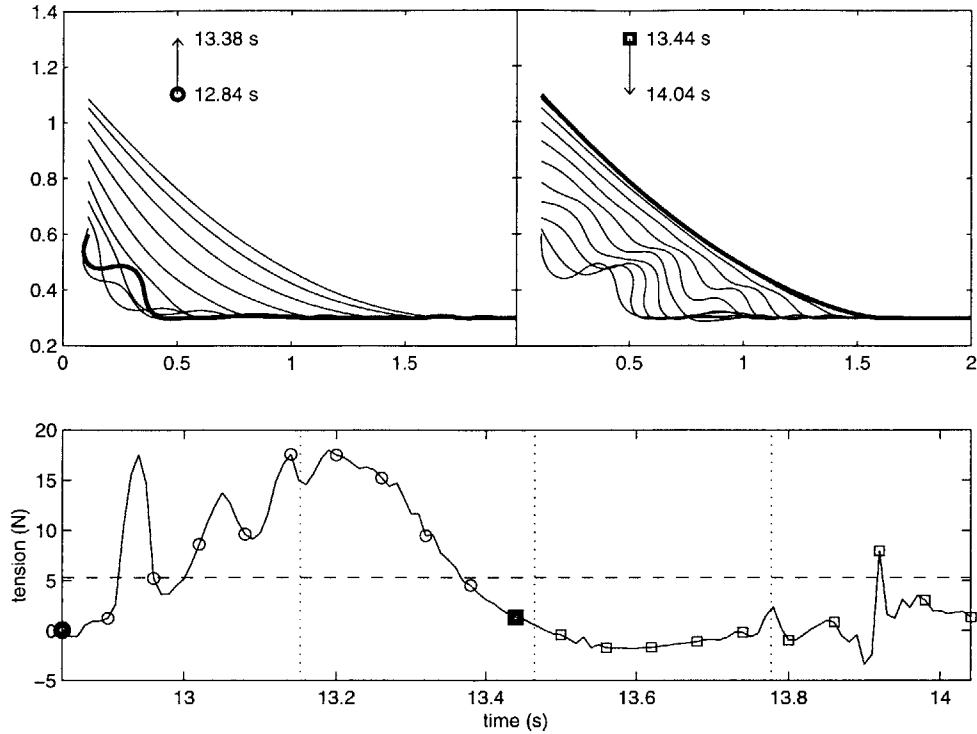
Figure 7-31: Simulated response with $EI = 0.01$ N/m^2 over one cycle at 1.25 s excitation period, 0.25 m excitation amplitude, and $\Delta\tau \approx 0.80$.

agate energy in the presence of zero tension is the very reason for incorporating bending stiffness into the equations of motion in the first place. With too high a stiffness, however, unrealistic bending effects can propagate into areas with low, but not necessarily zero tension. Given the tensions in this model scale system, $EI = 0.01$ N/m^2 is not scaled properly to prevent this. This improper scaling is not an issue with the lower frequency excitation because flexural waves are never introduced into the system.

The conclusion of this comparison then is that the elastic foundation is accurate for both supersonic and subsonic TDP motions. For the subsonic case this is no surprise given the validated accuracy of the simulations of full scale moorings. In the supersonic case, there are several qualifiers to this conclusion. Primary among them is the substantial sensitivity of the simulation results to parametric variations in bottom properties and bending stiffness. This adds additional complexity to the task of defining the simulated system. Also, it should be noted that the numerical simulations at the faster excitation periods required a higher node density (1601 nodes over the 3.29 m length of the chain) than the slowest period cases (401 nodes) to succeed. All of the simulations were run with

202

a 0.001 s base time step.

Much of the reason for this added difficulty in solutions with tension shocks arises from the consequences of the shock condition described in equation 7.11. The non-zero impact force gives rise to a dynamic excitation of the elastic bottom. Also, substituting the non-zero slope at the TDP into equation 7.9 implies a non-zero vertical velocity for the chain at the TDP, enhancing the bottom damping forces at that point. To maintain the overall accuracy of the simulation, these vibrations must be resolved by increasing the spatial and/or temporal resolution of the simulation. The lack of these exciting mechanisms in the subsonic case explains the lack of sensitivity of those solutions to variations in bottom parameters.

7.6 Implications for full scale moorings

With the validation of the elastic foundation approach it is possible to investigate the formation of tension discontinuities in full scale moorings, such as that used in the SWEX field experiment. As discussed above these tension discontinuities have several implications for the design and analysis of these types of moorings. Snap loads and increased wear of chain along the bottom may require that design life be shortened or that a heavier material be used.

Tension and TDP and wave speeds for a relatively high resolution numerical simulation of the SWEX mooring under the storm conditions of the 3 January 1999 data set is shown in figure 7-32. For simplicity, the AxPacks were removed and 401 nodes were used to discretize a single 80 m length of chain. The simulation time step was 0.01 s (compared to 0.1 s for the simulations in chapter 5 and 6). Snapshots of motion and tension along the entire length of the mooring were saved at 0.1 s intervals and used to calculate the TDP and wave speeds. Under these extreme conditions the shock condition is exceeded during both loading and unloading. The loading shocks correspond to the snap loads that are apparent in the time series of top tension (the snap loads are not as clear in the experimental tension record because of the analog filtering in the instrumentation).

To more fully investigate the conditions under which tension discontinuities occur, the response of the uniform version of the SWEX mooring was simulated under a range of mean tensions and sinusoidal excitations. Current was applied in a linear ramp from top
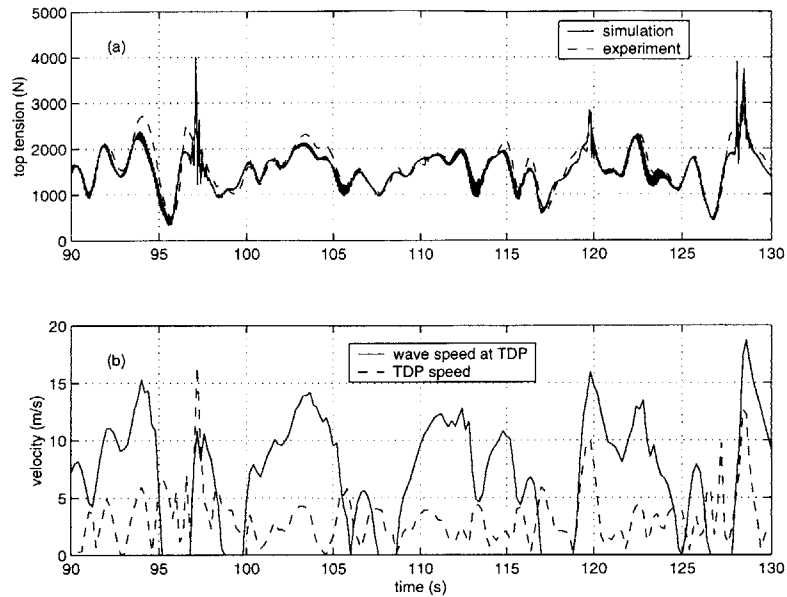
Figure 7-32: (a) Tension at the top of the mooring and (b) TDP speed and transverse wave speed at the TDP for a portion of a simulation of the full scale SWEX mooring using environmental conditions from the 3 January 1999 storm event. The experimentally recorded tension is shown in (a) for reference.

to bottom, with magnitudes 1.0, 0.6, 0.3, and 0.1 m/s at the top and zero current at the bottom. These currents produced non-dimensional mean tensions of 0.245, 0.089, 0.023, and 0.003, respectively. Excitation amplitude and period ranged from 0.1 to 2.5 m and 3.0 to 10.0 seconds. The position and tension at all nodes was recorded every 0.1 seconds over the course of each 60 second simulation. This information allows for calculation of the position and speed of the touchdown point (in a procedure similar to that used for the video data) and a calculation of the wave speed based on the actual instantaneous tension at the TDP.

Figure 7-33 shows the maximum observed difference in the calculated instantaneous wave and TDP speeds over the course of the entire simulation during unloading portions of the motion. The distinction between loading and unloading motions is made using the sign of the TDP speed. Unloading means that chain is being laid down and the TDP speed is positive. Exceeding the shock criterion during this portion of the motion implies that the chain is being laid down slack. Positive differences in figure 7-33 indicate an exceedance of the criterion. The differences are plotted as a function of the ratio between the amplitude of the dynamic tension at the top of the mooring and the static tension at the static TDP, $T_0(0)$.

204
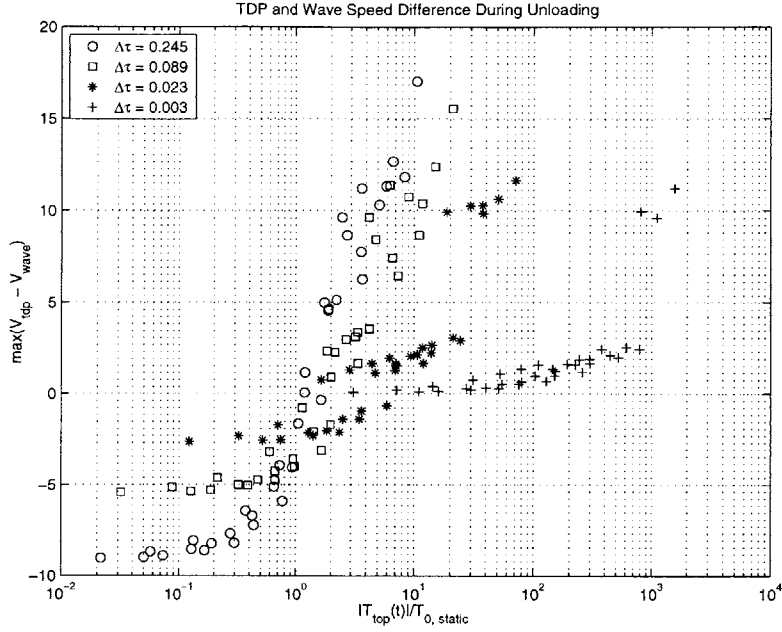
Figure 7-33: Maximum difference in the wave and TDP speeds during unloading for simulations with sinusoidal excitation. At low values of $\Delta\tau$ the results appear clustered because there are critical thresholds of input velocity, $A\omega$, at which the maximum speed difference jumps considerably.

When the dynamic tension amplitude approaches the static TDP tension, the total tension at the TDP approaches zero. With near zero tension the wave speed is very low and the shock criterion is easily exceeded. This argument and the results in figure 7-33 suggest that a reasonable design goal is to keep the value of this ratio below unity to avoid tension discontinuities during unloading[2]. As mean tension decreases this goal could be relaxed somewhat. Several of the simulation results for the lower values of $\Delta\tau$ are below the shock limit but have tension ratios of between two and six.

The maximum difference between wave and TDP speeds during loading is shown in figure 7-34. In this case the difference is plotted as a function of the ratio between the input velocity at the top of the mooring (the TDP speed will typically be proportional to this) and the wave speed at the TDP calculated from the static tension at the TDP,

$$V_{\text{wave}}(0) = \sqrt{\frac{T_0(0)}{m}}. \tag{7.14}$$

[2] In slack conditions, this goal is nearly impossible to achieve because the static tension at the TDP is nearly zero. The effect of the shocks may be slight in these cases, however, because the lack of horizontal forces means that the lateral motions at the TDP will be very small.

205
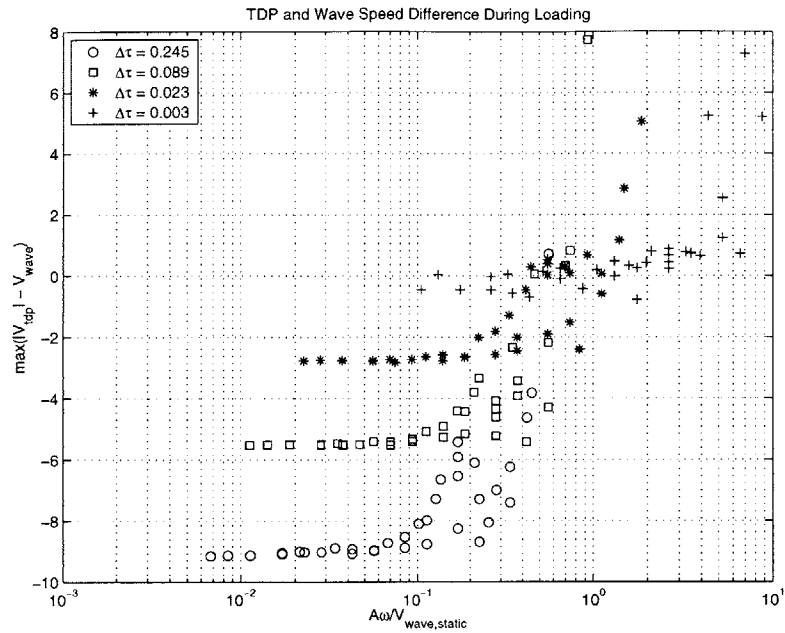
Figure 7-34: Maximum difference in the wave and TDP speeds during loading for simulations with sinusoidal excitation.

For unloading motion, a tension ratio was used because the shocks are largely dependent on low tensions at the TDP. Loading shocks typically form when both wave and TDP speeds are non-zero, making a velocity dependence more meaningful.

As this ratio increases, the TDP is moving faster and faster relative to the wave speed and shocks forms. From figure 7-34 an approximate critical value for this velocity ratio is 0.5. The shock criterion was exceeded for most of the simulations with ratios above this value. There are fewer exceedances of the shock criterion during loading than unloading. During unloading, 91 of the 140 simulations exceeded the shock criterion (105 simulations have a tension ratio greater than unity). During loading, only 41 simulations exceeded the shock criterion (47 simulations have a velocity ratio greater than 0.5). That loading shocks (snap loads) are more rare than unloading shocks (slacks and lateral motion along the bottom) is consistent with the experimental results where the results for 3.0 second excitation period had no shocks, 2.0 second period had unloading shocks, and only the fastest excitation cases had both loading and unloading shocks. No simulations in the above cases had only loading shocks.

The critical values of the tension and velocity ratios described above can be used along with the simple model for dynamic tension described in chapter 6 to develop a procedure

206

for estimating the likelihood of tension discontinuities in full scale moorings. Given an input wave spectrum, spectra of heave velocity and acceleration can be computed and used in equation 6.31 to calculate a spectrum of tension at the top of the mooring. Assuming that the tension is a Gaussian random process, the expected number of times that the dynamic tension will exceed the TDP static tension, $T_0(0)$, per second is [73]

$$N_T = \frac{1}{2\pi}\sqrt{\frac{M_2^T}{M_0^T}}e^{-T_0^2(0)/2M_0^T},$$

(7.15)

where M_0^T and M_2^T are the moments of the tension spectrum,

$$M_0^T = \int_0^\infty S_T(\omega)d\omega = \sigma_T^2,$$

(7.16)

$$M_2^T = \int_0^\infty \omega^2 S_T(\omega)d\omega.$$

(7.17)

The probability of at least one exceedance in a period $\bar{t}$ is

$$P(|T| > T_0(0) \text{ in } \bar{t}) = 1 - e^{-\bar{t}N_T}.$$

(7.18)

Similarly, for loading shocks the number of exceedances of the input velocity of the level $\frac{1}{2}V_{\text{wave}}(0)$ per second is

$$N_v = \frac{1}{2\pi}\frac{\sigma_a}{\sigma_v}e^{-V_{\text{wave}}^2(0)/8\sigma_v^2},$$

(7.19)

and the probability of at least one exceedance in $\bar{t}$ is

$$P(A\omega > 0.5V_{\text{wave}}(0) \text{ in } \bar{t}) = 1 - e^{-\bar{t}N_v}.$$

(7.20)

In the above, the variances of velocity and acceleration have been substituted for the zero- and second-order moments of velocity.

To test these guidelines, this same mooring configuration was simulated with the steady state and dynamic excitation conditions observed from the SWEX experiment. Each of the 119 simulations was run for 200 seconds ($\bar{t} = 200$ s). The moments for tension were calculated using equation 6.31 with model coefficients calculated from a fit to the simulation results ($M = 158.0$ kg, $C_d = 0.288$). From the simulation results, 10 data

207

shock type	correct +	correct −	false +	false −
unloading	112	0	7	0
loading	4	109	0	6

Table 7.2: Number of correct and incorrect predictions given a probability level of 0.9 in equations 7.18 and 7.20 as an indicator of the presence of shocks.

sets had loading shocks and 112 simulations had unloading shocks. Using a probability level greater than 0.9 as an indicator that a shock could be expected, the accuracy of equations 7.18 and 7.20 can be categorized in one of four ways: correct positive, correct negative, false positive, and false negative, where a positive is an exceedance of the shock condition. For example, a correct positive is a data set for which the calculated probability of an exceedance is greater than 0.9 and an exceedance was observed in that data set. Table 7.2 lists the number of data sets that fall into each category for both types of shock.

There are no negative predictions for the unloading case. The calculated probability of the tension ratio exceeding unity is nearly 1.0 for all data sets. The seven data sets in the simulation results that did not have an exceedance during unloading were amongst the twelve lowest of all data sets ranked in terms of dynamic tension (σ_T). Unloading shocks occurred under nearly all of the observed conditions. In this situation then, the probabilistic prediction of unloading shocks in all 119 cases is not unreasonable.

As observed in the study with sinusoidal inputs, loading shocks occur less frequently than unloading shocks. Equation 7.20 with a probability level of 0.9 appears to offer a reasonable predictive capability for loading shocks. However, for conservative design, the false negatives are a concern. The number of false negatives can be reduced, with a subsequent increase in the number of false positives, by decreasing the probability level. A value of 0.5 produces only two false negatives, but also yields three false positives.

Overall then, the design guidelines outlined above provide a reasonable prediction of the likelihood of tension discontinuities at the TDP. For the most accurate prediction, and for quantitative information about the magnitude of tension spikes and extent of lateral motion along the bottom associated with shocks, full numerical simulation (with accurate representation of bottom conditions) is still necessary.

Chapter 8

Conclusions

The most tangible contributions of this thesis are tools that can be used in the analysis and design of mooring systems. The generalized-α time integration scheme and algorithms for mesh refinement, adaptive time-stepping, and adaptive relaxation contribute to the numerical program and make it robust and relatively easy to use. The simple model for dynamic tension in chapter 6 can provide a mooring designer with a convenient and accurate predictor of tension given very simple inputs. On a more fundamental level, however, the tools are not themselves the end goal of this work. That goal is to develop a deeper understanding of the mechanics of these systems so that design methodologies can be improved, and more capable, longer lasting systems can be developed and deployed. Toward that end, the real importance of the tools is the insight that they yield in the analyses such as those of dynamic tension in chapter 6 and bottom interaction in chapter 7. Tools facilitate design and analysis, but ultimately, innovation must come from understanding.

8.1 Summary

8.1.1 Numerical model

The generalized-α time integration scheme for cable dynamics developed in chapter 2 offers significant advantages over the traditional box method [1] or other box method variants [60]. By retaining the box method's finite difference spatial integration, the method remains second-order accurate in the spatial dimension and is relatively easy to implement. For the temporal discretization the generalized-α algorithm provides:

- Controllable numerical dissipation without loss of second-order accuracy. Trapezoidal rule is only first-order accurate in the presence of numerical dissipation. The original box method temporal discretization has no numerical dissipation and therefore is subject to Crank-Nicolson noise and other numerical instabilities.

- Second-order accuracy. Box method variants using backward differences are only first-order accurate in time.

- The ability to implement other algorithms, including backward differences, trapezoidal rule, HHT-α, and WBZ-α, through appropriate choices of parameters.

- Improved numerical stability through the averaging of coefficient matrices.

These advantages were made clear in chapter 5 where the scheme allowed for robust solution of the instability in the two-dimensional hanging chain motion leading into three-dimensional whirling. This solution could not be obtained with the previous program that used the pure box method. The generalized-α scheme also facilitated the fast, accurate, and robust simulation of the entire range of conditions observed during the SWEX experiment in chapters 5 and 6.

8.1.2 Models for understanding dynamic tension

Chapter 6 contains a number of significant contributions regarding dynamic tension in geometrically compliant systems. The proposed model for dynamic tension was derived by first considering a SDOF spring-mass-dashpot system. By fitting motion and tension spectra for each data set individually to this form, model coefficients were derived for each data set. To understand the scatter in these coefficients, the individual tension mechanisms (inertia, drag, stiffness) were analyzed separately and in pairs. This analysis confirmed that the model coefficients should change roughly linearly with mooring shape (as measured by the non-dimensional mean tension) and that the different mechanisms are coupled together.

To account for scattering due to this coupling, relationships were sought among the statistics of the experimental data that presented low scatter. From these low scatter relationships the tension model was constructed based on the standard deviations of tension, heave acceleration, and heave quadratic velocity. Analyzing the model in relationship to

210

the spring-mass-dashpot model showed that coupling between mass and drag was a likely cause of much of the scatter in the coefficients fitted to individual data sets and that the spring terms could be neglected over the range of conditions present in the experimental data set. With just two parameters the simple model is compact and able to represent the experimental data with only slightly less accuracy than the model using the coefficients fitted to individual data sets.

Numerical simulations were then used to analyze the parametric dependence of the model mass and drag coefficients on actual system parameters, including normal and tangential drag coefficients, added mass coefficients, and bottom stiffness and damping. From these parametric dependencies, formulae were derived for the a priori prediction of the model coefficients. These formulae, together with the simple model, allow a designer to analytically calculate the dynamic tension response over a wide range of conditions without the need for experimental data or numerical simulation. This approach was validated using data from a second oceanographic mooring (the CMO experiment) and simulation of steel catenary and lazy wave riser configurations.

Several circumstances under which the simple model dynamic tension is not accurate were described. Among these are:

- The coupling between mass and drag is self-limiting. At high sea state, the coupling term in the model leads to an over prediction of the dynamic tension.

- At very low frequencies the only dynamic tension is due to stiffness effects which are neglected in the model. These effects are small.

- There is no model drag when the mooring is slack/vertical. If input velocities are high in such a case, the dynamic tension calculated from the model will be too low.

- The model is derived based on an assumption that the mooring materials are inextensible. If the mooring has significant elastic compliance then the model calculated tensions will be too high.

- The model assumes that adequate scope is always available for geometric compliance. When the mooring is pulled taut, model calculated tensions will be too low.

An additional limitation of the simple model is that as $\Delta\tau$, the non-dimensional mean tension, increases, dynamic tension due to horizontal motions becomes significant. In the

SWEX mooring, the non-dimensional mean tensions were low enough that surge and sway motion did not contribute significantly to the total dynamic tension. For oceanographic moorings in very shallow water, however, horizontal motions become important, as illustrated by the data from the NDBC Duck Pier mooring in 17 m depth. This situation is also more common in riser applications where mooring pre-tensioning can lead to very high values of $\Delta \tau$.

In the statistical domain, the contributions to the dynamic tension due to vertical and horizontal motions are linearly separable. Chapter 6 demonstrated that a model for dynamic tension due to horizontal motion can be developed using a procedure similar to that used for vertical motion. Summing the results from the two models yields a complete prediction for the dynamic tension in the presence of both vertical and horizontal input motions.

8.1.3 Bottom interaction

The experiments presented in chapter 7 represent the first direct observation of the shock condition at the touchdown point of a catenary mooring. They also illustrate the implications of the shocks. The mathematical implications of the shock are a non-zero impact force at the TDP and a loss of tangency as the mooring line leaves the bottom. Practically, the shock condition has different implications depending on whether the motion is loading, line being picked up off the bottom, or unloading, chain being laid down on the bottom.

In the unloading portion of the cycle, the tension discontinuity leads to zero tension at the TDP and the grounded line being laid down with slack. As the motion reverses the mooring line does not roll smoothly off the bottom but rather the TDP moves laterally along the bottom. This lateral motion may be a significant source of abrasion of mooring line in the touchdown region. This type of tension discontinuity is more common than shocks during loading.

During loading, the tension discontinuity of the shock is manifest as a snap load, leading to large impulsive tension spikes. This situation arises only after the shock criterion has been exceeded during the unloading motion. The snap occurs because the geometry of the mooring cannot change rapidly enough to accommodate the retensioning of the slack grounded line.

The qualitative features of the response of the mooring in the presence of tension shocks at the TDP do not change as the bottom type changes. On two softer artificial bottoms with higher friction, there were virtually no observable quantitative or qualitative changes in the motion or tension response. On a realistic sand bottom, the lateral motion of the TDP associated with unloading shocks caused a large trench to form in the touchdown region. The digging action required to produce this trench strongly supports the idea that mooring wear and abrasion will increase in the presence of unloading shocks.

The likelihood of both types of shocks can be predicted using relatively simple criteria. However, for the most accurate prediction of their occurrence and their implications, full numerical simulations should be used. The presence of the shocks make numerical simulations more difficult because the results are more sensitive to parametric variations in the bottom parameters and the mooring bending stiffness. The results from chapter 7 did verify that with the right parameters, the elastic foundation approach to modeling bottom interaction can capture the tension and motion response in the touchdown region quite accurately.

8.2 Recommendations for future work

In its current state of development the numerical program is relatively robust and capable. While not a focus of this thesis, additional work is still needed to improve the stability of static solutions, particularly for problems with mooring line on the sea floor. The current static solution procedures are adequate, but a fast, robust, fully automated scheme, coupled with the generalized-α based time integration scheme developed in this thesis would be a very powerful tool for mooring line simulation problems.

The instrumentation suite that was deployed for the field experiments provided good quality data for the validation of the numerical program and for the analysis of dynamic tension. It did not provide data that could be used for a full scale comparison with the results from the laboratory experiment. For that analysis, more complete information about the steady state configuration and along mooring motion are needed. Redeployment of the GPS receiver that failed in the SWEX experiment and an acoustically localized anchor position would yield high quality data about the very slow current and tidal induced motions of the mooring. The AxPack instruments would provide much more information

about motion over the length of the mooring with the addition of a compass and tilt sensor. In conjunction with the accelerometer data, this addition would provide high frequency earth referenced motion along the mooring.

For the laboratory experiments additional realistic bottom types need to be studied. More work is also needed to refer the laboratory observations to full scale bottom conditions. Bottoms such as mud will likely make the video data very difficult to process and additional analog instrumentation, such as very small inline accelerometers and load cells, may be necessary to develop an accurate picture of the system dynamics on these bottoms. An impact resistant, unobtrusive, inline load cell would also be useful in collecting tension data directly in the grounded portion of the chain.

An interesting laboratory experiment would also be one in which chain abrasion in the presence of tension shocks could be measured and compared to the wear experienced during more typical, smooth motions. Such an effort would require considerable thought about the practical aspects of runs that may last for many days or weeks. Together with design tools that can predict the occurrence of tension shocks, a catalog of this kind of data on various bottoms would be very valuable, as chain wear is one of the limiting factors in current oceanographic mooring practice.

As discussed in the summary for chapter 6, additional work is needed to develop design formulae for dynamic tension in compliant systems with horizontal input motions, analogous to equation 6.16 for vertical motions. A reduction to such a simple form may not be possible, but through the study of a range of systems in which horizontal motions are important some general design rules could certainly be formulated.

Appendix A

Derivation of 2D Equations of Motion

This appendix contains a derivation of the two-dimensional governing equations for a cable in water. A derivation of the three-dimensional equations can be found in Tjavaras [93]. The derivation assumes that the cable material is circular and homogeneous in cross-section (but not necessarily along the length), has a nonlinear tension–strain relationship and that Euler-Bernoulli beam theory can be applied. Fluid forces on the cable are modeled using a Morison formulation [29].

A.1 Kinematics and coordinate system

The governing equations are derived in the coordinate system defined by the local tangential $(\hat{t})$ and normal $(\hat{n})$ directions, as shown in figure A.1. The transformation between local and global $(\hat{i}, \hat{j})$ coordinates is

$$\begin{bmatrix} \hat{t} \\ \hat{n} \end{bmatrix} = \begin{bmatrix} cos\phi & sin\phi \\ -sin\phi & cos\phi \end{bmatrix} \begin{bmatrix} \hat{i} \\ \hat{j} \end{bmatrix} \tag{A.1}$$

$$\begin{bmatrix} \hat{i} \\ \hat{j} \end{bmatrix} = \begin{bmatrix} cos\phi & -sin\phi \\ sin\phi & cos\phi \end{bmatrix} \begin{bmatrix} \hat{t} \\ \hat{n} \end{bmatrix} \tag{A.2}$$
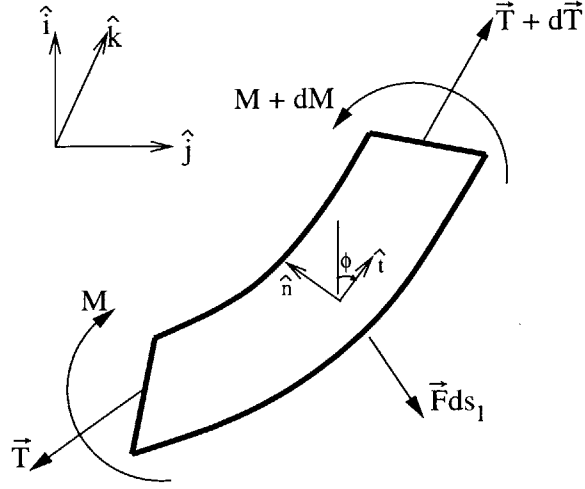
Figure A-1: Vector definitions for the local coordinate system.

The time derivative of a vector, $\vec{A}$, that is defined in the local frame is

$$\frac{d\vec{A}}{dt} = \frac{\partial \vec{A}}{\partial t} + \vec{\omega} \times \vec{A}, \qquad (A.3)$$

where $\vec{\omega}$ is the time rate of change of the orientation of the local frame. Likewise, the derivative of $\vec{A}$ with respect to the Lagrangian coordinate, s, along the cable length is

$$\frac{d\vec{A}}{ds} = \frac{\partial \vec{A}}{\partial s} + \vec{\Omega} \times \vec{A}, \qquad (A.4)$$

where $\vec{\Omega}$ is the spatial rate of change of the orientation of the local frame. For the two-dimensional case defined in figure A.1, $\vec{\omega}$ and $\vec{\Omega}$ are

$$\vec{\omega} = \frac{\partial \phi}{\partial t}\hat{k}, \qquad \vec{\Omega} = \frac{\partial \phi}{\partial s}\hat{k}. \qquad (A.5)$$

A.2 Cable stretch and buoyancy

If ds is the unstretched length of an infinitesimal element of cable and ds_1 is the stretched length then

$$ds_1 = (1 + \epsilon)ds, \qquad (A.6)$$

216

where ϵ is the cable strain. From conservation of mass, the mass and weight per unit length of the stretched element are

$$m_1 ds_1 = mds \quad \rightarrow \quad m_1 = \frac{m}{1 + \epsilon}, \tag{A.7}$$

$$w_1 ds_1 = wds \quad \rightarrow \quad w_1 = \frac{w}{1 + \epsilon}. \tag{A.8}$$

Based on Poisson's ratio, ν, the reduction from the nominal diameter, d, of the stretched cross-section is

$$\delta d = (-\nu\epsilon)d, \tag{A.9}$$

the change in cross-sectional area is

$$\delta A = \frac{pi}{4}\left[(d + \delta d)^2 - d^2\right] \approx \frac{\pi}{2}d\delta d, \tag{A.10}$$

and thus

$$\frac{\delta A}{A} = -2\nu\epsilon. \tag{A.11}$$

If $\nu = \frac{1}{2}$ we have conservation of volume[1]

$$A(1 - \epsilon)(1 + \epsilon)ds \approx Ads. \tag{A.12}$$

Finally, we can use a binomial expansion to write the stretched area and diameter in a more convenient form:

$$A_1 = A(1 - \epsilon) \approx \frac{A}{1 + \epsilon}, \tag{A.13}$$

---

[1] While $\nu = \frac{1}{2}$ is not strictly true for all cables (particularly metal chain and wire), the conservation of volume that it introduces greatly simplifies the treatment of the buoyancy forces on the cable [36]. Burgess [10] calculates the error associated with using $\nu = \frac{1}{2}$ when the true value of $\nu = 0$ (the maximum possible error in ν) as $\rho g z/E$. This term becomes significant only with large depths and very soft materials.

217

Reality is pressure on
element exterior only

Reality + pressure applied
at the two ends

Compensating tension vectors
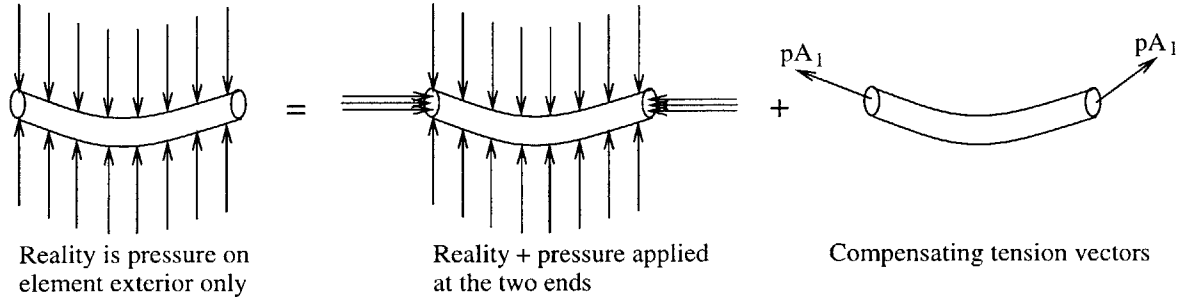
Figure A-2: Schematic diagram of pressure and effective tension terms.

and

$$d_1 = \frac{d}{\sqrt{1+\epsilon}}. \tag{A.14}$$

With the above definitions, we can easily treat hydrostatic forces on the cable by considering the effective tension. In reality, hydrostatic forces act only on the exterior of the element, not at the two ends. Following the procedure first suggested by Breslin [6], however, we can introduce a pressure force on the element end faces if we also introduce a compensating term into the tension force. This is shown schematically in figure A-2. Mathematically,

$$T_{\text{effective}} = T + pA_1, \tag{A.15}$$

where p is the hydrostatic pressure at the depth of the element. With the fictitious end pressures Archimedes' principle applies and the buoyancy force per unit length of the stretched element is simply

$$B_1 = A_1 \rho_w g = \frac{A}{1+\epsilon} \rho_w g, \tag{A.16}$$

where ρ_w is the density of water and g is the local acceleration due to gravity. The total of the weight and buoyancy forces on the stretched element are

$$\vec{F}_w = \left(\frac{A}{1+\epsilon} \rho_w g - \frac{w}{1+\epsilon} \right) \hat{\imath}. \tag{A.17}$$

If we define the wet weight of the material as $w_0 = w - A\rho_w g$, then

$$(1 + \epsilon)\vec{F_w} = -w_0\hat{i} = -w_0 \cos \phi \hat{t} + w_0 \sin \phi \hat{n}. \tag{A.18}$$

Introducing the effective tension and the wet weight frees us from any further consideration of the hydrostatic pressure; pressure effects are now simply rolled into any computed strain result [36]. Because tensions are always computed as a function of strain, all calculated tensions will be the effective tension. For simplicity in the remainder of the derivation of the governing equations we will use T to denote the effective tension.

A.3 Hydrodynamic forces

The hydrodynamic forces on the cable are the drag, added mass, and dynamic Archimedes forces. The drag forces arise from the relative velocity of the cable in a current field defined in global $\hat{i}, \hat{j}$ coordinates by U and V respectively. In local coordinates the relative velocities are

$$u_r = u - U \cos \phi - V \sin \phi, \text{and} \tag{A.19}$$

$$v_r = v + U \sin \phi - V \cos \phi. \tag{A.20}$$

The drag force in local coordinates is

$$\vec{F_d} = \begin{bmatrix} -\frac{1}{2}\rho_w \frac{\pi d}{\sqrt{1+e}}C_{d_t}\left(u - u_c\right)|u - u_c|\hat{t} \\ -\frac{1}{2}\rho_w \frac{d}{\sqrt{1+e}}C_{d_n}\left(v - v_c\right)|v - v_c|\hat{n} \end{bmatrix}. \tag{A.21}$$

For a solid circular cross-section cable, the added mass force has a component in the normal direction only. It is computed as a function of the relative acceleration between the fluid and the cable. The time derivative of the current velocity in local coordinates (assuming steady current) is

$$\dot{v_c} = -\left[U \cos \phi + V \sin \phi\right]\frac{\partial \phi}{\partial t}\hat{n}. \tag{A.22}$$

219

The added mass force is

$$\vec{F}_{am} = \frac{m_a}{1+\epsilon}\left[-\left(U\cos\phi + V\sin\phi\right)\frac{\partial\phi}{\partial t} - \frac{\partial v}{\partial t}\right]\hat{n},\tag{A.23}$$

where m_a is the added mass per length of the cable cross-section. Because the current velocity in local coordinates is changing in time, there is a pressure gradient that gives rise to the dynamic Archimedes force [69]. Like the added mass force, the only component of this force on a solid circular cable is in the normal direction. It is defined as

$$\vec{F}_{ar} = -\rho_w\frac{\pi d^2}{4(1+\epsilon)}\left(U\cos\phi + V\sin\phi\right]\frac{\partial\phi}{\partial t}\hat{n}.\tag{A.24}$$

For cables with non-solid, or non-circular cross-sections (such as chains) there can be both added mass and dynamic Archimedes forces in the tangential direction. The time derivative of the current velocity in the tangential direction is

$$\dot{u}_c = \left[-U\sin\phi + V\cos\phi\right]\frac{\partial\phi}{\partial t}\hat{t}.\tag{A.25}$$

With the appropriate tangential components equations A.23 and A.24 become

$$\vec{F}_{am} = \left[\begin{array}{c}\frac{m_{a_t}}{1+\epsilon}\left[\left(-U\sin\phi + V\cos\phi\right)\frac{\partial\phi}{\partial t} - \frac{\partial u}{\partial t}\right]\hat{t}\\\frac{m_{a_n}}{1+\epsilon}\left[-\left(U\cos\phi + V\sin\phi\right)\frac{\partial\phi}{\partial t} - \frac{\partial v}{\partial t}\right]\hat{n}\end{array}\right]\tag{A.26}$$

$$\vec{F}_{ar} = \frac{mg - w_0}{g(1+\epsilon)}\left[\begin{array}{c}\left(-U\sin\phi + V\cos\phi\right]\frac{\partial\phi}{\partial t}\hat{t}\\-\left(U\cos\phi + V\sin\phi\right]\frac{\partial\phi}{\partial t}\hat{n}.\end{array}\right]\tag{A.27}$$

The term $\frac{mg-w_0}{g}$ defines the mass of the fluid displaced by the irregular cross-section. This formulation also requires two terms to describe the cross-section added mass, m_{a_t} for tangential motion, and m_{a_n} for normal motion.

A.4   Balance of forces

A summation of the forces on the cable element shown in figure A.1 yields

$$\frac{d}{dt}\left(m_1 ds_1\vec{V}\right) = \vec{T} + d\vec{T} - \vec{T} + \vec{F}ds_1.\tag{A.28}$$

If we expand the derivatives according to equations A.3 and A.4 and eliminate stretched variables we find

$$m \left[\frac{\partial \vec{V}}{\partial t} + \vec{\omega} \times \vec{V} \right] = \frac{\partial \vec{T}}{\partial s} + \vec{\Omega} \times \vec{T} + \vec{F}(1 + \epsilon). \qquad (A.29)$$

Substituting $\vec{F} = \vec{F}_{am} + \vec{F}_{ad} + \vec{F}_w + \vec{F}_d$ and collecting terms in the normal and tangential directions yields

$$m \left(\frac{\partial u}{\partial t} - v \frac{\partial \phi}{\partial t} \right) = \frac{\partial T}{\partial s} - S_n \frac{\partial \phi}{\partial s} - w_0 \cos \phi - \frac{1}{2} \rho_w \pi d C_{d_t} \left(u - u_c \right) |u - u_c| \sqrt{1 + \epsilon} \quad (A.30)$$

$$m \left(\frac{\partial v}{\partial t} + u \frac{\partial \phi}{\partial t} \right) = \frac{\partial S_n}{\partial s} + T \frac{\partial \phi}{\partial s} - m_a \frac{\partial v}{\partial t} - \left(m_a + \rho_w \frac{\pi d^2}{4} \right) \left(U \cos \phi + V \sin \phi \right) \frac{\partial \phi}{\partial t}$$
$$+ w_0 \sin \phi - \frac{1}{2} \rho_w d C_{d_n} \left(v - v_c \right) |v - v_c| \sqrt{1 + \epsilon}. \qquad (A.31)$$

A.5   Balance of moments

For the two-dimensional element, the only moment balance involves moments about the out-of-plane axis. The tension force does not contribute a moment in this case because in the infinitesimal limit the tangential and normal directions at the two opposite ends have the same direction and opposite magnitudes. The remaining moment contributions are the rotational inertia, the couple due to shear, and the bending of the element:

$$\frac{d}{dt} \left(ds_1 \rho_c I_1 \frac{\partial \phi}{\partial t} \right) = S_n ds_1 + dM_1, \qquad (A.32)$$

where I_1 is the second-area moment of inertia of the stretched cable cross-section and ρ_c is the mass density of the cable. Using Euler-Bernoulli beam theory the bending moment, M, is the product of the flexural stiffness of the cable, EI, and cable curvature:

$$M_1 = EI_1 \frac{\partial \phi}{\partial s}. \qquad (A.33)$$

The area moment of inertia of a circular cross section is $\sim d^4$ and thus

$$M = M_1 \left(1 + \epsilon \right)^2 \qquad I = I_1 \left(1 + \epsilon \right)^2. \qquad (A.34)$$

Substituting equations A.33 and A.34 into equation A.32, eliminating ds_1, and dividing by ds yields

$$\frac{d}{dt}\left(\frac{\rho_c I}{1+\epsilon}\frac{\partial \phi}{\partial t}\right) = S_n\left(1+\epsilon\right) + \frac{d}{ds}\left(\frac{EI}{(1+\epsilon)^2}\frac{\partial \phi}{\partial s}\right). \tag{A.35}$$

Expanding derivatives and re-inserting the definitions for the spatial and temporal derivatives of ϕ given in equation A.5 so that the system remains a first-order PDE yields,

$$\rho_c I\left[(1+\epsilon)\frac{\partial \omega}{\partial t} - \omega\frac{\partial \epsilon}{\partial t}\right] = EI\left[\frac{\partial \Omega_3}{\partial s} - \frac{2\Omega_3}{1+\epsilon}\frac{\partial \epsilon}{\partial s}\right] + (1+\epsilon)^3 S_n. \tag{A.36}$$

Howell [46] used dimensional analysis to show that for both metal and synthetic cables the rotational inertia term and the second bending term containing the spatial derivative of strain are of significantly lower order than the remaining terms. If we drop these terms, the result is

$$EI\frac{\partial \Omega_3}{\partial s} + (1+\epsilon)^3 S_n. \tag{A.37}$$

Both terms could be retained without a significant loss of simplicity. Using equation A.37 over equation A.36 does offer the advantage that the additional dependent variable ω does not need to be stored.

A.6 Compatibility

Compatibility can be established by requiring continuity of the position of the cable in both space and time. If $\vec{R}(s,t)$ is a vector to a point on the cable then continuity requires

$$\frac{d}{dt}\left(\frac{d}{ds}\vec{R}\right) = \frac{d}{ds}\left(\frac{d}{dt}\vec{R}\right). \tag{A.38}$$

By definition

$$\frac{d\vec{R}}{dt} = \vec{V}, \tag{A.39}$$

and from analytic geometry we know that the derivative of a position vector to a space curve with respect to arc length is a unit vector tangent to the curve, in the direction of

increasing arc length [43]

$$\frac{d\vec{R}}{ds_1} = \hat{t} \rightarrow \frac{d\vec{R}}{ds} = (1 + \epsilon)\hat{t}. \tag{A.40}$$

Thus the continuity condition (equation A.38) reduces to

$$\frac{d}{dt}\left[(1 + \epsilon)\hat{t}\right] = \frac{d\vec{V}}{ds}. \tag{A.41}$$

Expanding the derivatives and collecting components in the tangential and normal directions gives

$$\frac{\partial u}{\partial s} = \frac{\partial e}{\partial t} - v\frac{\partial \phi}{\partial s}, \tag{A.42}$$

$$\frac{\partial v}{\partial s} = (1 + \epsilon)\frac{\partial \phi}{\partial t} - u\frac{\partial \phi}{\partial s}. \tag{A.43}$$

A.7 Matrix form of the governing equations

Equations A.5, A.30, A.31, A.36 or A.37, A.42, and A.43, define a system of either six equations and six unknowns (without rotational inertia) or seven equations and seven unknowns (if rotational inertia is retained in equation A.36). The six degree-of-freedom

form of the equations can be written as

$$T'(\epsilon)\frac{\partial e}{\partial s} - S_n\frac{\partial \phi}{\partial s} - m\frac{\partial u}{\partial t} + mv\frac{\partial \phi}{\partial t} - w_0 \cos \phi$$

$$- \frac{1}{2}\rho_w d\pi C_{d_t} u_r |u_r| \sqrt{1+\epsilon} = 0, \tag{A.44}$$

$$\frac{\partial S_n}{\partial s} + T(\epsilon)\frac{\partial \phi}{\partial s} - (m + m_a)\frac{\partial v}{\partial t} - \left[mu + \left(\rho_w\frac{\pi d^2}{4} + m_a\right)(U\cos\phi + V\sin\phi)\right]\frac{\partial \phi}{\partial t}$$

$$+ w_0 \sin \phi - \frac{1}{2}\rho_w dC_{d_n} v_r |v_r| \sqrt{1+\epsilon} = 0, \tag{A.45}$$

$$\frac{\partial u}{\partial s} - v\frac{\partial \phi}{\partial s} - \frac{\partial \epsilon}{\partial t} = 0, \tag{A.46}$$

$$\frac{\partial v}{\partial s} + u\frac{\partial \phi}{\partial s} - (1+\epsilon)\frac{\partial \phi}{\partial t} = 0, \tag{A.47}$$

$$\frac{\partial \phi}{\partial s} - \Omega_3 = 0, \tag{A.48}$$

$$EI\frac{\partial \Omega_3}{\partial s} + S_n(1+\epsilon)^3 = 0. \tag{A.49}$$

If we define $\mathbf{Y} = [\epsilon, S_n, u, v, \phi, \Omega_3]^{\mathrm{T}}$ then equations A.44 through A.49 can be written in matrix form as

$$\mathbf{M}\frac{\partial \mathbf{Y}}{\partial t} + \mathbf{K}\frac{\partial \mathbf{Y}}{\partial s} + \mathbf{F}(\mathbf{Y}, s, t) = 0. \tag{A.50}$$

The continuous forms of the mass matrix, "stiffness" matrix, and forcing vector are

$$\mathbf{M} = \begin{bmatrix} 0 & 0 & -m & 0 & mv & 0 \\ 0 & 0 & 0 & -(m+m_a)_{j-1} & -\left[mu + \left(\rho_w\frac{\pi d^2}{4} + m_a\right)(U\cos\phi + V\sin\phi)\right] & 0 \\ -1 & 0 & 0 & 0 & 0 & 0 \\ 0 & 0 & 0 & 0 & -(1+\epsilon) & 0 \\ 0 & 0 & 0 & 0 & 0 & 0 \\ 0 & 0 & 0 & 0 & 0 & 0 \end{bmatrix}, \tag{A.51}$$

$$
\mathbf{K} = \begin{bmatrix}
T'(\epsilon) & 0 & 0 & 0 & S_n & 0 \\
0 & 1 & 0 & 0 & T(\epsilon) & 0 \\
0 & 0 & 1 & 0 & -v & 0 \\
0 & 0 & 0 & 1 & u & 0 \\
0 & 0 & 0 & 0 & 1 & 0 \\
0 & 0 & 0 & 0 & 0 & EI
\end{bmatrix}, \text{and} \tag{A.52}
$$

$$
\mathbf{F} = \begin{bmatrix}
-w_0 \cos\phi - \frac{1}{2}\rho_w \pi d C_{d_t} u_r \,|u_r|\, \sqrt{1+\epsilon} \\
w_0 \sin\phi + \frac{1}{2}\rho_w d C_{d_n} v_r \,|v_r|\, \sqrt{1+\epsilon} \\
0 \\
0 \\
-\Omega_3 \\
S_n (1+\epsilon)^3
\end{bmatrix}. \tag{A.53}
$$

Note that the distribution of terms as either stiffness or force is somewhat arbitrary as spatial derivatives of ϕ could also appear as Ω_3. Experience has shown that given the dependence of the nonlinear solver (described in appendix C) on the Jacobian of the equations of motion, the solution typically proceeds more quickly when any dependence on ϕ is explicitly incorporated into the equations of motion. This is not surprising given the formulation outlined above in which ϕ is the primary variable used in describing the system geometry.

A.8 Static governing equations

The static governing equations can be derived from the dynamic equations (A.44 to A.49) simply by dropping time derivative and velocity terms. They are

$$T'(\epsilon)\frac{\partial \epsilon}{\partial s} - S_n\frac{\partial \phi}{\partial s} - w_0\cos\phi + \frac{1}{2}\rho_w d\pi C_{d_t}\left(U\cos\phi + V\sin\phi\right)\left|U\cos\phi + V\sin\phi\right|\sqrt{1+\epsilon} = 0,$$

$$\tag{A.54}$$

$$\frac{\partial S_n}{\partial s} + T(\epsilon)\frac{\partial \phi}{\partial s} + w_0\sin\phi + \frac{1}{2}\rho_w d C_{d_n}\left(-U\sin\phi + V\cos\phi\right)\left|-U\sin\phi + V\cos\phi\right|\sqrt{1+\epsilon} = 0,$$

$$\tag{A.55}$$

$$\frac{\partial \phi}{\partial s} - \Omega_3 = 0, \tag{A.56}$$

$$EI\frac{\partial \Omega_3}{\partial s} + S_n\left(1+\epsilon\right)^3 = 0. \tag{A.57}$$

Appendix B

Accuracy and von Neumann Stability Analysis of the Box Method

B.1 Stability

In this appendix we use the classical von Neumann method [48,82] to analyze the stability of the box method as a pure finite difference method. This contrasts with the amplification matrix method of stability analysis which operates on the semi-discrete equation of motion.

Like the amplification matrix method, we consider a single degree-of-freedom homogeneous problem

$$\frac{\partial y}{\partial t} + \omega \frac{\partial y}{\partial s} = 0. \tag{B.1}$$

The fully discrete form of this equation after applying the box method is

$$\frac{1}{2}\left[\frac{y_j^n - y_j^{n-1}}{\Delta t} + \frac{y_{j-1}^n - y_{j-1}^{n-1}}{\Delta t}\right] + \frac{1}{2}\omega\left[\frac{y_j^n - y_{j-1}^n}{\Delta s} + \frac{y_j^{n-1} - y_{j-1}^{n-1}}{\Delta s}\right] = 0. \tag{B.2}$$

The proposed solution is

$$y_j^n = \zeta^n e^{ijk\Delta s}, \tag{B.3}$$

where ζ is an amplification factor, $i = \sqrt{-1}$, and k is a spatial wave number. The condition for stability of the method is $|\zeta| < 1$.

Substituting equation B.3 into equation B.2 and dividing through by $\zeta^{n-1}e^{ijk\Delta s}$ yields

$$\zeta = \frac{\left(1 + e^{-ik\Delta s}\right) - \omega\frac{\Delta t}{\Delta s}\left(1 - e^{-ik\Delta s}\right)}{\left(1 + e^{-ik\Delta s}\right) + \omega\frac{\Delta t}{\Delta s}\left(1 - e^{-ik\Delta s}\right)}. \tag{B.4}$$

For all values of k, Δs, Δt, and ω, $|\zeta| = 1$, and as in chapter 2 we find that the box method is unconditionally stable with no numerical dissipation.

B.2 Accuracy

The truncation error of the box method is found using a procedure similar to that for the semi-discrete equations in chapter 2. Given an exact solution to equation B.1, $\tilde{y}$, Taylor series expansions for the solution near $s = j\Delta s$ and $t = n\Delta t$ are written as

$$\tilde{y}_j^{n-1} = \tilde{y}_j^n - \Delta t\left(\frac{\partial\tilde{y}}{\partial t}\right)_j^n + \frac{\Delta t^2}{2}\left(\frac{\partial^2\tilde{y}}{\partial t^2}\right)_j^n - \frac{\Delta t^3}{6}\left(\frac{\partial^3\tilde{y}}{\partial t^3}\right)_j^n + \ldots \tag{B.5}$$

$$\tilde{y}_{j-1}^n = \tilde{y}_j^n - \Delta s\left(\frac{\partial\tilde{y}}{\partial s}\right)_j^n + \frac{\Delta s^2}{2}\left(\frac{\partial^2\tilde{y}}{\partial s^2}\right)_j^n - \frac{\Delta s^3}{6}\left(\frac{\partial^3\tilde{y}}{\partial s^3}\right)_j^n + \ldots \tag{B.6}$$

$$\tilde{y}_{j-1}^{n-1} = \tilde{y}_j^n - \Delta t\left(\frac{\partial\tilde{y}}{\partial t}\right)_j^n - \Delta s\left(\frac{\partial\tilde{y}}{\partial s}\right)_j^n \tag{B.7}$$

$$+\frac{\Delta t^2}{2}\left(\frac{\partial^2\tilde{y}}{\partial t^2}\right)_j^n + \frac{\Delta s^2}{2}\left(\frac{\partial^2\tilde{y}}{\partial s^2}\right)_j^n + \Delta s\Delta t\left(\frac{\partial^2\tilde{y}}{\partial s\partial t}\right)_j^n$$

$$-\frac{\Delta t^3}{6}\left(\frac{\partial^3\tilde{y}}{\partial t^3}\right)_j^n - \frac{\Delta s^3}{6}\left(\frac{\partial^3\tilde{y}}{\partial s^3}\right)_j^n - \frac{\Delta t^2\Delta s}{2}\left(\frac{\partial^3\tilde{y}}{\partial s\partial t^2}\right)_j^n - \frac{\Delta t\Delta s^2}{2}\left(\frac{\partial^3\tilde{y}}{\partial s^2\partial t}\right)_j^n + \ldots$$

Because $\tilde{y}$ is an exact solution to equation B.1 we can write

$$\left(\frac{\partial\tilde{y}}{\partial s}\right)_j^n = -\omega\left(\frac{\partial\tilde{y}}{\partial s}\right)_j^n, \tag{B.8}$$

$$\left(\frac{\partial^2\tilde{y}}{\partial t^2}\right)_j^n = -\omega\left(\frac{\partial^2\tilde{y}}{\partial s\partial t}\right)_j^n, \tag{B.9}$$

$$\left(\frac{\partial^2\tilde{y}}{\partial s\partial t}\right)_j^n = -\omega\left(\frac{\partial^2\tilde{y}}{\partial s^2}\right)_j^n, \tag{B.10}$$

$$\left(\frac{\partial^3\tilde{y}}{\partial s\partial t^2}\right)_j^n = -\omega\left(\frac{\partial^3\tilde{y}}{\partial s^2\partial t}\right)_j^n. \tag{B.11}$$

Using these relationships and substituting the Taylor expansions for the exact solution into the approximate difference equation B.2 yields an expression for the truncation error [83],

$$\frac{1}{2}\left[\frac{\tilde{y}_j^n - \tilde{y}_j^{n-1}}{\Delta t} + \frac{\tilde{y}_{j-1}^n - \tilde{y}_{j-1}^{n-1}}{\Delta t}\right] + \frac{1}{2}\omega\left[\frac{\tilde{y}_j^n - \tilde{y}_{j-1}^n}{\Delta s} + \frac{\tilde{y}_j^{n-1} - \tilde{y}_{j-1}^{n-1}}{\Delta s}\right] =$$

$$\Delta t^2\left[\frac{1}{6}\left(\frac{\partial^3 \tilde{y}}{\partial t^3}\right)_j^n + \frac{\omega}{4}\left(\frac{\partial^3 \tilde{y}}{\partial s \partial t^2}\right)_j^n\right] + \Delta s^2\left[\frac{1}{4}\left(\frac{\partial^3 \tilde{y}}{\partial s^2 \partial t}\right)_j^n + \frac{\omega}{6}\left(\frac{\partial^3 \tilde{y}}{\partial s^3}\right)_j^n\right] + \text{H.O.T.} \quad \text{(B.12)}$$

The truncation error that results from using the difference equation in place of the exact PDE has terms of lowest order in Δt^2 and Δs^2. Thus, the method is second-order accurate in both space and time.

Appendix C

Solution of the Nonlinear Problem

For all combinations of boundary conditions, 2D or 3D and static or dynamic problems, the mathematical problem is posed as a system of coupled, nonlinear partial differential equations. These systems are solved numerically by discretizing the continuous (exact) forms of these governing equations onto a grid of nodes and calculating an approximate solution. As the grid becomes finer and finer the approximate solution will approach the exact solution. The cost of these finer discretizations which buy better solutions is an increase in computation time.

Both the static and the dynamic cable problems can be generalized as a system of N first-order nonlinear partial differential equations (at each time step the dynamic problem represents a quasi-static equilibrium problem),

$$\mathbf{K}\frac{\partial \mathbf{Y}}{\partial s} + \mathbf{F}\left(s, \mathbf{Y}\right) = 0, \tag{C.1}$$

where $\mathbf{Y}$ is the vector of the N dependent variables. For example, in the 2D static problem (the simplest of all possible cases), equation C.1 represents four equations in four unknowns: strain (from which we can always derive tension via a constitutive relationship), shear force, inclination angle, and curvature. This equation is discretized at the n nodal points using centered finite differences written on the half-grid points. At node j the discretized result is

$$\mathbf{Y}_j - \mathbf{Y}_{j-1} + \frac{s_j - s_{j-1}}{2}\left(\mathbf{F}_j + \mathbf{F}_{j-1}\right) = 0. \tag{C.2}$$

231

When combined with a total of N boundary conditions at the two ends, equation C.2 written at the $n - 1$ half-grid points represents a coupled system of $N \times n$ nonlinear equations in $N \times n$ unknowns. The system can be solved using a relaxation procedure similar to Newton-Raphson [82].

C.1   Newton-Raphson updates

Equation C.2 can only strictly be satisfied by an exact solution for Y_j. Given an inexact first guess at this solution, Y_j^0, we need to develop an iterative scheme to calculate successively better approximations, Y_j^i, through a series of update vectors, ΔY_j^i, such that

$$Y_j^{i+1} = Y_j^i + \Delta Y_j^i, \tag{C.3}$$

where Y_j^{i+1} brings us closer to satisfying the equality in equation C.2. In quantitative terms we want to iteratively minimize the error function

$$e_j^i \left(Y_j^i, Y_{j-1}^i \right) = Y_j^i - Y_{j-1}^i + \frac{s_j - s_{j-1}}{2} \left(F_j^i + F_{j-1}^i \right). \tag{C.4}$$

Neglecting for clarity the dependence on the previous nodal point $(j - 1)$, we can very loosely write

$$\frac{\left[e_j^{i+1} \left(Y_j^i + \Delta Y_j^i \right) - e_j^i \left(Y_j^i \right) \right]}{\Delta Y_j^i} \approx \frac{\partial e_j}{\partial Y_j}. \tag{C.5}$$

The derivatives on the right hand side of equation C.5 can be calculated analytically from the known form of the discretized governing equations (equation C.4). If we were to re-insert the dependence on Y_{j-1}, we would note that these derivatives actually constitute an $N \times 2N$ Jacobian matrix at each j (the matrix is composed of the derivatives of the N equations with respect to the $2N$ variables represented by Y_j and Y_{j-1}). We can assemble the Jacobian matrices from each node into a single global Jacobian matrix (much like element stiffness matrices are assembled into global stiffness matrices in the finite element method), add boundary condition information and formulate a linear system that will find ΔY_j^i to drive the updated error, e_j^{i+1}, to zero. If $\mathbf{J}^i$ is this global Jacobian matrix

evaluated at $\mathbf{Y}^i$ then we see from equation C.5 that

$$\mathbf{J}^i \Delta \mathbf{Y}^i = -\mathbf{e}^i. \tag{C.6}$$

Because only two nodes (j and $j-1$) are coupled by each individual Jacobian matrix the assembled global Jacobian matrix in equation C.6 will be very sparse, with the only non-zero entries clustered near the main diagonal. We can take advantage of this sparsity in solving equation C.6 by using a sparse Gaussian elimination algorithm, NSPIV, due to Sherman [85]. Sparse algorithms such as NSPIV exploit sparsity to reduce both memory requirements and computation time (normal Gaussian elimination is an $O(n^3)$ operation, sparse algorithms can be as efficient as $O(n)$). A distinct advantage of NSPIV over some other algorithms for sparse linear systems is that it can handle matrices with arbitrary sparsity patterns. This capability is important in dealing with systems that are not simply connected (i.e., multipoint moorings and moorings with segments that branch out from other segments).

C.2   Convergence criterion

The iterative updates of $\mathbf{Y}$ continue until the updates, $\Delta \mathbf{Y}$, become sufficiently small as to not warrant continuation of the process. The total error at iteration i, σ^i, is defined as

$$\sigma^i = \frac{1}{Nn} \sum_{k=1}^{N} \frac{1}{\chi_k} \sum_{j=1}^{n} \Delta \mathbf{Y}^i_{j,k}, \tag{C.7}$$

where $\Delta \mathbf{Y}^i_{j,k}$ are the N components of $\Delta \mathbf{Y}$ at node j and iteration i and χ_k are scaling constants appropriate to each of the physical variables represented within $\mathbf{Y}$. The stopping criterion is simply

$$\sigma^i \leq \text{specified tolerance.} \tag{C.8}$$

C.3 Relaxation

The actual update to Y is scaled by a relaxation factor μ_r

$$Y^{i+1} = Y^i + \mu_r \Delta Y^i. \tag{C.9}$$

The purpose of this relaxation factor is to slow (under-relax) the update in cases where strong nonlinearities may mean that the update is not quite as robust as we would like. For highly nonlinear problems, where small changes in parameters can mean large changes in system configuration, the approximation of equation C.5 becomes less valid and our update ΔY^i, if fully applied ($\mu_r = 1$), may actually increase the total system error. A small relaxation factor increases the accuracy of the linearized Taylor series expansion that equation C.5 represents. By slowing the process down ($\mu_r < 1$) the movement of the system from iteration to iteration towards equilibrium will be smoother because the steps between iterations will be smaller.

In many cases, it is desirable to have the relaxation factor vary as the solution progresses. This is particularly true in the static solution of some problems which may need very fine movement of the relaxation process as the solution approaches equilibrium. As an example, in cases with cable resting on the sea floor, the resolution of the location of the touchdown point can be very difficult because of the unilateral nonlinearity represented by the bottom. With too large a relaxation factor the update might pull a substantial amount of cable off the bottom, only to be followed by an update that drops too much onto the bottom.

To accommodate this behavior the actual relaxation factor used from iteration to iteration is varied according to the progress of the solution. If at any point during the solution the error increases from one step to the next, $\sigma^i > \sigma^{i-1}$, the relaxation factor applied to the update at that step is reduced from the factor used at the previous step,

$$\sigma^i > \sigma^{i-1} \quad \rightarrow \quad \mu_r^i = \frac{\mu_r^{i-1}}{R_1}, \tag{C.10}$$

where R_1 is a constant larger than unity. If the error is decreasing as it should then we take the opposite approach and try to speed the solution by increasing the relaxation

factor

$$\sigma^i \leq \sigma^{i-1} \quad \rightarrow \quad \mu_r^i = R_2 \mu^{i-1}, \tag{C.11}$$

where $1 \leq R_2 < R_1$. The relaxation factor is not allowed to increase beyond the baseline value, μ_r, and as a protection against pathological cases in which a very small relaxation can effectively bring the solution to a halt, it is not allowed to decrease beyond $\mu_r/1000$. In our implementation $R_1 = 1.1$ and $R_2 = 1.02$.

The adaptive procedure has the effect of driving the relaxation factor into an equilibrium at which the solution can make the best progress. For regions of the solution in which the baseline relaxation is too large and the solution starts to diverge, equation C.10 kicks in and the relaxation factor is reduced until the solution begins to converge again. Equation C.11 mitigates these reductions and prevents the relaxation factor from getting too small in response to an occasional wayward oscillation in an otherwise downwards solution path.

This procedure still requires a reasonable value for the baseline relaxation factor, but it avoids having to set that factor very low when in fact it may need to be very low only for a portion of a solution. For problems with cable on the sea floor the last part of the solution may require relaxation factors on the order of 10^{-3}, but may proceed quite well in the initial iterations with $\mu_r \sim 10^{-1}$. An example of the error progress during such a problem is shown in figure C-1. In the upper panel, the solid line charts the error in a solution with a baseline relaxation of 0.2. The bottom panel shows how the relaxation factor changes as the solution progresses. The dashed line in the upper panel shows the error in a solution with a constant relaxation of 0.004 (this is the largest constant relaxation factor that results in a solution convergent to $\sigma = 0.001$). Not only does the adaptive procedure save a significant amount of trial and error to determine that 0.004 is a reasonable relaxation, but it also reduces the number of iterations by more than a factor of two.

C.4 Dynamic relaxation

For certain problems, particularly moorings with cable on the bottom and very low levels of horizontal forcing (current and wind), the procedure outlined above can fail to converge when applied to the static equations. Because of the near infinite radius of curvature at the
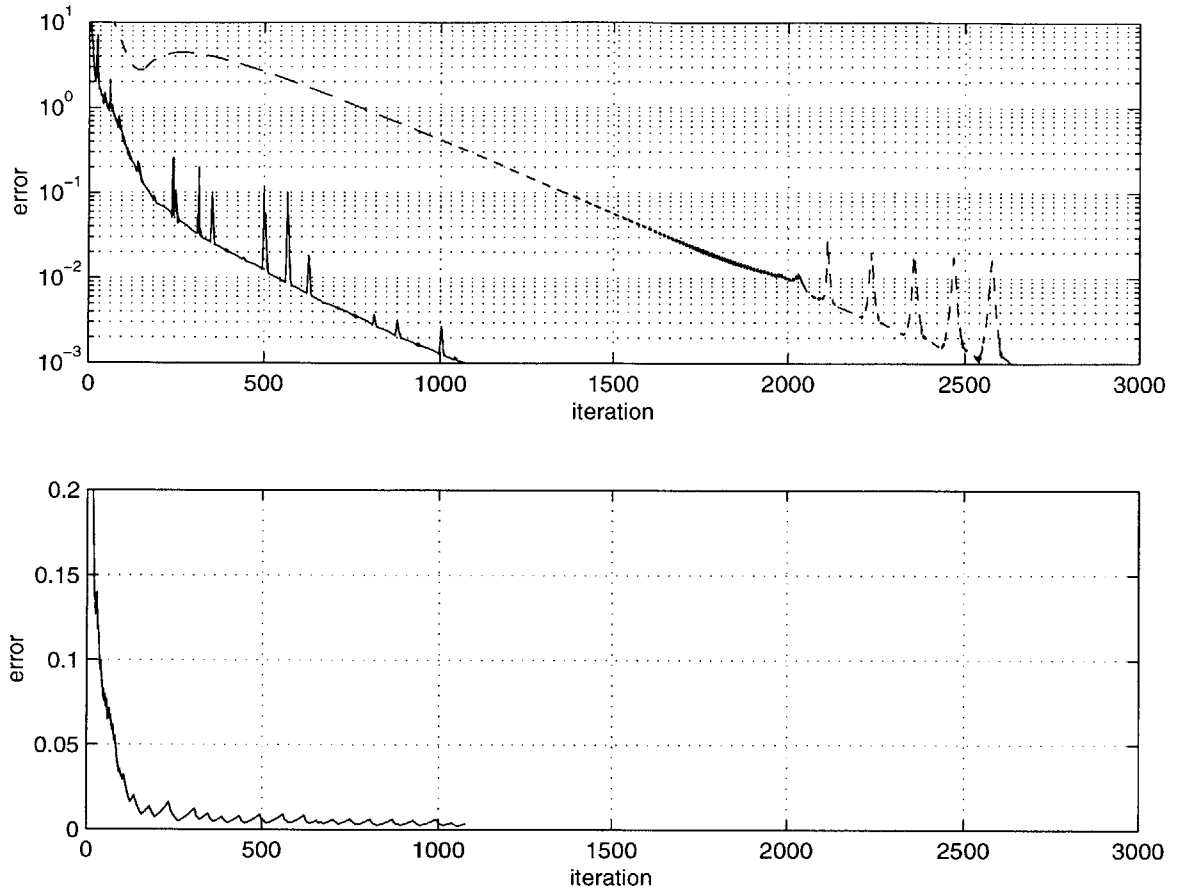
Figure C-1: Error and relaxation factor during the static solution of a mooring problem with line on the bottom. The dashed line in the upper panel is for a solution with the largest constant relaxation factor (0.004) that will result in a solution convergent to an error level of 0.001. The solid lines are the error and relaxation factor for a solution using the adaptive procedure described in the text.

touchdown point in these problems, both the shooting method initial guess (appendix D) and the subsequent relaxation method solution are difficult to obtain in any reasonable amount of computation time. A method that works well to overcome this difficulty is dynamic relaxation.

In dynamic relaxation, we use the standard procedure (shooting initial guess followed by relaxation of the static equations) to obtain a static solution for a problem with a higher level of horizontal forcing. This solution is then used as the initial condition in a dynamic problem with the true level of current and wind applied. As time progresses in the dynamic simulation the mooring falls back to its true equilibrium state at the lower forcing level. With adaptive time-stepping, adaptive relaxation, and the physical drag

and damping in the problem, solutions can be obtained for significantly lower levels of horizontal forcing than with the standard static solution procedure.

The procedure does not work well for three-dimensional problems in which the entire plane of the mooring may rotate as the true three-dimensional forces are applied. In these cases the time to equilibrium can be prohibitively long. Also, for either two- or three-dimensional cases in which the horizontal forcing is reversed from the high initial condition to the desired low condition, the solution can run into difficulty as the mooring crosses through a purely vertical configuration.

C.5 Coordinate integration

This solution procedure calculates the $N \times n$ dependent variables that are explicitly included in the governing equations. Because both static and dynamic governing equations in the formulation derived in appendix A do not explicitly include the coordinate positions of the nodes, these positions must be calculated in a separate procedure. The position of the nodes is critical to the solution; bottom boundary effects, wave forces, and current are all dependent on spatial position. For this reason, the coordinate positions of all the nodes are updated following each iteration. The integration procedure is described in appendix E.

Appendix D

Static Initialization Procedures

In order to solve equations A.54 through A.57 using the method outlined in appendix C we must calculate an initial guess at the solution. We can compute a very good first estimate of the solution using a shooting method to solve the governing equations without bending stiffness and with a simplified treatment of bottom interaction effects. Without bending effects the static problem reduces to two equations in two unknowns, ϵ and ϕ, and a simple form of the shooting method can be employed.

The shooting method solutions have the advantage that they are quite fast and provide a good initial solution for most problems. In many cases they are good enough to use for preliminary static design studies. Because of the simplifications used in these solutions, however, they do not provide appropriate initial conditions for the dynamic solution and thus we still must solve the complete static governing equations using the Newton-Raphson procedure described in appendix C when we want to study system dynamics. The implicit solutions of the complete static equations are also much more easily applied to cases in which the system is not singly connected – multipoint moorings and moorings with branches for example.

D.1 Integration procedure

We can derive the simplified equations from equations A.54 and A.55 by dropping the shear force terms,

$$T'(\epsilon)\frac{\partial e}{\partial s} - w_0 \cos\phi + \frac{1}{2}\rho_w d\pi C_{d_t} \left(U \cos\phi + V \sin\phi\right) |U \cos\phi + V \sin\phi| \sqrt{1 + \epsilon} = 0, \quad \text{(D.1)}$$

$$T(\epsilon)\frac{\partial \phi}{\partial s} + w_0 \sin\phi + \frac{1}{2}\rho_w d C_{d_n} \left(-U \sin\phi + V \cos\phi\right) |-U \sin\phi + V \cos\phi| \sqrt{1 + \epsilon} = 0.$$

$$\text{(D.2)}$$

Because the static boundary conditions depend on the x, y coordinates of the top and bottom node we also explicitly include equations for x and y. Those two equations are

$$\frac{\partial x}{\partial s} = (1 + \epsilon) \cos\phi, \quad \text{(D.3)}$$

$$\frac{\partial y}{\partial s} = (1 + \epsilon) \sin\phi. \quad \text{(D.4)}$$

For the direct integration of the governing differential equations that is inherent in the shooting method, this explicit inclusion of x and y is not significantly more computationally expensive than the integration of the coordinates after the solution that is described in appendix E.

The numerical integration of the simplified governing equations proceeds from the top node to the anchor. Given a set of trial boundary conditions at the top node we integrate downwards using an explicit, fourth-order accurate Runge-Kutta algorithm [82]. If during the integration the calculated vertical position of a node is on or below the sea floor we stop the integration and assume that the remainder of the mooring is on the sea floor with constant angle $\phi = \pm\frac{\pi}{2}$ and constant tension (equal to the tension at the touchdown node). Sea floor slope effects are neglected in this formulation; the bottom is assumed flat at $x = 0$.

D.2 Iterating on the boundary conditions

Like the outer loop iterations required to resolve the boundary conditions for the static solution using the relaxation procedure, shooting solutions require two levels of iteration.

The three types of static boundary conditions detailed in section 3.1.1 are:

1. A buoy is on the surface, but we do not know the buoy draft.

2. A platform is on the surface at some specified horizontal offset from the anchor. We do not know the mooring line tension or the angle ϕ at the top node.

3. A platform is on the surface with a known tension on the mooring line. We do not know the angle ϕ at the top node.

In all three cases we want to specify a value for strain (tension), ϕ, and an arbitrary horizontal position at the top node. We then iteratively specify a vertical position for the top node, integrating the simplified governing equations from node n to node 1 at each vertical position until the computed vertical position of the first or touchdown node is in fact on the bottom. The final value for the vertical coordinate of the top node is then used to compute corrected values for strain and ϕ in the outer loop. In the inner loop we are shooting for the correct position of the top node given some applied force. Within the outer loop we are shooting for the correct applied force.

We need outer loop iterations for the relaxation procedure because the coordinate positions do not enter directly into the governing equations. In this case, where we do have coordinate positions in the governing equations, outer loop iterations are necessitated by the simplified treatment of the bottom. In addition to the unknown boundary conditions at the top node we do not know the location of the touchdown node along the mooring. Because the simplified bottom treatment leads to a solution for the mooring only between the touchdown node and the top node, the position of the touchdown point is critical.

For the first type of boundary condition, given a guess at the draft we can calculate the drag and buoyancy forces and therefore T and ϕ at the top node. If our first two guesses at the draft are the maximum and minimum available (the minimum is defined as the draft that will float the weight of the buoy itself and nothing more) then subsequent guesses can be made using bisection until the position of the top node computed in the inner loop corresponds to a position based on the guessed draft within some specified tolerance. The standard tolerance is 1% of the maximum draft.

The third type of BC is similar in that a guess at ϕ and a known T provide a complete force specification at the top node. With two initial trials at $\phi = 0$ and $\phi = \frac{\pi}{2}$, the solution is bracketed and we can use bisection to calculate a sequence of successively better guesses

for ϕ. The stopping procedure is the same as for the first case – the position of the top node computed in the inner loop must correspond with the known vertical position at the top within some tolerance specified as a percentage of the mesh spacing, Δs, at the top node.

The second case is more complicated because we only know two, x and y, of the four boundary conditions. This requires that we iterate to find both ϵ and ϕ. Rather than employing a sophisticated multi-variable nonlinear root finding technique (such as Newton-Raphson) in the outer loop, we can use the same error correction procedure that we use with these boundary conditions in the outer iteration loop of the regular static solution. Given a guess at the vertical and horizontal components of the tension and the known horizontal position of the top node, we perform the inner iterations to calculate the vertical position of the top node. As in equation 3.7 we update the trial forces based on positioning error and a pseudo-"stiffness" constant, μ_p,

$$F_x^{k+1} = F_x^k - \mu_p x_{\text{td}}^k, \tag{D.5}$$

$$F_y^{k+1} = F_y^k + \mu_p y_{\text{anchor}}^k, \tag{D.6}$$

where $F_{x,y}^k$ are the trial forces at iteration k in the global vertical and horizontal directions, respectively, x_{td}^k is the calculated vertical coordinate of the touchdown node, and y_{anchor}^k is the calculated horizontal coordinate of the first node. The iterative update process is halted when the touchdown node is on the bottom and the anchor node is at the horizontal origin within a tolerance specified as a percentage of the mesh spacing at the anchor.

The primary complication with this approach is that there is no clear best choice for the initial guess at the forces, $F_{x,y}^0$, such that the iteration procedure will have a reasonable chance of rapid convergence. The initial forces in our implementation are based on an inclined catenary solution for a uniform cable with no current. Given a uniform cable with linear stiffness, EA, and weight per length, w_0, the catenary solution for the position of the top end is

$$x(L) = \frac{F_y}{w_0} \left[\sqrt{1 + \left(\frac{F_x}{F_y} \right)^2} - \sqrt{1 + \left(\frac{F_x - w_0 L}{F_y} \right)^2} \right] + \frac{F_x L}{EA}, \tag{D.7}$$

$$y(L) = \frac{F_y}{w_0} \left[\sinh^{-1} \left(\frac{F_x}{F_y} \right) - \sinh^{-1} \left(\frac{F_x - w_0 L}{F_y} \right) \right] + \frac{F_y L}{EA}, \tag{D.8}$$

where F_x and F_y are the applied forces at the top end in the global vertical and horizontal directions, respectively. Given the desired position of the top end of the mooring, we use a two-dimensional nonlinear Newton-Raphson root finding technique to solve equations D.7 and D.8 for $F^0_{x,y}$. In multi-segment applications, EA is calculated as the equivalent stiffness of all segments in series, with the stiffness of each segment computed as the slope of the tension strain relationship at a strain of 1%. The unit weight in these cases is computed by summing all weight and buoyancy forces in the system and dividing by total length.

D.3   Computing shear and curvature

As a final step before proceeding with the relaxation solution for the complete nonlinear problem, the shear force, S_n and curvature, Ω_3 are calculated numerically using centered differences according to equation A.56 (to calculate Ω_3) and equation A.57 (to calculate S_n using differences of the newly calculated Ω_3). For boundary condition cases one and three, the horizontal coordinates are also translated to bring the position of the anchor to the origin.

Appendix E

Coordinate Integration

Because the global coordinate variables x, y, z do not appear in any of the governing equations, they are integrated based on cable coordinates and cable orientation after each iteration of the nonlinear solver. While the coordinates do not enter directly into the governing equations it is important that they be updated because they are used in evaluating the current at a node and determining if a node is lying on the bottom.

E.1 Static solution

For the static problem we can write differential equations for the global coordinates, x and y,

$$\frac{\partial x}{\partial s} = (1 + \epsilon) \cos \phi, \tag{E.1}$$

$$\frac{\partial y}{\partial s} = (1 + \epsilon) \sin \phi. \tag{E.2}$$

Including these two equations directly into the static governing equations would simplify the handling of static boundary conditions in some cases, but only with a 50% increase in computational expense in the nonlinear solver. Trial implementations based on this approach also demonstrated convergence problems when the boundary conditions became part of the iterative solution. The current approach of iterating on the boundary conditions in a loop outside of the nonlinear solver appears to provide better stability and convergence.

Following the box method spatial discretization we discretize equations E.1 and E.2 as

$$2\left(\frac{x_j - x_{j-1}}{s_j - s_{j-1}}\right) = (1 + \epsilon_j)\cos\phi_j + (1 + \epsilon_{j-1})\cos\phi_{j-1}, \tag{E.3}$$

$$2\left(\frac{y_j - y_{j-1}}{s_j - s_{j-1}}\right) = (1 + \epsilon_j)\sin\phi_j + (1 + \epsilon_{j-1})\sin\phi_{j-1}. \tag{E.4}$$

With the first node always located at the origin, we can rearrange the discretized equations to derive recursion relationships for x_j and y_j, $j = 2 \ldots n$,

$$x_j = x_{j-1} + \frac{\Delta s_{j-1}}{2}\left[(1 + \epsilon_j)\cos\phi_j + (1 + \epsilon_{j-1})\cos\phi_{j-1}\right], \tag{E.5}$$

$$y_j = y_{j-1} + \frac{\Delta s_{j-1}}{2}\left[(1 + \epsilon_j)\sin\phi_j + (1 + \epsilon_{j-1})\sin\phi_{j-1}\right]. \tag{E.6}$$

Δs_{j-1} is the spacing between nodes j and $j - 1$.

E.2 Dynamic solution

For the dynamic problem, we have a choice in the integration method. Equations E.1 and E.2 are valid for the dynamic problem as are the temporal differential equations

$$\frac{\partial x}{\partial t} = u_j^i \cos\phi_j^i - v_j^i \sin\phi_j^i, \tag{E.7}$$

$$\frac{\partial y}{\partial t} = u_j^i \sin\phi_j^i + v_j^i \cos\phi_j^i. \tag{E.8}$$

Either pair of equations could be incorporated into the governing equations, but again, only with an increase in computation expense in the nonlinear solver. With x and y effectively decoupled from the other six dependent variables, integration outside of the nonlinear solver is more efficient.

Experience has indicated that integrating the spatial differential equations at each time step provides better results over long time simulations than does integration of the temporal equations. One explanation for this is that the spatial integration couples the coordinate positions of all the nodes together thus providing a strong notion of "connectedness" at each time step. In the temporal integration the positions of the nodes are independent of one another, with the evolution of a node's position in time dependent only on the nodal velocity and local orientation. In principle the two solutions should

be the same given the compatibility requirements enforced in the cable governing equations (equations A.46 and A.47), but compatibility cannot be strictly enforced given the necessarily inexact solution provided by the nonlinear Newton-Raphson procedure.

For the dynamic problem we integrate equations E.1 and E.2 using the standard half-grid spatial discretization and the generalized-α method. The discretized equations are

$$
2(1 - \alpha_k) \left[\frac{x_j^i - x_{j-1}^i}{\Delta s} \right] + 2\alpha_k \left[\frac{x_j^{i-1} - x_{j-1}^{i-1}}{\Delta s} \right]
$$
$$
- (1 - \alpha_k) \left[\left(1 + \epsilon_j^i\right) \cos \phi_j^i + \left(1 + \epsilon_{j-1}^i\right) \cos \phi_{j-1}^i \right]
$$
$$
- \alpha_k \left[\left(1 + \epsilon_j^{i-1}\right) \cos \phi_j^{i-1} + \left(1 + \epsilon_{j-1}^{i-1}\right) \cos \phi_{j-1}^{i-1} \right] = 0, \quad \text{(E.9)}
$$

$$
2(1 - \alpha_k) \left[\frac{y_j^i - y_{j-1}^i}{\Delta s} \right] + 2\alpha_k \left[\frac{y_j^{i-1} - y_{j-1}^{i-1}}{\Delta s} \right]
$$
$$
- (1 - \alpha_k) \left[\left(1 + \epsilon_j^i\right) \sin \phi_j^i + \left(1 + \epsilon_{j-1}^i\right) \sin \phi_{j-1}^i \right]
$$
$$
- \alpha_k \left[\left(1 + \epsilon_j^{i-1}\right) \sin \phi_j^{i-1} + \left(1 + \epsilon_{j-1}^{i-1}\right) \sin \phi_{j-1}^{i-1} \right] = 0. \quad \text{(E.10)}
$$

Rearranging terms yields the recursion relationships for the dynamic calculation of nodal coordinates

$$
x_j^i = x_{j-1}^i + \frac{\Delta s}{2(1 - \alpha_k)} \left[(1 - \alpha_k) \left[\left(1 + \epsilon_j^i\right) \cos \phi_j^i + \left(1 + \epsilon_{j-1}^i\right) \cos \phi_{j-1}^i \right] \right.
$$
$$
\left. + \alpha_k \left[\left(1 + \epsilon_j^{i-1}\right) \cos \phi_j^{i-1} + \left(1 + \epsilon_{j-1}^{i-1}\right) \cos \phi_{j-1}^{i-1} \right] - \frac{2\alpha_k}{\Delta s} \left[x_j^{i-1} - x_{j-1}^{i-1} \right] \right], \quad \text{(E.11)}
$$

$$
y_j^i = y_{j-1}^i + \frac{\Delta s}{2(1 - \alpha_k)} \left[(1 - \alpha_k) \left[\left(1 + \epsilon_j^i\right) \sin \phi_j^i + \left(1 + \epsilon_{j-1}^i\right) \sin \phi_{j-1}^i \right] \right.
$$
$$
\left. + \alpha_k \left[\left(1 + \epsilon_j^{i-1}\right) \sin \phi_j^{i-1} + \left(1 + \epsilon_{j-1}^{i-1}\right) \sin \phi_{j-1}^{i-1} \right] - \frac{2\alpha_k}{\Delta s} \left[y_j^{i-1} - y_{j-1}^{i-1} \right] \right]. \quad \text{(E.12)}
$$

Appendix F

Bootstrap Monte Carlo Confidence Intervals

The bootstrap method is a procedure for calculating the error in a statistically estimated value. The advantage to the procedure is that no assumptions are necessary about the underlying probability distribution of the estimated value. For the purposes of this thesis, the estimated values are regression coefficients calculated using least squares and the errors that are sought are the 95% confidence intervals of those coefficients.

The basic procedure, as outlined by Efron and Gong [26], is as follows. Given n independently observed data points $\mathbf{y}_1, \mathbf{y}_2, \ldots, \mathbf{y}_n$, the regression coefficients are calculated as

$$\hat{\mathbf{C}} = f\left(\mathbf{y}_1, \mathbf{y}_2, \ldots, \mathbf{y}_n\right). \tag{F.1}$$

$\hat{\mathbf{C}}$ represents the best available estimate of the true value of the coefficients, $\mathbf{C}$. For the dynamic tension model in chapter 6 $\mathbf{y}_i$ is defined as

$$\mathbf{y}_i = \left[\sigma_{a_i}, \sigma_{v|v|_i}, \sigma_{T_i}, \bar{T}_i\right]^{\mathrm{T}}. \tag{F.2}$$

The probability distribution for $\hat{\mathbf{C}}$ is estimated using bootstrap with Monte Carlo simulations. A bootstrap sample, $\mathbf{y}_1^*, \mathbf{y}_2^*, \ldots, \mathbf{y}_n^*$, is drawn from the original $\mathbf{y}_i$. The sample is constructed by making n random draws with replacement so that each of the original data points has probability $1/n$ of being selected for each of the locations in the bootstrap
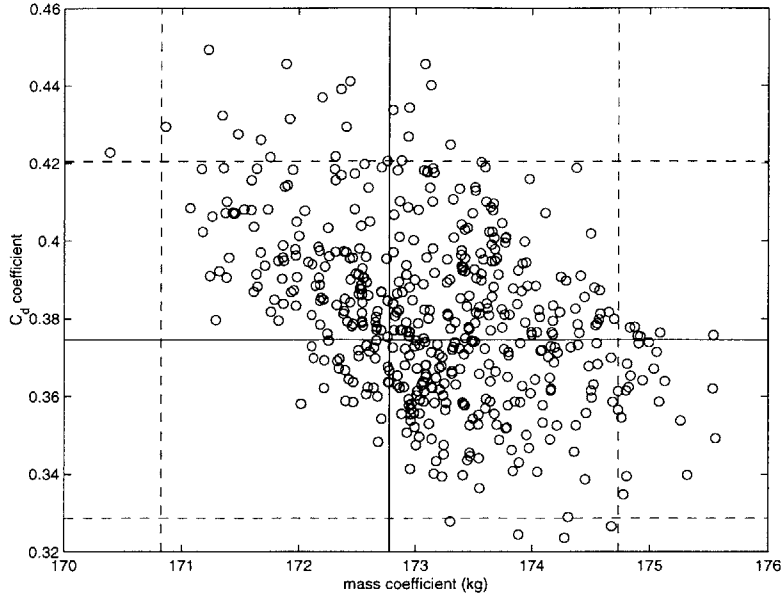
Figure F-1: m and C_d coefficients calculated in 500 distinct bootstrap Monte Carlo simulations. 95% symmetric confidence intervals for m and C_d are indicated by the dashed lines. The best estimates for m and C_d are indicated by the solid lines.

sample. From this bootstrap sample we calculate a bootstrap estimate of the regression coefficients,

$$\hat{\mathbf{C}}^* = f\left(\mathbf{y}_1^*, \mathbf{y}_2^*, \ldots, \mathbf{y}_n^*\right). \tag{F.3}$$

By repeating this procedure some large number of times, B, the distribution of $\hat{\mathbf{C}}$ is mapped out.

Figure F-1 shows the distribution of $\hat{\mathbf{C}}^* = \left[\hat{m}^*, \hat{C_d}^*\right]^{\mathrm{T}}$ for the dynamic tension model developed in chapter 6 with $B = 500$. Individual probability density functions for m and C_d with $B = 20000$ are shown in figures F-2 and F-3, respectively. With distributions for m and C_d there are two basic approaches to calculating confidence intervals. For equal-tailed confidence intervals, the bootstrap simulation results are sorted in ascending order and (for 95% confidence) the end-points of the interval are defined as those points at indices $0.025B$ and $0.975B$ in the sorted list. With this type of formulation there is equal probability that the true value lies above or below the interval. For mass for example, if the interval endpoints are defined as $\hat{m}^*_{0.025B}$ and $\hat{m}^*_{0.975B}$ and $\delta_1 = \hat{m} - \hat{m}^*_{0.025B}$, $\delta_2 = \hat{m}^*_{0.975B} - \hat{m}$,

probability functions for m are

$$P\left(\hat{m} - \delta_1 \leq m \leq \hat{m} + \delta_2\right) = 0.95, \tag{F.4}$$

$$P\left(m \leq \hat{m} - \delta_1\right) = 0.025, \tag{F.5}$$

$$P\left(m \geq \hat{m} + \delta_2\right) = 0.025. \tag{F.6}$$

Hall [41] showed that symmetric intervals have coverage error $O\left(B^{-2}\right)$ compared to $O\left(B^{-1}\right)$ for equal-tailed intervals. Because they are also slightly easier to present they are used throughout the thesis. The probability function for the mass coefficient with a symmetric confidence interval is written as

$$P\left(\hat{m} - \delta \leq m \leq \hat{m} + \delta\right) = 0.95. \tag{F.7}$$

In practice, δ is calculated using bisection. Because of the discrete nature of the count of points that fall in the interval, the search does not always converge to an interval with exactly $0.95B$ points. To be conservative, the bisection algorithm always returns an interval that contains at least $0.95B$ points.
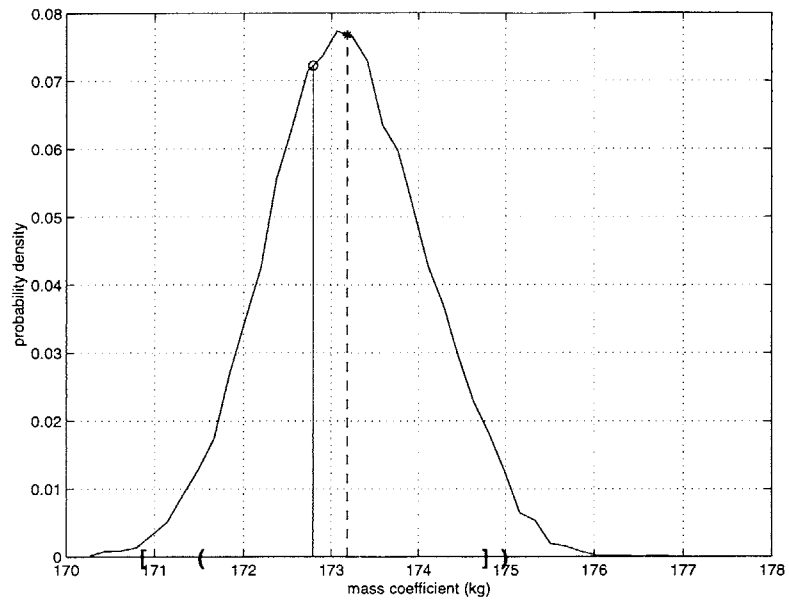
Figure F-2: Probability density function for m based on 20000 distinct bootstrap Monte Carlo simulations. The best estimate for m from the original least squares fit is indicated by the solid vertical line. The mean from the bootstrap simulations is indicated by the dashed vertical line. 95% symmetric [ ] and equal-tailed ( ) confidence intervals are indicated on the horizontal axis.
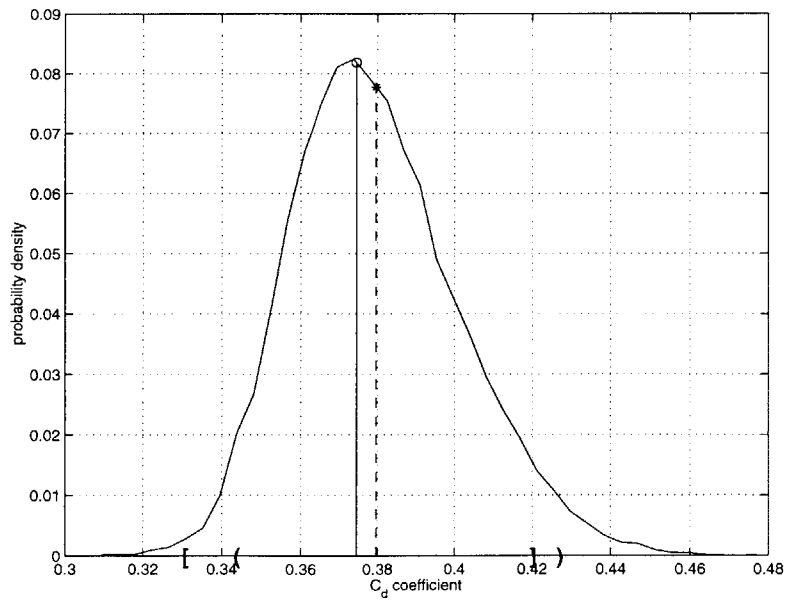
Figure F-3: Probability density function for C_d based on 20000 distinct bootstrap Monte Carlo simulations. Other markings are the same as in figure F-2.

Appendix G

Catenary formulae

For an inextensible line with no current, and vertical and horizontal forces applied at the top point, F_v and F_h, respectively, the catenary expression for the vertical coordinate of the top point is

$$z = \frac{F_h}{w_0} \left[\sqrt{1 + \left(\frac{F_v}{F_h}\right)^2} - 1 \right].$$

(G.1)

With excess scope remaining on the bottom the vertical force at the top of the mooring, F_v, must equal the suspended weight, $w_0 L$. The total tension, T, at the top is simply $\sqrt{F_h^2 + F_v^2}$. If the top of the mooring is at the surface, $z = H$, depth, tension and length are related by

$$T = w_0 H + \sqrt{T^2 - (w_0 L)^2}.$$

(G.2)

After some manipulation, the non-dimensional mean tension can be written as

$$\tau = \frac{1}{2}\left(1 + \frac{L^2}{H^2}\right),$$

(G.3)

$$\Delta\tau = \frac{1}{2}\left(\frac{L^2}{H^2} - 1\right).$$

(G.4)

The suspended length as a function of non-dimensional mean tension is

$$L = H\sqrt{2\Delta\tau + 1}.$$

(G.5)

The rate of increase of the suspended length with increasing $\Delta\tau$ is

$$\frac{dL}{d\tau} = \frac{H^2}{L}.$$

(G.6)

This rate slows as the scope of the mooring increases.

References

[1] C.M. Ablow and S. Schechter. Numerical simulation of undersea cable dynamics. *Ocean Engineering*, 10:443–457, 1983.

[2] J.A.P. Aranha, C.A. Martins, and C.P. Pesce. Analytical approximation for the dynamic bending moment at the touchdown point of a catenary riser. *International Journal of Offshore and Polar Engineering*, pages 293–300, 1997.

[3] G. Bazzi and E. Anderheggen. The ρ-family of algorithms for time-step integration with improved numerical dissipation. *Earthquake Engineering and Structural Dynamics*, 10:537–550, 1982.

[4] Julius S. Bendat. *Nonlinear systems techniques and applications*. Wiley-Interscience, New York, NY, 1998.

[5] Henri O. Berteaux. *Coastal and Oceanic Buoy Engineering*. H.O. Berteaux, Woods Hole, MA, 1991.

[6] John P. Breslin. Dynamic forces exerted by oscillating cables. *Journal of Hydronautics*, 8:19–31, 1974.

[7] D.T. Brown, G.J. Lyons, and H.M. Lin. Advances in mooring line damping. *Underwater Technology*, 21:5–11, 1995.

[8] D.T. Brown and S. Mavrakos. Comparative study on mooring line dynamic loading. Technical report, International Ship and Offsore Structures Congress (ISSC), 1998.

[9] B. Buckham and M. Nahon. Dynamics simulation of low tension tethers. In *Proceedings of Oceans '99*, volume 2, pages 757–766, Seattle, WA, 1999.

[10] J.J. Burgess. Bending stiffness in a simulation of undersea cable deployment. *International Journal of Offshore and Polar Engineering*, 3:197–204, 1993.

[11] R. Burridge and J.B. Keller. Peeling, slipping and cracking – some one-dimensional free-boundary problems in mechanics. *SIAM Review*, 20:31–61, 1978.

[12] Robert Burridge, Jay Kappraff, and Christine Morshed. The sitar string, a vibrating string with a one-sided inelastic constraint. *SIAM Journal of Applied Mathematics*, 42:1231–1251, 1982.

[13] R.H. Canada and D.R. May. Mooring developments and design philosophy at the National Data Buoy Center. In *Proceedings of Oceans '85*, pages 1336–1343, San Diego, CA, 1985.

[14] Mario J. Casarella and Michael Parsons. Cable systems under hydrodynamic loading. *Marine Technology Society Journal*, 4(4):27–44, 1970.

[15] I.K. Chatjigeorgiou and S.A. Mavrakos. Comparison of numerical methods for predicting the dynamic behavior of mooring lines. In *Proceedings of the Ninth International Offshore and Polar Engineering Conference*, Brest, France, 1999.

[16] R. Chiou and J.W. Leonard. Nonlinear modeling of sea floor interactions of mooring cables. In *Proceedings of the Fourth International Offshore and Polar Engineering Conference*, Osaka, Japan, 1994.

[17] R.B. Chiou and J.W. Leonard. Nonlinear hydrodynamic response of curved singly-connected cables. In *Computer modelling in ocean engineering*, pages 407–415. A.A. Balkena Publishers, Rotterdam, 1991.

[18] J. Chung and G.M. Hulbert. A time integration algorithm for structural dynamics with improved numerical dissipation. *Journal of Applied Mechanics*, 60:371–375, 1993.

[19] Jintai Chung and Gregory M. Hulbert. A family of single-step Houbolt time integration algorithms for structural dynamics. *Computer Methods in Applied Mechanics and Engineering*, 118:1–11, 1994.

[20] Robert E. Cornwell and David S. Malkus. Improved numerical dissipation for time integration algorithms in conduction heat transfer. *Computer Methods in Applied Mechanics and Engineering*, 97:149–156, 1992.

[21] Stephen H. Crandall, Dean C. Karnopp, Edward F. Kurtz, Jr., and David C. Pridmore-Brown. *Dynamics of mechanical and electromechanical systems*. Krieger Publishing Co., Malabar, FL, 1968.

[22] A. Dercksen, R.H.M. Huijsmans, and J.E.W. Wichers. An improved method for calculating the contribution of hydrodynamic chain damping on low frequency motions. In *Proceedings of the 24th Offshore Technology Conference*, Houston, TX, 1992. OTC 6967.

[23] Aaron Dinovitzer, Jean-Louis René, Reiner Silberhorn, and Michael Steele. The Mooring Selection Guide (MSG) software. In *Proceedings of Oceans '97*, pages 126–133, Halifax, Nova Scotia, 1997.

[24] James A. Doutt, George V. Frisk, and Hugh Martell. Using GPS to determine the range between a moving ship and a drifting buoy to centimeter level accuracy. In *Proceedings of Oceans '98*, pages 1344–1347, Nice, France, 1998.

[25] J.B. Edson, A.A. Hinton, K.E. Prada, J.E. Hare, and C.W. Fairall. Direct covariance flux estimates from mobile platforms at sea. *Journal of Atmospheric and Oceanic Technology*, 15:547–562, 1998.

[26] Bradley Efron and Gail Gong. A leisurely look at the bootstrap, the jackknife, and cross-validation. *American Statistician*, 37:36–48, 1983.

[27] Peter P. Eggleton. The evolution of low mass stars. *Monthly Notices of the Royal Astronomical Society*, 151:351–364, 1971.

[28] Alf Engseth, Arild Bech, and Carl M. Larsen. Efficient method for analysis of flexible risers. In *Behavior of Offshore Structures*, pages 1357–1371, 1988.

[29] Odd M. Faltinsen. *Sea Loads on Ships and Offshore Structures*. Cambridge University Press, Cambridge, England, 1990.

[30] J. Stephen Fries. Personal communication: email dated 1 February, 2000.

[31] Daniel E. Frye and W. Brechner Owens. Recent developments in ocean data telemetry at Woods Hole Oceanographic Institution. *IEEE Journal of Oceanic Engineering*, 16:350–359, 1991.

[32] I. Fylling, C.T. Stansberg, and K. Mo. Extreme motions and anchor line loads in turret mooring systems. In *Behavior of Offshore Structures*, 1992.

[33] D.L. Garrett. Dynamic analysis of slender rods. *Journal of Energy Resources Technology*, 104:302–306, 1982.

[34] Jason I. Gobat and Mark A. Grosenbaugh. The dynamics of shallow water oceanographic moorings: Experimental and numerical results. In *Proceedings of Oceans '99*, volume 1, pages 107–112, Seattle, WA, 1999.

[35] Jason I. Gobat, Mark A. Grosenbaugh, and Michael S. Triantafyllou. WHOI Cable: Time domain numerical simulation of moored and towed oceanographic systems. Technical Report WHOI-97-15, Woods Hole Oceanographic Institution, November 1997.

[36] Theodore R. Goodman and John P. Breslin. Statics and dynamics of anchoring cables in waves. *Journal of Hydronautics*, 10:113–120, 1976.

[37] Ramnarayan Gopalkrishnan. *Vortex-Induced Forces on Oscillating Bluff Cylinders*. PhD thesis, Massachusetts Institute of Technology and Woods Hole Oceanographic Institution Joint Program, Woods Hole, MA, February 1993.

[38] Mark Grosenbaugh. On the dynamics of oceanographic moorings. *Ocean Engineering*, 23:7–25, 1996.

[39] Mark A. Grosenbaugh. Designing oceanographic surface moorings to withstand fatigue. *J. Atmos. Oceanic Tech.*, 12:1101–1110, 1995.

[40] Mark A. Grosenbaugh, Jason I. Gobat, and Calvert F. Eck. Modeling the dynamics of a shallow-water oceanographic surface mooring using full-scale data. *International Journal of Offshore and Polar Engineering*, to appear, 2000.

[41] Peter Hall. On symmetric bootstrap confidence intervals. *Journal of the Royal Statistical Society, Series B*, 50:35–45, 1988.

[42] H.M. Hilber, T.J.R. Hughes, and R.L. Taylor. Improved numerical dissipation for time integration algorithms in structural dynamics. *Earthquake Engineering and Structural Dynamics*, 5:283–292, 1977.

[43] F.B. Hildebrand. *Advanced calculus for applications*. Prentice-Hall, second edition, 1976.

[44] C. Hoff and P.J. Pahl. Development of an implicit method with numerical dissipation from a generalized single-step algorithm for structural dynamics. *Computer Methods in Applied Mechanics and Engineering*, 67:367–385, 1988.

[45] C. Hoff and P.J. Pahl. Practical performance of the θ_1-method and comparison with other dissipative algorithms in structural dynamics. *Computer Methods in Applied Mechanics and Engineering*, 67:87–110, 1988.

[46] Christopher T. Howell. *Investigation of the dynamics of low-tension cables*. PhD thesis, Massachusetts Institute of Technology and Woods Hole Oceanographic Institution Joint Program, Woods Hole, MA, June 1992.

[47] Shan Huang. Dynamic analysis of three-dimensional marine cables. *Ocean Engineering*, 21:587–605, 1994.

[48] Thomas J.R. Hughes. *The Finite Element Method: Linear Static and Dynamic Finite Element Analysis*. Prentice-Hall, Englewood Cliffs, NJ, 1987.

[49] T.J.R. Hughes. Unconditionally stable algorithms for nonlinear heat conduction. *Computational Methods in Applied Mechanics and Engineering*, 10:135–139, 1977.

[50] T.J.R. Hughes and T. Belytschko. A precis of developments in computational methods for transient analysis. *Journal of Applied Mechanics*, 50:1033–1041, 1983.

[51] Gregory M. Hulbert. Limitations on linear multistep methods for structural dynamics. *Earthquake Engineering and Structural Dynamics*, 20:101–196, 1991.

[52] E. Huse. Influence of mooring line damping upon rig motion. In *Proceedings of the 18th Offshore Technology Conference*, Houston, TX, 1986. OTC 5204.

[53] E. Huse. New developments in prediction of mooring line damping. In *Proceedings of the 23rd Offshore Technology Conference*, Houston, TX, 1991. OTC 6593.

[54] E. Huse and K. Matsumoto. Practical estimation of mooring line damping. In *Proceedings of the 20th Offshore Technology Conference*, Houston, TX, 1988. OTC 5676.

[55] E. Huse and K. Matsumoto. Mooring line damping due to first- and second-order vessel motion. In *Proceedings of the 21st Offshore Technology Conference*, pages 135–148, Houston, TX, 1989. OTC 6137.

[56] Y. Inoue and S. Surendran. Dynamics of the interaction of mooring lines with the sea bed. In *Proceedings of the Fourth International Offshore and Polar Engineering Conference*, pages 317–323, Osaka, Japan, 1994.

[57] James D. Irish. Elastic tether mooring technology. *Sea Technology*, 38:61–69, 1997.

[58] H.M. Irvine and T.K. Caughey. The linear theory of free vibrations of a suspended cable. *Proceedings of the Royal Society of London, Series A*, 341:299–315, 1974.

[59] Neil Kitney and David T. Brown. Efficient prediction of mooring line dynamic loading with experimental verification. In *Proceedings of the 17th Internationl Conference on Offshore Mechanics and Arctic Engineering*, 1998.

[60] C.G. Koh, Y. Zhang, and S.T. Quek. Low-tension cable dynamics: numerical and experimental studies. *Journal of Engineering Mechanics*, 125:347–354, 1999.

[61] C.M. Larsen. Flexible riser analysis – comparison of results from computer programs. *Marine Structures*, 5:107–119, 1992.

[62] John W. Leonard and John H. Nath. Comparison of finite element and lumped parameter methods for oceanic cables. *Engineering Structures*, 3:153–167, 1981.

[63] Y.G. Liu and L. Bergdahl. Influence of current and seabed friction on mooring cable response: comparison between time-domain and frequency-domain analysis. *Engineering Structures*, 19:945–953, 1997.

[64] J.F. McNamara, P.J. O'Brien, and S.G. Gilroy. Nonlinear analysis of flexible risers using hybrid finite elements. In *Proceedings of the Fifth International Conference on Offshore Mechanics and Arctic Engineering*, volume 3, pages 371–377, Tokyo, 1986.

[65] F. Milinazzo, M. Wilkie, and S.A. Latchman. An efficient algorithm for simulating the dynamics of towed cable systems. *Ocean Engineering*, 14:513–526, 1987.

[66] Toshio Nakajima, Seizo Motora, and Masataka Fujino. On the dynamic analysis of multi-component mooring lines. In *Proceedings of the 14th Offshore Technology Conference*, pages 105–120, Houston, TX, 1982. OTC 4309.

[67] M. Nakamura, W. Koterayama, and Y. Kyozuka. Slow drift damping due to drag forces acting on mooring lines. *Ocean Engineering*, 18:283–296, 1991.

[68] Ali Hasan Nayfeh and Dean T. Mook. *Nonlinear Oscillations*. Wiley-Interscience, New York, Wiley Classic Library edition, 1995.

[69] J.N. Newman. *Marine Hydrodynamics*. MIT Press, Cambridge, MA, 1977.

[70] N.M. Newmark. A method of computation for structural dynamics. *Journal of the Engineering Mechanics Division, ASCE*, 85(EM3):67–94, 1959.

[71] Jarmo Niemi. A_0 stable family of single step methods for semidiscretized parabolic problems. *International Journal for Numerical Methods in Engineering*, 38:2829–2836, 1995.

[72] P.J. O'Brien and J.F. McNamara. Analysis of flexible riser systems subject to three-dimensional seastate loading. In *Behavior of Offshore Structures*, pages 1373–1388, 1988.

[73] Athanasios Papoulis. *Probability, random variables, and stochastic processes*. McGraw-Hill Book Company, New York, second edition, 1984.

[74] K.C. Park. Evaluating time integration methods for nonlinear dynamic analysis. In T. Belytschko, J.R. Osias, and P.V. Marcal, editors, *Finite Element Analysis of Transient Non-linear behavior*, ASME Applied Mechanics Symposia Series, pages 35–58. ASME, New York, 1975.

[75] W. Paul, A. Bocconcelli, and P.R. Boutin. The SSAR drifting buoy system, a new approach for a reliable telemetry link to a suspended sensor. In *Proceedings of the 1994 Conference of the Marine Technology Society*, pages 398–408, Washington, D.C., 1994.

[76] W. Paul, A. Bocconcelli, and M. Grosenbaugh. Drifting buoy systems using elastic rubber stretch hoses. In *Behavior of Offshore Structures*, volume 2, pages 213–225, Cambridge, MA, 1994.

[77] Walter Paul, Jim Irish, Jason Gobat, and Mark Grosenbuagh. Coastal mooring design: Taut elastomeric and chain catenary surface buoy moorings. In *Proceedings of Oceans '99*, volume 1, pages 419–426, Seattle, WA, 1999.

[78] J.R. Paulling and W.C. Webster. A consistent, large-amplitude analysis of the coupled response of a TLP and tendon system. In *Proceedings of the Fifth International Conference on Offshore Mechanics and Arctic Engineering*, pages 126–133, Tokyo, 1986.

[79] C.P. Pesce, J.A.P. Aranha, and C.A. Martins. The soil rigidity effect in the touch down boundary-layer of a catenary riser. In *Proceedings of the Eighth International Offshore and Polar Engineering Conference*, volume 2, pages 207–213, Montreal, Canada, 1998.

[80] C.P. Pesce, J.A.P. Aranha, C.A. Martins, O.G.S. Ricardo, and S. Silva. Dynamic curvature in catenary risers at the touch down point region: an experimental study and the analytical boundary-layer solution. *International Journal of Offshore and Polar Engineering*, 8:303–310, 1998.

[81] H. Polachek, T.S. Walton, R. Mejia, and C. Dawson. Transient motion of an elastic cable immersed in a fluid. *Mathematics of Computation*, 17:60–63, 1963.

[82] William H. Press, Brian P. Flannery, Saul A. Teukolsky, and William T. Vetterling. *Numerical Recipes in C: The art of scientific computing*. Cambridge University Press, Cambridge, England, second edition, 1989.

[83] Robert D. Richtmyer and K.W. Morton. *Difference methods for initial-value problems*. Interscience Publishers, New York, NY, second edition, 1967.

[84] Joel V. Sanders. A three-dimensional dynamic analysis of a towed system. *Ocean Engineering*, 9:483–499, 1982.

[85] Andrew H. Sherman. Algorithms for sparse Gaussian elimination with partial pivoting. *ACM Transactions on Mathematical Software*, 4:330–338, 1978.

[86] Y. Sun, J.W. Leonard, and R.B. Chiou. Simulation of unsteady oceanic cable deployment by direct integration with suppression. *Ocean Engineering*, 21:243–256, 1994.

[87] Yang Sun and John W. Leonard. Dynamics of ocean cables with local low-tension regions. *Ocean Engineering*, 25:443–463, 1998.

[88] Chung-Chu Teng and Richard D. Patton. Field experiments for buoy/mooring dynamics – experiment setup and preliminary results. In *Oceans Community Conference Proceedings*, volume 2, pages 592–596, 1998.

[89] Chung-Chu Teng and Henry T. Wang. Mooring of surface wave following buoys in shallow water. In *Proceedings of the Fourteenth International Conference on Offshore Mechanics and Arctic Engineering*, volume I-B, pages 223–230, Copenhagen, 1995.

[90] David O. Thomas. *A numerical investigation of time integration schemes applied to the dynamic solution of mooring lines*. PhD thesis, The University of Newcastle upon Tyne, Newcastle, UK, 1993.

[91] D.O. Thomas and G.E. Hearn. Deepwater mooring line dynamics with emphasis on seabed interference effects. In *Proceedings of the 26th Offshore Technology Conference*, volume 3, pages 203–214, Houston, TX, 1994. OTC 7488.

[92] William T. Thomson. *Theory of vibrations with applications*. Prentice Hall, Englewood Cliffs, NJ, third edition, 1988.

[93] Athanassios A. Tjavaras. *Dynamics of highly extensible cables*. PhD thesis, Massachusetts Institute of Technology, Cambridge, MA, June 1996.

[94] Michael S. Triantafyllou, Antoine Bliek, and Hyunkyoung Shin. Dynamic analysis as a tool for open-sea mooring system design. *SNAME Transactions*, 93:302–324, 1985.

[95] M.S. Triantafyllou. Personal communication, 1999.

[96] M.S. Triantafyllou, D.K.P. Yue, and D.Y.S. Tein. Damping of moored floating structures. In *Proceedings of the 26th Offshore Technology Conference*, pages 215–224, Houston, TX, 1994. OTC 7489.

[97] Michael S. Triantafylloy, Antoine Bliek, Jim Burgess, and Hyunkyoung Shin. Mooring dynamic for offshore applications: Part 1 theory. Technical Report MITSG 86-1, MIT Sea Grant College Program, January 1986.

[98] Thomas S. Walton and Harry Polachek. Calculation of transient motion of submerged cables. *Mathematics of Computation*, 14:27–46, 1960.

[99] William C. Webster. Mooring induced damping. *Ocean Engineering*, 22:57–591, 1995.

[100] W.L. Wood. *Practical Time-Stepping Schemes*. Clarendon Press, Oxford, 1990.

[101] W.L. Wood, M. Bossak, and O.C. Zienkiewicz. An alpha modification of Newmark's method. *International Journal for Numerical Methods in Engineering*, 15:1562–1566, 1981.

[102] O.C. Zienkiewicz, W.L. Wood, and N.W. Hine. A unified set of single step algorithms part 1: general formulation and applications. *International Journal for Numerical Methods in Engineering*, 20:1529–1552, 1984.

[103] Robert F. Zueck. Local/global approach to nonlinear simulation of compliant marine structures. Technical Report TR-2073-OCN, Naval Facilities Engineering Service Center, June 1997.